Atomically-Precise Gold and Silver Electrocatalysts for Superior Nitrate Reduction and Detection

---

A Thesis Submitted in Partial Fulfilment of the Requirements for the Degree of Master of Science in Chemistry

---

Ryan Maxwell Kirk

Department of Chemistry

University of Canterbury

2018

Acknowledgements

First, I would like to express my sincere thanks to my supervisors, Associate Professor Vladimir Golovko and Dr Aaron Marshall, who have not only encouraged my professional development during this study but have also given their time, effort and enthusiasm to ensuring that I may always attain a standard of work truly representative of my best abilities.

I would like to give thanks to the past and present members of the Golovko and Marshall research groups, particularly Ms Mai Tesana and Mr Sam Nesbitt, who have shared the same passion for the pursuit of knowledge and the enthusiasm for research that I myself have been so proud to gain during this work. I give sincere gratitude to Mr Hani Taleshiahangari for his assistance with collecting non-aqueous electrochemical data, and Dr Jared Steven for sharing his accumulated knowledge and practical skills during the initial stage of my research. I warmly extend this appreciation to members of the Kruger research group, who have so effortlessly created and maintained a light-hearted working environment with such stimulating and thought-provoking discussions. To members of the Downard research group, particularly Dr Anna Farquhar who so readily assisted me with any and all aspects of electrochemistry. On a more personal level, I would like to give my sincere thanks to Dr James Ward and Mr Morkel Zaayman for their continued support, insight and encouragement during this work; friends, scholars, and gentlemen whom I so deeply respect and admire.

I am grateful to the academic staff in the Department of Chemistry who have so passionately shared their knowledge and critical insight during my studies, and to visiting fellows who have exposed me to so many fascinating topics, fields and concepts outside of my focus which I would not have otherwise had the opportunity to be introduced to. To all the technical staff in the department, I extend my thanks for ensuring the continuous up-keep and maintenance of essential provisions and services; without them, this work would not have been possible. I would like to thank Dr Marie Squire and Dr Matthew Polson for assistance with mass. spec., NMR and XRD data collection. I also give thanks to the University of Canterbury for the many experiences I have had here, and to KiwiNet for their funding of this project.

Last, but most definitely not least, I would like to thank my parents Dianne and Laurence, who have supported me unconditionally throughout my studies and whose love, encouragement and belief have made me the person I am today. I dedicate this thesis to them.

Abstract and Foreword

This study investigates the electrocatalytic performance of chemically-synthesised gold and silver nanoclusters for nitrate reduction, with the intent of designing an accurate, sensitive and robust electrochemical nitrate sensing platform. An exhaustive literature survey has identified no prior reports which have used such compounds for this specific role, nor have any analogous studies performed such an extensive electrochemical testing nor treatment of experimental data. As such, the majority of findings and conclusions presented in this thesis are without precedent; they establish a rich and varied landscape for future work. Notably, all small gold clusters used in this work are found to be considerably active electrocatalysts for nitrate reduction, in direct contrast to conventional knowledge which has placed bulk gold in an inert status. The respective activity of individual carbon-supported gold-phosphine nanoclusters is also evaluated, and during the course of this thesis an interesting explanation will be offered to rationalise the trends observed, which are independent of size however are contingent on deeper, underlying physiochemical properties.

In Chapter 1, the reader will be introduced to fundamental concepts of electrochemical sensing and the electrochemical reduction of nitrate alongside the specific aims of this work, whilst in Chapter 2 physiochemical aspects of gold nanoclusters and their synthesis will be given. Chapter 3 will summarise current knowledge of the specific nanoclusters synthesised herein, while Chapter 4 will elaborate on their non-aqueous electrochemical behaviour where the first of many novel observations are made. Chapter 5 presents the results and discussion of the detailed investigation into the electrochemical behaviour of carbon-supported gold and silver nanomaterials. Chapter 6 presents a detailed kinetic perspective on the electrocatalytic performance of these catalysts towards the reduction of nitrate. This is concluded with a compelling, novel and logical argument on the nature of nitrate electroreduction at small gold clusters which has not yet been attempted in the scientific literature. Chapter 7 will briefly investigate the best-performing undecagold-based catalyst for the electrochemical sensing of nitrate in both artificial and authentic environmental matrices, followed by a brief conclusion to this work and avenues for future work are outlined. Finally, Chapter 8 provides a detailed description of experimental procedures and characterisation data.

This author proudly presents the results of this substantial study herein, with the hope that the reader will find it as much a pleasure to examine as it was for him to write.

List of Symbols, Abbreviations and Compounds

Listed below are the major symbols used in several chapters of this thesis, as are relevant sections where their meaning is introduced. The electrochemical vocabulary follows that used by Bard and Faulkner.[1]

Roman Symbols

Symbol	Meaning	Typical Units	Section Reference(s)
A	Geometric area	cm^2	1.2
A_{SPR}	Absorbance peak of surface-plasmon resonance band	nm	3.2.1
b	Tafel slope	mV/decade	6.2.5, 6.2.8
$C_x(0,t)$	Surface concentration of species x (at electrode, after an elapsed time t)	mol/cm^2	1.2
C_x^*	Bulk concentration of species x (in solution)	mol/cm^3	1.2
d	Diameter; nanoparticle size	nm	3.2.1
D	Diffusion coefficient	cm^2/s	6.2.1
D^σ	Superatomic (molecular) orbital with azimuthal quantum number $\ell = 2$	-	2.4.2, 4.2
E	Potential	V	1.2
E^0	Standard potential; with respect to NHE at standard conditions	V	1.2
E_{eq}	Equilibrium Potential	V	1.2
E_p	Peak potential	V	1.2
$E_{p/2}$	Half-peak potential	V	6.2.3
$E_{p,a}$	Anodic (oxidation) peak potential	V	6.1.1
$E_{p,c}$	Cathodic (reduction) peak potential	V	6.1.1
ΔE_g	Electrochemical gap/charge-transfer barrier (in DPV)	eV	4.2
F	Faraday constant; total charge on one mole of electrons	C/mol	1.2
f	Abbreviation for $\frac{nF}{RT}$	J/C	1.2
i	Current	A	1.2
i_0	Exchange current	A	1.3, 6.2.5
i_a	Anodic (oxidising) current	A	1.2
i_c	Cathodic (reducing) current	A	1.2
δI	Differential current in DPV	A	4.2
j	Current-density	A/cm^2	6.2
Δj	Differential current-density in CV	A/cm^2	6.1
Δj_p	Differential peak current-density in CV	A/cm^2	6.1.1
k_0	Electrochemical (electron-transfer) rate-constant	cm/s	1.2, 6.2.4, 6.2.6
m_o	Mass-transport coefficient	cm^2/s	1.2, 6.3.1
n	Number of electrons	unitless	1.2, 6.2.2
n'	Number of electrons preceding and inclusive of the rate-limiting step	unitless	6.2.1, 6.2.2, 6.4
O	a) Oxidised form of electroactive compound b) Oxidation peak (in DPV)	- V	a) 1.2, 6.6.1 b) 4.2

P^{σ}	Superatomic (molecular) orbital with azimuthal quantum number $\ell = 1$	-	2.4.2, 4.2
R	a) Reduced form of electroactive compound b) Reduction peak (in DPV)	- V	a) 1.2, 6.6.1 b) 4.2
$\mathcal{R}$	Universal gas constant	J/K·mol	1.2
R_{ct}	Charge-transfer resistance	Ω·cm2	1.3, 6.2.7
S^{σ}	Superatomic (molecular) orbital with azimuthal quantum number $\ell = 0$	-	2.4.2, 4.2
T	Temperature	K	1.2
X	Generic chemical species X	-	6.6.1
Y	Generic chemical species Y	-	6.6.1

Greek Symbols

Symbol	Meaning	Typical Units	Section Reference(s)
α	Charge-transfer coefficient	unitless	1.2, 6.2.2, 6.2.3, 6.2.4, 6.2.8, 6.4
δ	Chemical shift (NMR)	Parts per million	-
λ_{SPR}	Surface-plasmon peak wavelength	nm	3.2.1
η	Overpotential; deviation of E from E_{eq}	mV	6.1.1, 1.3
υ	Scan-rate	mV/s	6.2.1
υ_c	Critical scan-rate; horizontal-axis intercept of Laviron plot	mV/s	6.2.4
ψ	Nicholson-Shain parameter; measure of electrochemical reversibility	unitless	6.3.3
ζ	Matsuda-Ayabe parameter; measure of electrochemical reversibility	unitless	6.3.2

Abbreviations

Term	Meaning
AC	Activated Chemisorption (Model)
Ag/AgCl	Silver/Silver-Chloride reference electrode (saturated KCl solution)
AuO_x	Representative gold-oxide species; mixture of Au(II) and Au(III) compounds.
$[Au_n]^z$	Generic gold cluster of n atoms with a charge of z units and unspecified ligand periphery
$[Au_6]^{2+}$	Used in place of $[Au_6(dppp)_4]^{2+}$; ligands implied
$[Au_8]^{2+}$	Used in place of $[Au_8(PPh_3)_8]^{2+}$; ligands implied
$[Au_8Pd_1]^{2+}$	Used in place of $[Au_8Pd_1(PPh_3)_8]^{2+}$; ligands implied
$[Au_9]^{3+}$	Used in place of $[Au_9(PPh_3)_8]^{3+}$; ligands implied
$[Au_{11}]^{+}$	Used in place of $[Au_{11}(PPh_3)_8Cl_2]^{+}$; ligands implied
$[Au_{13}]^{3+}$	Used in place of $[Au_{13}(dppe)_5Cl_2]^{3+}$; ligands implied
Au_6	A cluster of six gold atoms; ligands unspecified or assumed to be removed
Au_8	A cluster of eight gold atoms; ligands unspecified or assumed to be removed
Au_8Pd_1	A cluster of eight gold atoms and one palladium atom; ligands unspecified or assumed to be removed

Au_9	A cluster of nine gold atoms; ligands unspecified or assumed to be removed
Au_{11}	A cluster of eleven gold atoms; ligands unspecified or assumed to be removed
Au_{13}	A cluster of thirteen gold atoms; ligands unspecified or assumed to be removed
CV	Cyclic Voltammetry
DPV	Differential-Pulse Voltammetry
ESI-MS	Electrospray-Ionisation Mass-Spectrometry
eV	Electron-volt; equal to the potential energy change of one electron accelerated across a potential difference of one volt
HER	Hydrogen Evolution Reaction; $2H^+ + 2e^- \rightarrow H_2$
HR-TEM	High-Resolution Transmission Electron Microscopy
HOMO	Highest-Occupied Molecular Orbital
IHOAM	Incipient Hydrous-Oxide/Adatom Mediator (Model)
LUMO	Lowest-Unoccupied Molecular Orbital
m/z	Mass to charge ratio
M	Molar; mol/L
mM	Milli-molar; $\times 10^{-3}$ mol/L
μM	Micro-molar; $\times 10^{-6}$ mol/L
NHE	Normal Hydrogen Electrode, potential of a Pt electrode in strong acid solution ($[H^+]$ = 1 M); E^0 = 0.00V at 25 °C and 1 atmosphere of pressure
nm	Nanometre(s); $\times 10^{-9}$ m
NMR	Nuclear Magnetic Resonance
NP	Nanoparticle
ppm	Parts Per Million
PSEPT	Polyhedral-Skeletal Electron-Pair Theory
SD	Standard Deviation
UV-Vis	Ultra-Violet/Visible Light Spectroscopy
VC	Vulcan™ Carbon; mesoporous carbon support, *ca*. 250g/m^2 specific surface-area
XPS	X-ray Photoelectron Spectroscopy

Major Compounds

Species	**Name**
$[AuCl_4]^-$	Tetrachloroaurate
$AuPPh_3Cl$	Triphenylphosphine-gold chloride
$AuPPh_3NO_3$	Triphenylphosphine-gold nitrate
$Au_2(dppe)Cl_2$	(1,2-bis(diphenylphosphino)ethane)digold dichloride
Bu_4NPF_6	Tetra-*n*-butylammonium hexafluorophosphate
$CHCl_3$	Chloroform
CH_2Cl_2	Dichloromethane
Cl^-	Chloride
dppe	1,2-bis(diphenylphosphino)ethane; $Ph_2P(CH_2)_2PPh_2$
dppp	1,3-bis(diphenylphosphino)propane; $Ph_2P(CH_2)_3PPh_2$
Et_2O	Diethyl ether
EtOH	Ethanol; CH_3CH_2OH
H_2SO_4	Sulphuric acid
$HAuCl_4$	Tetrachloroauric acid
HCl	Hydrochloric acid
$HSPhMe_2$	2,4-dimethylbenzene thiol
KCl	Potassium chloride
KOH	Potassium hydroxide

MeOH	Methanol; CH_3OH
N_2	Dinitrogen
N_2O	Nitrous oxide
Na_2SO_4	Sodium sulphate
$Na_3C_6H_5O_7$	Trisodium citrate
$NaBH_4$	Sodium borohydride
Nafion-117™	Sulphonated tetrafluoroethylene polymer
$NaNO_2$	Sodium nitrite
$NaNO_3$	Sodium nitrate
NH_2OH	Hydroxylamine
NH_3	Ammonia
NO	Nitric oxide
NO_2	Nitrogen dioxide
$[NO_2]^-$	Nitrite
$[NO_3]^-$	Nitrate
$Pd(PPh_3)_4$	Tetrakis(triphenylphosphine)palladium(0)
Pet. ether	Petroleum ether; aliphatic hydrocarbon blend
PPh_3	Triphenylphosphine
$[PPh_4]^+$	Tetraphenylphosphonium
$^iPr_2O$	Diisopropyl ether
^{i}PrOH	Isopropanol; $(CH_3)_2CHOH$
PR_3	Generic tertiary phosphine ligand; R usually aryl
SCN^-	Thiocyanate
SR^-	Generic thiolate ligand; R aryl or alkyl
THF	Tetrahydrofuran; C_4H_8O
THT	Tetrahydrothiophene; C_4H_8S
X^-	Generic anion

List of Figures and Tables

Figures

Tables

Table of Contents

Chapter 1

Introduction to Electrochemical Sensing and the Electrochemistry of Nitrate

1.1 – Nitrates in Freshwater

Interest into chemical sensors is driven by the prospect of cost-effective, accurate and on-demand analytical methods to detect and quantify the presence of contaminants in environmental samples. The continuous release of pollutants into the global environment has led to a concerted focus on developing sophisticated and robust technologies for monitoring and remediation purposes. Among the key pollutants, the family of inorganic nitrogenous species, such as dissolved *nitrates* (NO_3^-) and *nitrites* (NO_2^-), is ubiquitous and is some of the most damaging in aquatic environments.[2] These species have been identified as principal contributors to adverse ecological effects such as: 1) the excessive growth and proliferation of primary producers such as algae, leading to eutrophication of aquatic ecosystems; 2) the promotion of anoxic waters by depletion of the dissolved oxygen content; 3) irreparable harm to aquatic organisms in the case of pollution at the near-toxic levels, impairing their ability to grow, survive and reproduce.[2, 3] High levels of inorganic nitrogen pose a significant risk to the fragile aesthetic and ecological condition of waterways globally, and especially so in countries such as *Aotearoa*-New Zealand that value a strong cultural and economic relationship with the wider environment.

Many compounds of nitrogen, such as nitrate, occur naturally as components of the global nitrogen cycle. Major sources of non-anthropogenic nitrate in the environment include the erosion of mineral deposits, the decomposition of organic matter and bacterial nitrogen-fixation in plants and soils.[4] However, the widespread and inefficient distribution of agricultural fertilisers, effluent run-off from grazing livestock, and atmospheric NO_x generation from fossil-fuel combustion contributed to two-fold increase in nitrate levels in global waterways since the 1950's.[5] The facile solubility of nitrates enables percolation through soils into ground-waters and aquifers, posing a significant public health hazard if such sources are used for municipal drinking water supplies.[4, 5] For example, an excess consumption of nitrate through diet has been linked to *methemoglobinemia*, a condition that affects the ability of haemoglobin to transport oxygen throughout the human body.[6] Chronic effects of a high-nitrate intake include cell, tissue and organ damage, hypertension and various *in utero* developmental effects.[6, 7] In addition, nitrate is metabolised in the body to nitrite by reductase-enzymes. There is scientific evidence that nitrites are further converted *in vivo* to *N*-nitrosamines, [8-10] a family of organic-nitrogen compounds that are potently genotoxic and carcinogenic.

In New Zealand, the Maximum Acceptable Value (MAV) set by the Ministry of Health for nitrate in drinking water is 50 mg/L (50 parts per million, ppm),[11] in accordance with World Health Organisation recommendations. Note that compared to other drinking water contaminant standards, this MAV *does not* contain a typical 10- or 100-fold safety-factor to guarantee sufficient protection. It is therefore likely that an innocuous level of nitrate in drinking water is significantly lower than 50 mg/L. The occurrence of excessive nitrate in waterways from which drinking waters are sourced is a risk to public health, and thus concentrations should be actively monitored to avoid adverse effects and expensive remediation of water supplies. Reviews in 2015 by Environment Canterbury (ECan) have identified that large areas of mid- and south-Canterbury are at moderate-to-high risk for exceeding the MAV for nitrate in groundwater supplies.[12] However, these reviews are commissioned intermittently as the large cost of such wide-scale sampling program is a limiting factor. For this reason, it is often difficult to establish models over time to pinpoint exact geographical origins of and specific accumulation pathways for nitrate in the wider environment. In regions where intense agricultural activity dominates the local economy, such as New Zealand, the pollution of waterways and groundwaters with nitrate becomes a persistent issue that necessitates active monitoring. For many agencies and governing bodies, the real-time assessment of nitrate levels in surface- and ground-waters is imperative for predictive, legislative and preventative action. However, current laboratory methods are time-consuming, inconvenient and expensive. Importantly, there are limited commercial options for remote, real-time automated systems for nitrate detection at present. *Electrochemical nitrate sensors* offer a viable and economic means by which this vision can be realised.

1.2 – Principles of Electrochemical Sensing

Electrochemical sensors are devices that utilise a chemical event at an electrode surface to detect and quantify the presence of an analyte in solution. Specifically, this event is an interaction with the *sensing element* to perturb some physical property (*e.g.* electrical current, potential, resistance) of the sensor. The extent of disturbance to this property, termed the *sensor response*, can be mathematically related to the amount of analyte undergoing the chemical event (*vide infra*), and hence the quantity present in the sample.[13] Those sensors that operate within the domain of *amperometry* are by far the most mature group investigated in the

literature, where information is gained from a *current-concentration relationship*. In this approach, a suitable potential difference is applied between two electrodes immersed in the sample matrix, initiating charge-transfer to the analyte of interest.[13] Electrons are either supplied or withdrawn across the working electrode-electrolyte interface to continuously reduce or oxidise the analyte in a process of *electrolysis.* These reactions are generalised below in reaction 1.1:

$$O + ne^- \rightleftarrows R \tag{1.1}$$

Where O and R are the oxidised and reduced forms of the analyte participating in the charge-transfer reaction, which may or may not be chemically-reversible. At any time t during electrolysis, the net measured current i is a function of the applied potential E and of the respective concentrations of O and R at the working electrode surface, $C_O(0,t)$ and $C_R(0,t)$, given by the *current-potential* (i-E) *relationship*:[1]

$$i = nFAk_0[C_O(0,t)e^{-\alpha f\left(E-E_{\mathrm{eq}}\right)} - C_R(0,t)e^{(1-\alpha)f\left(E-E_{\mathrm{eq}}\right)}] \tag{1.2}$$

Where n is the number of electrons transferred per reacting molecule of analyte, F is the Faraday constant, A is the geometric area of the working electrode, k_0 is the electrochemical rate-constant for the reaction, α is a unitless kinetic parameter (the charge-transfer coefficient; Section 6.2.2), f is an abbreviation for $\frac{nF}{\mathcal{R}T}$, and E_{eq} is the *formal equilibrium potential* for the $O \rightleftarrows R$ couple, which varies with experimental context. Note that if $E = E_{\mathrm{eq}}$ then equilibrium between O and R is established and i is now the *exchange current* i_0, which reflects the kinetic facility of the system to maintain equilibrium. If, however, E departs from the equilibrium potential then the individual contributions from either reduction ($E < E_{\mathrm{eq}}$; $O \rightarrow R$) or oxidation ($E > E_{\mathrm{eq}}$; $R \rightarrow O$) reactions become dominant and the reverse component can be negated, giving the *cathodic* and *anodic* currents i_c and i_a respectively. Within the context of an amperometric nitrate sensor, the analyst is primarily concerned with the cathodic reaction, that is:

$$NO_3^- + 2e^- + 2H^+ \rightarrow NO_2^- + H_2O \tag{1.3}$$

Where the *standard thermodynamic reduction potential* of the nitrate anion in the half-cell above, denoted E^0, is +0.94 V *vs.* NHE.[14, 15] In practice, the equilibrium potential E_{eq} is seldom equal to E^0, for kinetic reasons which will be outlined in Section 1.3. At sufficiently negative potentials the reverse reaction (nitrite oxidation) is essentially inoperative, and the i-E relationship simplifies to a current-concentration proportionality:

$$i_c \propto C_{NO_3^-}(0,t) \text{ for } E < E_{\text{eq}} \quad (1.4)$$

Here, i_c is the cathodic current due to reduction of NO_3^- anions, which have local concentration $C_{NO_3^-}(0,t)$ at the working electrode surface after time t. If the applied potential E is made increasingly negative relative to E_{eq}, the rate of NO_3^- reduction will increase exponentially as the energy of reactant electrons ascend and the activation-barrier for the reaction is further exceeded.[1] However, since the population of NO_3^- in the vicinity of the working electrode will deplete during electrolysis, the magnitude of i_c is eventually constrained by the rate at which *mass-transport* (diffusion) delivers NO_3^- from the bulk solution to the electrode surface to reconcile a concentration gradient. The reaction rate will reach a maximum at peak potential E_P where i_c is under mass-transport limited conditions, and *all* NO_3^- that arrives at the electrode surface immediately undergoes reduction. The surface concentration $C_{NO_3^-}(0,t)$ is now effectively equivalent to the bulk concentration $C^*_{NO_3^-}$,[16] and therefore the *mass-transport limited current* $i_{l,c}$ is *directly* proportional to the concentration of NO_3^- in the entire sample, described by an analytically-useful *linear* relationship:[13]

$$i_{l,c} = nFAm_o C^*_{NO_3^-} \text{ for } E = E_P \quad (1.5)$$

Where m_o is the mass-transport coefficient of NO_3^- through the sample matrix, which incorporates both k_0 and the exponential term in the *i-E* relationship and therefore varies with E. Note that for the above relationship to hold, mass-transport must *exclusively* take place *via* diffusion (*i.e.* migration and convection effects must be negated by experiment design). As it is always possible (in principle) to apply a potential sufficiently large to instantaneously generate mass-transport limited conditions, the bulk concentration of NO_3^- in a sample can be determined simply by measuring the *maximum reduction current* $i_{l,c}$ at E_P.[16] This is a fundamental electroanalytical principle by which this amperometric NO_3^- sensor will operate.

1.3 – Nitrate Electroreduction: Thermodynamics, Kinetics and Mechanics

It is curious that the rather positive value of E^0 for the nitrate/nitrite half-cell (+0.94 V *vs.* NHE[14, 15]; reaction 1.3) indicates the nitrate anion should be a good oxidising agent, and from a thermodynamic perspective reduction should be favourable at ambient temperature and pressure.[17, 18] However, it is almost always the case that NO_3^- *electro*reduction is experimentally observed at substantially more-negative potentials than the

standard reduction potential, E^0, demands. The discrepancy arises chiefly due to sluggish interfacial kinetic effects associated with a step-wise, heterogeneous, electrochemical reaction involving adsorption, charge-transfer and molecular rearrangement.[19] Since the extent of structural reorganisation to the nitrate anion is minor (scission of one N-O bond) reduction is *chemically* reversible, however nitrate may be further transformed to dinitrogen (N_2) or ammonia (NH_3), or indeed any one of many other possible intermediate products (*e.g.* NO_2, NO, N_2O, NH_2OH etc.); in such cases reduction is practically *irreversible* and consumes between 3 and 10 electrons at *different* values of E^0.[19] The irreversibility of further reduction (*i.e.* beyond nitrite) can be ascribed to the formation of gaseous species which only weakly bind to the electrode surface, and physically desorb before the reverse reaction can take place. The relative adsorption strength of these intermediate species to the electrode surface is one explanation for the respective product selectivity observed at different materials.

Mechanistically, the *rate-determining step* for heterogeneous NO_3^- reduction is usually electron-transfer into the vacant π^* orbital (LUMO) of the nitrate anion.[20] Initial charge-transfer kinetics may be slow due to the relatively high-lying energy of the nitrate LUMO[21, 22] compared to the electronic band-structures of most common electrode materials (*e.g.* transition metals) at ambient temperature.[1] Such universally poor kinetics are often indicated by comparatively small values of k_0 and i_0,[1, 13] and additional energy must often be supplied *beyond* the thermodynamic requirement to drive charge-transfer at an appreciable rate. Moreover, the reasonably high enthalpy of NO_3^- adsorption to metal surfaces (*c.f.* in co-ordination chemistry the nitrate anion is, at best, a weakly binding ligand and may easily be displaced), which is a necessary but generally *not* rate-limiting step,[22-24] is known to further hinder electrolysis.[20] Therefore, some form of catalyst is usually required to enhance the rate of nitrate electrolysis by lowering the kinetic obstruction to charge-transfer (presenting reactant electrons an alternative tunnelling path[25]), or offering energetically favourable adsorption sites, or both. The excess energy demanded for heterogeneous charge-transfer is measured by the deviation of E from E_{eq}, a quantity expressed as the *overpotential* η:[1, 16]

$$\eta = \left|E - E_{\mathrm{eq}}\right| \tag{1.6}$$

The overpotential corresponding to $E = E_P$ (where electrolysis is driven at a sufficient rate such that mass-transport controls the magnitude of i) serves as a metric of the *kinetic activation energy-barrier* for the

electrochemical reaction:[1, 16, 26] Therefore, η may be utilised as a convenient (but never solitary) index of electrocatalytic performance. If charge-transfer is the rate-determining step in a heterogeneous electrochemical reaction, such that the overpotential is only considered to involve surmounting the activation-energy barrier (*i.e.* adsorption contains a comparatively small energy penalty), and if the magnitude of η is not excessively large (<< 1 V), the i-E relationship may be algebraically distilled to the *current-overpotential* (i-η) *characteristic*:[1, 16]

$$i = i_0 f \eta \tag{1.7}$$

Where inspection confirms that small exchange-currents (i_0) indeed require greater overpotentials to displace the $O \rightleftarrows R$ equilibrium and extract an appreciable rate of electrolysis, i. The ratio $\frac{\eta}{i}$ has units of resistance and is reminiscent of Ohm's law, giving one definition of the *charge-transfer resistance*, R_{ct}:[1, 16]

$$R_{ct} = \frac{1}{f i_0} \tag{1.8}$$

The charge-transfer resistance, like i_0 and k_0, is a meaningful descriptor of the kinetic facility of electrolysis when equilibrium is disturbed, and the electrochemical reaction is driven by the application of η. More specifically, R_{ct} is indicative of the electronic obstruction to the charge-transfer step during electrochemical reactions, if an electrolytic cell is modelled as an equivalent electrical circuit and R_{ct} is the resistance component across the electrode/electrolyte interface.[1, 27] A facile electrochemical process is characterised by a small resistance from the system against that process to occur, and *vice-versa* for sluggish electrochemical reactions.[27] Together, i_0, k_0, η and R_{ct} are characteristic of the *unique* interactions between the electrode and analyte as an electrochemical reaction proceeds, and mathematically unify the concept of *electrocatalysis*.

Ideally, a suitable electrocatalyst for nitrate reduction would have the following physical characteristics:

i. Large i_0: ability to displace the $O \rightleftarrows R$ equilibrium towards a net $O \rightarrow R$ or $R \rightarrow O$ reaction.
ii. Large k_0: kinetic facility of heterogeneous charge-transfer to both O and R.
iii. Small η: energy expended to overcome kinetic effects and surmount the activation-barrier.
iv. Small R_{ct}: physical opposition to a charge-transfer event across electrode-electrolyte interface.

1.4 – Catalysts for Nitrate Electroreduction

1.4.1 *Bulk Metal Electrodes*

The electrochemical reduction of nitrate in water is well-studied in the literature, with technological relevance to waste-water denitrification (*i.e.* the complete conversion of pollutant NO_3^- and NO_2^- to benign N_2),[28] the treatment of nitrate-containing nuclear-fuel wastes (to avert the solubilisation of hazardous radioisotopes during storage),[29] and the "green" synthesis of industrially-valuable products (*e.g.* NH_3, N_2H_4 and NH_2OH).[30] The hydrogenation of NO_3^- offers complimentary approaches[31] to these goals with parallels and concepts directly applicable to electroreduction, and reviews summarising key concepts, catalyst development and mechanistic aspects of nitrate reduction using electricity, hydrogen, light, enzymes or other chemical species have been published.[17, 19, 32-35] For the analyst pursuing an efficient (or novel) catalyst for electrochemical nitrate sensing, a great deal of information can be gained from these works, since the initial NO_3^- reduction step is a mutually common objective.

As outlined in Section 1.3, the electroreduction of nitrate in aqueous media can be surprisingly difficult to accomplish, and some form of catalyst is usually required to enable a satisfactory rate of reaction for practical purposes. The exact choice of electrode material is crucial for *efficient* NO_3^- electroreduction, and therefore to the performance of a superior amperometric nitrate sensor. In principle, any suitably conducting material can accomplish this reaction, however in practice many electrodes – particularly bare metal surfaces – possess disappointing electrocatalytic activity.[36]

As it is with many electrochemical reactions, the *specific* physiochemical interactions between electrode surface and the electroactive species determine the overall facility of charge-transfer kinetics,[37] and the catalytic nature of certain electrode materials is evident by which overpotentials are moderated. Since the electroreduction of nitrate is so strongly dependant on experimental conditions (*e.g.* pH, supporting electrolyte, NO_3^- concentration, other electroactive species *etc.*)[17] it is difficult to establish an "absolute" scale of catalytic performance covering *all* electrode materials under *all* possible electrolytic settings. However, it is generally found that nitrate electroreduction is comparatively facile on polycrystalline Cu,[38-42] Rh[43-46] and Sn[47-50] electrodes, where catalytic activity is normally sufficient to induce mass-transport limited conditions at smaller overpotentials.[36] Noble-metals, primarily Pd,[23] Pt[22, 23, 44, 46, 51-54] and Au[55, 56] show disappointingly sluggish

performance and usually require higher overpotentials to generate mass-transport limited currents, which frequently overlap with the hydrogen evolution process.[57] Other transition metals, including Ag, Fe, Ni and Ir, show a range of intermediate activities,[40, 53, 58-61] as do most *p*-block metals such as Bi, Cd, In and Pb.[29, 48-50, 60, 62-67]

Studies on single-crystal electrodes with low-index planes suggest that the high activity of Cu may arise from the formation of surface-bound Cu^+ on (111) steps during electrochemically-induced structure evolution;[68-70] the cuprous ion being a known homogeneous catalyst for NO_3^- reduction.[71] Furthermore, the Cu (100) surface is found to be particularly stable in acidic medium and opposes the spontaneous dissolution that normally takes place at the (110) and (111) orientations and at polycrystalline Cu.[24, 68] For this reason, the (100) surface possesses lower activity for nitrate reduction, possibly due to a decreased concentration of surface-bound Cu^+ and Cu^{2+} species. Interestingly, the Cu (100) surface also appears to favour a six-electron reduction of NO_3^- to NH_2OH whereas the (110) and (111) facets preferentially form NH_3 in an eight-electron process.[24, 68] It is not yet known if similar process operate on specific Rh or Sn crystal planes, however analogous experiments on single-crystal Pt electrodes find that the (110) surface is significantly more active than (111) or (100) faces,[72, 73] albeit the former shows higher susceptibility to deactivation in the presence of strongly adsorbing ions such SO_4^{2-}, Cl^- or H^+.[74-77] It is also noteworthy that Pd and Pt – two of the least active transition metals for NO_3^- reduction – are highly active for the reduction of NO_2^- onwards[78] and possess greater product selectivity for N_2 formation,[19, 32] making these materials excellent candidates for denitrification purposes; non-noble-metals appear unable to catalyse N-N bond formation to any appreciable extent. Overall the most-active metals for the rate-limiting NO_3^- to NO_2^- step,[36] and generally more active themselves in alkaline media[38, 44, 69] (curious, since protons are a reagent during nitrate reduction; in practice H^+ adsorption may exert an inhibitory effect.[79] Additionally, OH^- ions are thought to participate in a electrocatalytic redox cycle involving hydrous-metal oxides; Section 6.6.3), polycrystalline Cu and Rh often favour the *irreversible* formation of NH_3 and NH_2OH, respectively, as the major products.[19, 32] It is frequently found that intermediate gaseous products (usually NO_2 or NO) are irreversibly formed at Sn, and most other *p*-block metals.[47]

A major disadvantage of employing bare metal surfaces for practical applications involving nitrate reduction is the fact that electrodes are highly prone to physical malfunctions, such as corrosion, fouling, passivation or poisoning, and chemical malfunctions such as poor electrocatalytic activity, an excessive energy demand

(especially on larger scales) or unsatisfactory product selectivity. For example, nitrate reduction on Cu and Rh electrodes may be inhibited by halide ions (though this is not exclusive to these metals),[41, 80] and in even weakly acidic media are prone to electrochemically-induced surface-corrosion over time.[81, 82] These factors lead to an inevitable and regrettable decrease in performance, and limit any real application in a nitrate-sensing device. It is also unfortunate that noble-metal electrodes, such as Pt and Au, which undeniably possess far-superior surface-stability towards corrosion or fouling, do not possess sufficient electrocatalytic activity for nitrate reduction to justify the exorbitant cost of these materials. The use of the *p*-block elements, such as Cd, Pb or Sn which generally show moderate activity with acceptable surface-stability,[64, 83] is ultimately undesirable due to the relative toxicity of these materials to aquatic organisms or those handling or fabricating a sensor device. Despite the practical and economic advantages of employing bare-metal electrodes, the electrochemical sensing of nitrate demands unrivalled catalytic activity, surface-stability and analyte specificity that cannot be easily attained unless the electrode surface is suitably modified.

1.4.2 *Modified Electrodes*

It is interesting that, in isolation, the majority of *p*-block elements do not display competitive catalytic activity to equal the performance of Cu or Rh (with the lone exception of Sn), however exhibit a peculiar synergistic effect when paired with the noble-metals. The phenomenon of *p-block activation* on the otherwise quiescent catalytic activity of Au, Pd and Pt is curious, and the union of sub-monolayers of Cd, Ge and Sn (which are usually the three-best performing *p*-block elements[47, 62]) with the aforementioned supporting metals is typically found to attain cathodic currents superior to either individual species on its own.[62] Moreover, and perhaps an equally attractive feature of these bimetallic systems, adatoms of *p*-block elements such as Ge and Tl increase the selectivity of Pt electrodes in the presence of species which would otherwise inhibit nitrate reduction *via* competitive adsorption (*e.g.* Cl^-, SO_4^{2-}).[62, 84-86] Sub-monolayers of Ge on Pt electrodes are also found to adjust the product selectivity during nitrate reduction away from gaseous species such as NO_2 , NO and N_2O (typically observed with other *p*-block/Pt combinations) and towards valuable compounds like NH_3 and NH_2OH.[87]

Other investigations have identified several promising binary combinations of *promoter* and *selector* catalysts such as Cu/Pd(Pt),[88-93] Rh/Pd(Pt),[46, 92, 94] and Sn/Pd(Pt)[95-98] for denitrification; an appreciable NO_3^- conversion

rate (contribution from the *promoter* – Cu, Rh, Sn) coupled with markedly enhanced N_2 formation (contribution from the *selector* – Pd or Pt). In these cases, binary electrodes consisting of a noble-metal electrode decorated with active-catalyst materials are found to possess far greater stability in acidic media. Such bimetallic ensembles also exhibit impressive turnover during the liquid-phase hydrogenation of NO_3^- to NH_3 through cooperative heterometal interactions.[99, 100] Bare Ag and Au electrodes may also become "activated" by surface modification: sub-monolayers of *p*-block elements such as Cd, Pb and Sn,[97, 101-105] as well as alkali metals,[55] are able to impart an appreciable improvement on reduction current-densities. Moreover, the simple addition of a Ag sub-monolayer to Au electrodes elicits (comparatively) impressive catalytic activity.[20, 106] A remarkably unexpected result since Ag – and to a much greater extent Au, are not particularly active for nitrate electroreduction themselves.

Attempts have been made to circumvent the practical shortcomings of bare metal electrodes by employing tethered *molecular catalysts* composed of discrete coordination complexes. Often used as conceptual models for biological nitrification processes, inorganic compounds containing divalent metal cations such as Cu^{2+}, Fe^{2+}, Ni^{2+} and Co^{2+} ligated by large polyaromatic heterocycles such as porphyrins,[107-109] phthalocyanines,[110, 111] cyclams,[112-116], triazine networks,[117] or other artificial mimics of reductase enzymes[118] show good electrocatalytic activity for the reduction of NO_3^-. Additionally, the interfacial kinetic effects associated with planar electrode surfaces are largely eliminated and instead solution-phase (homogeneous) kinetics generally become predominant.[32, 119] Such discrete centres are at an intersection between heterogeneous and homogeneous catalysis and carry the advantages of the latter for deconvoluting the inherent mechanistic complexity of the former. It is unfortunate that their relevance to nitrate reduction technology is more of fundamental scientific importance, and the use of molecular catalysts is prohibitively hindered by complicated electrode fabrication and only weak adsorption of the catalyst to the electrode surface, with low coverages to avoid excessive non-faradaic currents (*e.g.* tether desorption or cross linking).[13]

Although great advances have been made with regards to electrocatalyst development for nitrate reduction (this short review has been unavoidably and regrettably selective in its discussion), it is unfortunate that for the majority of electrode materials – modified or otherwise – electrolysis may be inhibited by secondary species, or vulnerable to poor surface-stability in either strongly acidic or strongly alkaline conditions. While these issues could be circumvented by possible pre-treatment of nitrate-containing waste-waters (to adjust pH

or account for poisoning species), or the innovative use of non-metal-based electrode materials (*e.g.* indium-tin oxide or boron-doped diamond), it is recognised that several promising candidates for *complete* nitrate reduction have been identified (*e.g.* Cu/Pd alloys). However, the rate-limiting step for this process remains a *kinetically-sluggish* two-electron NO_3^- to NO_2^- reduction which, on the time-scale of electrochemical analysis (seconds or minutes), *represents a major challenge to overcome* for catalyst design.

1.5 – Nitrate Detection and Quantification

1.5.1 *Physical Methods for Nitrate Detection*

The quantitative analysis of NO_3^- is well-studied in the literature. Indeed, there are a wide variety of complimentary approaches, depending on the sample matrix and preference of the analyst. The most popular techniques are predominantly instrument-based, and include spectrophotometry, chemiluminescence and chromatography-coupled mass-spectrometry.[120] Historically, the *de facto* method for nitrate/nitrite determination in aqueous samples has been by colorimetric analysis, commonly known as *Griess' method*. The procedure involves the diazotisation of an aromatic amine by acidified NO_2^-, followed by coupling to a bicyclic amine to generate a vivid chromophore.[121] The concentration of inorganic nitrogen can be inferred from the intense absorption of the azo-dye at the appropriate wavelength. It is worth noting that Griess' method is inherently best suited for *nitrite* detection, though the technique may be amended for nitrate by the addition of a suitable reducing agent such as hydrazine[122] or a Cu/Cd alloy[123] to generate NO_2^-, which is then captured by Griess' reagents. Alternative methods to a Griess' assay are numerous, and include ion chromatography,[124] direct ultra-violet spectroscopy,[125] fluorescence spectroscopy[126] and potentiometric (ion-selective) electrodes,[127] or indeed any of the methods listed above. However, inherent instrumental complexity, sample preparation, cost or specialised operation associated with these methods often limits their utility to a laboratory setting. The increasing demand for "on-site" and real-time analysis of environmental samples has driven the development of electrochemical methods, especially as such techniques are rapid, amenable to miniaturisation, economic to manufacture in large-scale and offer the possibility of remote operation.

1.5.2 *Electroanalytical Methods for Nitrate Detection*

Very early examples (1940's – 70's) of electroanalytical nitrate detection commonly employed polarographic methods,[128, 129] requiring the presence of polyvalent metal promoters such as Cr^{3+}, Mo^{3+} or Zr^{4+} in solution to improve sluggish reaction kinetics at Hg electrodes.[130-132] Notwithstanding impressive (for the time) detection limits (in the 50-1000 μM range), these approaches were characterised by narrow linear ranges (*if* linearity was even observed), a strong pH dependence, and complicated electrochemical behaviour[133, 134] at low nitrate concentrations in the presence of nitrite (autocatalytic reactions may regenerate nitrate anions). Frustratingly, NO_2^- reduction often occurs at similar potentials to NO_3^- reduction – processes which may inevitably overlap and obscure any meaningful analytical information (though this is not exclusive to Hg electrodes).[135] Typical environmental anions such as Cl^-, PO_4^{3-}, and SO_4^{2-} are also found to severely impact analytical performance at Hg electrodes.[135] Because of this, a movement away from polarography as a detection strategy was observed, coinciding with early studies investigating the voltammetry of nitrate reduction at bulk metal electrodes, such as Cu, Pb and Pt. However, it soon became clear that the use of bare electrodes – whilst convenient for the analyst – is often met with variable catalytic performance and limited analytical utility (*vide supra;* Section 1.4). Factors such as high overpotentials, slow kinetics, unsatisfactory detection limits, irreproducible behaviour from cumulative electrode passivation/corrosion *etc.*, hampering any genuine application in a laboratory (or field) setting. Therefore, the use of functionalised electrodes is desirable to overcome these limitations and produce *efficient* nitrate detection *via* increased flexibility in catalyst design. The effect of this is to make the electrode more sensitive to nitrate reduction, increasing the magnitude of cathodic currents, increasing the sensor response and therefore decreasing detection limits. Several strategies have been developed and refined in the literature, mostly targeting the nature of the electrode surface and its furnishing with catalytic functionality.

1.5.3 *Contemporary Methods for Electroanalytical Nitrate Detection*

A rather pervasive approach in the recent literature has been the use of nanostructured materials, particularly those of Cu or Ag as the active electrocatalyst for nitrate electroreduction, where current-responses to nitrate reduction are usually sufficient to achieve detection limits in the micro-molar (μM) range or lower. It appears

the high catalytic activity of Cu (and to a lesser extent, Ag) translates effectively into the micro- and nanoscale regimes, as one may rightfully expect. For this reason (and for the fact that another candidate, Rh, is a rather uneconomical choice) Cu and Ag are promising materials for this application and many novel nanostructured forms of these elements (*e.g.* nanoparticles, sheets, wires, pores) have surfaced. For example, Comisso *et al.*[136] have prepared nanoporous Cu electrodes by exploiting the HER to simultaneously electrodeposit Cu^{2+} cations using the gaseous H_2 bubbles produced as a form of template and incorporated this into a flow-injection system for amperometric nitrate detection. With the addition of Rh the sensitivity and selectivity of the Cu-device toward nitrate could be greatly increased, whilst alloying with Ni would improve stability and longevity in acidic electrolytes. More recently, Compton *et al.*[137-139] have electrodeposited Cu onto boron-doped diamond microelectrodes and developed these surfaces for nitrate sensing, creating vertically aligned Cu-pyramids *ca.* 5-50 nm tall and *ca.* 2-20 nm in diameter. *Ex-situ* experiments showed that a fresh Cu surface was imperative for optimum performance, however the technique was effective for nitrate detection by linear-sweep voltammetry and presented insignificant interference from chloride or nitrite with sub-μM detection limits.

Guadagnini and Tonelli have fabricated Ag-modified carbon electrodes, exploring the specific nature of the support (glassy-carbon or layered graphite) towards the simultaneous detection of NO_3^-, NO_2^- and IO_3^-.[140] The morphology of the Ag nanostructures was found to depend strongly on the support, with well-dispersed nanoparticles *ca.* 10 nm in diameter formed at glassy-carbon, and irregular dendritic species at graphite (< 30 nm). Detection of nitrate was by chronoamperometry and though the sensitivity of the glassy-carbon-based electrode was twice that of the graphite, common anions such as SO_4^{2-}, HCO_3^-, Cl^- and F^- did not affect performance. The authors note that surface-oxide formation at Ag, regardless of morphology, was detrimental to performance and although could be removed by aggressive electrochemical treatment, irreversible damage would occur to the active species and thus the sensor had a short lifetime of *ca.* 1 day. Bonyani *et al.*[141] have prepared Ag/Fe_2O_3 composites by a wet-chemical approach for the detection of nitrate in neutral media. Scanning electron microscopy showed that Ag formed *ca.* 15 nm sized deposits on larger amorphous Fe_2O_3 particles (*ca.* 100 nm), and energy dispersive X-ray spectroscopy confirmed that Ag ensembles existed in a near-homogeneous distribution with regions of Fe. Interestingly, electrochemical characterisation of the Ag/Fe_2O_3 electrode discovered behaviour comparable to that of metallic Ag, but no features attributed to the Fe^{2+}/Fe^{3+} couple were observed. Thus, the authors propose that Ag is the true active species for nitrate reduction

whilst Fe_2O_3 plays a significant role in adsorption, or possibly immobilises the Ag catalyst against aggregation. This platform yielded a low-μM detection limit. Noteworthy (though not surprisingly) is the realisation that reports of Au-based nitrate sensors are comparatively scarce. In fact, this author was only able to fine *one* such platform which incorporates Au, in the form of Se-coated Au nanoparticles which have been employed for the electrochemical detection of both NO_3^- and Hg^{2+} by differential-pulse voltammetry (Section 4.1 for an overview of this technique). A detection limit of *ca.* 8 μM was attained for the nitrate in 0.1 M Na_2SO_4.[142]

A survey of the literature finds an enormous collection of similar accounts, and regrettably the topic is simply too broad to cover in this short introduction to nitrate sensing. In almost all cases, the use of nanoparticles or other nano-sized features is precedent. The advantages of incorporating nanomaterials into (electro)chemical sensor design are numerous: unique physiochemical properties compared to bulk materials, an increased electrochemically-active surface-area, cooperative catalyst/support interactions and the conception of reactive chemical environments such as edges, planes, adatoms or defects.[143-146] At a most basic understanding, the global increase in catalytic activity of nanomaterials is rationalised by the considerable increase in the exposed surface-area. Depending on the size and coverage of nano-sized features, individual diffusion zones may partially overlap creating regions with varying mass-transport effects. If the global feature size is decreased, the radii of individual diffusion zones will also decrease and eventually overlap to approximate a smooth electrode surface.[147] This concept is exploited in electrochemical sensors that utilise nanoparticles as a catalytic layer on an electrode surface, maintaining a *pseudo*-smooth diffusion zone whilst improving electron-transfer to the analyte.

1.5.3 *Gold for Electroanalytical Nitrate Detection*

At this point, it is helpful to pause and consider that despite the *numerous* collection of published (and patented) electrochemical nitrate sensing platforms, *very few* have presently reached commercial fruition. Indeed, one may naturally ask *why* this is the case when a review of the literature yields an abundance of (purportedly) appealing materials and technologies for this purpose. This author offers two possible explanations: i) the active sensing component (catalyst) has one or more critical weaknesses/disadvantages that prevent the translation from laboratory to field settings, which the authors have chosen not to divulge or are harmlessly

unaware of or ii) the active sensing component (catalyst) is difficult, impractical or uneconomical to fabricate on a large scale.

In contrast with conventional approaches, nanostructured gold catalysts (supported on amorphous carbon materials) have been chosen as a candidate to accomplish this. Several reasons are outlined to justify this selection instead of Cu, Rh, Ag or Sn, for example: i) gold possesses a greater intrinsic opposition to the formation of surface oxides, which are noted to be detrimental to electrocatalytic performance at the aforementioned elements (Rh less-so); ii) the stability of gold surfaces, particularly in acidic media, is beneficial where an authentic nitrate sensor may be expected to operate in natural freshwaters which are often slightly acidic by virtue of their geographic source or by anthropogenic effects; iii) more-so for Cu and Ag, nitrate electroreduction at these materials is often prone to interference from dissolved oxygen and environmentally-relevant species such as halides, NO_2^-, SO_4^{2-}, PO_4^{3-}, ClO_2^-, ClO_3^-, BrO_3^-, surfactants…; needless to say the list of possible interferences is extensive,[148] whereas gold does not show appreciable susceptibility to the sorption of such compounds;[149] iv) whilst bulk gold surfaces are, generally-speaking, catalytically quiescent, gold nanostructures often show extraordinary activity in catalytic settings. Such compounds have not yet been widely explored for nitrate electroreduction and may offer some as-yet undiscovered (at least, until this work) performance for this task.

Finally, this author would like to draw attention to a combined computational-experimental study performed by Calle-Vallejo and co-workers,[20] who have modelled several plausible Ag/Au surfaces (surface alloy, sub-surface alloy, Ag monolayer, Ag sub-monolayer, discrete Ag adatoms) and their interaction with the nitrate anion *via* density-functional theory (DFT). For these model surfaces, maximum activity was predicted for a sub-monolayer of Ag atoms (*ca*. two-thirds coverage) on the Au (111) plane which corresponded to an optimum adsorption enthalpy, and this was subsequently confirmed *via* cyclic voltammetry studies. Interestingly, their DFT analysis also suggested that several alternative surface arrangements would also be comparatively active for nitrate adsorption and reduction, specifically undercoordinated Ag and Au sites such as edges, steps and *ensembles of neighbouring adatoms*. The authors did not experimentally verify this hypothesis in their work, and (until the present study) this remains unconfirmed in the scientific literature. This addendum by Calle-Vallejo and co-workers[20] was the inspiration and motivation for the research herein.

Ultra-small nanoparticles, colloquially termed “nanoclusters” may serve as conceptual models for adatom/defect sites on bulk metal surfaces and present an interesting and – at present – grossly underexplored opportunity for electrocatalytic and electroanalytical applications. In the forthcoming chapter the reader will be introduced to these compounds, their unique physiochemical properties which contrast to the bulk samples, the various methods for their synthesis and fundamental structural and bonding principles.

1.6 – Specific Aims of this Thesis

Listed below are six overarching objectives this thesis endeavours to accomplish:

1) To synthesise a range of atomically-precise gold and silver nanoclusters, following established literature preparations and characterise these to the extent to which identity can be unambiguously confirmed.
2) To deposit the above compounds on amorphous carbon and investigate their electrocatalytic performance for the electroreduction of nitrate in aqueous media.
3) To evaluate, from both qualitative and quantitative approaches, the electrocatalytic performance of atomically-precise gold and silver nanoclusters for nitrate electroreduction and compare these to other reported electrocatalysts in the scientific literature.
4) To optimise, as much as reasonably possible within the limited timeframe, methods for electrode fabrication and characterise these electrodes using electrochemical microscopic and spectroscopic techniques.
5) To utilise the best performing catalyst(s) within an electrochemical sensing platform for the detection of the nitrate anion in aqueous media, to optimise electroanalytical techniques for this process and evaluate the performance of this platform compared to those reported in the scientific literature.
6) To evaluate the performance of this sensing platform in an authentic environmental matrix, in the presence of typical environmentally-relevant interferences.

Chapter 2

Introduction to Atomically-Precise Gold Nanoclusters

2.1 – Introduction to Gold Nanoparticles

2.1.1 *Catalytic Properties of Gold Nanoparticles*

Historically, the scientific interest in gold nanoclusters has roots in the study of their ancestral counterparts, *colloidal nanoparticles,* the discovery of which is often credited to Michael Faraday who in 1857 prepared colloidal gold by the reduction of Au^{3+} salts with elemental phosphorus in a biphasic water/CS_2 system.[150] Shortly thereafter, Gustav Mai would model their interaction with electromagnetic radiation as a function of particle size,[151] and contributions by Zsimondy[152] and Gans[153] would recognise the importance of particle shape on the optical behaviour of metallic gold particles. By the mid-1930's, colloidal preparations of many transition-metal elements were known,[154] and various parameters which directly affected intrinsic behaviour were uncovered.[155] Notable was the realisation that metal nanoparticles were only *metastable* species and, given sufficient time, would revert to the metallic lattice in a thermodynamically spontaneous process.[156] Fortunately for the synthetic chemist, the exact timescale involved in this transformation is often of little practical consequence and metal nanoparticles (and by association, nanoclusters) are therefore said to possess intrinsic *kinetic stability.*

The size-, shape- and composition-dependent variation in the properties of gold colloids was a fascinating aspect of science as it remains so today, and synthetic innovations (exemplified by the Turkevich[157] and Brust-Schiffrin[158] methods) improved the accessibility of these materials for wider applications, particularly in catalysis. Unsurprisingly, bulk gold surfaces are found to possess unremarkable or entirely absent catalytic activity and were thus overlooked for a significant amount of time while the catalytic utility of other noble-metal elements (*e.g.* Rh, Pd, Pt) flourished. It was therefore intriguing to the chemical community when the first *active* gold-containing heterogeneous catalyst (a Pd-Au alloy) was patented in 1965 for the production of vinyl acetate.[159] Simultaneous and independent observations in the 1980's by Haruta *et al.*[160] and Hutchings *et al.*[161] established the exceptionally-high catalytic activity of pure gold nanoparticles for CO oxidation and acetylene hydrochlorination, respectively. These discoveries contributed to the emergence and evolution of gold-based catalysis as a major research field, and consequently both pure and alloyed gold nanoparticles were studied extensively, confirming their potent catalytic performance.[162-165] The major advantage of using metal nanoparticles in catalytic settings is a significantly higher surface-to-volume ratio and decreased cohesion-

energy, revealing a large population of coordinatively-unsaturated surface atoms.[166] However, catalytic activity does not scale linearly with size (nor shape or composition): the reduction of particle dimensions to minimise material usage or increase total surface-area will not necessarily yield optimal catalytic performance. Instead, *site specific* topologies on the nanoparticle exterior (such as planes, steps, terraces, corrugations, adatoms, heterometallic junctions) often possess remarkably high chemical reactivity for particular substrates, which will account for the majority of observed catalytic turnover.[167]

2.1.1 *The Need for Atomic Precision*

Significant advances in nanomaterial chemistry (including computational approaches) have created numerous opportunities to uncover reaction-specific structure-activity relationships.[166] However, further catalytic progress (and acceptance into industry) is hindered by the inherent *polydispersity* of a nanoparticle sample: an unavoidable artefact of any fabrication procedure where a broad range of sizes, shapes and/or compositions will be formed. Therefore, it is fundamentally difficult to correlate observed catalytic performance with any one individual species, and it is with reluctance that many nanoparticle-based catalysts cannot be embraced on an industrial-scale until the identity of the *authentic* catalyst site(s) is known.[168] Nevertheless, a major breakthrough has been the use of small, molecular metal clusters with well-defined structures as proxies for active sites that may be found on nanoparticle exteriors.[169] Since it is challenging to *directly* investigate the adsorption of small molecules (*e.g.* H_2, O_2, CO, alkenes) on catalyst surfaces, ligand-protected metal clusters may serve as convenient models for such processes as they are usually amenable to spectroscopic and/or crystallographic interrogation. This may provide useful conceptual information or mechanistic arguments on the nature of surface-ligand interactions ("the cluster-surface analogy"),[170] perhaps leading to tailored synthetic-strategies for designing *optimised* nanoparticle-based catalysts. Recently, metal clusters have become a promising class of functional catalysts themselves, where the issue of polydispersity in conventional nanoparticle catalysts is all but eliminated.[171] The discovery, synthetic progression and structural elucidation of *atomically-precise* noble-metal (chiefly Pd, Ag, Pt and Au) nanoclusters stabilised by organic ligands has yielded an extensive library of increasingly-accessible catalysts[172] with many novel and possibly as-yet unexplored physiochemical properties.

2.2 – Introduction to Gold Nanoclusters

Atomically-precise pieces of matter composed of tens-to-hundreds of metal atoms, grouped under the term "*nanoclusters*" are a class of functional nanomaterial with many unanticipated but nevertheless exciting physiochemical properties. Though once considered a scientific curiosity when first reported in the 1960's, fundamental aspects have since been addressed by theoretical interpretations and many diverse practical applications have been identified. As unique species, nanoclusters are fundamentally intriguing compounds since they appear to be a unifying point of contact between the bulk-metal-like nanoparticles and individual metal atoms/ions (the "metal-to-molecule" transition). This transitional character during the evolution from atomic to metallic states manifests in the peculiar "molecule-like" properties of nanoclusters which have generated keen interest in recent years.

2.2.1 *Gold Nanoclusters: Every Atom Counts*

Nanoclusters are generally defined as ultra-small nanoparticles with sub-2 nm sizes that can be described by an unambiguous, *atomically-precise* chemical composition and structure (though this distinction is not always maintained in the literature, it will be the one adopted in this work).[173] Nanoclusters are viewed as a simple core of metal atoms encapsulated by an organic ligand periphery, and the cluster core may assume a variety of geometries depending on the number of metal atoms and the steric/electronic demands of the protecting ligands. The characterisation of many ligand-protected gold nanoclusters by single-crystal X-ray diffraction has been a landmark achievement in rationalising numerous structure-dependent physiochemical properties over the last decade or so. Many of the emerging properties of nanoclusters emphasise a *clear* molecular character which is distinctly different from the plasmonic behaviour of conventional nanoparticles, or indeed of the corresponding bulk metal.

Currently, the accepted explanation for the emergence of molecular character in small metal clusters is the pronounced quantum-confinement of delocalised electrons. Whereas conventional gold nanoparticles (< 100 nm) will display broad plasmonic features distinctive of bulk-continuum *metallic* character, small nanoparticles (< *ca.* 5 nm) begin to display prominent transitions in optical spectra, signifying discrete energy-

levels.[174] The discrepancy in optical profiles deviates significantly from those predicted by Mie's calculations,[151] which had held true for larger particle sizes and is based on the assumption of a *quasi*-continuous band of energy-levels.[175] Abruptly, as the dimensions of the particle transcend *ca.* 2 nm (the de Broglie wavelength of an electron at the Fermi level of gold at 298 K), the spacings between energy-levels become mathematically appreciable and *quantisation* leads to the formation of discrete molecular orbitals (Section 2.4).[176, 177] Generally, the energy spacing between molecular orbitals is seen to increase with decreasing size,[178] and specific electronic events (*e.g.* HOMO-LUMO transitions) can be intimately correlated with nanocluster structure and symmetry.[179] Whereas the properties of nanoparticles *will* be significantly affected by the addition or subtraction of entire monolayers of *fcc*-packed atoms,[180] the contribution an individual metal atom (the appendage or deletion thereof) makes is considered insignificant; for nanoclusters sub-2 nm this is not the case. The extent of quantisation is such that the addition, subtraction or substitution of a *single metal atom* to the cluster drastically adjusts the energies (and occupancy) of molecular orbitals, leading to pronounced effects on physiochemical behaviour and the adage "*every atom counts*".[181] Fairly-recent experimental observations[182] supported by quantum-mechanical calculations[183] suggest the "metal-to-molecule" transition occurs between 140 and 180 gold atoms, tentatively estimated as a nanoparticle with *ca.* 1.8 nm core diameter (and imposed icosahedral geometry). The conceptual evolution from atomic and molecular behaviour towards metallic character as a function of size is illustrated in Figure 2.1.

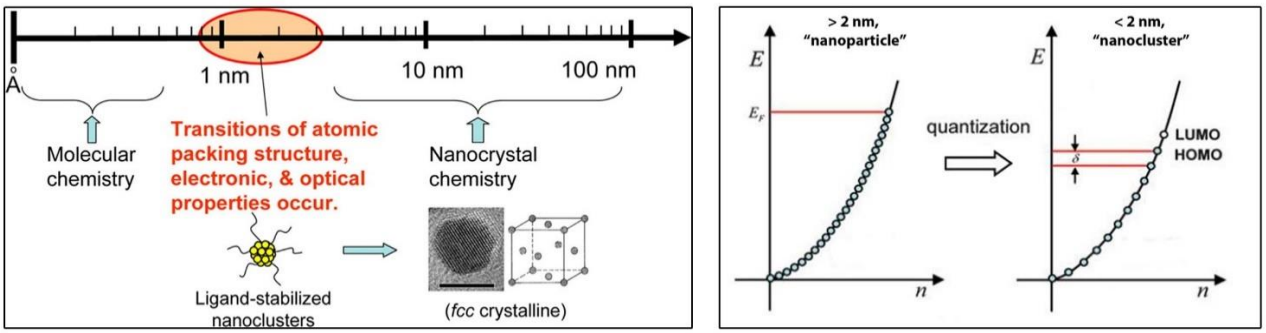

Figure 2.1 – Evolution of molecular and metallic structure as a function of spatial dimension (left panel); Quantisation of energy-levels as particle size decreases towards 2 nm, departing from continuous bands in bulk metal towards discrete states in nanoclusters. Reproduced from Ref. 176 with permission from The Royal Society of Chemistry and Ref.177 with permission from The American Chemical Society.

2.2.2 *Electrochemical Properties of Gold Nanoclusters*

Evidence for the "metal-to-molecule" transition is also visible in the respective electrochemical profiles of colloidal nanoparticles and atomically-precise nanoclusters. In contrast to changes in optical properties (which take place rather abruptly near *ca.* 2 nm in size), the size-dependent variation in electrochemical features are, to the fortune of the analyst, more gradual. For nanoclusters, pronounced quantum-confinement effects permit successive, single-electron transfer events corresponding to the generation of discrete molecular charge-states.[178, 184] These phenomena are often well-resolved in voltammetric spectra (although irregularly spaced), and give rise to the redox behaviour of gold nanoclusters for electrocatalytic (electron-transfer) processes.[185, 186] Such redox events may be *reversible* (quantised-charging of the cluster: "molecular capacitors"[187, 188]) or *irreversible* (leading to cluster disintegration[189]), however it is generally observed that the sizeable separation between formal redox-couples (*the electrochemical gap*, or *the charge-transfer barrier*) further increases with decreasing size (*c.f.* increasing HOMO-LUMO gap with decreasing size – Figure 2.2, Panel A). The lability of irreversibly oxidised or reduced cluster species also decreases with descending size, meaning the lifetime of electronically unstable clusters should increase as more atoms are present to share excess charge.[190] Indeed, this has been shown for $[Au_{25}(SR)_{18}]^z$, where three unique charge-varied isomers (z = 1+, 0, 1-) have been prepared, isolated, and structurally-characterised.[191]

Furthermore, one may arrive at the *ca.* 2 nm criterion for quantum-confinement by observing the electrochemical properties of nanoclusters possessing between about 140 and 180 gold atoms, and in such cases behaviour that appears somewhat intermediate of molecular and metallic character is visible.[192] In this size domain, electron-transfer events take place at approximately regular intervals (Figure 2.2, Panel B), suggesting the stepwise double-layer charging of the nanoparticle surface which is unassignable to any formal redox process (erroneously performed in the literature *pre*-2000, before a clearer model of nanoclusters was available).[193] As the charge-storing ability of any capacitor largely depends on the surface-area of the capacitor itself, this intuitively means that larger particles may accommodate a greater number of surplus charge-carriers (electrons). Indeed, upwards of hundreds of electrons may be (reversibly) stored on single nanoparticles,[144] whereas nanoclusters may only (reversibly) accept a handful of additional charge-carriers.[194] In this light, all small (*ca.* 2 nm) nanoparticles and nanoclusters (< 2 nm) are *intrinsically electroactive* and may behave as

electron donors/acceptors to the extent of their respective capacitance properties.[144] Above *ca.* 10 nm in diameter, the peak separation between electron-transfer events is frequently so minuscule that they merge to resemble a *continuous* charging band, characteristic of bulk-continuum behaviour associated with an influential presence of metallic character.[144, 195] The above discussion is summarised in Figure 2.2.

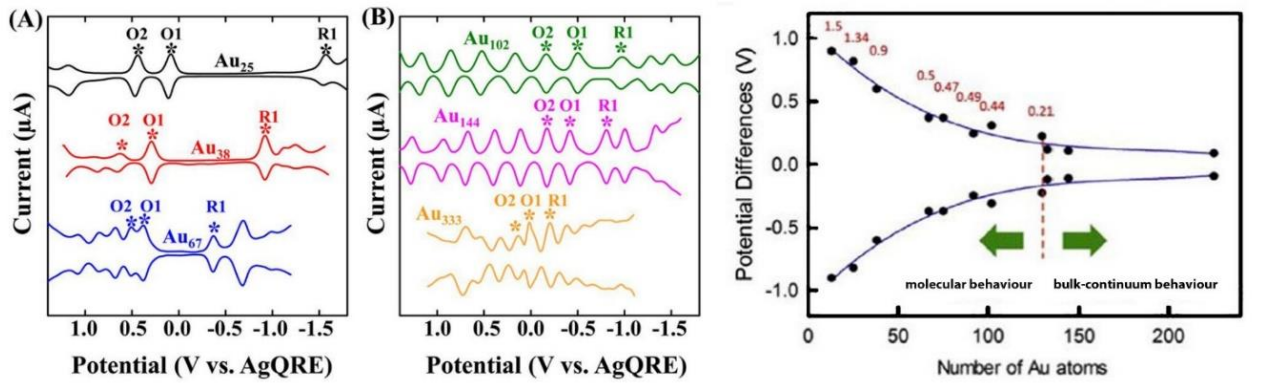

Figure 2.2 – Evolution of electrochemical profiles as a function of cluster size. The distance between discrete redox events is observed to decrease with an increasing number of atoms as molecular character diminishes, and bulk behaviour is approached. Reproduced from Ref. 178 with permission from Elsevier and Ref. 184 with permission from The American Chemical Society.

Knowledge of the electrochemical behaviour of molecular nanoclusters is important not only for understanding the effects of quantum-confinement in sub-nanometre sized pieces of matter (and how this varies with size), but also for rationalising intrinsic catalytic performance during electrochemical processes. As reactant electrons must be of appropriate energy to tunnel from the electrode into a vacant molecular orbital on an electroactive species nearby,[1] assigning formal redox-pairs may allow the analyst to identify electron-energy states that are available for electrocatalytic processes. Such an approach will be employed later in this work, in Section 6.8.

2.2.3 *Electrocatalytic Properties of Atomically-Precise Gold Nanoclusters*

Redox active gold-nanoclusters have previously been employed for several electrocatalytic/electron-transfer roles, however there is still significant scope for further work: Lee *et al.*[196] have investigated the effect of doping $[Au_{25}(SC_6H_{13})_{18}]^-$ with a single Pt atom for the hydrogen-evolution reaction (HER) using trifluoroacetic acid as a sacrificial proton source. The bimetallic analogue $[Au_{24}Pt_1(SC_6H_{13})_{18}]^{2-}$ was able to achieve turnover rates several orders of magnitude greater than the monometallic variant, ascribed to the superior ability of a Pt heteroatom to chemisorb hydrogen. Specific redox-transitions of the $Au_{24}Pt_1$ cluster also appeared to coincide

with the reduction of protons. Chen and Chen[197] have employed gold nanoclusters of various core-sizes (Au_{11}, Au_{25}, Au_{55} and Au_{102}) supported on glassy-carbon electrodes for oxygen reduction in 0.1 M KOH electrolyte. These authors find a size-based trend wherein current-densities increase with decreasing number of gold atoms, although no explanation for this was offered. Antonello and co-workers[185] have prepared a cationic $[Au_{25}(SC_2H_4Ph)_{18}]^+$ cluster and employed this species as a homogeneous electrocatalyst for the reduction of several aromatic peroxides: in this case, both redox couples $[Au25]^+/[Au25]^0$ and $[Au25]^0/[Au25]^-$ were able to catalyse O-O bond cleavage and no cluster disintegration was detected. Jin *et al.*[198] have performed a similar study involving the oxidation of oxoammonium cations by $[Au_{25}(SC_2H_4Ph)_{18}]^-$ in the homogeneous phase.

Moreover, atomically-precise gold nanoclusters have been employed for electrochemical sensing purposes: Kumar and co-workers[199] have prepared $[Au_{25}(SC_6H_{13})_{18}]^-$ nanoclusters entrapped in silicate networks for the amperometric sensing of ascorbic and uric acids in 0.1 M KCl, with detection limits of 0.068 and 0.071 μM, respectively. Baek *et al.*[200] have followed a similar procedure to unify $[Au_{25}(SC_6H_{13})_{18}]^-$ and *ca.* 150 nm ZnO nanorods which were used for the amperometric sensing of alkaline phosphatase in 0.1 M KCl. Kwak *et al.*[201] have managed to prepare a novel ionic liquid composed of $[Au_{25}(SC_6H_{13})_{18}]^-$ anions and imidazolium cations, and by incorporating glucose oxidase were able to design an electrochemical sensing platform for the detection of glucose with a detection limit of 3.4 μM in 0.1 M KCl. Further examples of such electroanalytical applications may be found in the literature.[202] In all cases, it is usually the reversible nature of the gold nanocluster redox-states that are able to facilitate charge-transfer in a catalytic manner. The non-linear dependence of catalytic activity on size probably arises from the electronic structure of the cluster itself,[144, 184] whereby a particular arrangement of molecular orbitals or the specific placement of a redox-transition may account for favourable charge-transfer kinetics to an electroactive analyte. These redox transitions may be examined using non-aqueous voltammetry to observe the *electrochemical profile* of the nanocluster, from which valuable information (such as the electrochemical gap, or the charge-transfer barrier ΔE_g) may be extracted. Such a process will be performed and discussed in greater detail in Chapter 4.

2.3 – General Synthesis of Gold Nanoclusters

Phosphine-protected gold clusters have been known since the late 1960's, and the first structural characterisation by single-crystal X-ray diffraction was achieved in 1970's for $Au_{11}(PPh_3)_7I_3$, an incomplete icosahedron with C_{3v} core-symmetry.[203] In the time since, numerous gold-phosphine clusters of various sizes with a diverse range of protecting ligands have been reported and their structures solved by crystallographic techniques. One notable exception, $Au_{55}(PPh_3)_{12}Cl_6$ prepared by Schmid *et al.* in 1981,[204] is the largest reported gold-phosphine cluster to date however has so far resisted crystallisation. Furthermore, many interesting examples of gold-phosphine nanoclusters containing one or more catalytically-important *heterometals* (*e.g.* Rh, Pd, Pt) have been synthesised and structurally-characterised.[205] Since the early 2000's, phosphine-protected gold clusters have slowly been overtaken by a new family of compounds prepared with thiolate (RS^-) ligands. Now the largest group of gold nanoclusters, most recipes are derived from the Brust-Schiffrin method[158] for preparing alkylthiolate-protected gold nanoparticles.[206] Noteworthy examples from the literature include $[Au_{25}(SR)_{18}]^-$,[207, 208] $Au_{38}(SR)_{24}$ [209] and $Au_{102}(SR)_{44}$ [210] which are especially stable and have had their molecular structures determined crystallographically. The synthetic-accessibility of these compounds has widened considerably in recent years, leading to an extensive collection of gold-thiolate nanoclusters. Such species will not be covered further in this introduction (except where useful illustrative examples are found), however many excellent reviews are available.[172, 173, 177, 181, 211-215]

Synthetic techniques for preparing gold-phosphine nanoclusters generally fall into one of three categories:

1) Chemical reduction of gold(I)-phosphine compounds
2) Evaporation and condensation of Au vapour into mixtures of gold(I)-phosphine compounds
3) Interconversion of pre-formed gold-phosphine clusters

Only methods 1 and 3 are routine in the contemporary literature, primarily due to the convenience and ease of handling of reagents, though one may find older reports which frequently employ the second route above.

2.3.1 *Synthesis of Gold-Phosphine Nanoclusters by Direct Reduction*

The direct reduction of triarylphosphine-gold(I) precursors ($AuPR_3X$) in ethanol by sodium borohydride ($NaBH_4$) is the most common recipe found. In this approach, specific molar quantities of these reagents are

mixed together, invoking the aggregation of gold-ligand fragments as Au^{+} ions are reduced to atoms with formally mixed-valent character between 0 and 1.[216] Other reducing agents such as $Ti^{0}(\eta\text{-tolyl})_2$ [217] and gaseous B_2H_6 [204] have been previously employed, as has the creation of reducing agents *in-situ via* the photolysis of gold-azide salts.[218] Mechanistically, there are uncertainties over the exact identities of intermediates formed, however it is generally believed that a mixture of cluster sizes are initially generated in a kinetically-driven process.[219] Over time, decomposition or collision of the least-stable species followed by recombination narrows the product distribution in the reaction mixture towards one (or more) predominant compounds in an iterative process of thermodynamic selection.[220, 221] Introducing a second metal precursor prior to reduction may, in some cases, invoke the formation of bimetallic clusters.[205] Subtle adjustments to experimental parameters (gold/reducing-agent ratio, solvent, reduction rate *etc.*) give some influence over the reaction pathway, and in some cases can direct the reaction towards a specific compound.[222] Additionally, steric hindrance on the phosphine ligand or the use of bridged-diphosphines can affect the extent of cluster growth,[219] as can the coordinating ability of counterions in the reaction mixture.[222] As will be discussed in forthcoming *Structure and Bonding* section (Section 2.4), kinetic or thermodynamic factors usually prevail in most cases affording a greater propensity of specific sizes (*e.g.* undecagold "Au_{11}" clusters) for a given reaction mixture. Deviations from this demonstrate the importance of reaction-specific conditions on the nucleation and assembly of gold-ligand fragments during direct reduction syntheses.

2.3.2 *Synthesis of Gold-Phosphine Nanoclusters by Interconversion*

Whilst the synthesis of gold-phosphine nanoclusters *via* direct reduction is often unpredictable (disregarding reputable preparations), it has proved possible to establish strategies which can straightforwardly convert one species to another. Apart from the synthetic importance of such interconversions, the reactions between gold-phosphine clusters and nucleophiles, labile gold-phosphine complexes, free phosphines or oxidising agents are useful for studying their intrinsic reactivity.[222, 223] Due to the flexible nature of the cluster skeleton and the soft potential-energy surfaces connecting alternate geometries,[224, 225] such treatments may result in either growth or decay of the cluster core and permit the emergence of novel clusters that are not immediately accessible by the direct reduction of gold precursors. There are four distinct types of cluster interconversion reaction, and they are: *substitution*, in which the cluster framework is maintained however one or more ligands are exchanged;

dissociation-association, in which an equilibrium is established between the departure or entrance of a ligand or gold-ligand fragments; *fragmentation*, where the cluster core is etched to smaller sizes by an excess of ligand or nucleophile; *aggregation*, where the cluster core is enlarged to greater sizes by an excess of ligand or nucleophile. A remarkable aspect of these reactions is their surprising facility, which conceptually must require a complicated series of disintegration and recombination steps to occur nearly instantaneously, and therefore suggests that cluster formation is, kinetically, a most rapid process.[226] An interesting side note, whereas gold-thiolate nanoclusters may be doped with heterometal atoms *via* post-synthetic metathesis between pre-formed clusters and metal cations,[215] a survey of the literature finds that similar reactions have not yet been reported for gold-phosphine nanoclusters. For the synthetic chemist, this may offer an interesting pursuit towards novel heterometallic cluster compounds, if reliable and predictable strategies can be established. The synthesis of specific gold-phosphine nanoclusters will be elaborated further within the context of the present work in Section 3.1.

2.4 – Structure and Bonding in Gold-Phosphine Nanoclusters

2.4.1 *Cluster Structure and the PSEPT Approach to Bonding*

The general formulae of gold-phosphine clusters may be summarised as $[Au_N(PR_3)_M(X)_L]^{z+}$ where N > z and tertiary phosphines PR_3 (R usually aryl) serve as the primary protecting-ligand. Additional ligands X, usually halides (Cl^- or I^-) or *pseudo*-halides (*e.g.* SCN^-, CN^-, CNO^-) may coordinate to gold atoms or serve as charge-balancing counterions. The choice of organic protecting ligand is exceedingly important from a geometric perspective: thiolate-protected species often yield deformed or distorted polyhedral gold-cores encapsulated by oligomeric metal-ligand staples.[177, 211] There are mechanistic arguments for this particular arrangement,[173] however it is generally observed to restrict the size of the cluster to > 20 gold atoms. On the other hand, phosphine-protected gold nanoclusters display more regular topologies with a purely-organic ligand periphery.[219] This simpler structure generally favours species possessing ≤ 13 gold atoms (though exceptions are known), with the geometry of the gold-core predetermined by the number of metal atoms, the steric demands of the tertiary phosphine ligands, and simple electron-counting rules such as the polyhedral skeletal electron-pair theory (PSEPT):[227] For lower-nuclearity clusters (3 – 7 gold atoms) the large steric circumscription of tertiary phosphine ligands is often incompatible with compact structures containing only a

few gold atoms, and therefore expansive *prolate* topologies with 12*n* + 14 electrons are preferred (*n* = number of $AuPR_3$ fragments).[225] Higher-nuclearity compounds (8 – 13 gold atoms) are characterised by the presence of an interstitial atom at the centre of a hexagonal-chair of gold atoms, a feature that maximises the number of radial Au(centre)-Au(vertex) interactions.[224] These centred geometries can be further distinguished by topological features, whereby *spherical* clusters possess peripheral gold atoms lying on the surface of an approximate icosahedron with 12*n* + 18 electrons.[225] Those compounds with 12*n* + 16 electrons display peripheral atoms lying on the perimeter of an approximate torus, and such clusters are said to be *oblate*.[225] For a graphical illustration of these topologies, please refer to Figure 2.3 below.

2.4.2 *Cluster Structure and the Superatom Approach to Bonding*

Whilst the PSEPT approach is a sufficient *qualitative* description for the topologies of gold clusters based on predictable electron-counting rules, a more flexible molecular-orbital treatment is required for a precise understanding of underlying electronic features. For gold clusters, metal-metal bonding arises primarily from the multi-centre overlap of Au[*6s*] orbitals and metal-ligand bonding from the overlap of Au[$5d_z^2$] and P[$3p_z$] orbitals, both in a σ-style fashion.[228] Considering that $s - d_z^2 - p_z$ hybrids of the individual $Au(PR_3)^{\delta+}$ fragments will also overlap to encourage the most-effective delocalisation,[225] the free-electron count n^*, of ligand-protected gold clusters is therefore given by the elegantly simple formula:

$$n^* = N_X(v_X) - L - z \qquad (2.1)$$

Where N_X is the number of metal atoms of element X, v_X is the valence of those atoms (*e.g.* for Au, v_X = 1; *d*-electrons do not contribute to n^*), L is the number of one-electron withdrawing ligands, and z is the overall charge of the cluster.[224, 229] Note that the free-electron count above (or the *superatom* electron count; *vide infra*) is simply the PSEPT valence-electron count with contributions from Au[$5d_z^2$] and P[$3p_z$] orbitals disregarded. A molecular-orbital analysis[230] of this bonding pattern yields a simple spectrum of energy-levels, expressed by *pseudo*-spherical harmonics with nodal planes reminiscent of familiar atomic orbitals.[225] The molecular orbitals of gold-phosphine clusters are arranged thusly: $[1S^\sigma]^2$; $[1S^\sigma]^2[1P^\sigma]^6$; $[1S^\sigma]^2[1P^\sigma]^6[1D^\sigma]^{10}$; *etc.* wherein $S, P, D\ldots$ denote angular-momentum characters (ℓ = 0, 1, 2…) and uppercase letters are used to distinguish these from atomic orbitals (σ-superscript signifies *pseudo*-spherical symmetry).[229] *Aufbau* filling

of these orbitals leads to shell-closing for 2, 8, 18… free-electrons giving exceptionally stable *spherical* clusters. The resultant gain in thermodynamic stability upon shell-closing is partly responsible for the propensity of a few specific cluster sizes observed during synthesis,[229] rather than a continuous distribution of compounds (*c.f.* colloidal nanoparticles). For *non-spherical* clusters, the asymmetry induced by prolate or oblate distortions can be sufficient to remove the degeneracy of the $1P_x^{\sigma}$, $1P_y^{\sigma}$ and $1P_z^{\sigma}$ orbitals.[225] If the energy-gap is adequately large, stabilisation can be granted from incomplete shell-closing configurations *i.e.* 4 and 6 free-electrons for prolate and oblate topologies, respectively. These distortions arise in order to quench the possibility of the cluster possessing unpaired electrons with high-spin multiplicity as a result of partial shell-closing.[231] The effect of cluster geometry on the population of molecular orbitals is given schematically below (Figure 2.3), as are examples of such clusters and their respective electron counts:

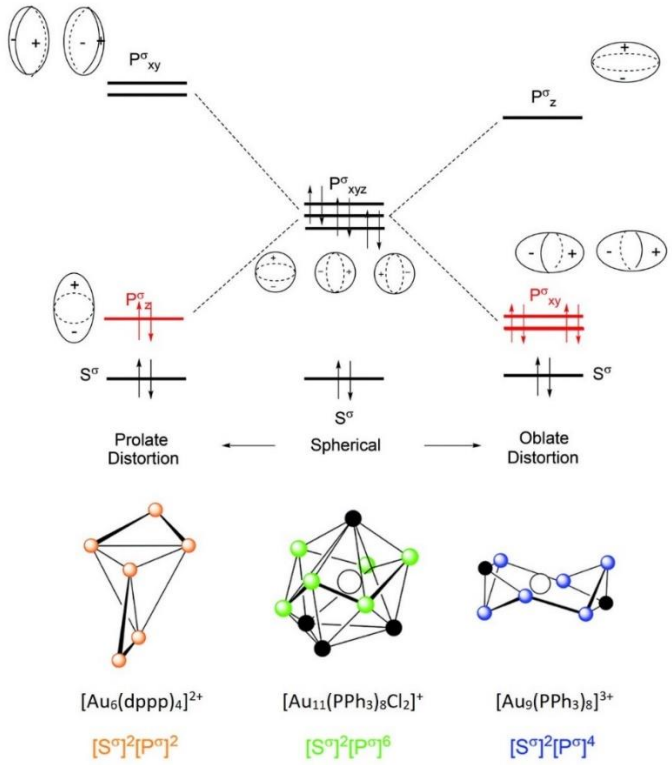

Figure 2.3 – Schematic diagram illustrating the correlation between gold-phosphine cluster geometry and superatom electron configuration, giving either prolate (left), oblate (right) or spherical (centre) topologies depending on the Jahn-Teller-like distortion to superatomic P^{σ} orbitals. The three examples above are all clusters synthesised in this work. Reproduced from Ref. 225 with permission from the Royal Society of Chemistry.

Since electrochemical events will alter the population of molecular orbitals, it therefore follows that charge-transfer should lead to geometric isomerisation of gold-phosphine nanoclusters. Indeed, this has been observed for the reversible reduction of $[Au_9(PPh_3)_8]^{3+}$ (n^* = 6, oblate) to $[Au_9(PPh_3)_8]^{+}$ (n^* = 8, spherical),[232] and the irreversible oxidation of $[Au_8(dppp)_4]^{2+}$ (n^* = 6, oblate) to $[Au_8(dppp)_4]^{4+}$ (n^* = 4, prolate).[189] The irreversibility of some redox events leading to cluster disintegration can be explained by a similar argument, whereby the new electron configuration is unsupported by the geometric constraints of the cluster framework and/or the steric demands of the protecting ligands. Such an approach will be employed to assign features observed the in non-aqueous electrochemical profiles of gold-phosphine nanocluster in Section 4.2.

Chapter 3

Synthesis of Gold and Silver Nanomaterials

3.1 – Synthesis of Six Cationic Gold-Phosphine Nanoclusters

Six atomically-precise gold-phosphine nanoclusters, namely $[Au_6(dppp)_4]^{2+}$, $[Au_8(PPh_3)_8]^{2+}$, $[Au_8Pd_1(PPh_3)_8]^{2+}$, $[Au_9(PPh_3)_8]^{3+}$, $[Au_{11}(PPh_3)_8Cl_2]^{+}$ and $[Au_{13}(dppe)_5Cl_2]^{3+}$, have been synthesised according to published literature methods and characterised by electrospray-ionisation mass-spectrometry (ESI-MS) and ^{31}P nuclear magnetic resonance (^{31}P NMR) to confirm identity (Section 8.2). In this chapter, the preparation and some notable features of these compounds will be discussed, although a complete summary of synthetic procedure followed can be found in Section 8.2.

3.1.1 *The Synthesis of $[Au_9(PPh_3)_8]^{3+}$*

The structure of $[Au_9(PPh_3)_8]^{3+}$ is well-known, and in the solid-state can be described as a bi-capped centred-chair with D_{2h} core-symmetry.[233] This arrangement is stereochemically non-rigid, and in solution rapidly isomerises to a centred-toroid (D_{4d} core-symmetry) which, despite substantial bond rearrangement, demonstrates the energy barrier separating these alternative geometries must be inherently low.[234] Such a skeletal change is also accompanied by the electrochemical reduction of $[Au_9(PPh_3)_8]^{3+}$ (centred-toroid, $n^* = 6$) to $[Au_9(PPh_3)_8]^{+}$ (bi-capped centred-chair, $n^* = 8$).[232, 235] It is likely that crystalline-packing enforces the more compact capped-chair framework for $[Au_9(PPh_3)_8]^{3+}$,[236] in which a marginal increase in steric interactions between phosphine ligands is offset by a modest increase in radial Au(centre)-Au(vertex) bonding.[224] Since the framework is to some extent flexible, solvation may relieve steric strain giving the preferred toroidal-geometry demanded by topological electron counting rules.[224, 237] In this work, the synthesis of $[Au_9(PPh_3)_8]^{3+}$ was achieved by the rapid borohydride reduction of $AuPPh_3NO_3$ in a 1:4 molar ratio in ethanol, as per the method described by Anderson *et al.*[238] and originally reported by Wen *et al.*[233] Crystallisation was by the vapour diffusion of diethyl ether into a methanolic solution of the product over one week, in a yield of *ca.* 30% by Au atom. Identity was confirmed by ^{31}P NMR in $CDCl_3$ (singlet, $\delta_1 = 57$ ppm *vs.* 85% H_3PO_4; Figure 8.1) and ESI-MS in 1:20 methanol/acetonitrile ($m/z \approx 1290$ ($[Au_9(PPh_3)_8]^{3+}$); Figure 8.3).

3.1.2 *The Synthesis of* $[Au_6(dppp)_4]^{2+}$

$[Au_9(PPh_3)_8]^{3+}$ is a useful precursor to other many other gold-phosphine clusters, particularly by ligand etching. As described by Van der Velden *et al.*,[239] the reaction of this with a 20-fold molar excess of 1,2-bis(diphenylphosphino)propane (dppp; $Ph_2P(CH_2)_3PPh_2$) in CH_2Cl_2 produces $[Au_6(dppp)_4]^{2+}$ exclusively. The mechanism has been investigated,[240] and it is likely the driving force for this conversion is the displacement of PPh_3 ligands *via* a chelate-type effect of dppp.[221] The greater steric enclosure of the bridged diphosphine also enforces a non-spherical geometry (Au_4 tetrahedron + two *exo*-Au atoms; C_{2v} core-symmetry), leading to Jahn-Teller-like distortions of superatomic orbitals in which the degeneracy of $[1P^{\sigma}]$ sub-shells are removed (Section 2.4.2). The electronic properties of this and other core + *exo* gold-phosphine clusters have been investigated,[241-243] and for such species, isolated absorption bands within optical spectra are a characteristic feature arising from these perturbations to electronic structure (Figure 8.4, Panel A). In the present work, the ligand-etching reaction proceeds for 15 minutes, after which time the product is recovered by precipitation from hexane and crystallised by the vapour diffusion of diethyl ether into a methanolic solution of the product over one week. Large purple/red-plate crystals were recovered in a yield of *ca.* 60% by Au atom. This cluster is light sensitive and slowly degrades to an unknown yellow product. Identity was confirmed by ^{31}P NMR in CD_3OD (two singlets of equal intensity, $\delta_1 = 62$ ppm and $\delta_2 = 54$ ppm *vs.* 85% H_3PO_4; Figure 8.1) and ESI-MS in 1:20 methanol/acetonitrile ($m/z \approx 1415$ ($[Au_6(dppp)_4]^{2+}$); Figure 8.3).

3.1.3 *The Synthesis of* $[Au_8(PPh_3)_8]^{2+}$

Similarly, $[Au_8(PPh_3)_8]^{2+}$ may be obtained by the etching of $[Au_9(PPh_3)_8]^{3+}$ with free PPh_3 in CH_2Cl_2 following the method described by Anderson *et al.*[238] and originally reported (simultaneously and independently) by Vollenbroek *et al.*[244] and Manassero *et al.*[245] Mechanistically, etching is believed to proceed *via* the generation of an $[Au_8(PPh_3)_7]^{2+}$ species which then recombines with free PPh_3 to generate the product.[246] By virtue of their reactivity, it is possible to accomplish the reverse transformation by the addition of $AuPPh_3NO_3$ to $[Au_8(PPh_3)_8]^{2+}$.[247] The above exchange reactions have been studied in detail,[222] and in this case equilibrium is achieved rapidly which suggests an invariably small energy barrier separating the geometries of these species. It is also worthy of note that whilst $[Au_9(PPh_3)_8]^{3+}$ can be obtained by the direct reduction of $AuPPh_3NO_3$,

$[Au_8(PPh_3)_8]^{2+}$ cannot be prepared this way,[248] or at least a synthetic approach that does not utilise the conversion of other clusters has not yet been devised. The structure of $[Au_8(PPh_3)_8]^{2+}$ can be considered a capped centred-chair in which all Au atoms bond to a single PPh_3 ligand each *and* an interstitial gold atom is present, giving C_{3v} core-symmetry.[245] Unsurprisingly, it is a derivative of the closely-related $[Au_9(PPh_3)_8]^{3+}$ species in the solid-state (bi-capped centred-chair). In this work, $[Au_9(PPh_3)_8](NO_3)_3$ is reacted with a 10-fold excess of PPh_3 in CH_2Cl_2 for 30 minutes, after which time precipitation from hexane followed by solvent washing gives the crude orange/red product. Crystallisation follows the same method as for Au_9, and the yield was *ca.* 80% by Au atom. Identity was confirmed by ^{31}P NMR in $CDCl_3$ (singlet, δ_1 = 59 ppm *vs.* 85% H_3PO_4; Figure 8.1) and ESI-MS in 1:20 CH_2Cl_2/acetonitrile (m/z ≈ 1836 ($[Au_8(PPh_3)_8]^{2+}$); Figure 8.3).

3.1.4 *The Synthesis of $[Au_{11}(PPh_3)_8Cl_2]^+$*

It is possible to generate higher-nuclearity species from the aggregation of parent clusters in the presence of nucleophiles, such as anionic or neutral Lewis bases. Often the reaction outcome is unpredictable, and the mechanism poorly understood, however for those protocols reported this can be a useful route to other gold-phosphine clusters. For example, $[Au_{11}(PPh_3)_8Cl_2]^+$ may be obtained by the reaction between $[Au_9(PPh_3)_8]^{3+}$ and excess Cl^- in CH_2Cl_2, as described by Vollenbroek *et al.*[223, 246] Conversely, treatment with excess SCN^- in an identical manner leads to the genesis of the related isomer, $Au_{11}(PPh_3)_7(SCN)_3$.[246] The first step of both above reactions involves the formation of $[Au_8(PPh_3)_8]^{2+}$ and $[AuX_2]^-$,[246] however subsequent transformations which lead to the assembly of undecagold species are only speculative and remain undiscovered. Regardless, further fragmentation of $[Au_8(PPh_3)_8]^{2+}$ and/or $[Au_9(PPh_3)_8]^{3+}$ species must occur to make the reaction possible. The preparation of $[Au_{11}(PPh_3)_8Cl_2]^+$ from the reaction between $[Au_9(PPh_3)_8](NO_3)_3$ and Et_4NCl in CH_2Cl_2 was attempted during this work. Indeed, the method proceed cleanly to yield the target cluster in isolation, however poor yields (< 15%) were obtained from a prohibitively expensive precursor ($[Au_9(PPh_3)_8](NO_3)_3$).

Alternatively, undecagold clusters may be prepared in more satisfactory quantities *via* the direct reduction of $AuPPh_3Cl$ in ethanol as per $[Au_9(PPh_3)_8](NO_3)_3$. Note that in the presence of a strongly coordinating anion, the cluster may grow to a higher nuclearity since vertex Au atoms can, beyond seven or eight phosphines, bond to additional ligands (*e.g.* Cl^-, I^-, SCN^-, CO) as permitted by steric demands. Notwithstanding the directing effect

of strongly coordinating anions towards the assembly of Au_{11} clusters, their presence does not necessarily guarantee this outcome: an interesting counterexample is the reduction of $AuPPh_3Cl$ by Ti^0 reagents (Section 2.3.1), which is reported to produce $[Au_9(PPh_3)_8]^{3+}$.[249] In this case, the resultant Ti cations may act as halide scavengers and therefore cluster growth is restricted to the *enneagold* species. Triarylphosphine-protected Au_{11} clusters are best described as an incomplete centred-icosahedron with C_{3v} core-symmetry (bridged-diphosphine Au_{11} species[242] tend to be of the core + *exo* variety; *viz.* $[Au_6(dppp)_4]^{2+}$). Note that there is no *named* polyhedron which can summarise the geometry of $[Au_{11}(PAr_3)X_{3-n}]X_n$, however this can conceptually can be thought of as a modified bi-capped centred-chair (*e.g.* $[Au_9]^{3+}$) wherein one cap has been replaced by a triangular face of Au atoms. Similar to the case for $[Au_8(PPh_3)_8]^{2+}$ and $[Au_9(PPh_3)_8]^{3+}$, the energy-barrier distinguishing the structures of $[Au_{11}(PPh_3)_8Cl_2]^+$ and $Au_{11}(PPh_3)_7Cl_3$ is probably small, since interconversion is synthetically facile.[222] As a result, it is likely both isomers will be generated in a given reaction mixture, and this was indeed discovered (Figure 8.2) following the method described by Anderson *et al*.[238] and originally reported by Woerhle *et al*.,[250] which involves the reduction of $AuPPh_3Cl$ in ethanol with an equimolar amount of $NaBH_4$. Separation of the two isomers proved difficult and impractical without resorting to elaborate chromatographic techniques, although this could eventually be achieved by laborious crystallisation efforts.

Recently, McKenzie *et al*. have reported complimentary synthetic approaches[251] to *selectively* prepare either isomer of PPh_3-protected undecagold clusters, and this protocol was successfully carried out during this work to obtain $[Au_{11}(PPh_3)_8Cl_2]Cl$. Briefly, a sub-molar quantity of $NaBH_4$ (one-quarter to Au) was added to $AuPPh_3Cl$ in CH_2Cl_2/ethanol (5:1 v/v), and after stirring overnight the orange product is collected by precipitation from hexane. After solvent washing, the product is extracted into CH_2Cl_2 and initially crystallised from the vapour diffusion of diethyl ether over one week, in a yield of *ca.* 30% by Au atom. The crude product was found to contain trace amounts (by ^{31}P NMR) of the other isomer, which was removed by judicious crystallisation (Section 8.2.5). Alternatively, $Au_{11}(PPh_3)_7Cl_3$ is synthesised by adding a five-fold molar excess of $NaBH_4$ to $AuPPh_3Cl$ in THF/ethanol (1:1 v/v). This isomer appeared to be less thermally-stable than the abovementioned analogue (McKenzie and co-workers also note this[251]), and would decompose to metallic gold during crystallisation which regretfully lead to the omission of this cluster species from any further work. Identity was confirmed by ^{31}P NMR in $CDCl_3$ (singlet, $\delta_1 = 52$ ppm *vs.* 85% H_3PO_4; Figure 8.1) and ESI-MS in 1:20 CH_2Cl_2/acetonitrile ($m/z \approx 1421$ ($[Au_{11}(PPh_3)_8]^{3+}$); Figure 8.3).

3.1.5 *The Synthesis of* $[Au_8Pd_1(PPh_3)_8]^{2+}$

The synthesis of $[Au_8Pd_1(PPh_3)_8]^{2+}$ was carried out following the method described by Matsuo *et al.*,[252] though in contrast to the protocol for $[Au_9(PPh_3)_8]^{3+}$, reduction is carried out slowly and Au-phosphine fragments assemble around a central Pd^0 atom. It is interesting to note that the presence of strongly coordinating Cl^- in this mixture does not favour the formation of undecagold (Au_{11}) species, or Pd-doped analogues thereof. It is possible the presence of Pd^0 atoms in the reaction mixture has a greater influence on cluster assembly than Cl^- ions do. It has also been shown that Pd-doping of Au_9 results in a more rigid cluster framework which resists geometric isomerisation observed in the latter compound (*viz*. Section 3.1.1).[253] Whilst the centred-crown and chair forms of Au_8Pd_1 are predicted to be similar in energy,[253] the decreased flexibility of the cluster skeleton is attributed is attributed to the difference in electron-affinities between Pd^0 and $Au^{\delta+}$ atoms which places more electron-density on lateral Au-PPh_3 fragments, increasing their repulsion and yielding a less-dynamic framework. Since structural deformation is required for isomerisation, a reduction in vibrational entropy prevents interconversion and therefore Au_8Pd_1 only inhabits a centred-crown form.

$AuPPh_3Cl$ and $Pd(PPh_3)_4$ are co-dissolved in CH_2Cl_2/ethanol and to this is slowly added *solid* $NaBH_4$ (equimolar with respect to Au + Pd). It was found that the yield of the reaction could be greatly improved by carrying out the reduction step *as slowly as possible* over a significant amount of time. After stirring for 1 hour after all borohydride is added, the red/brown product is precipitated by hexane and washed to remove starting materials. At this point, the authors of the original method would subject the crude mixture to further etching with excess PPh_3, possibly as a size-focusing step to increase yields. This was omitted in this work as only the target cluster was observed by ^{31}P NMR. The removal of residual $Pd(PPh_3)_x$ species proved challenging, however was achieved through copious non-polar solvent washings. The product was crystallised by the vapour diffusion of diethyl ether into an ethanolic solution of the residue over one week at ambient temperature, in a yield of *ca.* 65% by Au atom. Identity was confirmed by ^{31}P NMR in CD_2Cl_2 (singlet, δ_1 = 51 ppm *vs.* 85% H_3PO_4; Figure 8.1) and ESI-MS in 1:20 CH_2Cl_2/acetonitrile ($m/z \approx 1889$ ($[Au_8Pd_1(PPh_3)_8]^{2+}$); Figure 8.3).

3.1.6 *The Synthesis of* $[Au_{13}(dppe)_5Cl_2]^{3+}$

Following the method reported by Shichibu and Konishi,[254] the direct reduction of $Au_2(dppe)Cl_2$ (dppe, 1,2-bis(diphenylphosphino)ethane, $Ph_2P(CH_2)_2PPh_2$) in CH_2Cl_2/ethanol with a 10-fold molar equivalent of $NaBH_4$, followed by post-synthetic treatment with concentrated HCl overnight leads to the convergent formation of $[Au_{13}(dppe)_5Cl_2]^{3+}$ as the sole product. A regular icosahedron with five equatorial diphosphine ligands and two axial chloride ligands giving I_h core-symmetry, Au_{13} is an example of a cluster motif which displays outstanding thermal and kinetic stability, attributed to complete electron-shell and polyhedral-shell closing.[255] Other noteworthy examples where such an Au_{13} fragment imparts exceptional thermal stability include the gold-thiolate clusters $[Au_{25}(SR)_{18}]^z$ (icosahedral core)[207] and $Au_{38}(SR)_{24}$ (face-fused bi-icosahedral core).[209] The mechanism of formation is interesting in itself, and is an example of kinetically-driven cluster interconversion in the presence of a Lewis base: reduction of $Au_2(dppe)Cl_2$ is believed to generate a polydisperse mixture of clusters with core-sizes ranging from 9 to 15 gold atoms (as postulated by Shichibu and Konishi). Treatment with HCl is then thought to weaken core-ligand interactions by the cooperative coordination of H^+ and Cl^- across the dative Au-P bond, driving the reversible dissociation and re-association of labile Au-ligand fragments leading to accumulation of the thermodynamic product, $[Au_{13}(dppe)_5Cl_2]^{3+}$.[254] In the present work, 10 molar-equivalents of $NaBH_4$ in ethanol are added to a solution of $Au_2(dppe)Cl_2$ in CH_2Cl_2, and after 3 hours the dark red residue is dried, re-dissolved in ethanol and to this is added 1mL of *ca.* 12M HCl. After stirring overnight, the target cluster was obtained after drying and purification by repeated solvent washings to remove residual $Au_2(dppe)Cl_2$. Crystallisation was by the vapour diffusion of diethyl ether into a methanolic solution of the product over one week, forming large red-block crystals in *ca.* 80% yield by Au atom. Identity was confirmed by ^{31}P NMR in CD_3OD (singlet, δ_1 = 67 ppm *vs.* 85% H_3PO_4: Figure 8.1) and ESI-MS in 1:20 methanol/acetonitrile ($m/z \approx 1541$ ($[Au_{13}(dppe)_5Cl_2]^{3+}$); Figure 8.3).

3.2 – Synthesis of Colloidal Gold Nanoparticles

Gold Nanoparticles (AuNPs) were prepared following the method described by Padayachee *et al.*[256] and originally reported by Kimling and co-workers.[257] This method is a modification of the prototypical Turkevich protocol[157] for synthesising citrate-capped water soluble AuNPs, and involves the rapid addition of a heated

trisodium citrate ($Na_3C_6H_5O_7$) solution to a heated solution of acidified tetrachloroaurate ($[AuCl_4]^-$) in water. Reduction takes place immediately and the particle size-distribution of the resultant colloidal solution may be controlled, usually to a satisfactory degree, by varying the gold:citrate molar ratio. Following the quantities outlined by both Padayachee[256] and Kimling,[257] a ten-fold molar equivalent of trisodium citrate was added to the aforementioned acidified $[AuCl_4]^-$ solution to (reportedly) produce *ca.* 14 nm AuNPs. UV-Vis absorption spectra feature a broad band at *ca.* 533 nm, indicating the successful synthesis of plasmonic gold nanoparticles.[175] These were used without further purification, and their concentration in solution estimated from the average particle size calculated in the forthcoming discussion (Section 3.2.1).

3.2.1 *Estimation of Gold Nanoparticle Diameter*

The average size of (approximately spherical) AuNPs may be estimated from Mie's model,[151] which predicts that the position of the surface-plasmon resonance peak wavelength (in nm) is exponentially proportional to particle diameter. The equation derived by Haiss *et al.*[258] in their study of the optical properties of various-sized AuNPs (equation 3.1),

$$\lambda_{SPR} = \lambda_0 + L_1 e^{L_2 d} \tag{3.1}$$

allows an estimation of average particle size for particles in the range *ca.* 35-110 nm, where the terms L_1 and L_2 are experimentally determined best-fit parameters (6.53 and 0.0216, respectively), λ_0 is equal to 512 nm (the predicted absorbance maxima for a particle 35 nm diameter[151]), λ_{SPR} is the measured plasmonic peak wavelength and d is the average particle diameter (both in nm). For particles smaller than 35 nm, equation 3.1 cannot be used as this model deviates sharply from linearity as this boundary is approached.[258] This is due to the increasing influence the ligand periphery, temperature, solvent medium and divergence from true spherical dimensions has on the mean-free path of interacting photons with decreasing particle size,[175] where errors become significant and equation 3.1 grossly *overestimates* the average diameter. For decreasing AuNP size, the absorbance maxima corresponding to surface-plasmon resonance is increasingly dampened (due to the aforementioned effects); this feature may be exploited as a measure of particle size, and as an alternative Haiss *et al*. propose the following model to estimate average diameter within the range *ca.* 5-35 nm,:[258]

$$d = e^{B_1 \frac{A_{SPR}}{A_{450}} - B_2} \quad (3.2)$$

Where B_1 and B_2 are experimentally-determined best-fit parameters (3.00 and 2.20, respectively), A_{SPR} is the measured absorbance maxima at λ_{SPR} and A_{450} is the absorbance measured at 450 nm (this value is chosen to avoid the influence non-spherical particles have on the mean-free path of photons at longer wavelengths and is not arbitrary). Employing equations 3.1 and 3.2, alongside λ_{SPR} (533 nm), the best-fit parameters recommended by Haiss *et al.* and other values from UV-Vis studies (A_{SPR} and A_{450}), yields average diameter estimates of 54 nm and 9.5 nm, respectively. The UV-Vis absorbance profile of these AuNPs (as prepared, in water) is shown in Figure 8.4, Panel H. Now, since the absorbance maxima for the AuNP sample prepared in this work is *ca.* 533 nm, these species *must* have an average diameter *greater* than 35 nm and are not *ca.* 14 nm particles, nor are they likely to be *ca*. 9.5 nm NPs. In fact, Mie's model predicts that *ca.* 14 nm particles will have a surface-plasmon absorbance situated at *ca.* 520 nm,[151] which is measurably smaller than that obtained in this work and the difference (*ca.* 13 nm) is far greater than the instrumental resolution of the spectrophotometer used. It is therefore probable that the AuNPs synthesised in this work are larger than 14 nm in diameter and are closer to 50-60 nm. This author notes that for a wide-ranging distribution of particle sizes (indicated by a rather broad plasmonic peak; Figure 8.4, Panel H), equation 3.2 will *underestimate* particle size, which may explain the unreasonable value of *ca.* 9.5 nm calculated from this approach.[258]

Of course, one concedes that electron microscopy imaging would yield a far more accurate estimate of the *true* particle size of this AuNP sample; as is noted in Sections 5.2.1 and 6.3.1 (*vide infra*), such studies have been requested from colleagues at Flinders University (Adelaide, South Australia) however at the time of writing such results have not yet been received by this author. Hence, the estimation of particle size from a theoretical approach above. Regardless of true particle size, the AuNPs prepared in this work are likely large enough that their exteriors can be considered representative of metallic gold surfaces, and in forthcoming sections these will simply be donated as "large AuNPs".

3.3 – The Synthesis of $[Ag_{25}(SPhMe_2)_{18}]^-$

The synthesis of $[Ag_{25}(SPhMe_2)_{18}]^-$ was carried out following the method described by Bakr *et al.*,[259] which follows a similar protocol to that of gold-thiolate nanoclusters. In this approach, Ag^+ ions are dissolved in an organic solvent mixture (with cooling) and to this is added the thiolate ligand, in this case 2,4-dimethylbenzenethiol ($HSPhMe_2$) in a three-fold molar excess. At this point, it is believed that insoluble silver-thiolate oligomers are formed.[259] An aqueous solution of $NaBH_4$ (two-fold molar excess to Ag) is then added dropwise over several minutes. A stark colour change, from yellow to black, is typical for thiolate-protected nanoclusters of both gold and silver. Although Bakr and co-workers carry out their preparation in ambient conditions, it was found an atmosphere of N_2 would greatly improve the crude yield of the target cluster. It was discovered at this point that excessive drying of the crude product would invoke the irreversible degradation of the target cluster to yellow silver-thiolate oligomers (insoluble) and an unknown orange species, which is soluble in polar-organic solvents and exhibited a large absorption-band within the plasmonic region of the visible-light spectrum. Therefore, it is recommended by this author that the title compound, $[Ag_{25}(SPhMe_2)_{18}]^-$, be recovered by precipitation from non-polar organic solvents. It is also noteworthy that the target cluster is somewhat unstable in solution and will degrade over a few hours at ambient temperature to insoluble yellow oligomers (storage at low temperatures may prolong this to over a week). It may also be somewhat light-sensitive. Therefore, manipulations involving this cluster should be carried out in a timely manner. Nevertheless, the crystallisation of this compound may be achieved by layering a solution of the crude product (in CH_2Cl_2) with cold *n*-hexane below 0°C over about one week. The yield was *ca.* 15% (by Ag atom). Characterisation by ESI-MS proved difficult to achieve, and despite replicating the instrument parameters stated by Bakr *et al.*[259] no signal was located which could be assigned to the target compound. Therefore, a single-crystal X-ray diffraction study was performed (with the generous assistance of Dr James Ward; Section 8.4.4) which unambiguously confirmed the identity of this species (Figure 8.5).

Chapter 4

Non-Aqueous Voltammetry Studies of Gold-Phosphine Nanoclusters

4.1 – Introduction to Differential-Pulse Voltammetry

The electronic structure and redox behaviour of gold-phosphine nanoclusters were investigated with differential-pulse voltammetry (DPV). DPV is an electroanalytical technique whereby a series of regular voltage pulses are superimposed on a linear potential sweep. The current is sampled at two separate time intervals: immediately prior to pulse application, and immediately before the pulse terminates. The resultant difference between final and initial currents (δI) is taken as a function of potential E. The advantage of DPV in electrochemical analysis derives from the superior elimination of non-faradaic background currents (*e.g.* capacitive effects),[16] which manifest in conventional potential-sweep methods such as cyclic voltammetry (CV). Since background processes are suppressed by experiment design, electron-transfer events are readily extracted with higher sensitivity than is possible with CV, and for this reason DPV is a popular method for interrogating the redox properties of gold nanoclusters.[189, 194, 233, 260-262]

Differential-pulse voltammograms were collected in anhydrous CH_2Cl_2 with 0.1 M Bu_4NPF_6 (tetra-*n*-butylammonium hexafluorophosphate) supporting electrolyte underneath an argon atmosphere, with a nanocluster concentration of *ca.* 0.2 mM. *All potential values in this chapter are reported with respect to* E_{eq} *of the ferrocene/ferrocenium (*Fc/Fc^+*) couple under the same conditions*. A full summary of the experimental apparatus and instrument parameters can be found in Section 8.4. Differential-pulse voltammograms for all six gold-phosphine clusters prepared in this work are shown in Figure 4.1. Cathodic (red, negative-going) and anodic (blue, positive-going) segments of each voltammogram are plotted separately either side of the open-circuit potential, and distinct peaks arising from both the reduction and oxidation of gold-phosphine clusters are present. These features observed in non-aqueous DPV spectra may be interpreted from a superatom perspective, and the electrochemical profiles will be discussed for each cluster sequentially in the following sections.

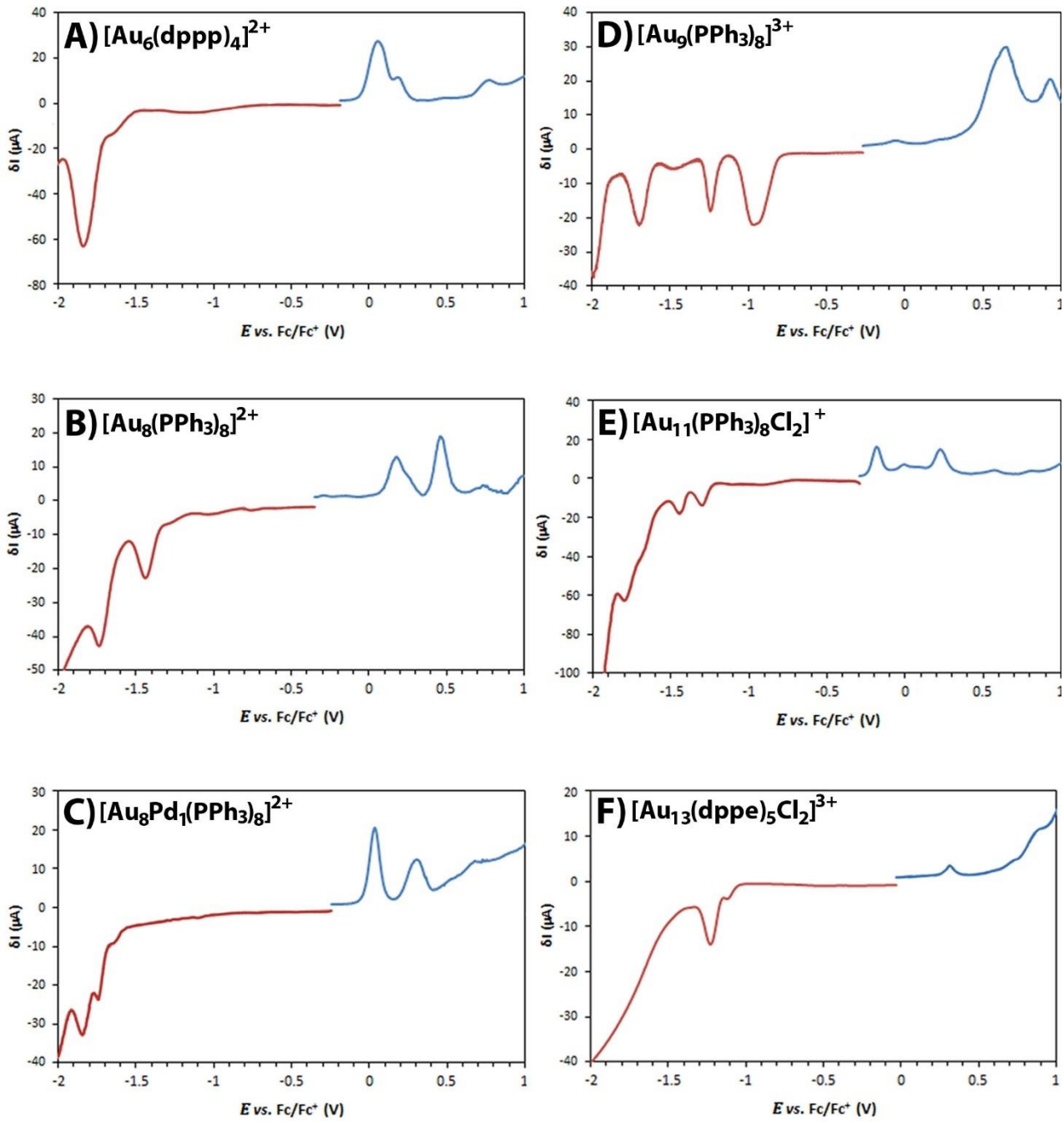

Figure 4.1 – Differential-pulse voltammograms (DPV) for A) $[Au_6(dppp)_4]^{2+}$; B) $[Au_8(PPh_3)_8]^{2+}$; C) $[Au_8Pd_1(PPh_3)_8]^{2+}$ D) $[Au_9(PPh_3)_8]^{3+}$ E) $Au_{11}(PPh_3)_8Cl_2]^{+}$; F) $[Au_{13}(dppe)_5Cl_2]^{3+}$ in Ar-purged anhydrous CH_2Cl_2 with 0.1 M Bu_4NPF_6 supporting electrolyte and a cluster concentration of *ca.* 2 mM. Cathodic (blue) and anodic (red) scans are shown separately about the open-circuit potential. Potentials are given with respect to the ferrocene/ferrocenium redox couple.

4.2 – Non-Aqueous Electrochemical Profiles of Gold-Phosphine Nanoclusters

The reversibility of charge-transfer events observed in voltammetry data was determined by measuring the separation between peaks for each redox event during cathodic and anodic potential sweeps if such peaks appeared during both directions of the potential sweep. In most cases, this separation was typically between

ca. 20 - 40 mV, which is close to the predicted 29 mV for a reversible one-electron charge-transfer event.[1] If no reverse peak was observed in either cathodic or anodic scans, or the magnitude of such a peak was less than *ca.* 25% the size of the same peak on the opposite scan, this event was designated irreversible (an example of each case is given in Figure A.1 (Appendices)). The cathodic and anodic scans are split at the open-circuit potential, and the remaining portion of each scan omitted for clarity: in most cases, including this portion of the data would cause the scale of the vertical-axis to grow considerably and thus render some electrochemical features difficult to observe in DPV plots.

4.2.1 $[Au_6(dppp)_4]^{2+}$

The electrochemical profile of $[Au_6(dppp)_4]^{2+}$ (in 0.1 M Bu_4NPF_6/CH_2Cl_2 – Figure 4.1, Panel A) displays two reduction events within the potential window interrogated, corresponding to generation of the $[Au_6(dppp)_4]^{+}$ ($[1S^{\sigma}]^2[1P^{\sigma}]^3$; R1 = -1.65 V) and $[Au_6(dppp)_4]^{0}$ ($[1S^{\sigma}]^2[1P^{\sigma}]^4$; R2 = -1.84 V) species. These reductions are subsequently found to be reversible. The small spacing between R1 and R2 peaks (*ca.* 200 mV) is probably indicative of the preference to pair electrons in the remaining degenerate $[1P_x^{\sigma}]$ or $[1P_y^{\sigma}]$ orbitals and avoid the generation of high-spin multiplicity states.[225] As mentioned in Section 2.4, this would intuitively require a geometry change from prolate to oblate topologies, which may be accommodated by the flexibility of the propane bridge linking the terminal phosphorus atoms in dppp ligands. Two oxidation events, O1 (+0.08 V) and O2 (+0.21 V) occur and these are found to be irreversible. This can be explained by considering that oxidation would generate the $[Au_6(dppp)_4]^{3+}$ species with a $[1S^{\sigma}]^2[1P^{\sigma}]^0$ electron count. Such a configuration is typical of spherical clusters,[225] however as has been discussed the large steric demand of tertiary phosphine ligands is unlikely to accommodate such a compact topology and therefore cluster decomposition (or significant molecular rearrangement) results. A small irregularly-shaped oxidation peak at *ca.* +0.79 V is likely from the opportunistic infiltration of water during setup of the electrochemical cell.[263] The electrochemical gap, or the charge-transfer barrier of $[Au_6(dppp)_4]^{2+}$ (denoted ΔE_g) is found by taking the potential difference between R1 and O1 peaks,[144] which conceptually represents the energy penalty for transporting *one* electron through the cluster during a hypothetical electron-transfer role. This is found to be 1.87 eV. The

electrochemical profile of $[Au_6(dppp)_4]^{2+}$has not (to the best of this authors knowledge) yet been reported in the literature.

4.2.2 $[Au_8(PPh_3)_8]^{2+}$

The electrochemical profile of $[Au_8(PPh_3)_8]^{2+}$ (in 0.1 M Bu_4NPF_6/CH_2Cl_2 – Figure 4.1, Panel B) also displays two reversible reduction waves, at -1.43 V (R1) and -1.73 V (R2), and two irreversible oxidation waves at +0.21 V (O1) and +0.49 V (O2). The spacing between R1 and R2, or O1 and O2 is *ca.* 300 mV. A survey of the literature finds this to be a typical charging-energy for gold nanoclusters, which appears mostly invariable of size for those reported though it is mathematically predicted[264] to be inversely proportional to cluster size. As before, the presence of residual water in the cell gives rise to an oxidation wave at *ca.* +0.78 V. The electrochemical gap ΔE_g is decreased upon the hypothetical (albeit grossly oversimplified) appendage of two gold atoms to the $[Au_6]^{2+}$ core and is now 1.64 eV, in agreement with that previously reported.[248] It is noteworthy that $[Au_8(PPh_3)_8]^{2+}$ is often classed as spherical by PSEPT count[225] (also supported by crystallographic analysis[248]) however incomplete electron-shell closing ($[1S^\sigma]^2[1P^\sigma]^4$) suggests an oblate topology should arise.[224, 225] This discrepancy has not been discussed in the literature (as far as this author is aware), however it may be that the steric demand of eight PPh_3 ligands causes the core to depart from an oblate topology towards a spherical geometry. This conclusion is partially supported by the fact that an isomer, $[Au_8(PPh_3)_7]^{2+}$ is fully oblate by both electron-counting rules and crystallographic analysis,[247] so it is not unreasonable that the addition of one PPh_3 ligand increases steric interactions which are relieved by geometric distortion. Additionally, a transition from oblate to spherical topology would greatly improve the accessibility of radial interactions between interstitial and vertex Au atoms.[224, 226] Alternatively, $[Au_8(PPh_3)_8]^{2+}$ may indeed possess spherical geometry *in the solid state* (as crystallographically observed[248]), however in solution and free from packing interactions it may indeed revert to the electronically preferred oblate topology. In any case, a two-electron reduction would populate the $[1P_z^\sigma]$ orbital, leading to complete electron-shell closing and enforce a definite spherical geometry, whereas a two-electron oxidation would produce an electron configuration with (sterically unsupported) prolate geometry ($[1S^\sigma]^2[1P^\sigma]^2$) and subsequent decomposition.

4.2.3 $[Au_8Pd_1(PPh_3)_8]^{2+}$

The electrochemical profile of $[Au_8Pd_1(PPh_3)_8]^{2+}$ in 0.1 M Bu_4NPF_6/CH_2Cl_2 is shown in Figure 4.1, Panel C. The conceptual addition of a Pd atom to $[Au_8(PPh_3)_8]^{2+}$ is observed to shift all electrochemical features toward more negative potentials, with two reduction waves at -1.64 V (R1) and -1.84 V (R2), which are found to be reversible however are partially overlapping. These are assigned to the generation of $[Au_8Pd_1(PPh_3)_8]^{+}$ ($[1S^{\sigma}]^2[1P^{\sigma}]^5$) and $[Au_8Pd_1(PPh_3)_8]^{0}$ ($[1S^{\sigma}]^2[1P^{\sigma}]^6$) species. It is noteworthy that the spacings between R1 and R2 are narrowed by the addition of a Pd atom (*ca.* 200 mV) compared to R1 and R2 for $[Au_8(PPh_3)_8]^{2+}$(*ca.* 300 mV; Section 4.2.2), whereas oxidation waves at +0.04 V (O1) and +0.33 V (O2) display a *ca.* 300 mV separation of a similar magnitude. The presence of trace impurities of water is observed as an oxidation wave at *ca.* +0.78 V, and the electrochemical gap ΔE_g is widened to 1.72 eV, in agreement with that previously reported in the literature.[252] It is interesting that the presence of a slightly electropositive heterometal (relative to Au) appears to encourage further electron acquisition (decreased reductive charging-energy), and discourage electron confiscation (increased oxidative charging-energy). Recent computational predictions supported by single-crystal X-ray diffraction studies have found that the presence of a Pd atom in $[Au_8Pd_1(PPh_3)_8]^{2+}$ prohibits isomerisation upon solvation (as is observed for $[Au_9(PPh_3)_8]^{3+}$; Section 4.2.4 *vide infra*) from crown-shaped to butterfly-shaped geometries (Section 3.1.5).[253] Whilst both arrangements are strictly toroidal, a two-electron reduction would intuitively generate a spherical topology (*e.g.* centred bi-capped hexagonal chair). The energy-barrier separating the latter geometry from the centred-crown in $[Au_8Pd_1(PPh_3)_8]^{2+}$ has been calculated as 0.18 eV by density-functional theory,[253] which this author notes is similar to the energy separation between R1 and R2 peaks in Figure 4.1, Panel C (*ca.* 0.2 eV). It is not difficult to imagine that a geometry change would not appreciably occur until complete population of the vacant $[1P_z^{\sigma}]$ orbital following a two-electron reduction.

4.2.4 $[Au_9(PPh_3)_8]^{3+}$

The electrochemical profile of $[Au_9(PPh_3)_8]^{3+}$ in 0.1 M Bu_4NPF_6/CH_2Cl_2 is shown in Figure 4.1, Panel D. In contrast to $[Au_8Pd_1(PPh_3)_8]^{2+}$, the hypothetical addition of an Au atom to $[Au_8(PPh_3)_8]^{2+}$ shifts redox features more positive potentials. There are now three reduction waves at -0.94 V (R1), -1.24 V (R2) and -1.96 V (R3), of which R3 is subsequently found to be irreversible. The potential spacing between R1 and R2 is *ca.* 300 mV,

and between R2 and R3 almost 600 mV, an exceptionally large charging-energy. These reduction events could be attributed to the formation of $[Au_9(PPh_3)_8]^{2+}$ ($[1S^{\sigma}]^2[1P^{\sigma}]^5$) and $[Au_9(PPh_3)_8]^{2+}$ ($[1S^{\sigma}]^2[1P^{\sigma}]^6$) species, alongside a (possibly unstable) $[Au_9(PPh_3)_8]^{0}$ ($[1S^{\sigma}]^2[1P^{\sigma}]^6[1D^{\sigma}]^1$). Whilst the two-electron reduction of $[Au_9(PPh_3)_8]^{3+}$ is known to induce a structural-conformation change from toroidal to spherical geometries,[232, 262] the topological implications of $[1D^{\sigma}]$ orbital population in gold-phosphine nanoclusters has not yet been discussed in the literature. Since this phenomenon is found to be irreversible, it is possible that this electronic level corresponds to an anti-bonding molecular orbital with a large energy-gap from the nearest bonding orbital (*i.e.* $[1P^{\sigma}]$); this would explain the unprecedented charging-energy between R2 and R3. Two oxidation waves at +0.66 V (O1) and +0.95 V (O2) are also observed to shift to more positive potentials compared to $[Au_8(PPh_3)_8]^{2+}$, and these are found to be irreversible (due to the likely formation of a sterically-unsupported prolate topology) with a charging-energy of *ca.* 300 mV. The electrochemical gap ΔE_g of $[Au_9(PPh_3)_8]^{3+}$ is found to be smaller than that of $[Au_8(PPh_3)_8]^{2+}$ at 1.62 eV, in agreement with the literature.[232, 235, 262]

4.2.5 $[Au_{11}(PPh_3)_8Cl_2]^+$

The electrochemical profile of $[Au_{11}(PPh_3)_8Cl_2]^+$ (in 0.1 M Bu_4NPF_6/CH_2Cl_2 – Figure 4.1, Panel E) displays three reduction waves at -1.30 V (R1), -1.44 V (R2) and -1.74 V (R3), of which R1 and R2 are found to be reversible and R3 is irreversible. Conceptually, the two-electron reduction of $[Au_{11}(PPh_3)_8Cl_2]^+$ would lead to the formation of an *anionic* 10-electron superatom $[Au_{11}(PPh_3)_8Cl_2]^-$ with a $[1S^{\sigma}]^2[1P^{\sigma}]^6[1D^{\sigma}]^2$ configuration. It is noteworthy that *no* anionic gold-phosphine clusters have been prepared *via* wet-chemical syntheses, since electron-counting rules mathematically prohibit such an attribute when the number of gold atoms is small (< 13; Section 2.4 and Equation 2.1).[225] Regardless, the reversibility of this process suggests such a species is at least somewhat stable within the present experimental context. It is uncertain if population of the $[1D^{\sigma}]$ orbitals would lead to geometric changes within the $[Au_{11}]^{3+}$ core, but *if* such energy-levels are anti-bonding in nature then it is expected some degree of destabilisation will result. Tofanelli and Ackerson[265] have noted that a one-electron reduction of the cluster $[Au_{25}(SC_6H_{11})_{18}]^-$, which presumably places an electron in a $[1D^{\sigma}]$ orbital, does not lead to significant distortions to cluster geometry. It may be possible to isolate an anionic $[Au_{11}(PPh_3)_8Cl_2]^-$ (if it is indeed isolable) by sustained electrolysis at -1.74 V < E < -1.44 V, which could possess interesting chemical functionality distinct from the parent $[Au_{11}(PPh_3)_8Cl_2]^+$. A subsequent

single-electron reduction at more-negative potentials (R3) would intuitively generate $[Au_{11}(PPh_3)_8Cl_2]^{2-}$ possessing a third unpaired D^{σ} electron with paramagnetic properties. Two oxidation waves are found at -0.16 V (O1) and +0.24 V (O2), and in a similar manner to previous clusters these are irreversible events. Removal of two electrons to generate the $[Au_{11}(PPh_3)_8Cl_2]^{3+}$ species gives an electronic structure that is expected to demand a geometric shift to oblate topologies ($[1S^{\sigma}]^2[1P^{\sigma}]^4$), which may be sterically disfavoured by significant non-bonding interactions between tertiary phosphine ligands, and lead to irreversible cluster disintegration. The electrochemical gap ΔE_g is found to be unusually small for gold nanoclusters in this size regime, only 0.83 eV. This is an especially curious result, since a well-known and structurally-similar neutral isomer $Au_{11}(PPh_3)_7Cl_3$ [251, 266] possesses a computed HOMO-LUMO gap of *ca.* 2 eV.[229] Subtracting a typical charging-energy of 0.3 eV would yield an estimated electrochemical gap ΔE_g of *ca.* 1.7 eV, at least twice that of $[Au_{11}(PPh_3)_8Cl_2]^{+}$ employed in this work.

This is surprising since the only difference between either isomer is the replacement of one PPh_3 ligand for a Cl^- ligand, with retention of cluster topology and electron count. The large deviation between ΔE_g values for these isomers may be an interesting consequence of the structure-dependent properties of metal nanoclusters, and certainly warrants further investigation. The electrochemical profiles of $[Au_{11}(PPh_3)_8Cl_2]^{+}$ and $Au_{11}(PPh_3)_7Cl_3$ have not yet been reported in the literature. It is regrettable however that in this work the synthesis of $Au_{11}(PPh_3)_7Cl_3$ in satisfactory quantities and purity proved exceedingly difficult (Section 3.1.4). Admittedly, the significantly smaller value of ΔE_g for $[Au_{11}(PPh_3)_8Cl_2]^{+}$ is somewhat questionable, when considering the comparatively gradual variation across the remaining gold-phosphine clusters used in this work. Moreover, both isomers possess similar ^{31}P NMR shifts (Figure 8.2) which one would not expect if the respective electronic properties of each cluster were to have an appreciable influence on the magnetic properties of the ligand-phosphorus atoms. On the other hand, inconsistencies between measured values for ΔE_g may be found in the literature, and in some cases this data was collected under virtually identical conditions. For instance, the gold-thiolate nanocluster $Au_{38}(C_2H_4Ph)_{24}$ is reported by Murray *et al.*[263] to have a ΔE_g value of 1.62 eV, whilst Jin *et al.*[261] measure ΔE_g as 1.20 eV. Both values were obtained by DPV in CH_2Cl_2 at ambient temperature at a Pt electrode. It is plausible that either the estimated HOMO/LUMO gap for $Au_{11}(PPh_3)_7Cl_3$ (from which ΔE_g was obtained above) suffers from unavoidable constraints imposed by computational approaches (*e.g.* the approximation of PPh_3 ligands with PH_3, or the exclusion of solvent

interactions), or the ΔE_g measured for $[Au_{11}(PPh_3)_8Cl_2]^+$ in this work is simply incorrect, for reasons which are not immediately obvious to this author. The possibility of drifting potentials at the Ag *pseudo*-reference electrode can be ruled out, since other gold-phosphine nanoclusters yield values of ΔE_g consistent with that reported in the literature.

4.2.6 $[Au_{13}(dppe)_5Cl_2]^{3+}$

The electrochemical profile of $[Au_{13}(dppe)_5Cl_2]^{3+}$ (in 0.1 M Bu_4NPF_6/CH_2Cl_2 – Figure 4.1, panel F) displays a comparatively unfeatured electrochemical profile to that of previous clusters: two reversible reduction waves which are partially overlapping at -1.11 V (R1) and -1.22 V (R2), and a single oxidation wave at +0.34 V (O1) which is irreversible. In a manner not dissimilar to $[Au_{11}(PPh_3)_8Cl_2]^+$, reduction is expected to populate one $[1D^\sigma]$ orbital which may or may not be anti-bonding in nature. However, the high thermodynamic and kinetic stability of the icosahedral $[Au_{13}]^{5+}$ motif[229, 255] may be able to accommodate some degree of destabilisation resulting from such a process. Additionally, the flexibility of the ethylene bridge within the diphosphine ligands may be able to relieve steric interactions upon electrochemically-induced structural changes (if these do indeed occur upon reduction of a spherical $[1S^\sigma]^2[1P^\sigma]^6$ cluster). This may explain the observed reversibility of two-electron reduction, and the small charging-energy spacing between R1 and R2 (*ca.* 100 mV) may imply that the pairing of electrons in a $[1D^\sigma]$ orbital is not thermodynamically disfavoured. Oxidation of the parent $[Au_{13}(dppe)_5Cl_2]^{3+}$ cluster in a one-electron process would generate $[Au_{13}(dppe)_5Cl_2]^{2+}$ with a $[1S^\sigma]^2[1P^\sigma]^5$ electron configuration, recalling that of an elemental halogen atom with a single electron vacancy. This apparently does not undergo any further oxidation in the potential window examined, possibly mirroring the substantial second ionisation-energy of the halogens. The electrochemical gap ΔE_g of $[Au_{13}(dppe)_5Cl_2]^{3+}$ is measured to be 1.45 eV, and although the electrochemical behaviour of this cluster has not yet been reported in the literature, ΔE_g of the hypothetical $[Au_{13}]^{5+}$ moiety (de-ligated) has been estimated to be *ca.* 1.50 eV,[212] in reasonable agreement with the experimental results herein.

4.3 – Summary and Remarks

The electrochemical properties of six atomically-precise gold-phosphine nanoclusters have been investigated by differential-pulse voltammetry in 0.1 M Bu_4NPF_6/CH_2Cl_2. An examination of the data by incorporating a superatom perspective of gold nanoclusters has permitted the rationalisation of some features observed. Namely, all gold-phosphine clusters in this work undergo reversible two-electron reduction. Conversely, oxidation is irreversible and probably leads to disintegration of the parent cluster. This has been explained on established principles of electronic and geometric stability, such as the dependence of cluster topology on the population of molecular orbitals and the non-bonding steric interactions between tertiary phosphine protecting-ligands. The absence of further redox events after a previously irreversible electron-transfer has occurred suggests that the decomposition product(s) are electrochemically quiescent inside this potential window. Results are validated by good agreement with previously reported data in the literature (for eight and nine-membered clusters), except for $[Au_6(dppp)_4]^{2+}$ and $[Au_{13}(dppe)_5Cl_2]^{3+}$; data for which have not yet been reported in the literature. Of note, $[Au_{11}(PPh3)_8Cl_2]^{+}$ is found to possess an exceptionally small value of ΔE_g which deviates significantly from a structurally-similar isomer, $Au_{11}(PPh_3)_7Cl_3$; a particularly interesting result that deserves further investigation to expose the underlying factors involved. Furthermore, it is noteworthy that there are no reports in the literature which investigate and compare the electrochemical features of a range of gold-phosphine nanoclusters under identical conditions. It is possible that some overlapping redox events in the electrochemical spectra herein could be resolved by decreasing the temperature of the apparatus (*e.g.* acetone/dry-ice bath at -78 °C), however this was regrettably not possible in this work for practical reasons with the instrumental set-up. A table summarising the numerical results of this study, alongside literature values for comparison, is given overleaf (Table 4.1).

Cluster	$[Au_6(dppp)_4]^{2+}$	$[Au_8(PPh_3)_8]^{2+}$	$[Au_8Pd_1(PPh_3)_8]^{2+}$	$[Au_9(PPh_3)_8]^{3+}$	$[Au_{11}(PPh_3)_8Cl_2]^{+}$	$[Au_{13}(dppe)_5Cl_2]^{3+}$
R1	-1.65 V (*R*)	-1.43 V (*R*)	-1.64 V (*R*)	-0.94 V (*R*)	-1.30 V (*R*)	-1.11 V (*R*)
R2	-1.84 V (*R*)	-1.73 V (*R*)	-1.84 V (*R*)	-1.24 V (*R*)	-1.44 V (*R*)	-1.22 V (*R*)
R3	N/O	N/O	N/O	-1.96 V (*I*)	-1.74 V (*I*)	N/O
O1	+0.08 V (*I*)	+0.21 V (*I*)	+0.04 V (*I*)	+0.66 V (*I*)	-0.16 V (*I*)	+0.34 V (*I*)
O2	+0.21 V (*I*)	+0.49 V (*I*)	+0.33 V (*I*)	+0.95 V (*I*)	+0.24 V (*I*)	N/O
ΔE_g **(eV)†**	1.87	1.64	1.72	1.62	0.83	1.45
ΔE_g **(eV)#**	N/R	1.60[248] **($)**	1.74[252]	1.67[233] **($)**	N/R	1.50[212] **(∗)**

Table 4.1 – Summary of non-aqueous DPV results for all six gold-phosphine clusters investigated in this work, in Ar-purged anhydrous CH_2Cl_2 with 0.1 M Bu_4NPF_6 supporting electrolyte. Potentials are given with respect to the ferrocene/ferrocenium redox couple measured under identical conditions. Key: (*R*) = electrochemically-reversible; (*I*) = electrochemically-irreversible; N/O = not observed within the potential window interrogated; N/R = not reported in the literature; † = this work; # = reported in literature; **($)** = obtained under different experimental conditions to that herein; **(∗)** = Predicted.

Finally, it should be mentioned that the non-aqueous electrochemical profile of $[Ag_{25}(SPhMe_2)_{18}]^-$ has been reported by Kang *et al.*,[260] alongside those of the bimetallic analogues $[Ag_{24}M_1(SPhMe_2)_{18}]^z$, where M = Pd, Pt (z = 2-) and Au (z = 1-). Regrettably in this work, the quantity of pure Ag_{25} obtained after multiple synthesis attempts was miniscule and as a result it was not feasible to conduct DPV studies with this species. The silver cluster $[Ag_{25}(SPhMe_2)_{18}]^-$ was found to have a ΔE_g value of 1.82 eV, which was decreased by the single-atom doping of Au and Pd (1.76 and 1.71 eV, respectively) and increased by the single-atom doping of Pt (1.96 eV).

Chapter 5

Electrochemical Behaviour of Carbon-Supported Gold and Silver Catalysts

5.1 – Electrode Preparation

Electrode preparation was found to have a considerable impact on the measured electrochemical performance of the carbon-supported catalyst, and as such a substantial amount of time was dedicated to perfecting this technique. Unfortunately, the fact that electrodes were "hand-made" unequivocally remains the largest source of error in this work. One concedes that an automated fabrication method would undoubtedly reduce the magnitude of these errors; such an instrument does exist in the Department of Chemical and Process Engineering laboratories at the University of Canterbury; this was unfortunately suffering a physical malfunction which could not be resolved within a convenient timeframe.

Several challenges were encountered during the electrode fabrication process, which regrettably consumed a considerable amount of time during this work, however a brief summary of resolutions will be given (a full description of fabrication method can be found in Section 8.3.2): i) the inclusion of a thin Nafion-117 undercoat was found to vastly increase both the mechanical durability of the carbon layer and the overall electrical conductivity of the electrode surface, and decreased noise in cyclic voltammetry data. It is likely that improved adhesion or contact between the titanium surface and the amorphous carbon particulate is achieved by this action, more-so than what can be obtained by including Nafion-117 within the carbon-layer itself; ii) lowering the temperature of the electrode prior to application of the carbon layer was found to yield a smoother and more-even catalyst surface, which actually improved the quality of features in cyclic voltammetry data. Keeping the temperature of the titanium disk at *ca.* 110 °C yielded erratic j_p vs. $\upsilon^{1/2}$ plots (Figure A.2 (Appendices)). This could be due to a rapid evaporation of the carrier solvent creating microscopic surface defects such as faults, cracks, bubbles or fissures that expose the underlying titanium surface, or weaken the adhesion of the carbon-layer to this surface, or both. Additionally, a higher temperature could simply invoke decomposition of the cluster catalyst, which would of course lead to diminished feature in cyclic voltammetry data. A temperature of 80 °C was chosen as a compromise between the preservation of electrochemical features and sufficient evaporation of the carrier solvent; iii) it was found that electrode performance would diminish severely if a significant amount of time elapsed between electrode fabrication and collection of electrochemical data (*i.e.* overnight). The author cannot offer a reasonable explanation for this; nevertheless, to preserve catalytic activity electrodes were always used

within 30 minutes of their preparation; iv) a similar effect was noticed for the carbon "ink", and it was therefore always prepared and used when fresh.

5.2 – Short-Term Electrochemical Behaviour of Carbon Supported Catalysts

Cyclic voltammograms were collected in N_2-purged 0.1 M Na_2SO_4 in a standard three-electrode cell, containing a Ag/AgCl (sat. KCl) reference electrode (*all potentials in this chapter are given with respect to this reference*) and a coiled platinum wire counter electrode (area *ca.* 3 cm^2). Representative cyclic voltammograms (at least 4 separate electrodes examined) for each catalyst deposited on Vulcan carbon are shown in Figure 5.1. A description of the electrode fabrication procedure is given in Section 8.3.2. Electrochemical profiles of all carbon-supported catalysts were collected at a scan-rate of 50 mV/s over 10 cycles (from light-blue to dark-blue, first cycle in dashed-black) between +1.4 and 0 V.

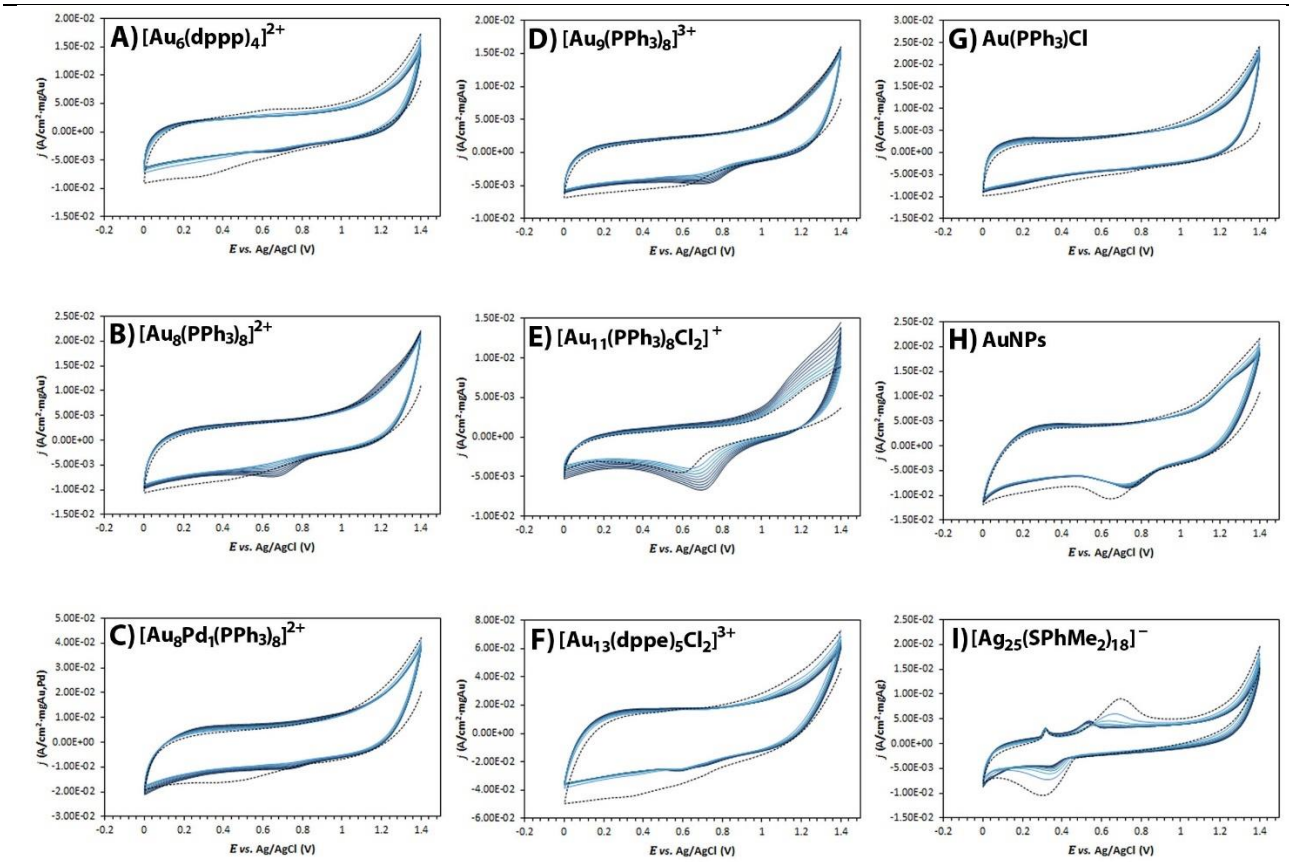

Figure 5.1 – Representative cyclic voltammograms of all carbon-supported catalysts examined in this work, collected in N_2-purged 0.1 M Na_2SO_4 at a scan-rate of 50 mV/s, over 10 cycles (from light-blue to dark-blue; first cycle shown in dashed-black) for: A) Au_6; B) Au_8; C) Au_8Pd_1; D) Au_9; E) Au_{11}; F) Au_{13}; G) $AuPPh_3Cl$; H) AuNPs and I) Ag_{25}. Note that vertical-axes measuring normalised current-densities (j) have different scales.

5.2.1 *Short-Term Electrochemical Behaviour of Carbon-Supported Gold Catalysts*

It is immediately clear that all gold-phosphine clusters (Figure 5.1, Panels A-F) display similar voltammetric profiles when deposited on a carbon support, in contrast with markedly different non-aqueous differential-pulse voltammograms. A common feature which is readily apparent is a broad reduction wave at *ca.* + 0.6 - 0.7 V, which is more prominent at Au_8, Au_8Pd_1, Au_9 and Au_{11} catalysts (*i.e.* those clusters protected by *mono*phosphine ligands). This wave is less-conspicuous at Au_6 and at Au_{13} catalysts (protected by *di*phosphine ligands), and an additional small reduction wave is seen at *ca.* +0.6 V for Au_{13}. As the bare Vulcan carbon support (not shown) only displayed features ascribed to capacitive-charging of the electrode surface, cathodic waves for the abovementioned catalysts can be attributed to a process pertaining to the reduction of gold-phosphine clusters. No equally-sharp oxidation waves are observed on the positive-going sweep (within 10 voltammetric cycles), suggesting that this electrochemical event is probably irreversible. Catalysts prepared with $AuPPh_3Cl$ (Figure 5.1, Panel G) display no redox events within the potential window interrogated and instead only capacitive double-layer charging of the electrode surface is seen.

Catalysts containing large gold nanoparticles (Figure 5.1, Panel H) also display a prominent reduction wave, however this is postponed to a more-positive potential (*ca.* +0.8 V) compared to the gold-phosphine clusters. A small oxidation wave is also observed at *ca.* +1.3 V, which can be attributed to the formation of gold-oxides (AuO_x) that usually occur at *ca.* +1.4 - 1.5 V at bulk-gold.[267, 268] Padayachee *et al.* have noted that gold-oxide formation takes place at less-negative potentials at gold nanoparticles compared to bulk-gold,[256] and similar behaviour has also been observed at small carbon-supported Pd and Pt nanoparticles during electrochemical cycling.[269-271] This is usually attributed to an increasing oxophilicity of the particle surface as size descends (from 100 to *ca.* 5 nm),[269] or a decreased lattice stabilisation-energy as metallic properties diminish and the atomic-structure departs from *fcc* packing.[180, 268, 272]

Based on this trend, one would expect that AuO_x formation would be rather facile at gold-phosphine clusters, since the fraction of surface-atoms is equal or near-to unity and therefore all gold atoms could – in principle – participate in the Au-AuO_x redox process. However, this does not appear to be the case as no evidence of gold-oxide formation is seen within 10 electrochemical cycles. Increasing the anodic limit to +1.6 V (in parallel experiments, not shown) did not produce any features which could be indicative of gold-oxide formation. The

anodic dissolution of gold-phosphine clusters to Au^{+} or Au^{3+} ions, which for small nanoparticles (< 10 nm) has been observed to take place at or below *ca.* +0.6 V (*vs.* Ag/AgCl in 0.1 M $KClO_4$, shifting to more-negative potentials as size descends),[273] is similarly not observed. Decreasing the cathodic limit to -0.4 V (in parallel experiments, not shown) did not produce any features associated with the formation of cationic gold. Steven *et al.*[274] have also noted that Au_9 clusters deposited on Vulcan carbon do not display voltammetric profiles typical of larger gold nanoparticles (and are not easily oxidised *via* electrochemical treatment), though it is possible that the phosphine ligands inhibit the formation of gold-oxides during electrochemical cycling. However, Boyen and co-workers[275] have observed that chemically-synthesised Au_{55} clusters (on silicon surfaces) are extraordinarily resistant to oxidation even upon removal of the phosphine-ligand periphery, as are sub-nanometre Cu clusters.[276] Gas-phase experiments have also found that bare $[Al_{13}]^{-}$ clusters are granted an increased stability towards oxidation,[277] and similar results are obtained from "naked" sub-nanometre Pb, Fe and Co clusters grown on solid supports by vapour-deposition methods.[278, 279]

5.2.2 *Comment on the Short-Term Electrochemical Behaviour of Carbon-Supported Gold Catalysts*

The possible absence of gold-oxide formation for all gold-phosphine cluster catalysts is an interesting result on its own, and points to unique chemical properties that may only be apparent in sub-nanometre sized ensembles of matter. It is a frequent observation that the (electro)chemical properties of gold nanoclusters diverge considerably from bulk-gold behaviour.[146, 280-282] Others note that both the propensity and the reversibility[283] of the Au-AuO_x redox process is much diminished as particle size descends below *ca.* 1-3 nm, which nicely corresponds to the onset of molecular behaviour in nanoclusters (Section 2.2). It is also known that the initial kinetics of gold-oxide formation depend on the type of exposed crystal face and the particular arrangement of surface atoms, and may also be hindered by a defect-rich surface.[284, 285] Therefore, it could be that the unique polyhedral geometries of gold clusters cannot accommodate oxide formation or even support an oxide structure without first aggregating into a larger bulk-gold lattice.[286, 287]

Alternatively, it is plausible the feature at *ca.* + 0.6 - 0.7 V could be attributed to gold-oxide reduction at carbon-supported gold nanoclusters, since it is also observed at *ca.* +0.8 V for large AuNPs which would most-

certainly undergo this surface-phenomenon due to a substantial presence of metallic character. Compton *et al.*[288] find *ca.* 40 nm gold nanoparticles deposited on glassy-carbon electrodes undergo AuO_x reduction at *ca.* +0.8 V *vs*. SCE (Hg/Hg_2Cl_2; *ca.* +0.85 V *vs*. Ag/AgCl) and AuOx formation at *ca.* +1.25 V (*vs*. SCE; *ca.* +1.3 V *vs*. Ag/AgCl). However, they also note the occurrence of a very weak oxidation wave prior to bulk surface oxidation (*ca.* +1 V *vs.* SCE) which others[289, 290] find is directly proportional to the density of surface-defects on gold nanoparticle exteriors. Though small metal clusters could be, at least conceptually, constructed entirely of defect-like adatoms, no such event is observed in this work. It is possible that either oxidation processes could be occurring in the cyclic voltammetry data herein (Figure 5.1) though any signal may be dominated by the magnitude of the current near the anodic limit. In any case, the fact that small metal clusters are intrinsically resistant to oxidation likely explains why no immediate evidence of oxide or oxide-like formation is found in voltammetric data.

Therefore, the irreversibility of the cathodic feature at around + 0.6 - 0.7 V is likely a result of permanent molecular reorganisation to the cluster and instead could be an indication of ligand dissociation, partial aggregation of neighbouring clusters, or interactions with functional groups on the surface of the carbon support. The reductive de-ligation of the gold cluster catalyst *might* be an explanation for the origin of this prominent reduction wave, since it is enhanced for clusters possessing monophosphine ligands (Au_8, Au_8Pd_1, Au_9, Au_{11}) and supressed for clusters prepared with diphosphine ligands (Au_6, Au_{13}). It is logical then that electrochemically-induced ligand dissociation would be more difficult for the latter group of catalysts, since diphosphines are expected to exert a chelate-type effect on the cluster core,[254, 291, 292] possess larger binding energies to monophosphines,[293, 294] and – presumably – require the simultaneous scission of two separate Au-P bonds.

On the other hand, such a feature could be evidence for an interesting redox-cycle described by the Incipient Hydrous-Oxide/Adatom Mediator (IHOAM) model,[268, 272, 295] which has previously been employed to rationalise the unexpected catalytic activity of polycrystalline gold electrodes for certain electrochemical reactions. The significance of this concept to this work will be discussed in Section 6.6.3, however at the present time it is sufficient to say that the IHOAM model describes the electrocatalytic role of adatoms or atoms in low-coordination sites on the surface of noble-metal electrodes during demanding electrochemical reactions. A cycle between hydrous-oxide ($[Au_2(OH)_9]^{3-}$) and adatom(s) is mediated by the external current,

whereby the former is generated on the anodic-sweep of cyclic voltammetry experiments, and likewise the latter is produced during the cathodic-sweep (the reader is referred to Figure 6.5 for an illustration of this process).

In short, the large cathodic wave exhibited by carbon-supported gold-phosphine clusters at *ca.* + 0.6 - 0.7 V is conspicuously located in a similar potential window where the reduction of hydrous-gold oxides is believed to occur at polycrystalline Au electrodes (*ca.* 0.7 - 0.9 V *vs.* NHE in alkaline media). It is worthwhile to reiterate that metal clusters *can* serve as conceptual models for adatom/defect sites on bulk surfaces. If this were the case, then the voltammetry data presented in Figure 5.1 (Panels A-F) would seem to suggest that the hydrous-oxide/adatom redox cycle is more facile at certain gold-phosphine clusters, namely Au_8, Au_8Pd_1, Au_9 and Au_{11}. Intuitively, such a process would also be coupled with phosphine ligand dissociation, since this must presumably take place during formation of the hydrous-gold oxide species and could explain the prominence of this feature for monophosphine-protected clusters, and its obscurity for diphosphine-protected clusters. A similar argument can be made for the possible appearance of hydrous-oxide reduction at carbon-supported AuNPs (Figure 5.1, Panel H), where the same cathodic wave is observed at *ca.* +0.8 V and are presumed to possess an adatom/defect-rich surface. The fact that a cationic gold-phosphine complex, $AuPPh_3Cl$, does *not* display this feature (Figure 5.1, Panel G) may suggest that Au-Au bonds are by some means necessary for this process to occur: this author notes that *two* Au atoms are required to generate the hydrous-gold oxide. The IHOAM model will be revisited in Section 6.6.3, when the electrocatalytic activity of small gold clusters for nitrate reduction has been evaluated.

5.2.3 *Short-Term Electrochemical Behaviour of a Carbon-Supported Silver-Thiolate Catalyst*

Catalysts containing Ag_{25} display comparatively feature-rich voltammograms over 10 cycles compared to other materials: a large reduction wave at *ca.* +0.30 V which diminishes in size and shifts to +0.36 V over successive cycling; a small – but sharp – oxidation wave also at *ca.* +0.32 V which is static over 10 cycles; a rather pronounced oxidation wave at *ca.* +0.71 V, which recedes within a few cycles concomitant with the growth of a new oxidation wave at *ca.* +0.54 V that remains essentially unchanging up to 10 measurements.

The electrochemical behaviour of chemically-synthesised silver clusters supported on mesoporous carbon is currently without precedent, however Giovanna and Pumera[296] report that silver nanoparticles deposited on glassy-carbon electrodes display a similar time-dependent voltammetric profile to that observed for Ag_{25} herein. In their investigation, they note that the anodic dissolution of *ca.* 10 nm Ag NPs takes place at *ca.* +0.6 V (*vs.* Ag/AgCl in 0.1 M phosphate-buffered solution) with the cathodic electrodeposition of Ag^+ occurring at *ca.* +0.2 V, where the magnitude of both features diminishes and undergo a potential shift over time. This was attributed to the sintering of nanoparticles and the nucleation of larger nanostructures affiliated with a decrease in the available electrochemically-active surface-area, and eventually led to a redox-stable species. Since the voltammetric profile of Ag_{25} supported on Vulcan carbon is similar to that observed by the abovementioned authors, it is therefore possible that cluster disintegration takes place within a few cycles, leading to the anodic dissolution of Ag_{25} clusters with relative facility at *ca.* 0.54 V. This process appears to be fully reversible, and the re-deposition of Ag^+ ions to form as-yet unidentified, but electrochemically-robust secondary nanostructures takes place at *ca.* +0.36 V. Others note the reversible anodic dissolution of silver nanoparticles takes place at more-negative potentials as size decreases.[297-299]

The anodic feature at +0.33 V, which is cycle-independent and does not appeared to be coupled with any cathodic process, is more difficult to assign. Giovanna and Pumera[296] could not offer an origin for this event, however Compton *et al.*[288] observe that *ca.* 4 nm gold nanoparticles deposited on glassy-carbon electrodes exhibit a distinct, irreversible peak prior to the onset of gold-oxide formation. They, and others,[284, 300, 301] attribute this to a local restructuring of adatoms/defect sites which takes place prior to the onset of AuO_x formation. As discussed in Sections 5.2.2 and 6.6.3, this could be the result of the hydrous-oxide formation process. In line with a discussion on single-atom electrocatalysis given by O'Mullane,[25] it is speculative that a similar process is occurring at Ag_{25} clusters herein, whereby a molecular-restructuring event takes places prior to the onset of the anodic dissolution of Ag^+ ions. Burke *et al.*[302] have extended the IHOAM model to encompass polycrystalline Ag electrodes, however hydrous-silver oxides are currently ill-defined species (compared to gold) and as such this author cannot make further comment on this possibility. The interesting electrochemical behaviour of carbon-supported chemically-synthesised silver clusters warrants further investigation, not least to identify the nature of secondary nanostructures that evolve with progressive electrochemical cycling. There are no known reports in the literature that describe the stability of chemically-

synthesised silver clusters on carbon supports under electrochemical duress. Indeed, at present there are only a handful of reports which explore the application of atomically-precise silver clusters in heterogeneous catalysis,[303, 304] and none which investigate electrocatalytic roles.

5.3 – Long-Term Electrochemical Behaviour of Carbon-Supported Catalysts

To assess the long-term stability of the gold-phosphine cluster catalysts under extended periods of electrochemical performance, 100 successive cyclic voltammograms were conducted in nitrogen-purged 0.1 M Na_2SO_4, and representative profiles (2 separate electrodes examined) are shown in Figure 5.2 overleaf (from light blue to dark blue: 25th, 50th, 75th and 100th cycles. 10th cycle shown in dashed-black).

5.3.1 *Long-Term Electrochemical Behaviour of Carbon-Supported Gold Catalysts*

All gold-phosphine cluster catalysts are observed to undergo significant changes within their respective voltammetric profiles over 100 electrochemical cycles. This is not unexpected considering the rather-high weight loading of gold on the carbon support (10 wt %), so some degree of catalyst aggregation or sintering is expected to occur. For all catalysts, extensive changes take place between the 10th and 25th cycles, wherein voltammetric profiles begin to resemble that of large AuNPs and the growth (or continuous growth) of the prominent cathodic feature at *ca.* + 0.6 - 0.7 V takes place. For Au_8, Au_8Pd_1 and Au_9 the peak position is seen to experience a gradual potential shift of *ca.* 30-40 mV in the anodic direction between the 10th and 100th cycles (Figure 5.2, Panels B, C and D). Interestingly, Au_{11} displays the opposite trend where an initial positive shift of *ca.* 40 mV between the 10th and 25th cycles is negated by a negative potential shift of *ca.* 50 mV over cycles 26-100, for a net shift of *ca.* 10 mV in the cathodic direction (Figure 5.2, Panel E). If such a feature can be ascribed to hydrous-oxide reduction (Section 5.2.2) then the potential shift would indicate that, for Au_8, Au_8Pd_1 and Au_9 this process becomes less energetically-demanding, and *vice-versa* for Au_{11}, for which this author regrettably cannot offer a clear explanation at this stage.

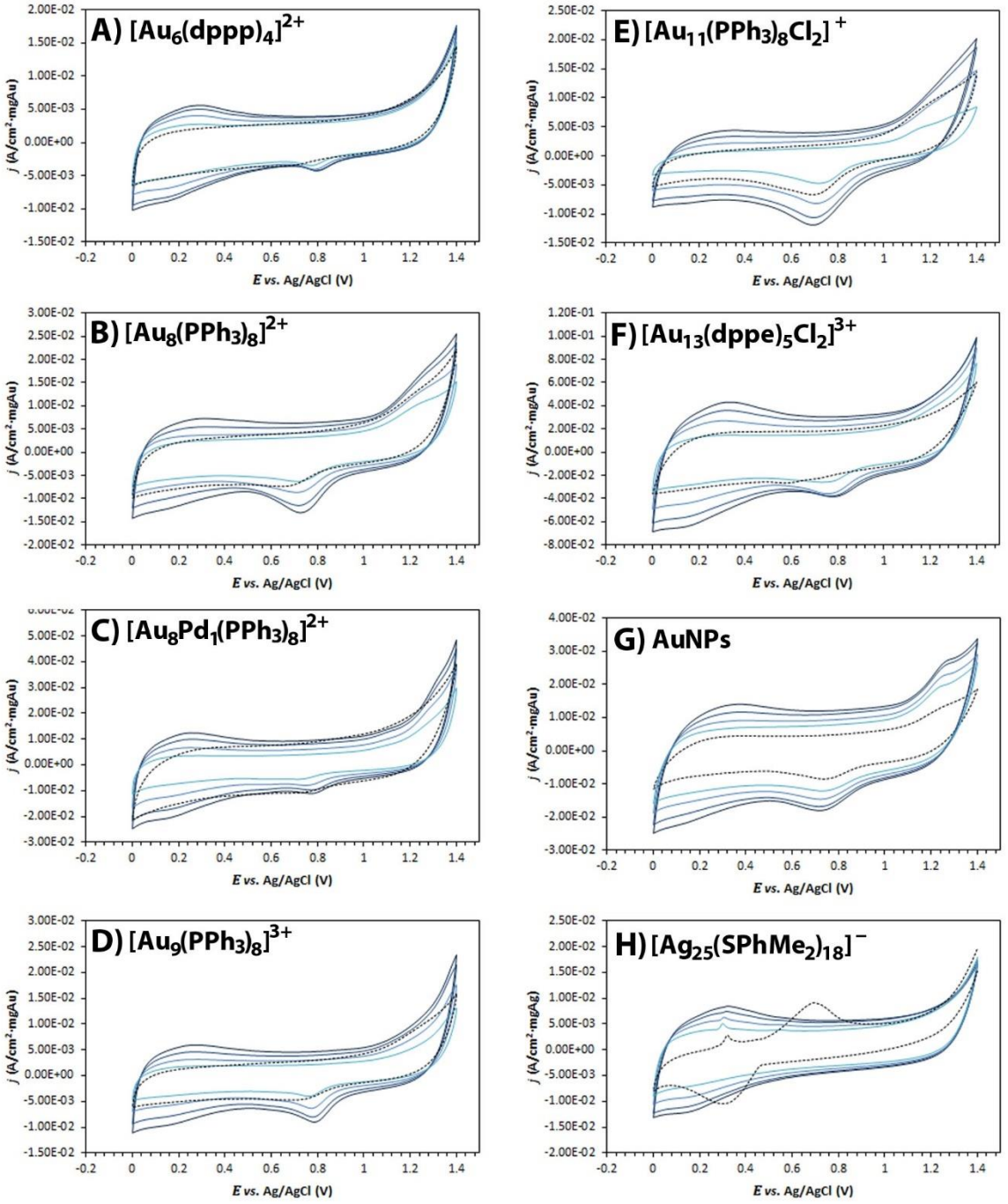

Figure 5.2 – Representative cyclic voltammograms of all carbon-supported catalysts examined in this work, collected in N_2-purged 0.1 M Na_2SO_4 at a scan-rate of 50 mV/s over 100 cycles (25^{th}, 50^{th}, 75^{th} and 100^{th} cycles from light-blue to dark-blue; 10^{th} cycle shown in dashed-black) for: A) Au_6; B) Au_8; C) Au_8Pd_1; D) Au_9; E) Au_{11}; F) Au_{13}; G) AuNPs and H) Ag_{25}. $AuPPh_3Cl$ underwent no significant changes over 100 cycles and is omitted from this figure. Note that vertical-axes measuring normalised current-densities (*j*) have different scales.

It is interesting that Au_6 and Au_{13} do not display the large reduction wave at *ca.* + 0.6 - 0.7 V in the initial 10 electrochemical cycles, however this *does* appear within the next 15 measurements (Figure 5.2, Panels A and F). This may be further evidence for ligand dissociation as one possible origin for this event, and since diphosphines are expected to be more difficult to remove, this feature would arrive chronologically-later than for catalysts containing monophosphine-protected clusters. Steven *et al.*[274] suggest this initial increase in the

prominent cathodic feature is at least partially due to ligand dissociation (in their study on the stability of carbon-supported gold nanoparticles), though a contribution from improved contact between electrolyte and the electroactive gold species cannot be excluded. For Au_8Pd_1 (Figure 5.2, Panel C), a different case occurs, and the cathodic wave at *ca.* +0.7 V in the 10th cycle is seen to be of virtually equal magnitude to that in the 100th cycle. The fact that voltammetric profiles for Au_8Pd_1 recede within the first *ca.* 75 cycles implies a decrease in the overall electroactive surface-area which is only reclaimed after significant electrochemical stimulus, which could possibly be due to aggregation. No evidence of gold-oxide formation is observed for any gold-phosphine cluster over 100 cycles (though this occurs after 25 cycles for large AuNPs at *ca.* +1.25 V). A broad anodic wave at *ca.* +0.2 - 0.3 V also arises within 25-50 cycles for all gold-containing catalysts and this continues to grow up to 100 cycles, which may be coupled to a very weak cathodic event at *ca.* +0.1 - 0.2 V. Steven *et al.*[274] and others[305] also observe these features and attribute them to the formation of an (unspecified) redox-active gold species on the surface of the carbon support (though this cannot be any hydrous-oxide species, since this takes usually place some 600 mV more-positive). These features grow at similar rates regardless of the nature of protecting ligand or the size of the cluster.

Catalysts containing $AuPPh_3Cl$ were found not to display these features over 100 cycles (in fact, this catalyst was found to undergo virtually no changes in voltammetric profiles except for a steady increase in background double-layer charging currents: it is thus omitted from Figure 5.2), however these *were* observed at catalysts containing large AuNPs, suggesting it may be an intrinsic electrochemical feature of nanoscale gold particles. The fact that gold-phosphine nanoclusters do not undergo the Au-AuO_x process even up to 100 cycles suggests that either significant aggregation to larger nanostructures (for which gold-oxide formation is increasingly facile[273]) *has not* occurred, or the partially/fully de-ligated clusters retain an intrinsic opposition to oxidation. Admittedly, it would be appropriate to obtain electron microscopy images or surface-characterisation data (XPS) to corroborate these changes during extended electrochemical cycling, such that the features observed in cyclic voltammetry data could be correlated with any of the explanations given above. A sample of the carbon layer has been carefully removed from the electrode surface and these materials have been dispatched to colleagues at Flinders University (Adelaide, South Australia) for XPS and HR-TEM analysis to assess whether cluster aggregation has occurred; unfortunately, at the time of writing these results have not yet been received.

5.3.2 *Long-Term Electrochemical Behaviour of a Carbon-Supported Silver-Thiolate Catalyst*

The long-term electrochemical behaviour of carbon-supported Ag_{25} is shown in Figure 5.2, Panel H. It is immediately obvious that significant changes to the voltammetric profile of this material take place between the 10^{th} and 25^{th} measurements: the large anodic wave at *ca.* +0.71 V which only appeared within the first 10 cycles completely disappears, as does the large cathodic feature at +0.36 V. It is therefore possible that these events are linked to a redox cycle involving a relatively unstable (or electrochemically-fragile) species. The sharp oxidation event at *ca.* +0.32 V slowly diminishes in magnitude over 50 cycles, and by the 75^{th} cycle is only just observable above the background current. It is possible that this event is consumed by the growth of the broad anodic wave centred at the same potential concomitant with the evolution of a broad (and weak) cathodic feature at *ca.* +0.18 V. These latter features are also visible in the voltammetric profiles of carbon-supported gold catalysts, which may indicate the presence of a common redox species. Since the only common species between these materials would be the carbon-support itself, the most obvious candidates include the various functional groups that decorate the amorphous carbon surface. *In-situ* FT-IR studies could be undertaken during successive electrochemical cycling to establish whether this feature does in fact arise from the oxidation and subsequent reduction of carbon-containing functional groups. Although a bare-carbon electrode (*i.e.* without any gold or silver-containing catalyst) was taken through 100 electrochemical cycles to test this hypothesis (not shown), only non-faradaic capacitive-charging of the electrode surface was observed and no broad redox event centred at *ca.* +0.25 V was found. This would then seem to suggest that this feature arises *specifically* from the presence of a foreign electroactive species on the carbon surface, though it is mostly independent of the chemical nature of the species itself (at least, within the range of catalysts used in this work).

Regretfully (albeit highlighting the novelty of this work), there are no precedents in the literature which can be directly applied to these particular results – few reports exist which study the electrochemical behaviour of carbon-supported silver nanoparticles, and as previously mentioned electron-microscopy and XPS data are, at the time of writing, unavailable to this author for inclusion in this work. Nevertheless, the interesting voltammetric behaviour of carbon-supported Ag_{25} nanoclusters highlights the vast scope of further work that can be performed in future.

5.3 Summary and Remarks

In this chapter, the electrochemical behaviour of six carbon-supported gold-phosphine nanoclusters, gold nanoparticles, a cationic gold-phosphine complex and a silver-thiolate nanocluster have been examined. It was found in Chapter 4 that all six gold-phosphine nanoclusters were able to undergo multiple redox events (in solution), whereas these features are invisible when deposited on a solid support (at least, within the potential window interrogated). Instead, only one prominent cathodic wave at *ca.* + 0.6 - 0.7 V was observed. This wave has been attributed to some form of irreversible molecular rearrangement to the cluster itself, such as ligand dissociation or hydrous-oxide reduction, or both. The fact that $AuPPh_3Cl$ does not display this feature is interesting and could be explained by the fact that hydrous-oxide formation may only take place when Au-Au bonds are present. Long-term electrochemical cycling found that the gold-oxide formation/reduction process did not take place at gold-phosphine clusters which may indicate an intrinsic resistance to oxidation. Conversely – and as expected – large gold nanoparticles exhibited prominent evidence for AuO_x formation. The short-term electrochemical behaviour of carbon-supported Ag_{25} is comparatively featured and displays several irreversible charge-transfer events which are attributed to the probable disintegration of the cluster, and the formation of secondary nanostructures. Long-term, carbon-supported Ag_{25} was found to undergo significant changes between 10 and 25 electrochemical cycles, however after further cycling was found to attain a similar profile to carbon-supported gold catalysts. This may point to some form of unique, but non-specific interaction between the amorphous carbon support and an electroactive species which resides on its surface. It is noteworthy that the electrochemical behaviour of gold-phosphine clusters deposited on carbon supports has not been well-explored in the literature, and many of the observations herein are without precedent. It is therefore unfortunate that electron-microscopy images and XPS data were not available to assist with interpreting these observations. These results are, to the best of this authors' knowledge and with the lone exception of Au_9, the first investigations into the electrochemical behaviour of carbon-supported gold clusters. Further work is needed to establish specific processes occurring over long-term electrochemical duress.

Chapter 6

Electrocatalytic Reduction of Nitrate by Carbon-Supported Gold-Phosphine Clusters

6.1 – Atomically-Precise Catalysts for Nitrate Electroreduction

The electroreduction of nitrate by carbon-supported gold-phosphine clusters has been evaluated by cyclic voltammetry in nitrogen-purged 0.1 M Na_2SO_4 and $[NO_3^-]$ = 5 mM, between +1.4 and 0 V *vs.* Ag/AgCl at a scan rate of 50 mV/s. Current-densities have been normalised with respect to both the electrode area (0.196 cm^2) and the metal loading in mg (taken as 10% of the mass-difference between electrodes before and after catalyst coating, having subtracted the expected quantity of Nafion-177 present), and typical voltammograms collected for all six gold clusters, one silver cluster, a cationic gold complex, large AuNPs, and bare carbon support are shown in Figure 6.1 (at least 4 separate electrodes were prepared and examined). A description of the electrode fabrication process can be found in Section 8.3.2. Note that all voltammograms display different current scales, and that some electrode materials simply displayed larger background currents than others. The reason for this is uncertain, however has been corrected-for by the normalisation process mentioned above.

6.1.1 *Carbon-Supported Gold-Phosphine Catalysts*

Prior to the addition of 5 mM $NaNO_3$, all electrodes have undergone 10 cycles in nitrogen-purged 0.1 M Na_2SO_4 as an activation process (*vide infra* Section 6.1.3), and the 10^{th} cycle (taken as a "blank" signal) is shown in dashed-black. Voltammograms collected in the presence of 5 mM $NaNO_3$ are shown in blue. For all gold-phosphine clusters and $AuPPh_3Cl$, it is immediately obvious that the addition of nitrate exaggerates the native cathodic wave at *ca.* + 0.6 - 0.7 V and a corresponding oxidation wave at *ca.* +0.8 - 1.0 V appears. Bare Vulcan carbon did not produce any cathodic features although the oxidation wave was observed, however this was weak in magnitude. Parallel experiments in which 5 mM $NaNO_2$ was introduced to the supporting electrolyte (instead of $NaNO_3$; not shown) produced voltammograms with an identical oxidation wave at *ca.* +0.8 - 1 V, but no apparent growth in cathodic features was observed until at least one voltammetric cycle was complete. Thus, it is concluded that all gold-phosphine clusters and a cationic gold-phosphine complex are active catalysts for nitrate electroreduction. The major product of this transformation is likely the nitrite anion, the oxidation of which is also catalysed by the same electrode material.

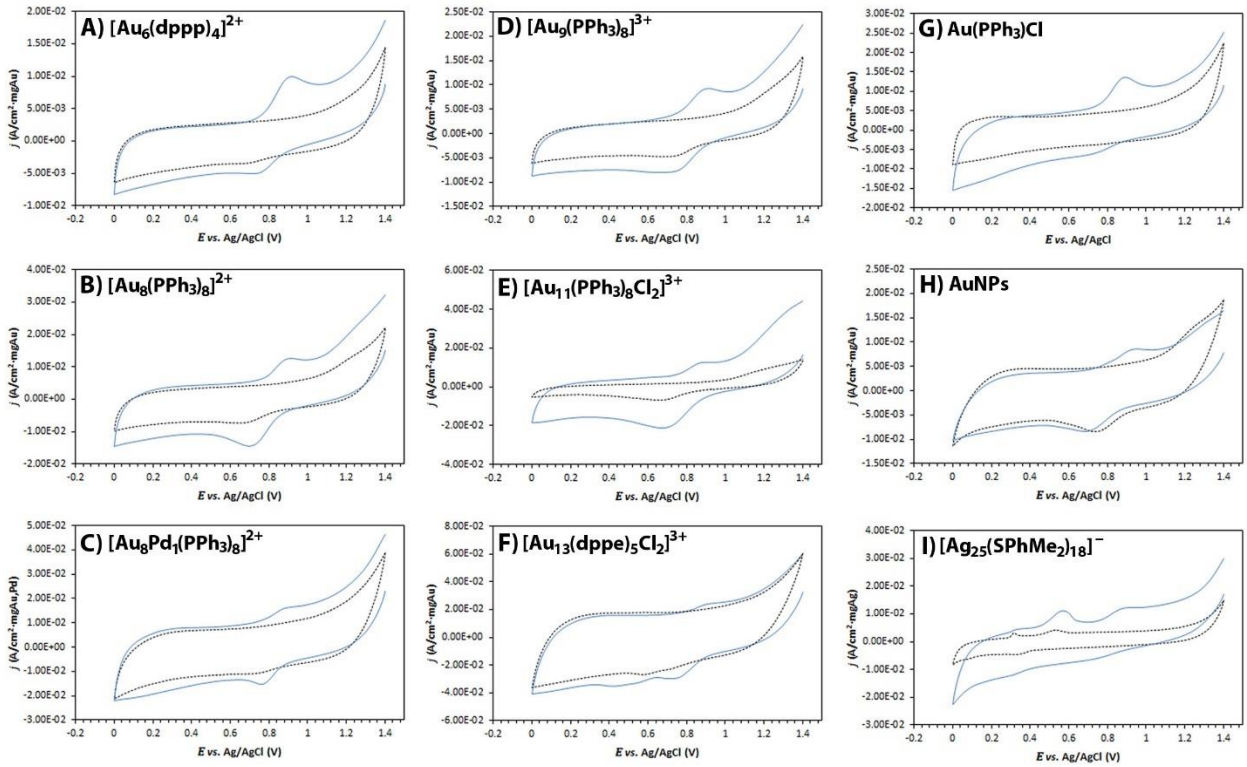

Figure 6.1 – Cyclic Voltammograms recorded at 50mV/s in N_2-purged 0.1 M Na_2SO_4 in the absence (dashed black line) and presence (solid blue line) of 5 mM $NaNO_3$ for A) Au_6; B) Au_8; C) Au_8Pd_1; D) Au_9; E) Au_{11}; F) Au_{13}; G) $AuPPh_3Cl$; H) AuNPs; I) Ag_{25} after 10 previous cycles in background electrolyte.

The novelty of this important result cannot be understated by this author, and it is worth reiterating at this point that polycrystalline gold surfaces are essentially *inactive* for nitrate electroreduction. It is also interesting that this redox cycle is to some extent reversible, indicated by the presence of a nitrite oxidation wave on the positive-going reverse sweep in electrolytes containing $NaNO_3$. This contrasts with other studies in the literature concerning bulk metal electrodes such as polycrystalline Cu, Pt, and Sn where nitrate reduction is generally found to be *irreversible* and gaseous products (*e.g.* NO_2, NO, N_2O, N_2) are often detected.[19, 46, 49, 69, 74] It is also noteworthy that the present gold-based catalysts are *inactive* for *nitrite* reduction, since no growth in the native cathodic wave at *ca.* + 0.6 - 0.7 V nor the formation of any new reduction features took place in electrolytes containing 5 mM $NaNO_2$ until at least one voltammetric cycle was complete (not shown). Polycrystalline Au electrodes are known to be poor catalysts for nitrite reduction,[78] although this author cannot offer a reasonable explanation for this result since the catalytic properties of bulk gold surfaces and gold nanoclusters diverge considerably (as has been shown here for *nitrate* reduction). This could be an interesting avenue for future work to establish the origin of product selectivity for nitrate reduction at gold-phosphine electrocatalysts.

The fact that $AuPPh_3Cl$-based catalysts (which formally contain the Au^+ ion) *are* active for both nitrate reduction and nitrite oxidation may give insight as to why small gold clusters (but *not* metallic gold) are also themselves active: in a similar fashion to the Cu^+ ion, which is a known catalyst for nitrate reduction,[71] it may simply be a feature of cationic gold to mediate the nitrate/nitrite redox cycle. As polycrystalline gold surfaces are extraordinarily resistant to oxidation, and even upon oxidation it is Au^{3+} – not Au^+ – that is formed in appreciable quantities,[268, 272] this may compliment the commonly-cited "poor chemisorber" explanation[295] for the quiescent catalytic activity of bulk gold electrodes for nitrate reduction (Section 6.8). Large AuNPs are clearly active for nitrate reduction, since the anodic wave at *ca.* +0.8 - 1 V attributed to nitrite oxidation is observed in electrolytes containing 5 mM $NaNO_3$, however no analytically-useful reduction wave can be found as no appreciable growth in the cathodic feature at *ca.* + 0.6 - 0.7 V was exhibited. There are no reports in the literature which find large gold nanoparticles to be a competitive catalyst against Cu-based materials in terms of both performance and economy. Though the underlying carbon support was also found to be active for nitrate reduction (since nitrite oxidation was observed to take place in the presence of NO_3^-), no obvious cathodic features resulting from this reaction were observed in the potential window interrogated. A summary of typical peak potentials for both nitrate reduction and nitrite oxidation, for all catalysts prepared in this work is given below in Table 6.1.

Catalyst	**Au^+**	**Au_6**	**Au_8**	**Au_8Pd_1**	**Au_9**	**Au_{11}**	**Au_{13}**	**AuNPs**	**Ag_{25}**
$E_{p,c}$	+0.718V	+0.742V	+0.717V	+0.774V	+0.749V	+0.675V	+0.744V	+0.639V	–
$E_{p,a}$	+0.901V	+0.919V	+0.925V	+0.914V	+0.898V	+0.919V	+0.923	+0.928V	+0.886V

Table 6.1 – Typical peak cathodic and anodic potentials ($E_{p,c}$ and $E_{p,a}$, respectively) for nitrate reduction and nitrite oxidation at carbon-supported gold and silver catalysts. Results are an average of four separate electrodes in N_2-purged 0.1 M Na_2SO_4 after 10 cycles in the background electrolyte, with $[NO_3^-]$ = 5 mM and scan rate = 50 mV/s.

Some key parameters of electrocatalytic performance may be readily extracted from the above voltammetry data. The activation overpotential η, which is a direct measure of the energy required to surmount the activation-barrier for a heterogeneous charge-transfer reaction, may be calculated using equation 6.1:

$$\eta = \left|E_p - E_{\mathrm{eq}}\right| \tag{6.1}$$

Where E_p is the peak electrolysis potential (for either a reduction or oxidation reaction), and E_{eq} is the equilibrium potential for the $NO_3^- \rightleftharpoons NO_2^-$ redox couple, experimentally-defined by equation 6.2:

$$E_{\text{eq}} = \frac{E_{p,a} - E_{p,c}}{2} \tag{6.2}$$

Where the terms $E_{p,a}$ and $E_{p,c}$ represent the peak potentials for the individual anodic and cathodic reactions, respectively. Using these relationships, average cathodic overpotentials for nitrate electroreduction at all six gold-phosphine clusters, a cationic gold complex and AuNPs have been calculated (Table 6.2).

Catalyst	Au^+	Au_6	Au_8	Au_8Pd_1	Au_9	Au_{11}	Au_{13}	AuNPs
E_{eq}	+0.810 V	+0.831 V	+0.821 V	+0.844 V	+0.819 V	+0.919 V	+0.923 V	+0.811 V
η	92 mV	89 mV	104 mV	70 mV	79 mV	129 mV	90 mV	118 mV

Table 6.2 – Typical equilibrium potentials (E_{eq}) and overpotentials (η) for nitrate electroreduction at carbon-supported gold catalysts. Results are an average of four separate electrodes in N_2-purged 0.1 M Na_2SO_4 after 10 cycles in the background electrolyte, with $[NO_3^-]$ = 5 mM and scan rate = 50 mV/s.

Finally, it is possible to compare the voltammetric responses of catalysts to nitrate by considering the percentage growth of the native cathodic wave at *ca.* + 0.6 - 0.7 V. Such data is given for both nitrate reduction and nitrite oxidation signals, collected from four separate electrodes for each catalyst. Percentages are measured as the fraction-increase growth of the normalised background current-density (Δj_p) in the presence of 5 mM $NaNO_3$ at $E_{p,c}$ (Table 6.3) and $E_{p,a}$ (Table 6.4).

Catalyst	Au^+	Au_6	Au_8	Au_8Pd_1	Au_9	Au_{11}	Au_{13}
Δj_p- Electrode 1	+58%	+50%	+119%	+49%	+87%	+207%	+49%
Δj_p- Electrode 2	+69%	+37%	+101%	+58%	+69%	+219%	+45%
Δj_p- Electrode 3	+37%	+37%	+85%	+51%	+98%	+194%	+37%
Δj_p- Electrode 4	+53%	+53%	+91%	+45%	+104%	+201%	+42%
Δj_p- Average	**+54**%	**+54**%	**+99**%	**+51**%	**+90**%	**+205**%	**+43**%
S.D.	**13.29**	**13.53**	**14.87**	**5.48**	**15.37**	**10.59**	**5.05**

Table 6.3 – Percentage increases in the measured cathodic current-densities at $E_{p,c}$ for carbon-supported gold catalysts in the presence of 5 mM $NaNO_3$, with respect to the background current-density at the same potential in N_2-purged 0.1 M Na_2SO_4. Scan-rate = 50 mV/s. Currents have been normalised by the weight-percent of gold and electrode area. S.D. = standard deviation.

Catalyst	Au^+	Au_6	Au_8	Au_8Pd_1	Au_9	Au_{11}	Au_{13}
Δj_p- Electrode 1	+164%	+190%	+143%	+47%	+164%	+404%	+19%
Δj_p- Electrode 2	+153%	+181%	+163%	+51%	+181%	+379%	+25%
Δj_p- Electrode 3	+156%	+208%	+151%	+44%	+173%	+395%	+22%
Δj_p- Electrode 4	+175%	+196%	+139%	+58%	+144%	+421%	+21%
Δj_p- Average	**+162%**	**+194%**	**+149%**	**+50%**	**+165%**	**+399%**	**+22%**
S.D.	**9.85**	**11.32**	**10.53**	**6.01**	**15.94**	**17.94**	**2.50**

Table 6.4 – Percentage increases in the measured anodic current-densities at $E_{p,a}$ for carbon-supported gold catalysts in the presence of 5 mM $NaNO_3$, with respect to the background current-density at the same potential in N_2-purged 0.1 M Na_2SO_4. Scan-rate = 50 mV/s. Currents have been normalised by the weight-percent of gold and electrode area. S.D. = standard deviation

From this data, the largest growth (*ca*. 200%) in nitrate reduction signals is enjoyed by catalysts containing Au_{11}, twice that of the next-best performer Au_8 (*ca*. 100%) and over five-times that of the lowest performer, Au_{13} (*ca*. 40%). Additionally, Au_{11} elicits the greatest nitrite oxidation signal compared to that of the background current (*ca*. 400%), whilst the Au_{13} produces the poorest nitrite oxidation signal (only 22%). It is notable that the addition of a Pd atom to Au_8, or the replacement of a Au atom in Au_9 to yield the Au_8Pd_1 cluster elicits a dramatic decrease in Δj_p for both nitrate reduction and nitrite oxidation. This contrasts with several other catalytic systems[159, 306-309] whereby the alloying of Au with Pd significantly *increases* catalytic performance and is usually attributed to the ability of the Pd-dopant to chemisorb hydrogen. However, Gauthard and co-workers[99] find the alloying of Pt and Pd with Au produces no promoting effect during nitrate reduction compared to alloys with Cu or Ag, although these authors could not provide a clear explanation for this result. Note however, that in Table 6.2 Au_8Pd_1 was found to possess the *smallest* overpotential for nitrate reduction, which *would* indicate the greatest catalytic activity. This discrepancy highlights the importance of not relying on one sole metric for comparing electrocatalyst performance, and further work is needed to establish a clear reason for a decreased current response to nitrate activity upon Pd-atom doping; this author notes that analogous Au_8Pt_1 and Au_8Rh_1 clusters have been reported[310, 311] and such species could yield an interesting point of comparison. Catalysts are initially ranked based on the average magnitude of Δj_p:

NO_3^- electroreduction: $Au_{11} > Au_8 > Au_9 > Au^+ \approx Au_6 > Au_8Pd_1 > Au_{13}$.

NO_2^- electrooxidation: $Au_{11} > Au_6 > Au_9 > Au^+ > Au_8 > Au_8Pd_1 > Au_{13}$.

This measure of activity is employed to observe the direct voltammetric response of the catalysts to the presence of the nitrate anion. Since amperometric sensors operate by measuring changes in current with respect to a known background, it is logical that a catalyst which delivers the greatest voltammetric response to a given concentration of analyte will, in principle, allow the lowest detection limit.

6.1.2 *Carbon-Supported Silver-Thiolate Catalyst*

Curiously, an atomically-precise thiolate-protected silver cluster, Ag_{25}, does not appear to have appreciable catalytic activity for nitrate electroreduction. Though parallel experiments with 5 mM $NaNO_2$ confirm that the large anodic feature at *ca.* +0.88 V results from nitrite oxidation, no analytically-useful nitrate reduction wave can be identified. Any signal is likely to be weak and may be obscured by non-faradaic background currents, as only a steady growth towards the region of hydrogen-evolution is observed. A freshly-prepared electrode which had not undergone any previous electrochemical cycling similarly did not produce a useful cathodic wave in the presence of NO_3^-, nor did extending the cathodic scan limit to -0.4 V. As catalysts containing Ag_{25} were observed to undergo significant molecular reorganisation after 10 voltammetric cycles in the background electrolyte (Section 5.2.3) this strongly suggests that neither carbon-supported Ag_{25} nor any nanostructures potentially derived from Ag_{25} herein are appreciably active for nitrate reduction.

This result is peculiar, and in direct contrast with other literature reports which find both bulk- and nano-scale silver materials are highly active catalysts for nitrate reduction,[36, 58, 99, 140, 312, 313] and indeed more-so than Au. Furthermore, Calle-Vallejo and co-workers[20] have shown *via* both computational and experimental approaches that ensembles of Ag atoms (*e.g.* clusters) *are* comparatively active for nitrate reduction. It could be that electrochemical treatment induces the disintegration of Ag_{25} clusters into Ag^+ cations, which are then captured by electrolyte SO_4^{2-} anions and form poorly-soluble, and electrochemically-dormant Ag_2SO_4 deposits. Alternatively, electrochemical treatment could invoke the restructuring of clusters into secondary nanostructures which then become (electrochemically) passivated by oxides, deactivating the silver catalyst and preventing nitrate adsorption. The electroreduction of nitrate is often supressed at noble-metal electrodes

in the presence of SO_4^{2-} due to competitive adsorption,[62] and Burke *et al.* report that nitrate reduction is also inhibited by the presence of sub-surface oxygen at defect-sites on silver electrodes.[302] Finally, chemical interactions of the thiolate ligands with silver clusters/nanostructures could be sufficiently strong that few sites are available for nitrate anions to adsorb, and the (pre)catalyst is effectively poisoned by the thiophilic nature of Ag. However, if this explanation were wholly correct it stands that nitrite oxidation should also be equally inhibited; the experimental data clearly showed the reverse transformation is facile at Ag_{25} catalysts (*ca*. +0.9 V; Figure 6.1, Panel I). In any case, carbon-supported Ag_{25} may be a promising candidate for amperometric *nitrite* sensing, however as nitrate reduction signals were not clearly observable in voltammetric spectra, this cluster will be excluded from any foregoing discussions.

6.1.3 *Long-Term Electrocatalytic Activity*

To evaluate the long-term response of gold-phosphine cluster catalysts to nitrate, freshly-prepared electrodes were subjected to either 2, 10, 25, 50, 75 or 100 electrochemical cycles in 0.1 M Na_2SO_4 (50 mV/s) before the addition of 5 mM $NaNO_3$. The percentage growth of the native cathodic wave at *ca.* + 0.6 - 0.7 V during nitrate reduction, and the percentage growth of the nitrite oxidation wave above the background (both Δj_p) was calculated, and these data over time for all six gold-phosphine clusters are shown in Figure 6.2:

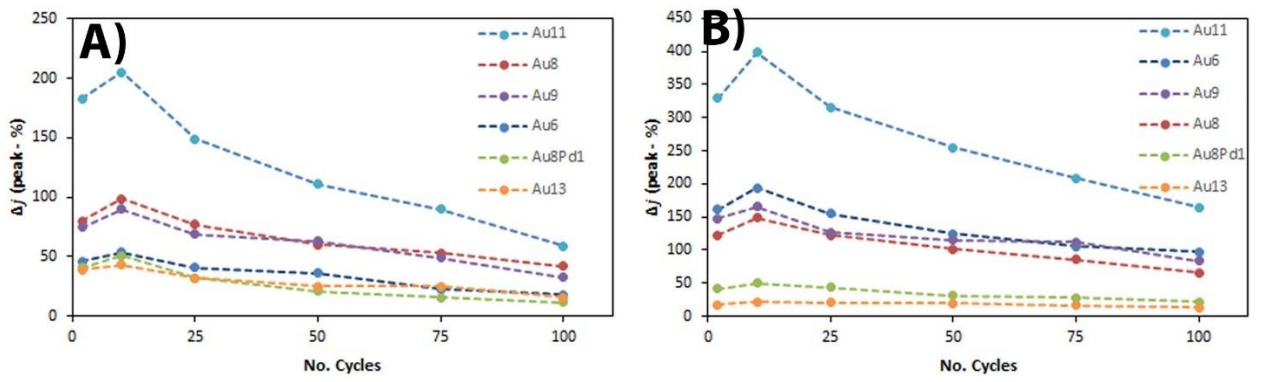

Figure 6.2 – Normalised voltammetric response to nitrate (Δj_p) for all six gold-phosphine cluster catalyst up to 100 electrochemical cycles during A) nitrate reduction and B) nitrite oxidation. Data collected in N_2-purged 0.1 M Na_2SO_4 at 50 mV/s and 5 mM $NaNO_3$. Note that Δj_p for nitrate reduction (A) is plotted with a positive sign, though cathodic currents are negative.

Overall, the activity of each catalyst (towards both nitrate reduction and nitrite oxidation) steadily decreases within 100 electrochemical cycles, however it is interesting that the overall activity trend remains over this time. For instance, even after 100 cycles Au_{11} still enjoys a greater voltammetric response to the nitrate/nitrite

cycle than all other catalysts. For nitrate reduction, the activity of Au_6 remains consistently low, as does the activity of Au_{13} during nitrite oxidation. This could be due to the entrapment of a small population of clusters within the pores of the amorphous carbon support,[274] which are isolated from aggregation yet are still accessible to the electrolyte and the overall activity trend therefore persists. Note that in Figure 6.2 above, it would appear the activities of Au_8Pd_1 and Au_{13} for nitrite oxidation (Panel B) are invariant over 100 cycles. This is simply due to the scale of the vertical-axis giving cathodic peak currents for these catalysts a diminutive appearance. Also note that (due to time constants) each data point represents a measurement from one electrode (except for the tenth cycle, which is an average of four electrodes and is taken from Tables 5.3 and 5.4). Therefore, it should be kept in mind that this data does not carry the same statistical certainty as the data in Tables 5.3 and 5.4. Perhaps the most interesting observation from these experiments is the large peak in activity at the tenth cycle for all catalysts; since voltammetric responses decrease after 25 measurements, maximum activity is therefore expected within 3-24 electrochemical cycles. As outlined by a previous member of this laboratory (Dr Jared Steven)[274] during a similar study of carbon-supported gold nanoparticles during electrochemical cycling, this gain in activity is probably due to the progressive dissociation of phosphine ligands which expose a greater number of active catalytic sites. The overall loss in activity (Δj_p at the one-hundredth cycle as a percentage of Δj_p at the tenth cycle) is presented in Table 6.5:

Catalyst	**Au_6**	**Au_8**	**Au_8Pd_1**	**Au_9**	**Au_{11}**	**Au_{13}**
Δj_p – cathodic decrease	-67%	-57%	-76%	-62%	-71%	-62%
Δj_p – anodic decrease	-50%	-55%	-57%	-49%	-59%	-38%

Table 6.5 – Percentage decreases in the peak voltammetric response (Δj_p) to nitrate reduction and nitrite oxidation between the tenth and one-hundred electrochemical cycle, for all six gold-phosphine cluster catalysts in this work. Electrochemical cycling was carried out in N_2-purged 0.1 M Na_2SO_4 at 50 mV/s before 5 mM $NaNO_3$ was added.

In general, all catalysts are found to lose between *ca.* 50-70% of the maximum measured activity between ten and one-hundred electrochemical cycles, except for Au_{13} which only experiences a 38% decrease in normalised nitrite oxidation peak density. This could be due to significant aggregation of neighbouring clusters induced by repetitive electrochemical cycling, as Steven *et al.*[274] have noted, or it could be a result of electrochemical dissolution of gold atoms into the supporting electrolyte. As noted in Section 5.2.1, a sample of the carbon layer for each electrode was carefully removed from the electrode surface, and these materials have been

dispatched to colleagues at Flinders University (Adelaide, South Australia) for XPS and HR-TEM analysis to assess whether cluster aggregation has occurred; unfortunately, at the time of writing these results have not yet been received. Furthermore, a reasonable level of catalytic activity remains even after one-hundred electrochemical cycles. It is therefore possible that i) some catalytically-active sites remain on the carbon support (in the form of complete, un-aggregated gold-phosphine clusters), or ii) secondary nanostructures formed during electrochemical cycling also possess modest catalytic activity.

Whilst a decrease in electrocatalytic performance severely restricts the operational life-time of a functional amperometric sensor, this author notes that the *rate of activity-loss* for all catalysts generally decreases with successive electrochemical cycling, suggesting that (eventually) an electrochemically-robust species could be formed which may still possess appreciable catalytic activity for nitrate reduction, nitrite oxidation, or both. Unfortunately, due to time constraints this hypothesis could not be tested in this work. The observation that at least ten electrochemical cycles demonstrated an apparent activating effect on electrocatalytic performance has been exploited, and as a result all electrodes are subjected to this treatment prior to any further measurements.

6.1.4 *Summary and Remarks*

In this section, the reduction of nitrate and the oxidation of nitrite by carbon-supported gold-phosphine clusters, a carbon-supported cationic gold-phosphine complex, carbon-supported gold nanoparticles and a carbon-supported silver-thiolate cluster has been examined. All materials, except those prepared with the silver cluster Ag_{25}, were found to be active. To the best of this authors' knowledge, this is the first known report of nitrate electroreduction and nitrite electrooxidation catalysed by small gold clusters; since bulk gold has previously been described as electrocatalytically-quiescent for nitrate reduction this finding clearly demonstrates the unique molecular properties enjoyed by these species. It is interesting that a silver cluster could not catalyse nitrate reduction with any appreciable activity, as both bulk and nanoparticulate silver have well-documented performance for this reaction. It is also peculiar that the reduction of nitrate does not appear to proceed beyond nitrite, which is a promising feature for electrochemical sensing where these species are often found to act as an interference to the other. The reason(s) for this phenomenon are not obvious to the author at present. There is an apparent trend in the catalytic activity of carbon-supported gold-phosphine clusters for mediating the

nitrate/nitrite redox cycle, wherein Au_{11} and Au_8 display the greatest voltammetric response, and Au_{13} and large Au nanoparticles the least. Long-term performance was found to initially improve, however diminished with subsequent repetitive electrochemical cycling, with the latter activity loss a probable result of cluster aggregation, fragmentation and/or dissolution. Interestingly, a peak in electrocatalytic activity was observed between 3 and 24 electrochemical cycles, and this has been explained by gradual ligand dissociation which exposes more catalytically active sites. Moreover, the trend in catalytic activity after prolonged electrochemical cycling mirrored that of trends after ten cycles, where activity was the greatest. Whilst undesirable for the operational life-time of an electrochemical sensing device, the fact that appreciable electrocatalytic activity remained after 100 electrochemical cycles is promising and it is possible that a redox-stable species may eventually be formed. The observation that nitrate reduction does not proceed beyond nitrite means that carbon-supported gold clusters are clearly a poor choice of catalyst for waste-water denitrification (N_2 genesis), however the fact that nitrite oxidation is also facile means that such materials could be used for the electrochemical detection of either nitrate or nitrite. Importantly, these redox signals display prominent plateaus and are therefore able to achieve *mass-transport limited currents*, which are imperative for amperometric chemical sensing. Due to time constraints the focus of this discussion and of this thesis will remain with nitrate sensing, though this result should be kept in mind and is undeniably a promising avenue for future work.

6.2 – Kinetics of Nitrate Electroreduction at Carbon-Supported Gold-Phosphine Clusters

To begin a kinetic analysis of nitrate reduction at gold-phosphine cluster catalysts and an evaluation of their relative electrocatalytic activity, several descriptors of catalytic performance will be evaluated from cyclic voltammetry data. These include many important electrochemical parameters that describe the kinetics of nitrate reduction, such as the charge-transfer coefficient (α), the exchange-current (i_0), the charge-transfer resistance (R_{ct}), the diffusion coefficient (D), Tafel slopes (b), three measures of electrochemical reversibility (m_o, ζ, ψ), the electrochemical rate-constant (k_0) and the rate-limiting step (n').

6.2.1 *Effect of Scan Rate on Nitrate Electroreduction*

The effect of scan-rate on nitrate reduction and nitrite oxidation peak currents was examined by cycling the gold-phosphine catalysts in N_2-purged 0.1 M Na_2SO_4 containing 5 mM $NaNO_3$, after 10 previous cycles in the background electrolyte, at scan-rates from 5 – 100 mV/s. Typical cyclic voltammograms for all six gold clusters are shown in Figure 6.3. It is clear the scan rate has a pronounced effect on redox signals (both nitrate reduction and subsequent nitrite oxidation), with peak currents increasing alongside scan rate and peak potentials shifting more-negative for nitrate reduction, and more-positive for nitrite oxidation. Such potential shifts are typical of electrochemical reactions with slow electron-transfer kinetics and indicate a *quasi-reversible* process.[1, 16] The reversibility of nitrate reduction at gold-phosphine cluster catalysts will be evaluated later in Section 6.5.

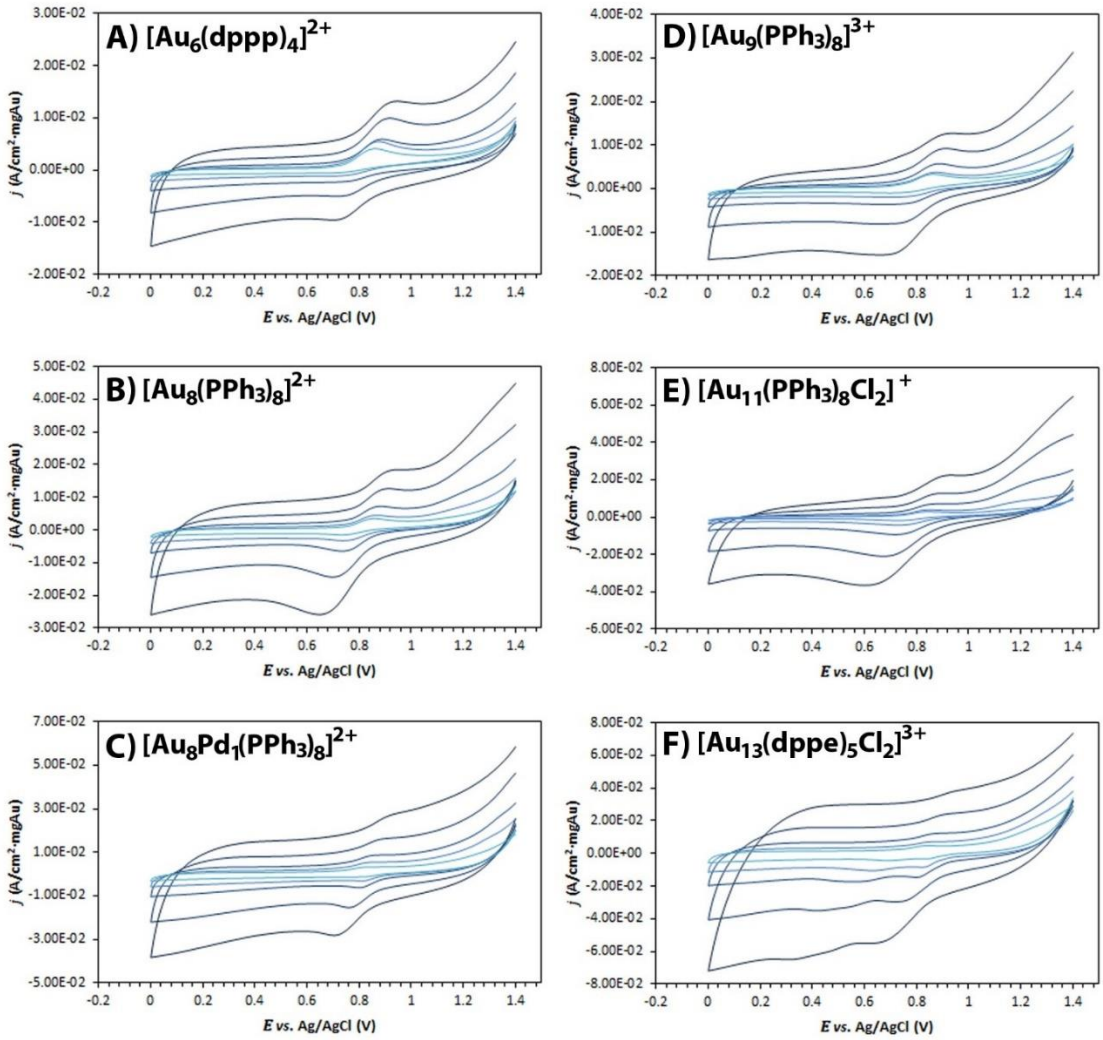

Figure 6.3 – Cyclic Voltammograms recorded at various scan-rates (5, 10, 20, 50 and 100 mV/s, light-blue to dark-blue) for A) Au_6; B) Au_8; C) Au_8Pd_1; D) Au_9; E) Au_{11}; F) Au_{13} in N_2-purged 0.1 M Na_2SO_4 with [NO_3^-] = 5 mM, after 10 previous cycles in background electrolyte.

A linear relationship between normalised peak current-density j_p (A/cm^2 per mg Au) and the square-root of the scan rate υ (in V/s) is indicative of an electrochemical reaction under mass-transport control and is described quantitatively by the *Randles-Sevcik* equation.[1]

$$j_p = -2.99\text{x}10^5 An(\alpha n')^{1/2} D^{1/2} \upsilon^{1/2} C^* \quad (6.3)$$

Where n is the total number of electrons transferred per reactant molecule, α is the charge-transfer coefficient (unitless), n' is the number of electrons transferred up-to and including the rate-limiting step, D is the diffusion coefficient (in cm^2/s), and C^* is the bulk concentration of the species undergoing electrolysis (in mol/cm^3). The relationship is useful for evaluating the diffusion coefficient of an analyte (through solution) undergoing electrochemical transformation, and according to the Randles-Sevcik equation a linear plot of j_p *vs.* $\upsilon^{1/2}$ will have a gradient from which D is readily accessible, provided $\alpha n'$ is known. Figure A.2 (Appendices) shows these plots for all six catalysts, and a linear relationship is found over the entire range of scan rates with satisfactory goodness-of-fit values. The numerical value of these slopes will be employed later in Section 6.2.9 to evaluate diffusion coefficients.

Others[38, 314] have found that the relationship between j_p and $\upsilon^{1/2}$ deviates from linearity for large υ (*e.g.* 1 V/s), which is attributed to faster potential-sweep rates not allowing sufficient time for nitrate anions to adsorb to the electrode surface. The non-zero intercept of the j_p- $\upsilon^{1/2}$ plots (for both nitrate reduction and nitrite oxidation) may infer that an adsorption process is taking place prior to electrolysis.[38] It is also noteworthy that the magnitude of the intercept with the vertical axis is greater for nitrate reduction than nitrite oxidation. This agrees with experimental findings that nitrate adsorption is, in general, a more energetically-demanding process than nitrite adsorption.[20, 315]

6.2.2 *Determination of the Charge-Transfer Coefficient*

To evaluate diffusion coefficients for all clusters, a numerical value for $\alpha n'$ must be determined. The charge-transfer coefficient α is a dimensionless kinetic parameter which describes the symmetry of the energy-barrier separating the reactants and products during in a heterogeneous electrochemical reaction.[1] More specifically, α signifies how the transition-state is affected by the application of an overpotential and the fraction of this

energy that is devoted to lowering the free-energy barrier for charge-transfer.[16, 316] A more rigorous definition may be found elsewhere,[317] the details of which are far beyond both the scope of this thesis and the ability of this author to articulate however the above interpretation is sufficiently accurate for application in this work. The parameter α lies between 0 and 1, but in most systems is found to have a value of 0.3 - 0.7, and where no experimental data is available can often be assumed to have a value of 0.5.[1, 16, 316] A precise value for α may (and will) be calculated, however it is more convenient at the present time to employ the expression $\alpha n'$ since the number of electrons involved in the rate-limiting step for nitrate reduction (either 1 or 2), is not yet known.

6.2.3 *The Shape Factor*

A value for $\alpha n'$ may be determined using equation 6.4, which describes the *shape-factor* $\left|E_p - E_{p/2}\right|$ of an irreversible or *quasi*-reversible electrochemical reaction.[318] The terms E_p and $E_{p/2}$ represent the peak and half-peak potentials, respectively.

$$\left|E_p - E_{p/2}\right| = 1.857\frac{\mathcal{R}T}{F\alpha n'} \tag{6.4}$$

Average values for the shape-factor have been calculated for all six gold-phosphine cluster catalysts at various scan rates in 0.1 M Na_2SO_4 and 5 mM $NaNO_3$. These tended to fall in the range 100-110 mV, and from these $\alpha n'$ was calculated for all clusters. This information is given in Table 6.6.

Catalyst	**Au_6**	**Au_8**	**Au_8Pd_1**	**Au_9**	**Au_{11}**	**Au_{13}**
$\left\|E_p - E_{p/2}\right\|$	103 mV	104 mV	101 mV	110 mV	105 mV	103 mV
$\alpha n'$	0.46	0.45	0.47	0.43	0.45	0.46

Table 6.6 – Values of $\left|E_p - E_{p/2}\right|$ and $\alpha n'$ calculated from cyclic voltammetry data for all six carbon-supported gold catalysts. Results are an average of four separate electrodes in 0.1 M Na_2SO_4 after 10 cycles in the background electrolyte, with $[NO_3^-]$ = 5 mM and scan-rates are 5, 10, 20, 50 and 100 mV/s.

6.2.4 *The Laviron Plot*

Alternatively, a value for the expression $\alpha n'$ can be found by employing equation 6.5, where E_p is taken as a function of the logarithm of scan rate v. For irreversible and *quasi*-reversible electrochemical reactions, the peak potential is predicted to shift $\frac{29.6}{\alpha n'}$ mV for every decade increase in scan rate:[1]

$$\left|\frac{dE_p}{d\log v}\right| = \frac{29.6}{\alpha n'} \tag{6.5}$$

A graphical representation of the relationship between E_p (in mV) against $\log v$ is shown in Figure A.3 (Appendices) and is called a *Laviron plot*,[319] from which $\alpha n'$ is extracted from the gradient. All six gold-phosphine clusters produce Laviron plots with excellent linearity, and from these values for $\alpha n'$ fall within the range 0.4 - 0.45, in good agreement with the values of *ca.* 0.45 determined above. These are shown in Table 6.7 below.

Catalyst	**Au_6**	**Au_8**	**Au_8Pd_1**	**Au_9**	**Au_{11}**	**Au_{13}**
$\boldsymbol{\alpha n'}$	0.45	0.41	0.42	0.42	0.40	0.43

Table 6.7 – Values of $\alpha n'$ calculated from Laviron plot gradients for all six carbon-supported gold catalysts. Results are an average of four separate electrodes in 0.1 M Na_2SO_4 after 10 cycles in the background electrolyte, with $[NO_3^-]$ = 5 mM.

Furthermore, the horizontal axis-intercept of Laviron plot v_c can be used to calculate the electrochemical rate-constant k_0 for nitrate reduction:[319]

$$k_0 = \frac{\alpha n' F v_c}{\mathcal{R}T} \tag{6.6}$$

Using this information, k_0 for all six catalysts have been calculated and fall in the range 5-8×10^{-3} cm/s.

Catalyst	**Au_6**	**Au_8**	**Au_8Pd_1**	**Au_9**	**Au_{11}**	**Au_{13}**
$\boldsymbol{k_0}$ (×10^{-3} cm/s)	5.61	7.58	6.28	6.17	8.06	5.81

Table 6.8 – Values of k_0 calculated from the x-axis intercept of Laviron plots (v_c) for all six carbon-supported gold catalysts. Results are an average of four separate electrodes in 0.1 M Na_2SO_4 after 10 cycles in the background electrolyte, with $[NO_3^-]$ = 5 mM.

As previously mentioned, k_0 numerically represents the kinetic facility of heterogeneous charge-transfer from an electrode to an adsorbed electroactive species. Rate-constants decrease in the order $Au_{11} > Au_8 > Au_8Pd_1 \approx Au_9 > Au_{13} \approx Au_6$, which roughly follows the trend in cathodic currents for nitrate reduction.

6.2.5 *Tafel Analysis*

Tafel analysis is commonly employed to gain quantitative understanding of charge-transfer kinetics occurring at electrode-electrolyte interfaces. Mathematically, the relationship between the overpotential η (in mV) and the rate of an electrochemical reaction i (in A) is given by the Tafel equation:[1, 13, 16]

$$\eta = a + b \log i \tag{6.7}$$

Which is an expression for a straight-line graph, where the parameter a is a constant and b is the Tafel slope, which has physical meaning (Section 6.2.8; *vide infra*) and is given by equation 6.8:

$$b = \frac{2.303\mathcal{R}T}{\alpha n' F} \tag{6.8}$$

The Tafel relationship holds only when an electrochemical reaction is under strict kinetic control in the absence of mass-transport effects. That is to say, equation 6.7 is only applicable when the magnitude of η is not excessively large (*i.e.* << 1 V).[13] A graph of η *vs.* $\log i$ is derived from cyclic voltammetry data and is called a Tafel plot, consisting of cathodic ($\eta > 0$) and anodic ($\eta < 0$) branches which correspond to $E < E_{\mathrm{eq}}$ and $E > E_{\mathrm{eq}}$, respectively. Both regions possess linear segments which extrapolate to an intercept with value $\log i_0$ (the exchange-current), however deviate sharply from linearity as η approaches zero ($E \approx \mathrm{E_{eq}}$) and the contribution of reverse reaction to the measured current is no longer negligible.[1] Tafel plots have been generated for all six clusters using cyclic voltammetry data collected at a scan rate of 50 mV/s in 0.1 M Na_2SO_4 and 5 mM $NaNO_3$, and are shown in Figure 6.4.

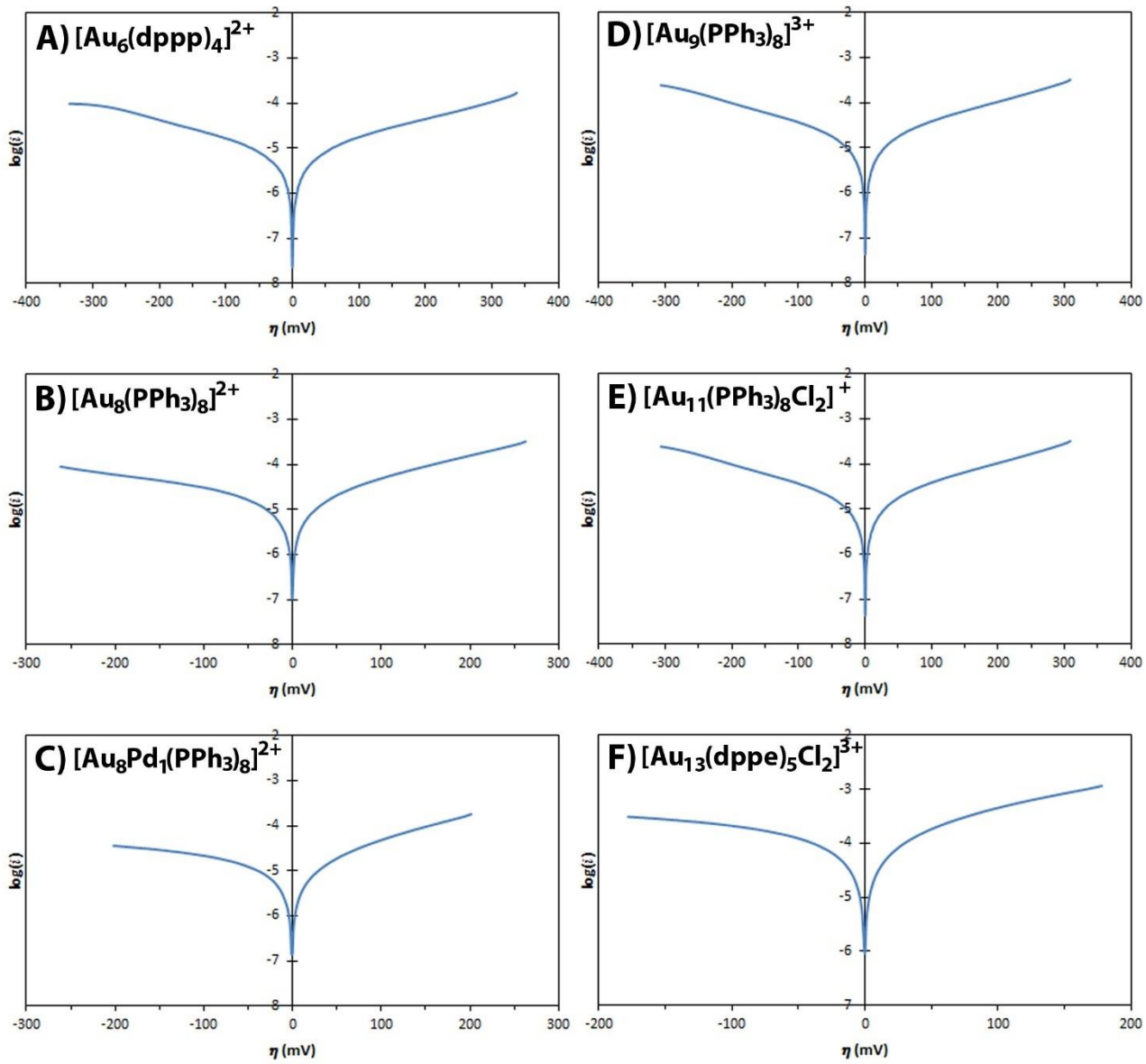

Figure 6.4 – Tafel plots of the logarithm of current (log i) as a function of overpotential (η) for A) Au_6; B) Au_8; C) Au_8Pd_1; D) Au_9; E) Au_{11}; F) Au_{13} in N_2-purged 0.1 M Na_2SO_4 with [NO_3^-] = 5 mM, after 10 previous cycles in background electrolyte.

Linear approximations to the cathodic branches of these Tafel plots (for values of *ca.* 100 mV < η < *ca.* 200 mV) have been extrapolated to the vertical-axis to find average exchange-currents for all catalysts, and these are tabulated below:

Catalyst	Au_6	Au_8	Au_8Pd_1	Au_9	Au_{11}	Au_{13}
i_0 ($\times 10^{-5}$ A)	1.28	1.62	1.36	1.45	1.79	1.36

Table 6.9 – Values of i_0 calculated from the vertical-axis intercept (log i_0) Tafel plots for all six carbon-supported gold catalysts. Results are an average of four separate electrodes in 0.1 M Na_2SO_4 after 10 cycles in the background electrolyte, with [NO_3^-] = 5 mM and a scan-rate of 50 mV/s.

Exchange-currents are seen to increase in the order Au_{11} > Au_8 > Au_9 > Au_{13} > Au_8Pd_1 > Au_6 which follows the general order of catalysts when ranked by amperometric response to nitrate (Δj_p) and electrochemical rate-constants. The exchange-current can be considered a bi-directional "idle current" for the exchange of charge across the electrode/electrolyte interface,[1] and the role of the overpotential is to displace equilibrium and drive a net reduction or oxidation reaction; should the desired electrolysis current exceed the exchange-current then considerable overpotentials are required to drive the electrochemical reaction at an appreciable rate. Larger values of i_0 therefore indicate charge-transfer may proceed with greater kinetic facility upon application of η. From this perspective, the exchange-current is a measure of an electrocatalysts' ability to deliver a net electrolysis current without a significant energy penalty due to surmounting the activation-barrier. This possibly explains why catalysts containing Au_{11} and Au_8 require the largest overpotentials to reach mass-transport limited currents, however are able to extract the greatest nitrate reduction currents, since their exchange-currents are slightly larger compared to other catalysts in this work. Note however that all exchange-currents are not too dissimilar from one other, and therefore one would not expect the large variation in catalytic activity as measured by peak cathodic currents in the presence of nitrate. It is therefore possible that other factors are contributing to the wide range of catalytic performances observed.

6.2.6 *The Electrochemical Rate-Constant*

It is possible to extract the electrochemical rate-constant from a Tafel analysis of cyclic voltammetry data, for the case where equilibrium exists at the working electrode surface,

$$NO_3^- + 2e^- \rightleftharpoons NO_2^- \tag{6.9}$$

the measured current is of course equal to i_0 (the exchange-current), which describes the specific condition where the forward and reverse reactions are occurring at the same rate. If Tafel behaviour is observed at low η, then $E \approx E_{\mathrm{eq}}$ and Equation 1.2 (the current-potential characteristic) now takes a special form (with rearrangement):[1]

$$k_0 = \frac{i_0}{nFAC^*_{NO_3^-}} \tag{6.10}$$

The convenience of evaluating k_0 at E_{eq} is that the exponential term in Equation 1.2 becomes equal to 1 and thus the charge-transfer coefficient need not be known to calculate the electrochemical rate-constant. Values for k_0 have been calculated using i_0 and are tabulated below:

Catalyst	**Au_6**	**Au_8**	**Au_8Pd_1**	**Au_9**	**Au_{11}**	**Au_{13}**
$\boldsymbol{k_0}$ ($\times 10^{-3}$ cm/s)	6.76	8.55	7.18	7.64	9.46	7.16

Table 6.10 – Values of k_0 calculated from i_0 and equation 6.10 for all six carbon-supported gold catalysts. Results are an average of four separate electrodes in N_2-purged 0.1 M Na_2SO_4 after 10 cycles in the background electrolyte, with [NO_3^-] = 5 mM and a scan-rate of 50 mV/s.

Values for k_0 as determined from the results of Tafel analysis are in general agreement with those extracted from Laviron plots (Section 6.4.4), however the former is seen to overestimate the electrochemical rate-constant by *ca.* 15-25% relative to the latter. This could be due to a slight error introduced during the approximation of Tafel plots with linear models, and their subsequent vertical axis-intercepts ($\log i_0$) whereby slight deviations are magnified during deconvolution of the logarithmic function. Trends in values for k_0 from a Tafel approach (equation 6.10) are seen to decrease in the order Au_{11} > Au_8 > Au_9 > Au_{13} > Au_8Pd_1 > Au_6, which mirrors that of k_0 from a Laviron approach (equation 6.6). Very few authors have calculated k_0 from nitrate reduction data, which *this* author finds surprising considering the wide interest in understanding the kinetics of this important reaction; Polatides and Kyriacou[320] have calculated k_0 to be 4.9×10^{-4} cm/s at a Sn/Cu alloy electrode in 0.1 M K_2SO_4, and De *et al.*[314] report a value of 4.18×10^{-7} cm/s at an iridium-modified carbon-fibre electrode in 1 M $NaClO_4$. Huang *et al.* [105] have obtained an exceptionally small k_0 value of 2.3×10^{-8} cm/s for a one-third Ag sub-monolayer on a polycrystalline Au electrode in 0.1 M KCl. The comparatively small values of k_0 for the latter-two studies could be rationalised by considering that bulk noble-metals electrodes are, generally speaking, poor catalysts for nitrate reduction (Section 1.4.1).[36] All carbon-supported gold-phosphine clusters used in this work are, when using k_0 as the sole metric of performance, superior catalysts to the above materials. Noteworthy is that these gold clusters extract electrochemical rate-constant an order of magnitude greater than a Sn/Cu alloy, which as noted in Section 1.4.2 possesses considerable electrocatalytic activity for this reaction.

6.2.7 *The Charge-Transfer Resistance*

Additionally, Tafel analysis of voltammetric data may yield a value for the *charge-transfer resistance*, which has units of $\Omega \cdot cm^2$ and is related to the exchange-current by equation 6.11:

$$R_{ct} = \frac{\mathcal{R}T}{Fi_0} \tag{6.11}$$

Alternatively, the charge-transfer resistance is the negative-reciprocal slope of an η-i curve at the origin, and approaches zero when the electrochemical rate-constant k_0 (and therefore i_0) is very large. This parameter has been calculated for all six gold phosphine cluster catalysts from values for i_0 using equation 6.11, and these results are tabulated below:

Catalyst	**Au_6**	**Au_8**	**Au_8Pd_1**	**Au_9**	**Au_{11}**	**Au_{13}**
$\boldsymbol{R_{ct}}$ ($\Omega \cdot cm^2$)	2005	1586	1888	1775	1434	1895

Table 6.11 – Values of R_{ct} calculated from i_0 and equation 6.11 for all six carbon-supported gold catalysts. Results are an average of four separate electrodes in N_2-purged 0.1 M Na_2SO_4 after 10 cycles in the background electrolyte, with $[NO_3^-]$ = 5 mM and a scan-rate of 50 mV/s.

Values for the charge-transfer resistance, calculated from a Tafel analysis of voltammetric data, are seen to increase in the order: $Au_{11} < Au_8 < Au_9 < Au_{13} < Au_8Pd_1 < Au_6$. The size of R_{ct} values can be rationalised by considering that this parameter is inversely proportional to k_0 and i_0, which themselves are noted to be on the order of 10^{-3} and 10^{-5}, respectively. Values for R_{ct} are comparable to those reported in the literature, though similar to the preceding case for electrochemical rate-constants, very few authors have calculated this value during their evaluation of nitrate electroreduction data. McCormac *et al.*[321] have assembled alternating thin-film layers of Cu or Ni heteropolyanions and silver nanoparticles on glassy-carbon electrodes, and used these for nitrate reduction in 0.1 M KCl. By electrochemical-impedance spectroscopy they report R_{ct} values between *ca.* 350 - 3500 $\Omega \cdot cm^2$, depending on the specific composition of the electrode layer(s). The charge-transfer resistances of all carbon-supported gold-phosphine clusters in this work are comparable in magnitude to these novel composite electrodes and are intermediate of the range found by the above authors. In contrast, Kondaviti and Min[322] find that commercially available Pt on carbon (10 wt/%) possessed a very large R_{ct} value of *ca.* 6200 $\Omega \cdot cm^2$ during nitrate reduction in 0.5 M H_2SO_4.

6.2.8 *The Tafel Slope*

The diagnostic meaning of the Tafel slope b is multifaceted and depending on the specific interpretation can allow both a quantitative and mechanistic analysis of an electrochemical process. Mathematically, it is a sensitivity parameter giving a measure of the rate of reaction that can be extracted from a given overpotential,[323] and is useful for evaluating the electrocatalytic activity of electrode materials: a promising catalyst will have a small Tafel slope which infers that less energy is required to achieve an order of magnitude increase in charge-transfer rate.[324, 325] Average Tafel slopes for all six catalysts from at least four separate electrodes each are shown in Table 6.12, and increase in the order $Au_{11} \approx Au_8 < Au_8Pd_1 < Au_9 \approx Au_6 < Au_{13}$, which is in general agreement with the ranking of catalysts by k_0, i_0 and R_{ct}. Alternatively, the magnitude of the slope may give mechanistic insight for a multi-step electrochemical process, and given that all catalysts possess values > 120 mV/decade[323] it is likely that the *first* electron-transfer is the rate-limiting step, in agreement with reports from other authors[36, 38, 39, 74, 326] and suggesting a mutually-common mechanism between these catalysts may be operative. On the other hand, if values of b were in the region of *ca.* 40 mV/decade a *second* electron-transfer would be rate-limiting, and values of *ca.* 60 mV/decade would imply a rate-limiting *chemical* step following a prior electron-transfer event.[327]

Applying these Tafel slopes in equation 6.8 yields a third set of values for the variable $\alpha n'$:

Catalyst	**Au_6**	**Au_8**	**Au_8Pd_1**	**Au_9**	**Au_{11}**	**Au_{13}**
Slope (mv/dec)	175	147	166	173	145	181
$\boldsymbol{\alpha n'}$	0.33	0.39	0.35	0.34	0.40	0.32

Table 6.12 – Tafel slopes and calculated values of $\alpha n'$ (from equation 6.8) for all six carbon-supported gold catalysts. Results are an average of four separate electrodes in N_2-purged 0.1 M Na_2SO_4 after 10 cycles in the background electrolyte, with $[NO_3^-]$ = 5 mM and a scan-rate of 50 mV/s.

Kinetic analysis of nitrate reduction by a Tafel approach is seen to underestimate the quantity $\alpha n'$ compared to Sections 5.4.3 and 5.4.4, and although the symmetry of the Tafel plot is related to the value of α (deviations from 0.5 imply that either reduction or oxidation is preferentially accelerated at the electrode[13]), it has been noted that there are several experimental reasons why this might occur. These explanations generally account for a greater-than-expected Tafel slope, from which a is derived and is inversely proportional to and include a

decrease in the electrochemically-active surface or the introduction of mass-transport effects at higher overpotentials.[323]

6.2.9 *Diffusion Coefficient for Nitrate Electroreduction*

With a numerical value for the parameter $\alpha n'$ averaged from three foregoing sections, the diffusion coefficient for nitrate reduction at all six gold cluster catalysts can be calculated from the Randles-Sevcik relationship. The slope of j_p *vs.* $v^{1/2}$ from Figure A.2 (Appendices) is used, alongside a value for n of 2 (since the nitrate to nitrite conversion is a two-electron process) and a known bulk nitrate concentration ($C^*_{NO_3^-}$) of 5×10^{-6} mol/cm^3:

$$slope = -2.99\text{x}10^5 n(\alpha n')^{1/2} D^{1/2} C^*_{NO_3^-} \quad (6.12)$$

Calculated values of D for all six catalysts are presented in Table 6.13:

Catalyst	**Au_6**	**Au_8**	**Au_8Pd_1**	**Au_9**	**Au_{11}**	**Au_{13}**
$\boldsymbol{\alpha n'}$ (avg.)	0.39	0.40	0.39	0.38	0.40	0.38
slope	-0.0337	-0.0997	-0.1065	-0.0561	-0.1416	-0.2058
$\boldsymbol{D}$ ($\times10^{-5}$ cm^2/s)	0.16	1.40	1.66	4.73	2.86	6.37

Table 6.13 – Average values of $\alpha n'$, Randles-Sevick slopes and diffusion coefficients for all six carbon-supported gold catalysts. Scan-rates were 5, 10, 20, 50 and 100mV/s in N_2-purged 0.1M Na_2SO_4 after 10 cycles in the background electrolyte (50mV/s), with [NO_3^-] = 5mM. Note: only one electrode was examined for each catalyst.

It can be seen, firstly, that diffusion coefficients are distinctly different for all clusters with no visible trend across cluster size, composition *etc.* and in fact an order-of-magnitude difference spans the smallest (Au_6) and greatest (Au_{13}) values of D. This is unexpected, given that at a macroscopic level all electrodes should have similar diffusion-zones as they are prepared from similar materials using the same method of fabrication. However, these diffusion coefficients are overall comparable with the reported literature. For example, using a polycrystalline silver electrode in NaOH electrolyte, Kim *et al.*[328] report D to have a value of 1.91×10^{-5} cm^2/s whilst Gartia *et al.* quote a value of 8.99×10^{-6} cm^2/s.[329] For copper electrodes, Aouina and co-workers[42] find

diffusion coefficients of 1.30-1.60×10^{-5} cm^2/s in various neutral electrolytes, and Reyter *et al.* have calculated this to be 2.00×10^{-5} cm^2/s in 0.1 M NaOH.[39]

Three reasons have been identified to account for the variation in calculated diffusion coefficients for all six electrocatalysts: i) the microscopic profile of the electrode surface(s) does not approximate a flat surface, and therefore the *diffusion zone* cannot be adequately described by planar diffusion (*i.e.* equation 6.3 is not completely valid). It is possible that rapid evaporation of the carrier solvent during electrode fabrication (Section 8.3.2) introduces microscopic faults, cracks or fissures in the carbon layer which, relative to the volume of the diffusion layer, are sufficiently large that planar diffusion is supplemented by other modes of mass-transport. Obviously, such features would be specific to each electrode; ii) migration effects (ionic gradient) can oppose diffusion effects (concentration gradient) when anions are undergoing reduction at cathodes,[1] and especially so at higher scan-rates which do not allow sufficient time for nitrate anions to adsorb to the electrode surface. Therefore, the mass-transport limited currents of nitrate reduction may not be fully described by diffusion alone, and a compensation may be needed to account for the counteracting effect of migration *away* from the electrode surface, which as before would be electrode specific; iii) the Nafion-117 polymer used to increase the electrical conductivity and the hydrophilicity of the carbon support may in fact repel nitrate anions to some extent, since the former possesses anionic sulfonate head-groups.[13] The permeability of Nafion-117 towards various anions, including nitrate and nitrite has been studied, and in general it is observed that the mobility of these species across Nafion-117 membranes is hindered compared to cations of comparable size.[330] Such a phenomenon would presumably affect the advance of nitrate anions towards the electrode surface, and increasingly so as the catalytically-active site is approached.

One anticipates no reason for all six catalysts to possess such mixed diffusion coefficients. It is this authors interpretation that although all electrodes may extract different mass-transport limited currents, these should still vary with scan-rate in a mutually-common way (since electrolyte composition and electrode surfaces are essentially identical) and therefore all j_p - $\upsilon^{1/2}$ plots *should* have similar gradients, irrespective of individual catalytic performance. In the absence of additional electrochemical data which may also provide a means to calculate D (*i.e.* electrochemical impedance spectroscopy), and for the purpose of further calculations, the values obtained herein are taken to be correct though it should be kept in mind that this result is unexpected and additional phenomena may be occurring.

6.3 – Reversibility of Nitrate Electroreduction

In this section, the relative reversibility (or irreversibility) of nitrate reduction at gold-phosphine cluster catalysts will be examined. First, it should be noted that *electrochemical* irreversibility carries an alternate meaning to the more commonly encountered *chemical* irreversibility: the latter means that one or more redox partners are removed from the electrode surface by a purely chemical reaction, and the former simply means that electron-transfer across an interface is somewhat sluggish.[331] The extent to which electron-transfer is hindered signifies the so-called "reversibility" of an electrochemical process, and is measured by several parameters including the electrochemical rate-constant k_0 and the charge-transfer resistance R_{ct}. However, electron-transfer is not the only phenomenon limiting the redox transformation of a particular species at an electrode surface: the compound itself must be delivered to the electrode surface by *mass-transport*, which is a linear combination of diffusion (concentration gradient), migration (ionic gradient) and convention (thermal gradient) effects and is collectively described by the parameter m_o.[1, 13, 16, 316]

6.3.1 *Comparison of Mass-Transport and Kinetic Effects*

The distinction between rapid and sluggish electrochemical kinetics is usually given by the prevailing rate of mass-transport (m_o) over electron-transfer (k_0) or *vice-versa*, wherein $k_0 >> m_o$ indicates electrochemical reversibility and the opposite case, $k_0 << m_o$, signifies electrochemical irreversibility. For $k_0 \approx m_o$ the term *quasi*-reversible is employed which describes electrochemical reactions intermediate of these extremes.[316] Thus, for reversible reactions the electron-transfer rate is, at all potentials, greater than the rate of mass-transport and therefore peak redox potentials are independent of scan-rate. In the case of *quasi*-reversible reactions, the rate of electron-transfer is comparable to the rate of mass-transport and peak redox potentials gradually shift with scan-rate (Figure 6.3). Finally, irreversible reactions possess electron-transfer rates which are significantly smaller than the rate of mass-transport, and peak redox potentials shift rapidly with scan-rate.[1, 316] There are different measures of electrochemical reversibility which have been developed from either theoretical or empirical approaches, or both. One of these is given by equation 6.14 which relates the mass-transport coefficient m_o of the species undergoing electrolysis to the diffusion coefficient D and the scan-rate υ during potential sweep measurements:

$$m_o = \left(\frac{DFv}{\mathcal{R}T}\right)^{1/2} \tag{6.14}$$

It should be noted that equation 6.14 predicts m_o varies with scan-rate (and therefore E), however D is strictly independent of v. Using values for D which have been previously determined in Section 6.4.9, the mass-transport coefficient for all six catalysts at 50 mV/s have been determined. These are tabulated and contrasted with average values for k_0 at the same scan-rate below:

Catalyst	**Au_6**	**Au_8**	**Au_8Pd_1**	**Au_9**	**Au_{11}**	**Au_{13}**
$\boldsymbol{k_0}$ (avg., $\times 10^{-3}$ cm/s)	6.18	8.07	6.73	6.91	8.76	6.49
$\boldsymbol{m_o}$ ($\times 10^{-3}$ cm^2/s)	1.79	5.22	5.69	3.03	7.45	11.14

Table 6.14 – Calculated values of the mass-transport coefficient m_o from equation 6.14, and average values of k_o from Sections 5.4.4 and 5.4.6 for all six carbon-supported gold catalysts at a scan-rate of 50 mV/s. Taken from cyclic voltammetry data collected in N_2-purged 0.1 M Na_2SO_4 after 10 cycles in the background electrolyte, with [NO_3^-] = 5 mM. Note that m_o is calculated from only one electrode for each catalyst.

Overall, values for k_0 are larger than m_o by a factor of between 1 and 3, *except* for Au_{13} where $m_o > k_0$. It is interesting that the latter result suggests nitrate reduction at Au_{13} is actually *irreversible* compared to all other catalysts. However, if one supposes that m_o is not exceedingly greater in magnitude than k_0 for Au_{13}, and k_0 is not excessively larger than m_o for the remaining five catalysts, it could be said that the electroreduction of nitrate is *quasi*-reversible, *i.e.* since $k_0 \approx m_o$. This is also complimented by the fact that peak electrolysis potentials for both nitrate reduction and nitrite oxidation are seen to shift with higher scan-rates, indicating the *quasi*-reversible case.[1] The present results therefore suggest that nitrate reduction is simply *less* reversible at catalysts containing Au_{13} clusters, and *vice-versa* for the remaining catalysts. Regrettably, this author could not find any reports in the literature which quantify the reversibility of nitrate electroreduction at a particular catalyst or electrode, and therefore no comparison to previous works are made in this section.

6.3.2 *The Matsuda-Ayabe Criteria for Electrochemical Reversibility and the ζ Parameter*

Matsuda and Ayabe[332] have suggested an alternative measure of electrochemical reversibility by introducing the dimensionless parameter ζ, given by equation 6.15:

$$\zeta = k_o \left(\frac{\mathcal{R}T}{FDv}\right)^{1/2} \tag{6.15}$$

Which is algebraically equivalent to an expression describing the ratio of k_o and m_o:

$$\zeta = \frac{k_o}{m_o} \tag{6.16}$$

Where Matsuda and Ayabe identify the following ranges corresponding to the reversibility of an electrochemical reaction: $\zeta \geq 15$ indicates full reversibility, $15 > \zeta > 10^{-3}$ indicates *quasi*-reversibility and $\zeta \leq 10^{-3}$ indicates total irreversibility.[316, 332] Values for the parameter ζ have been calculated from k_o and m_o and are tabulated below:

Catalyst	**Au_6**	**Au_8**	**Au_8Pd_1**	**Au_9**	**Au_{11}**	**Au_{13}**
ζ	3.44	1.54	1.18	2.27	1.17	0.58

Table 6.15 – Calculated values of the Matsuda-Ayabe parameter ζ as a measure of electrochemical reversibility for all six carbon-supported gold catalysts at a scan-rate of 50 mV/s. Taken from cyclic voltammetry data collected in N_2-purged 0.1 M Na_2SO_4 after 10 cycles in the background electrolyte (50 mV/s), with $[NO_3^-]$ = 5 mM.

Where all ζ clearly fall in the numerical range for *quasi*-reversible electrochemical reactions. Since ζ is simply a ratio of k_o to m_o, this metric follows the same size-dependent trend as that discussed in Section 6.5.1.

6.3.3 *The Nicholson-Shain Criteria for Electrochemical Reversibility and the ψ Parameter*

Nicholson and Shain[333, 334] have devised a method for establishing the relative reversibility of an electrochemical reaction by employing another dimensionless parameter ψ, which unifies the peak separation of a redox couple ΔE_p with the electrochemical rate-constant k_0 and the scan-rate v, given by relationship 6.17:

$$\psi = k_0 \left(\frac{\pi D n v F}{\mathcal{R}T}\right)^{-1/2} \tag{6.17}$$

At this point, it is worth mentioning that equation 6.17 may be employed as an alternative means to calculate k_0 for an electrochemical reaction upon consultation of a table which relates ΔE_p (at a given scan-rate) with ψ. Such a treatment of the data was attempted during this work, however calculated values of k_0 were found

to be in strong disagreement with Sections 5.4.4 and 5.4.6. This is attributed to the fact that many values of ΔE_p extracted from cyclic voltammetry data were not tabulated, and therefore ψ could not be accurately obtained. Furthermore, equation 6.17 is only valid for ΔE_p < *ca.* 200 mV,[333] a condition which was frequently exceeded at higher scan-rates (> 50 mV/s). Instead, the Nicholson-Shain relationship will be employed here as a measure of the electrochemical reversibility of nitrate reduction at 50 mV/s, where ΔE_p for all catalysts satisfy the above criterion. Values for ψ have been calculated and are tabulated below:

Catalyst	**Au_6**	**Au_8**	**Au_8Pd_1**	**Au_9**	**Au_{11}**	**Au_{13}**
ψ	1.38	0.62	0.47	0.91	0.47	0.23

Table 6.16 – Calculated values of the Nicholson-Shain parameter ψ as a measure of electrochemical reversibility for all six carbon-supported gold catalysts using values of D from Section 6.4.9. Taken from cyclic voltammetry data collected in N_2-purged 0.1 M Na_2SO_4 after 10 cycles in the background electrolyte (50 mV/s), with $[NO_3^-]$ = 5 mM.

Nicholson and Shain[334] identify the following conditions for electrochemical reversibility at a given scan-rate: Reversible processes will yield ψ > 7 where ΔE_p is independent of ψ, and irreversible processes will possess ψ < 0.001 where ΔE_p becomes increasingly large and the reverse peak may not be observed. *Quasi*-reversible cases will have ψ of an intermediate value which determines the peak separation ΔE_p. In agreement with earlier discussions of electrochemical reversibility, the data here clearly show that nitrate reduction in this work is *quasi*-reversible.

6.4 – Rate-Determining Step of Nitrate Electroreduction and the Current Function

In order to gain further understanding of electrode processes taking place during charge-transfer events, one can employ the *current function* to deconvolute mechanistic information from cyclic voltammetry data.[1] The current-functions for all six catalysts, $\frac{i_p}{v^{1/2}}$, are taken as a function of the scan-rate v and such plots are shown In Figure A.4 (Appendices). A smooth curve (dashed-line) is fitted to illustrate the relationship. Current-functions for all catalysts are seen to monotonously decrease with increasing scan-rate, typical for electrochemical reactions where a chemical step is coupled to an electron-transfer.[1, 316] Since the results of Tafel analysis indicated that the *first* electron-transfer during nitrate reduction is rate-limiting (*i.e.* n' = 1;

Section 6.2.5), it is therefore likely that any interposed chemical step is comparatively rapid and the nitrate-derived reagent (having acquired an additional electron) therefore be somewhat unstable. Evidence for this can also be extracted from values of $\alpha n'$, which for all catalysts was approximately 0.4. Note that the number of electrons transferred up-to and including the rate-limiting step for the reduction of nitrate to nitrite, n', must clearly be either 1 or 2. Ignoring the fact that the simultaneous tunnelling of more than one electron during heterogenous charge-transfer processes is – from a probabilistic viewpoint – unlikely,[317] is it rare that a value for α deviates significantly from *ca.* 0.5.[1, 13, 16, 21] Therefore, if n' is 2 then to satisfy these experimental observations α must be equal to *ca.* 0.2, which is somewhat low. It is therefore more reasonable that n' = 1 as this implies α is approximately 0.4, which is close to the commonly assumed value of 0.5. Dima *et al.* have studied nitrate reduction in acidic media using various transition metal electrodes and did find $\alpha n'$ to be approximately 0.5, based on which they suggested that the rate-limiting step is indeed the first electron-transfer to a nitrate anion (*i.e.* n' = 1).[36]

6.5 – Summary and Remarks

In this section, a kinetic analysis of cyclic voltammetry data collected for all six carbon-supported gold-phosphine cluster catalysts was performed. Parameters such as the electrochemical rate-constant (k_0), the charge-transfer resistance (R_{ct}), exchange-currents (i_0) and the charge-transfer coefficient (α) were extracted from a Tafel analysis, as was the observation that the rate-limiting step during nitrate reduction is the first electron-transfer. This was supported by the gradient of Laviron plots and by the magnitude of the shape-factor. Diffusion coefficients were found by employing the Randles-Sevcik relationship, and from this the *quasi*-reversibility of nitrate reduction was established by comparing mass-transport and kinetic effects, and by employing both the Matsuda-Ayabe and Nicholson-Shain measures of electrochemical reversibility. Current-functions for all six catalysts showed that a rapid chemical reaction is likely to be coupled with the first electron-transfer event. Two catalysts, namely those containing Au_8 and Au_{11} clusters, were consistently found to possess more favourable electrochemical characteristics during nitrate electroreduction in contrast to the 9-membered clusters Au_8Pd_1 and Au_9 and the diphosphine-protected clusters Au_6 and Au_{13}.

6.6 – Nitrate Reduction Mechanism

The total reduction of nitrate proceeds in a stepwise manner towards either NH_3 (eight electrons) or N_2 (ten electrons; a result of the wide range of formal oxidation states nitrogen may take, numerous products (*e.g.* NO_2, NO, N_2O, N_2, NH_2OH, NH_3) may be formed along several competing pathways. These are generally viewed as a sequence of successive discrete reactions, and mechanistic aspects have been discussed by others.[19, 32] It is almost universally-agreed that the rate-limiting (and most energetically-demanding) denitrification reaction is the two-electron reduction of nitrate to nitrite. In the following section, the reader will be presented with nitrate reduction mechanisms as a brief introduction to the discussion in Sections 6.6.2 and 6.6.3, critically arguing the possible nature of the electrocatalytically active species present at carbon-supported gold-phosphine clusters during nitrate electroreduction.

6.6.1 *Reaction Pathways and Mechanistic Considerations*

Fedurco *et al.*[335] have simulated the voltammetric response of several possible electrochemical mechanisms and compared these to experimental data for nitrate reduction at a silver electrode in 0.1 M $NaClO_4$; they propose a mechanism which follows an *ECE* sequence (electron-transfer, chemical reaction, electron-transfer) of the form:

$$O + e^- \rightarrow X \tag{6.18}$$

$$X \rightarrow Y \tag{6.19}$$

$$Y + e^- \rightarrow R \tag{6.20}$$

Where the reaction pathway is analogous to that which takes place during the photochemical reduction of NO_3^-.[336-339] In what is considered to be the rate-limiting step, the first electron-transfer to an adsorbed nitrate anion is believed to generate a short-lived and highly reactive $(NO_3^{\bullet})^{2-}$ dianion intermediate:

$$NO_3^- + e^- \rightarrow (NO_3^{\bullet})^{2-} \tag{6.21}$$

Which is then irreversibly consumed by a water molecule in a rapid chemical reaction:

$$(NO_3^{\bullet})^{2-} + H_2O \rightarrow NO_2^{\bullet} + 2OH^- \quad (6.22)$$

Followed by a second electron-transfer to generate the nitrite product:

$$NO_2^{\bullet} + e^- \rightarrow NO_2^- \quad (6.23)$$

The above reaction sequence has also been suggested by Fajerwerg *et al.*,[312] Korgel *et al.*[340] and Badea[38] who obtain similar kinetic results upon inspection of their cyclic voltammetry data to that herein. A disproportionation reaction involving the nitrogen dioxide radical produced in reaction 6.22 is also possible,[312, 335, 341] which may regenerate the original nitrate anion according to:

$$NO_2^{\bullet} + NO_2^{\bullet} + H_2O \rightarrow NO_3^- + NO_2^- + 2H^+ \quad (6.24)$$

Which would yield a one-electron reduction pathway, followed by a rapid chemical step giving an *EC* mechanism. Though possible, this sequence is not often encountered in the literature.[19] De *et al.*[314, 326] suggest an alternate reduction pathway in which electron-transfer is coupled with an adsorption process, indicated by a curiously-low value for α of *ca.* 0.2 and still consistent with an *ECE* mechanism. In their work, iridium-modified carbon-fibre electrodes were investigated for the electroreduction of nitrate in 1 M $NaClO_4$, and by taking n' to be 1 (alongside a detailed Tafel analysis of cyclic voltammetry data) they propose a rate-limiting step involving the formation of adsorbed hydrogen, *viz.*:

$$H_2O + e^- \rightarrow H_{(ads)}^{\bullet} + OH^- \quad (6.25)$$

Which then reduces the nitrate anion to nitrogen dioxide by oxygen abstraction in a chemical step:

$$NO_3^- + H_{(ads)}^{\bullet} \rightarrow NO_2^{\bullet} + OH^- \quad (6.26)$$

Followed by a second electron-transfer to generate the nitrite anion:

$$NO_2^{\bullet} + e^- \rightarrow NO_2^- \quad (6.23)$$

Katasunaros *et al.*,[48] Ambrosioni *et al.*[64] and Taguchi *et al.*[75] also find evidence for the formation of surface-bound hydride species during the reduction of nitrate at both Sn and Pt electrodes (implying the occurrence of reaction 6.25), however in these cases reduction *did* continue to N_2 *via* an unusual hyponitrite ($(NHO)_2^{2-}$) intermediate.

Notwithstanding the fact that nitrate reduction is highly dependent on electrochemical context,[18, 19] the mechanism itself is clearly very complex and there are conflicting theories in the published literature. The observations made in this work are consistent with a rate-limiting one-electron transfer, followed by a rapid chemical step which is presumably concluded by either a second one-electron transfer or a disproportionation reaction. It is however not possible with the present data to distinguish between these possibilities.

6.6.2 *Nitrate Electroreduction and the Catalytic Cycle of Carbon-Supported Gold-Phosphine Clusters*

It is interesting that nitrate reduction is apparently superimposed on the large cathodic wave already exhibited by gold-phosphine clusters at *ca.* + 0.6 - 0.7 V, indicating that gold nanostructures are acting electrocatalytically and reducing nitrate anions once they themselves are reduced by the external current or possibly *vice-versa*, *viz.*:

$$[Au_n]^z + 2e^- \rightarrow [Au_n]^{z-2} \tag{6.28}$$

$$[Au_n]^{z-2} + NO_3^- + H_2O \rightarrow [Au_n]^z + NO_2^- + 2OH^- \tag{6.29}$$

Where $[Au_n]^z$ represents an ensemble of n gold atoms either resembling a cluster or derived from a cluster, with an overall charge of z units and phosphine ligands omitted for simplicity. With the present experimental data, it would be difficult to deduce the order of this speculative mechanism with absolute certainty *i.e.* in what order the above reactions 6.28 and 6.29 may occur (*if* they occur), or indeed how the reverse reaction (nitrite oxidation) is accomplished. This uncertainty arises due to conflicting arguments about the nature of the nitrate reduction mechanism at bulk metal surfaces (*vide supra*; also including nanoparticles)[19] and whether this is supported by the Activated-Chemisorption (AC) model[324] which is thought to take place at Pt electrodes,[342] or the Incipient Hydrous-Oxide/Adatom Mediator (IHOAM) model[343] which has been suggested for Cu (Section 1.4.1).[38] At present, the reduction of nitrate by chemically-synthesised metal clusters (of any element) is largely unprecedented and therefore little information exists in the literature which can be directly applied to this work. Nevertheless, the IHOAM model may provide a deeper, if only speculative, understanding of the nature of the catalytically active site(s) at gold clusters during electrochemical reactions.

6.6.3 *The Incipient Hydrous-Oxide/Adatom Mediator Model of Electrocatalysis*

According to the IHOAM model, the *in-situ* oxidation of *adatoms* or *atoms in low coordination sites* on the surface of polycrystalline noble-metal electrodes leads to the conception of an active metal species which supplies or acquires electrons *via* interactions with dissolved oxidants or reductants, respectively.[344] During potential-sweep experiments (*e.g.* cyclic voltammetry), hydrous metal-oxide genesis takes place at adatom sites during the anodic-sweep at potentials *prior* to bulk-monolayer oxide formation.[295] Conversely, the active adatom is recovered from the hydrous-oxide during the cathodic sweep at potentials *before* bulk-gold oxide reduction. Regarding electrocatalysis, the IHOAM model proposes that for electrochemically-demanding processes, the oxidation of reductants at the electrode surface is mediated on the anodic-sweep by hydrous metal-oxides at potentials in the vicinity of their formation, whereas the reduction of oxidants during the cathodic-sweep commences in the region where hydrous-oxides are reduced to adatoms.[302] Both the hydrous-oxide and the active adatom may be regenerated by the external current, and this formal redox cycle (for gold) is illustrated in Figure 6.5 below:

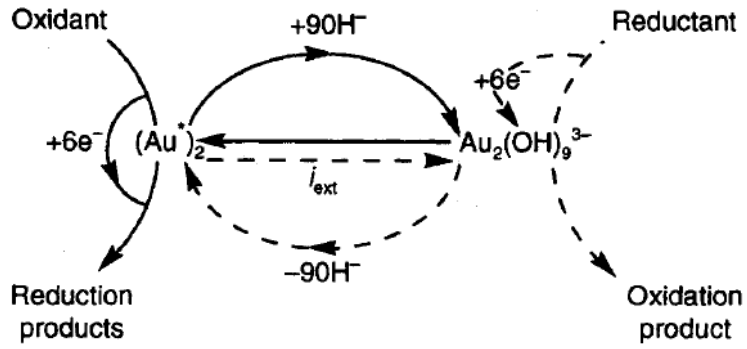

Figure 6.5 – Catalytic cycle proposed by the IHOAM model. The solid path follows the generation and subsequent action of a reduction catalyst (adatom, Au*), whilst the dashed path follows the generation and subsequent action of an oxidation catalyst (hydrous-gold oxide, $[Au_2(OH)_9]^{3-}$). Reproduced from Ref. 295 with permission from The Royal Society of Chemistry.

Details on the IHOAM model are given by Burke and colleagues,[268, 272, 295, 302, 343-350] and the reader is directed to these references for further discussion. The fundamental ideas of the IHOAM model have been outlined for Pt, Au and other noble-metal electrodes,[302, 345, 346, 348] and have been employed to explain the unexpectedly-high activity of polycrystalline Au electrodes for several electrocatalytic roles in *alkaline* media, including iodate and persulfate reduction,[346] and hydrazine,[345] glucose[347] and oxalic acid oxidation.[349] As small clusters of metal atoms could, at least in a hypothetical sense, recall adatom sites found on the exterior of bulk metal surfaces ("the cluster-surface analogy"), it is not unreasonable to suppose that the IHOAM model could also apply to electrochemical reactions involving these catalysts. In such a case, the question naturally arises as to

whether a *single* gold atom, or *several* gold atoms, or indeed the *entire* cluster is converted to an electrocatalytically active species at potentials in the region of so-called "pre-oxidation" (+0.9 - 1.1 V *vs.* NHE, *ca.* +0.7 - 0.9 V *vs.* Ag/AgCl for polycrystalline Au). The fact that the presence of dissolved nitrate exaggerates the native cathodic wave at *ca.* + 0.6 - 0.7 V may indicate the nitrate-to-nitrite conversion is catalysed by the oxidation of active gold adatoms (Au* in Figure 6.5; constituting clusters) to hydrous gold-oxides ($[Au_2(OH)_9]^{3-}$), which are then *immediately* reduced to a pre-oxidation state by the external current. Likewise, nitrite oxidation is observed to take place within the same potential window on the reverse scan. Burke *et al.*[346] note that a direct voltammetric response to the adatom/hydrous-oxide redox cycle is difficult to detect since coverages are typically quite low (< 0.1% of surface atoms are estimated to be in, or may readily attain, an adatom state[302, 346]), however such a process is amplified when the couple participates in an electrocatalytic manner. Cyclic voltammetry data collected in 0.1 M Na_2SO_4 (Figure 5.1) showed a prominent cathodic wave at *ca.* + 0.6 - 0.7 V *vs.* Ag/AgCl, which nicely corresponds to the potential window where the reduction of hydrous gold-oxides is purported to take place.[268, 272, 295, 345] Moreover, cyclic voltammetry data collected in the presence of 5 mM $NaNO_3$ (Figure 6.1) finds that this cathodic wave – in addition to experiencing a significant growth in measured current – is also observed to shift to slightly more-positive potentials as NO_3^- anions are reduced, typically about 50 mV for all catalysts (Table 6.17).

Catalyst	**Au_6**	**Au_8**	**Au_8Pd_1**	**Au_9**	**Au_{11}**	**Au_{13}**
$\boldsymbol{E_{p,c([Au_2(OH)_9]^{3-})}}$	+0.686V	+0.667V	+0.721V	+0.702V	+0.635V	+0.695V
$\boldsymbol{E_{p,c(NO_3^-)}}$	+0.742V	+0.717V	+0.774V	+0.749V	+0.679V	+0.744V
$\boldsymbol{\Delta E}$	+56mV	+50mV	+53mV	+47mV	+44mV	+49mV

Table 6.17 – Average potential shifts ($\boldsymbol{\Delta E}$) of the cathodic wave exhibited by carbon-supported gold-phosphine clusters (at *ca.* + 0.6 - 0.7 V; $\boldsymbol{E_{p,c([Au_2(OH)_9]^{3-})}}$) upon the addition of 5 mM NO_3^- ($\boldsymbol{E_{p,c(NO_3^-)}}$) in N_2-purged 0.1 M Na_2SO_4, at a scan-rate of 50 mV/s.

Which agrees with similar cyclic voltammetry studies[343, 344] wherein reduction reactions catalysed by polycrystalline Au electrodes are believed to commence at the *onset* of the hydrous-oxide reduction region (note however that nitrate reduction shifts this peak to more-negative potentials at AuNPs – an explanation for which this author regrettably cannot offer). Of course, this would imply that reaction 6.29 precede reaction 6.28 in the sequence above, whereby the nitrate anion *oxidises* an Au adatom(s) in a rate-limiting *one-electron* step (to remain consistent with experimental findings in Section 6.6) yielding a $(NO_3^{\bullet})^{2-}$ radical as per reaction

6.21, followed rapidly by reaction 6.22. Noteworthy is that reaction 6.22 generates hydroxide ions at the electrode surface, which are required to generate the hydrous-oxide $[Au_2(OH)_9]^{3-}$ and explains why the electrocatalytic activity of polycrystalline Au electrodes is generally greatest in *alkaline* media.[268, 272, 295] If one supposes that the active Au adatom(s) on the cluster exterior initially resided in a +1 oxidation state (a reasonable assumption during nanocluster-mediated catalysis[219, 351]) this would, presumably, generate a Au^{2+} species which donates a second electron to accomplish reaction 6.23 and form the nitrite product. This is not to discount the possibility of the alternate reaction mechanism (reactions 6.25 → 6.26 → 6.23) involving a rate-limiting discharge of water molecules to form adsorbed hydrogen; this author acknowledges that gold nanoclusters are predicted to chemisorb atomic hydrogen,[352-354] and have experimentally been shown to act as competent hydrogenation catalysts.[355-358] The cyclic voltammetry data collected herein, underneath a IHOAM interpretation of noble-metal electrocatalysis, could simply offer an interesting perspective for explaining the activity of small gold clusters for nitrate electroreduction.

The IHOAM model was developed to explain the unexpected electrocatalytic activity of bulk gold electrodes for certain oxidation reactions in alkaline media (*vide supra*), as according to the Activated-Chemisorption (AC) model gold should be a universally-poor electrocatalyst due to full occupancy of the *d*-orbital band.[165] The AC model, under certain conditions, is regarded as being deficient rather than incorrect,[345] and has difficulty explaining not only aspects of electrocatalysis at Au electrodes but also at Pt *e.g.* mechanistic features of methanol oxidation.[359] Confusingly, the AC model is a perfectly valid approach for explaining the *inactivity* of polycrystalline Au electrodes for nitrate reduction: the adsorption of nitrate to electroactive sites on the electrode surface is necessary for reduction to occur,[23, 24, 360] and is an oft-cited explanation for the inactivity of bulk gold (including nanoparticles) for *this* particular reaction.[22, 36] However, gold nanoclusters – which have properties that deviate strongly from metallic behaviour – *do* permit the adsorption and chemical activation of small molecules:[171] Superatomic orbitals within the electronic structure of the cluster may be of corresponding energy, symmetry, directionality or occupancy to interact with the relevant frontier molecular orbitals of substrate molecules. Moreover, asymmetric geometries akin to defect-like structures may result in an uneven distribution of electron-density over the surface of the cluster, forming complimentary Lewis acid/base sites that promote chemisorption and accelerate reactivity.[231] Such a process obviously depends on the correct geometric spacing between adsorption sites (*i.e.* gold atoms), however the principle has been

demonstrated at an atomic level for the gold nanocluster-catalysed activation of functional groups during alkyne semihydrogenation,[356] coupling reactions,[361] alkene epoxidation[362] and carbonyl hydrogenation.[358] Recall that the non-zero vertical-axis intercept of j_p *vs.* $v^{1/2}$ plots (Section 6.4.1) is evidence for an adsorption process prior to electron-transfer. Therefore, due to the unique electronic and geometric effects enjoyed by small gold clusters, chemisorption effects cannot be ruled out as a possible step in the catalytic pathways provided in Section 6.8.2. This process is only omitted from the speculative reaction sequence for simplicity. Instead, the reaction sequences 6.28 and 6.29 are included for a conceptual illustration of a catalytic process that could be taking place, which is consistent with experimental data whereby small clusters of gold atoms are able to reduce nitrate anions *via* an external electric circuit.

6.6.4 *Summary and Remarks*

Though atomically-precise clusters are themselves useful models for elucidating heterogeneous reaction mechanisms,[172, 363] the present experimental results *do* require further clarification. Any mechanism given here is only speculative and is drawn directly from models used to describe the nature of *bulk gold* electrocatalysis. Such information may be found from *in-situ* FT-IR studies to determine favourable binding modes between gold clusters and nitrate anions or uncover the presence of surface-bound hydride species, which could also be complimented by computational modelling. It was noted that electrodes formally containing the Au^+ cation ($AuPPh_3Cl$) were also active for nitrate reduction, and this could be evidence for the catalytic role of (partially) oxidised gold adatoms. The fact that small gold clusters could be viewed as an ensemble of adatoms, where nearly all constituent atoms occupy the surface of the cluster and are therefore available for hydrous-oxide formation, may be useful for further elucidating the nature of such species during charge-transfer reactions and could be used to support the IHOAM theory of electrocatalysis. Irrespective of the exact mechanism by which gold-phosphine clusters facilitate the electroreduction of nitrate, the preliminary findings of this work strongly suggest that such compounds do indeed perform a catalytic role in this process. To the best of this authors knowledge, this is the first example of nitrate electroreduction and nitrite electrooxidation catalysed by chemically-synthesised gold clusters. Furthermore, this is the first known example where the IHOAM model has been applied to explain the electrocatalytic activity of such compounds; no reports exist in the literature which investigate the IHOAM model beyond metallic surfaces.

6.7 – Ranking of Carbon-Supported Gold-Phosphine Clusters for Nitrate Electroreduction

In this section, each catalyst will be ranked based on the parameters of electrocatalytic performance identified and calculated earlier in this chapter. These include: activation-overpotential for nitrate reduction (η – Section 6.1.1); voltammetric response to nitrate (Δj (cathodic and anodic) – Section 6.1.1); exchange-current (i_0– Section 6.4.5); diffusion coefficient (D – Section 6.4.9); charge-transfer resistance (R_{ct}– Section 6.4.7) and electrochemical rate-constant (k_0 – Sections 6.4.4 and 6.4.6). These are tabulated below in order from 1-6, wherein 1 signifies the best performer and 6 the poorest in that category.

Rank	**1**	**2**	**3**	**4**	**5**	**6**
$\boldsymbol{\eta}$	Au_8Pd_1	Au_9	Au_6	Au_{13}	Au_8	Au_{11}
$\boldsymbol{\Delta j}$ (cathodic)	Au_{11}	Au_8	Au_9	Au_6	Au_8Pd_1	Au_{13}
$\boldsymbol{\Delta j}$ (anodic)	Au_{11}	Au_6	Au_9	Au_8	Au_8Pd_1	Au_{13}
$\boldsymbol{i_0}$	Au_{11}	Au_8	Au_9	Au_{13}	Au_8Pd_1	Au_6
$\boldsymbol{D}$	Au_{13}	Au_9	Au_{11}	Au_8Pd_1	Au_8	Au_6
$\boldsymbol{R_{ct}}$	Au_{11}	Au_8	Au_9	Au_{13}	Au_8Pd_1	Au_6
$\boldsymbol{k_0}$ (avg.)	Au_{11}	Au_8	Au_9	Au_8Pd_1	Au_{13}	Au_6

Table 6.18 – Relative ranking of all gold-phosphine cluster catalysts when employing the measures of electrocatalytic activity for nitrate reduction (in N_2-purged 0.1 M Na_2SO_4) identified in this work. Rankings are correct at a 50 mV/s scan-rate.

Generally, Au_6 and Au_{13} are found to be the poorest-performing catalysts, and Au_{11} and Au_8 the greatest. Au_8Pd_1 and Au_9 are found to have moderate activity when ranked by the above criteria. Inspection of the above data finds an overarching structural pattern whereby, in general: *monophosphine-protected clusters* > *diphosphine-protected clusters* and *spherical clusters* > *oblate clusters* > *prolate cluster* (though Au_{13}, which this author notes is spherical, is one of the least active catalysts and diverges from the latter trend). This could be evidence for a geometric effect, and might be related to the ability of nitrate to adsorb to the gold-cluster itself (spherical clusters generally possess shorter Au-Au bond-lengths,[219] which may simply present a more favourable chemisorption site for nitrate anions or atomic hydrogen), or it could be a stability effect wherein

spherical and oblate clusters (in this work) possess an interstitial gold atom which (as previously mentioned in Section 2.4) greatly enhance the rigidity of the cluster-core. The apparent ligand effect can be explained by the higher binding-strength of diphosphine ligands to the gold core, which may either i) impede nitrate adsorption; ii) require greater energy to dissociate or iii) do not expose active gold atoms to the electrolyte compared to a monophosphine ligand. It is also noteworthy that the addition of a Pd atom to an Au_8 cluster, or the replacement of an Au atom for a Pd atom in Au_9 to give Au_8Pd_1 results in an overall decrease in electrocatalytic performance (compared to the activities of Au_8 and Au_9). The reason for this is uncertain, however the introduction of a Pd atom to the Au_9 cluster is known to stiffen the gold-skeleton and prevent the reversible isomerisation (crown ⇌ butterfly) normally observed by the latter.[253] A more-rigid cluster framework may hinder phosphine ligand dissociation, or it may be due to electronic reasons whereby a Pd atom contributes less electron-density to superatomic orbitals and nitrate anions cannot be activated as effectively upon chemisorption. Clearly, each of the gold-phosphine clusters used in this work possess varying electrocatalytic activity and the reasons for this could arise from geometric or electronic effects, or a combination of both, and warrants further study.

6.8 – Possible Explanation of Electrocatalytic Activity Trend

Finally, this author would like to draw attention to an interesting correlation between the electrochemical gap of gold-phosphine clusters (ΔE_g – Chapter 4) with trends in catalytic activity, as measured by both the cathodic and anodic responses to nitrate (Δj – Section 6.1.1). This is given in Figure 6.6.

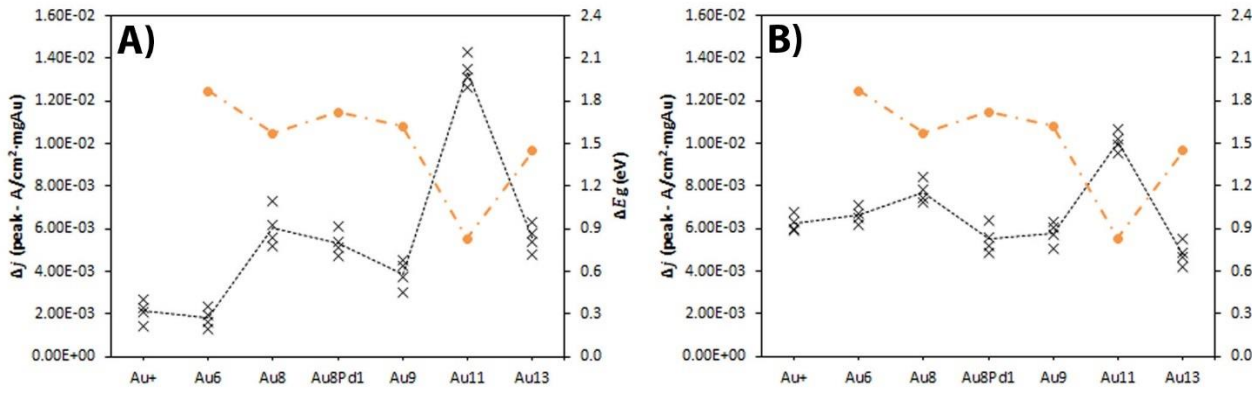

Figure 6.6 – Possible correlation between the electrochemical gap (ΔE_g – orange circles, right axis) of gold-phosphine clusters (in 0.1 M Bu_4NPF_6/CH_2Cl_2) and the voltammetric response to nitrate (Δj – black crosses, left axis) of carbon-supported gold-phosphine clusters (four electrodes, 50 mV/s in N_2-purged 0.1 M Na_2SO_4) for A) NO_3^- reduction and B) NO_2^- oxidation after 10 previous cycles in the background electrolyte (50 mV/s). Dashed-lines are included to illustrate the apparent relationship between these parameters across the range of clusters investigated in this work. ΔE_g for $AuPPh_3Cl$ was not measured.

Where, in general, larger voltammetric responses to both nitrate and nitrite are exhibited by clusters with smaller electrochemical gaps. For instance, Au_{11} possess the lowest ΔE_g and extracts the largest nitrate reduction and nitrite oxidation currents – conversely, Au_6 has the greatest ΔE_g and (using Δj as the sole metric) is the poorest performing electrocatalyst. The clusters Au_8, Au_8Pd_1, Au_9 and Au_{13} possess similar electrochemical gaps and a comparison between these four data sets finds that Δj is comparable for these catalysts, with a slight decrease in current response as ΔE_g increases across the Au_8 – Au_8Pd_1 – Au_9 triad and towards Au_{13}. The apparent inverse-proportionality between ΔE_g and Δj is more obvious in nitrite oxidation data, possibly because mass-transport effects are somewhat diminished (since nitrite is produced from the preceding reduction of nitrate) and is therefore already in proximity to the electrode surface. Moreover, the present correlation also extends to other measures of catalytic activity, such as the charge-transfer resistance R_{ct} of electrodes determined in Section 6.2.7. Recall that R_{ct} is indicative of the physical opposition to a charge-transfer event across electrode-electrolyte interface,[1] whereas ΔE_g signifies the energy penalty for transporting one electron through the cluster during a hypothetical charge-transfer role.

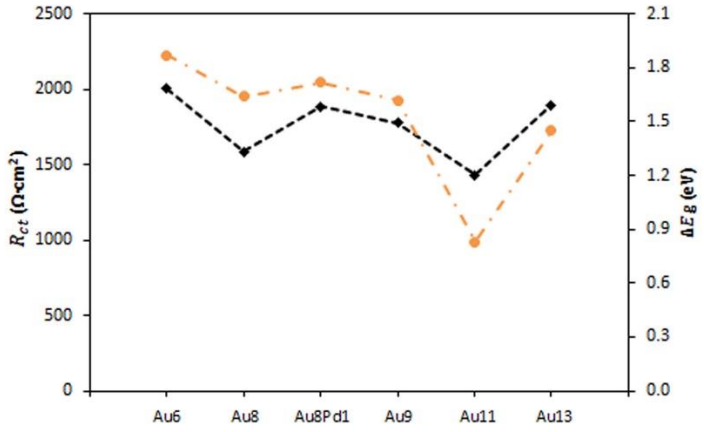

Figure 6.7 – Possible correlation between the electrochemical gap (ΔE_g – orange circles, right axis) of gold-phosphine clusters (in 0.1 M Bu_4NPF_6/CH_2Cl_2) and the charge-transfer resistance (R_{ct} – black diamonds, left axis) of carbon-supported gold-phosphine clusters (four electrodes, 50 mV/s in N_2-purged 0.1 M Na_2SO_4) after 10 previous cycles in the background electrolyte (50 mV/s). Dashed-lines are included to illustrate the apparent relationship between these parameters across the range of clusters investigated in this work.

Where, in general, lower charge-transfer resistances are attained by clusters with correspondingly small electrochemical gaps, which is a rather pleasing result and could account for the greater than expected catalytic activity of Au_{11} compared to other clusters. In the present experimental context, the electrochemical gap can be interpreted in two different ways: i) since ΔE_g contributes to the energy difference between the first reduction and first oxidation events in electrochemical spectra, it can be thought of as the energy demand to

transport a *single* electron through the cluster itself (*i.e.* the energy required to oxidise the compound then immediately reduce it to a pre-oxidation state, or *vice-versa*), provided a correction is made for the *charging energy* (since the oxidised cluster will have a different electron affinity to the reduced version and *vice-versa*). For this reason, the electrochemical gap is often called the *charge-transfer barrier.*[144, 184] It is plausible that a cluster with a greater charge-transfer barrier will therefore experience a greater difficulty mediating electrocatalytic reactions (permitting the thoroughfare of reactant electrons), and might give rise to greater values of R_{ct} as observed in Figure 6.7; ii) on the other hand, it is known that gold nanoclusters with smaller HOMO-LUMO gaps are generally less-stable (in both kinetic and thermodynamic terms) than clusters with larger HOMO-LUMO gaps.[178, 184, 231] Since the electrochemical gap/charge-transfer barrier is *directly* related to the HOMO-LUMO gap (by difference of the charging energy, which is typically on the order of *ca.* 300 mV for most gold nanoclusters), it therefore stands that ΔE_g is also indicative of cluster stability. If the IHOAM model correctly accounts for the electrocatalytic activity of small gold clusters for nitrate reduction, then it is expected that a less-stable cluster will undergo the hydrous-oxide/adatom redox cycle with greater ease since cluster fragmentation is more facile. This must presumably occur to generate the incipient hydrous-oxide species, $[Au_2(OH)_9]^{3-}$. Hence, clusters that are easily fragmented upon electrochemical treatment will generate a greater quantity of electrocatalytically active adatoms/hydrous-oxides and deliver larger electrolysis currents, as proposed in Figure 6.6.

This author acknowledges that both interpretations give somewhat conflicting accounts of the nature of the catalytically-active species: the first point above implies that the gold-phosphine cluster remains intact during both electrochemical cycling and heterogeneous charge-transfer, otherwise the concept of an electrochemical gap cannot apply if the molecular-structure of the cluster is disrupted, whereas the second point would require some form of cluster disintegration to allow the formation (and subsequent reduction) of hydrous gold-oxide species to mediate the nitrate/nitrite redox cycle. With the present experimental data, it is impossible to confidently differentiate between these possibilities. In either case, the relationship between ΔE_g and electrocatalytic activity in Figures 6.6 and 6.7 could (if true) have wider implications for electrocatalysis mediated by small gold clusters, namely either interpretation would seem to suggest that a cluster of eleven gold atoms would be a more active electrocatalyst (compared to other clusters investigated in this work) *for any electrocatalytic reaction* (under comparable experimental conditions). Such a realisation would be both a

remarkable and unprecedented hypothesis in the scientific literature, and unquestionably warrants further investigation with a much larger range of gold nanoclusters and electrochemical reactions.

6.9 – Summary and Remarks

In this chapter, the electrocatalytic reduction of nitrate by carbon-supported gold-phosphine clusters has been examined. A kinetic analysis of cyclic voltammetry data yielded several metrics of electrocatalytic activity which showed in a consistent fashion that the clusters $[Au_{11}(PPh_3)_8Cl]^+$ and $[Au_8(PPh_3)_8]^{2+}$, supported on Vulcan carbon, were more active for nitrate electroreduction than other clusters examined in this work. The clusters $[Au_6(dppp)_4]^{2+}$ and $[Au_{13}(dppe)_5Cl_2]^{3+}$ were found to possess the lowest activity and the nine-membered clusters $[Au_8Pd_1(PPh_3)_8]^{2+}$ and $[Au_9(PPh_3)_8]^{3+}$ intermediate performance. It was hypothesised that these clusters exhibited greater catalytic activity for charge-transfer reactions on the basis of the electrochemical gap (ΔE_g), where performance was inversely related to the magnitude of this parameter. A mechanistic interpretation of cyclic voltammetry data showed that the rate-limiting step for the two-electron reduction of nitrate to nitrite was the first electron-transfer, and this was likely followed by a rapid chemical reaction interposed between a second electron-transfer, giving an *ECE* mechanism. The peak potential of nitrate reduction, which was observed to overlap with a large cathodic feature exhibited by these catalysts in the absence of nitrate, lead to the hypothesis that the active site for this transformation could be described by the Incipient Hydrous-Oxide/Adatom Mediator model, wherein electrochemical reactions are mediated by a redox cycle involving coordinatively-unsaturated metal atoms. In the scientific literature, such a model has not yet been applied to describe the action of gold nanoclusters during electrocatalytic processes.

Chapter 7

Electrochemical Sensing of Nitrate by a Carbon-Supported Gold-Phosphine Nanocluster

7.1 – Electrochemical Sensing of Nitrate by a Carbon-Supported Gold-Phosphine Nanocluster using Cyclic Voltammetry

In this section, the amperometric sensing of nitrate has been investigated using cyclic voltammetry where carbon-supported Au_{11} was chosen as the best-performing catalyst for this purpose, following the results gathered in Chapter 6. A typical voltammogram collected in 0.1 M Na_2SO_4, at a scan-rate of 50 mV/s with a $NaNO_3$ concentration ranging from 1-10 mM is shown in Figure 7.1 Panel A, with the corresponding current response to the nitrate anion shown in Panel B.

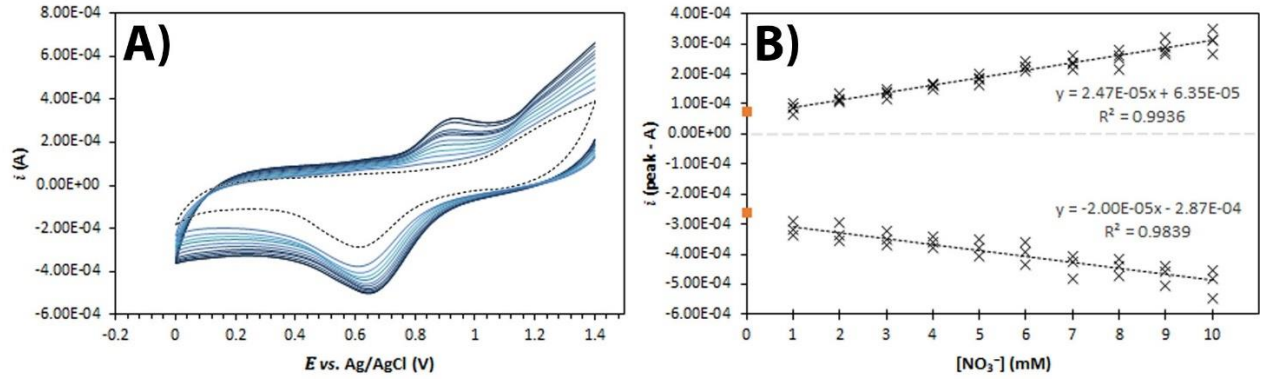

Figure 7.1 – Amperometric sensing of nitrate by cyclic voltammetry with carbon-supported Au_{11} clusters, in N_2-purged 0.1 M Na_2SO_4 at a scan-rate of 50 mV/s and $NaNO_3$ concentration of 1-10 mM (from light to dark blue – Panel A). Electrodes had previously undergone 10 cycles in the background electrolyte, and the tenth cycle is shown in dashed-black. Panel B shows the linear correlation between measured peak current (i_p) and nitrate concentration. Three separate electrodes were examined, and the average current response used to produce the linear relationship (dashed-black line). Orange data points are the measured current with no added $NaNO_3$, and currents have been normalised with respect to the mass of carbon catalyst applied.

Due to time constraints, only three separate electrodes were examined and for this reason it was not possible to estimate errors with any statistical certainty, hence the exclusion of this information in Figure 7.1. Nevertheless, a good linear response over the range 1-10 mM (62 – 620 ppm) is obtained by CV for the nitrate anion, and likewise for nitrite on the reverse anodic scan. In fact, a satisfactory linear response held until at least 25 mM (1550 ppm; parallel experiment with one electrode, not shown). Although this level of nitrate in an authentic freshwater sample is unlikely to be encountered by the analyst,[4] the impressive upper bound on the linear range should not be ignored. Regrettably, the lower bound on this linear range proved difficult to establish, since < *ca.* 0.5 mM (31 ppm) the peak cathodic signal could not be reliably distinguished above the background (blank) current. One also finds that the gradient of the linear current response in Figure 7.1, Panel B is greater for nitrite oxidation. That is to say, the *analytical sensitivity* of the catalyst towards nitrite (2.47×10^{-5} A/mM NO_3^-) is about 25% greater than the sensitivity of the catalyst towards nitrate (-2×10^{-5} A/mM NO_3^-); note this parameter is given with respect to the concentration of *nitrate* since the

surface-concentration of *nitrite* at the electrode surface (or indeed, in solution) is unknown. Of course, the amount of nitrite at the electrode surface undergoing oxidation should be approximately equal to the quantity of nitrate that had been reduced prior (though it will not be exactly equal since diffusion effects will remove some nitrite from the electrode surface in the time since it is produced). With this in mind, one may tentatively estimate the sensitivity of the catalyst towards nitrite to be *ca.* 2.5×10^{-5} A/mM NO_2^-. Additional experiments parallel to those herein could establish a more accurate value for this parameter. It should be mentioned that values of α (the charge-transfer coefficient; Section 6.2.2) which lie below 0.5 imply that oxidation reactions are preferentially accelerated at the electrode surface.[1] Since this value was calculated to be *ca.* 0.4 (for Au_{11}) this could be further evidence for a slightly greater sensitivity of the catalyst towards nitrite, compared to nitrate. This is in line with other studies[364-368] – many of which are not confined to an electrochemical setting, where gold nanoparticles are generally found to be potent oxidation catalysts.

In New Zealand, the MAV set by the Ministry of Health for nitrate in drinking water is 50 ppm,[11] in accordance with World Health Organisation recommendations and in line with other nations including Australia[369] and European Union member states.[370] It is disappointing that, below 1 mM concentrations of NO_3^- (62 ppm), the cathodic current response was difficult to distinguish above the background current by CV. By comparison, a simple Cu/Ni alloy electrode (70:30 by atom) is reported to attain a detection limit of *ca.* 20 μM (*ca.* 1.2 ppm) by CV.[371] The possibility that nitrate reduction currents are small because the concentration of NO_3^- at the electrode surface ($C_{NO_3^-}(0,t)$; Section 1.2) under mass-transport limited conditions is smaller than the concentration of Au_{11} clusters on the carbon support can be ruled out: the former is calculated to be on the order of *ca.* 10^{20} anions/cm^2 (at 1 mM bulk concentration) and the latter *ca.* 10^{13} clusters/cm^2 (at 10 wt.% metal loading). This author cannot offer a reasonable physiochemical explanation for the comparatively high limit of detection, when compared to other published nitrate sensing platforms[137-139, 371, 372] which frequently achieve μM-performance. Perhaps it is the case that the potentiostat employed in this work could not measure such small changes in reduction currents, whereas others[136, 148, 373] have employed much more sophisticated instruments with far greater current-resolutions.

This author would, however, like to reiterate that CV is not usually the preferred electroanalytical technique for measuring the concentration of analytes in solution; as outlined in Section 4.1, differential-pulse voltammetry may extract amperometric data with far greater sensitivity by experiment design. Such an

approach was attempted in this work, and typical differential-pulse voltammograms are shown in Figure A.5 (Appendices), however unfortunately no analytically-useful signal could be located in the potential window where nitrate reduction was believed to take place (*ca.* +0.7V). Instead, a prominent reduction wave was found at *ca.* +1.1V (which in retrospect could be evidence for the reduction of gold-oxides) and a broad wave at *ca.* +0.3V which grew considerably with successive measurements. Notably, the large cathodic wave observed in CV experiments that *could* be attributed to the reduction of hydrous gold-oxides (in the absence of nitrate, that is; Section 5.2.2) is completely non-existent in DPV profiles. Likewise, during the positive-going scan a noticeable oxidation wave is situated at *ca.* +1.2V which, again, may be an indication of gold-oxide formation in contrast to the hypothesis put forward in Section 5.2.2 that gold clusters intrinsically resist electrochemical oxidation when deposited on solid supports.

This is a peculiar finding since charge-transfer events should, in principle, become *more visible* in DPV due to a greatly improved signal-to-noise ratio (compared to CV).[372] Despite adjusting all possible experimental parameters, attempts to optimise this process were frustratingly unsuccessful and these signals could not be observed with any appreciable resolution. In fact, it appeared that the entire background current (for both positive- and negative-going scans) simply grew with $NaNO_3$ concentration (albeit in a non-linear fashion) which did not occur in the absence of nitrate during a parallel experiment. Narrowing the potential window to $+0.7 \pm 0.3$ V, under the working assumption that electrolysis events were poorly resolved because large differential currents near 0 V and +1.4 V heavily dictated the scale of the vertical-axis, was similarly unsuccessful at detecting nitrate by DPV.

Nevertheless – for completeness, and to evaluate the performance of this sensing platform under authentic environmental conditions, a water sample was collected from the Okeover stream (University of Canterbury Christchurch campus) and this matrix was spiked with $NaNO_3$ concentrations ranging from 1-10 mM and the current response measured by CV. For practical reasons, to this sample was also added an appropriate amount of solid Na_2SO_4 (to achieve a 0.1 M concentration). Without this supporting electrolyte the matrix was not sufficiently conductive for electroanalytical experiments and a large amount of noise was generated in CV profiles. No sample preparation was performed other than the addition of Na_2SO_4 above, followed by centrifugation and filtration through a 0.22 μm membrane filter-cartridge to remove any suspended organic solids or particulate. Samples were kept in amber-glass bottles at *ca.* 4 °C until required, although sensing

experiments were performed within *ca.* 3 hours of sample collection. The results of this are shown in Figure 7.2 (note that in this case, the sample matrix was not purged with N_2).

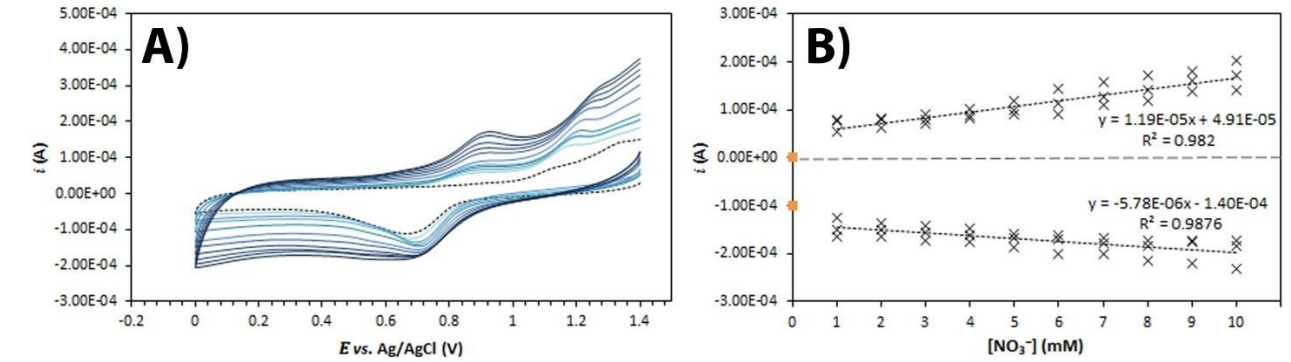

Figure 7.2 – Amperometric sensing of nitrate by cyclic voltammetry with carbon-supported Au_{11} clusters in a real water sample, with artificial nitrate concentrations of 1-10 mM (light to dark blue, Panel A), and 0.1 M Na_2SO_4 added. The solution was not purged with N_2 before measurements were taken. Electrodes had previously undergone 10 cycles in the background electrolyte, and the tenth cycle is shown in dashed-black. Panel B shows the linear correlation between measured peak current (i_p) and nitrate concentration. Three separate electrodes were examined, and the average current response used to produce the linear relationship (dashed-black line). Orange data points are the measured current with no added $NaNO_3$, and currents have been normalised with respect to the mass of carbon catalyst applied.

Overall, the sensing of nitrate by carbon-supported Au_{11} clusters using CV in a real environmental matrix under the ambient atmosphere gives an acceptable linear response over the range 1-10 mM (62-620 ppm). It is immediately apparent that lower sensitivities are extracted however, for both nitrate reduction and nitrite oxidation compared to parallel experiments in synthetic matrices under N_2. Due to time constraints it was regrettably not possible to establish which, if any, environmentally-relevant species would interfere with nitrate sensing. Therefore, it is not possible at present to establish the physiochemical reason for this lowered sensitivity, nor is it possible to attribute this to any one interfering compound(s). Similar to previous experiments (Figure 7.1), $NaNO_3$ concentrations below *ca.* 0.5 mM failed to produce cathodic currents that were reliably discernible above the blank signal. It is also interesting that in the presence of dissolved oxygen, gold-oxide formation is visible at *ca.* +1.2 V whereas under N_2 this did not appreciably occur at all, even up to 100 electrochemical cycles. Therefore, small gold clusters may actually be rather straightforward to oxidise in these conditions, in contrast with observations made in above and in Section 5.2.2. Nonetheless, the above data in Figure 7.2 clearly shows that this platform retains catalytic activity for nitrate reduction and nitrite oxidation in an authentic sample matrix, which is promising for further development of this platform. Whether this activity diminishes more rapidly in the presence of dissolved oxygen remains to be seen and is a clear avenue for future work.

7.3 – Summary and Remarks

In this chapter, the electrochemical sensing of nitrate by carbon-supported Au_{11} has been briefly investigated. Cyclic voltammetry experiments showed that a good linear relationship between peak current and nitrate concentration could be attained over the range 1-10 mM (62-620 pm), which remained until levels as high as 25 mM (1550 ppm). Unfortunately, below *ca.* 0.5 mM nitrate reduction signals could not be confidently distinguished from the background current, which admittedly does yield a comparatively high limit of detection for this sensing platform. However, since the MAV for NO_3^- in New Zealand drinking water is 50 mg/L (50 ppm), is it feasible that with further development this platform could be used, in the very least, as a pass/fail-type device for water quality assessment. Promising for this application is the fact that, despite an overall decreased sensitivity, a linear relationship between peak nitrate reduction current and nitrate concentration could still be attained in real freshwater samples. Future work should pursue with optimising pulse-voltammetry techniques such as DPV, or perhaps an alternative electroanalytical method, to improve the somewhat disappointing detection limit of *ca.* 1 mM (62 ppm) for NO_3^- and extend these advances to electrochemical NO_2^- sensing.

7.4 – Conclusion

In this work, several carbon-supported atomically-precise gold and silver nanoclusters have been prepared and characterised, and their electrocatalytic activity towards nitrate electroreduction has evaluated qualitatively and quantitively, with the overarching aim to evaluate their potential as candidates for an electrochemical nitrate sensor in aqueous matrices. These materials were subsequently found to display measurably different efficacies for this objective.

In Chapter 4, the non-aqueous electrochemical behaviour of these six gold-phosphine clusters was investigated by differential-pulse voltammetry. All six nanoclusters were found to undergo a reversible two-electron reduction process which presumably led to geometric isomerisation based on established electron-counting principles. Oxidation was irreversible for all compounds and this likely lead to rapid cluster decomposition. The potential-spacing of the first reduction and first oxidation events has been used to calculate the

electrochemical gap ΔE_g for all clusters, which conceptually represents the energy required to transport one electron through the cluster in a hypothetical charge-transfer role. Good agreement was found for three clusters ($[Au_8(PPh_3)_8]^{2+}$, $[Au_8Pd_1(PPh_3)_8]^{2+}$ and $[Au_9(PPh_3)_8]^{3+}$) to that previously reported in the literature. The remaining clusters, namely $[Au_6(dppp)_4]^{2+}$, $[Au_{11}(PPh_3)_8Cl_2]^{+}$ and $[Au_{13}(dppe)_5Cl_2]^{3+}$ have not yet had their non-aqueous voltammetry profiles reported in the literature, and this is the first known instance of their collection. Moreover, the findings of this work appear to confirm the theoretically predicted value of ΔE_g for $[Au_{13}(dppe)_5Cl_2]^{3+}$. Noteworthy is the measured ΔE_g for $[Au_{11}(PPh_3)_8Cl_2]^{+}$, which was found to be unexpectedly small for gold clusters in this size regime and in strong contrast to that predicted for a structurally-similar isomer, $Au_{11}(PPh_3)_7Cl_3$.

In Chapter 5, the short- and long-term electrochemical behaviour of carbon-supported nanomaterials was investigated by cyclic voltammetry in N_2-purged 0.1 M Na_2SO_4. Monophosphine-protected nanoclusters (Au_8, Au_8Pd_1, Au_9 and Au_{11}) were found to exhibit a large, irreversible reduction wave at *ca.* + 0.6 - 0.7 V (*vs.* Ag/AgCl) which was less-conspicuous at diphosphine-protected clusters (Au_6, Au_{13}), and was attributed to the relative facility of these ligands to dissociate from the cluster core. The origin of this event was hypothesised to be evidence for the Incipient Hydrous-Oxide/Adatom Mediator model, which has previously rationalised the electrocatalytic activity of polycrystalline gold electrodes for certain electrochemical reactions, although the reduction of gold-oxides cannot be ruled out. This feature was not observed at electrodes containing monovalent Au^+ cations, however *was* observed at those containing large gold nanoparticles, suggesting it may be a feature of defect-rich gold structures and not of cationic gold. Ag_{25} was found to display several events in cyclic voltammetry data, and these were attributed to the dissolution and re-deposition of Ag^+ ions which likely arose from the disintegration of the cluster over the first few cycles. Over long-term electrochemical cycling, the voltammetric profiles of all carbon-supported gold clusters progressively resembled that of large gold nanoparticles, however no clear evidence for gold-oxide formation was found for the former in contrast to the latter. The results of this chapter suggest that small gold clusters possess an intrinsic opposition to oxidation, in agreement with previous findings from other authors.

In Chapter 6, the electrocatalytic activity of carbon-supported gold and silver nanomaterials for nitrate electroreduction was investigated. All gold-phosphine clusters and a monovalent gold complex were found to have appreciable activity for this reaction, whereas large gold nanoparticles were poorly active; the lone silver

cluster was found to be essentially inactive. These results are in direct contrast to the large body of prior literature which consistently finds bulk and nano-sized Au to be a very poor catalyst for this reaction, and conversely bulk and nano-sized Ag holds modest activity; a particularly interesting consequence of the divergent physiochemical properties between metallic, nano and molecular states of gold and silver. Once again, the novelty of this result cannot be understated, and the results of this work confidently confirm the theoretical prediction by Calle-Vallejo *et al.*[20] (Section 1.5.3) that ensembles of gold adatoms are active electrocatalysts for nitrate reduction, however conflict with a similar production that ensembles of silver adatoms would also share this property. The product of nitrate reduction was concluded to be the nitrite anion, and this process was found to be *quasi*-reversible which, again, is in contrast with other literature findings where nitrate electroreduction is generally irreversible. Furthermore, these catalysts were found to be inactive for nitrite reduction. The long-term performance of these catalysts was also evaluated, and a curious peak in activity was observed between 3-24 electrochemical cycles which gradually declined over the next 76 cycles. This was attributed to the progressive stripping of ligands from the cluster core during initial cycling which exposed more catalytically-active sites, after which aggregation effects developed, and the overall number of these sites decreased significantly. Interestingly, the overall trend in voltammetric response to nitrate and nitrite held over 100 electrochemical cycles, which could indicate that a portion of clusters remained un-aggregated over this time and are possibly isolated within the pores of the carbon support. In the latter-half of Chapter 6, the kinetics of nitrate electroreduction at these six gold-phosphine cluster catalysts was examined in detail. Findings consistently showed that Au_{11} and Au_8 were the best-performing clusters for this reaction, whereas Au_6 and Au_{13} were the poorest and Au_8Pd_1 and Au_9 possessed intermediate activity. This trend in activity was hypothesised to arise, at least partially, from the respective size of the electrochemical gap wherein clusters with smaller ΔE_g possessed greater performance (expressed by Δj_p and R_{ct} values) and *vice-versa*. Mechanistic considerations suggest that the rate-limiting step for nitrate electroreduction over all gold clusters is the *first* electron-transfer to either the nitrate anion or to a water molecule, which is followed by a rapid chemical-step and concluded by a second electron-transfer to generate the nitrite product. Following this, the Incipient Hydrous-Oxide/Adatom Mediator model was applied to rationalise the activity of these novel catalysts based on the electrochemically-induced redox cycle involving gold adatoms (constituting clusters) and hydrous gold-oxides $[Au_2(OH)_9]^{3-}$, which catalyse the reduction of nitrate and the oxidation of nitrite,

respectively. Such a model has not yet been applied to electrocatalytic reactions mediated by chemically-synthesised clusters of gold.

In Chapter 7 the efficacy of the best performing catalyst identified in the foregoing chapter, carbon-supported Au_{11}, was briefly investigated. A good linear current-response to the nitrate anion was found over the concertation range 1-10 mM (62-620 ppm) using cyclic voltammetry, though unfortunately reduction signals could not be reliably distinguished from the background current below this limit. This sensing platform was inferred to have greater sensitivity towards nitrite than nitrate. Though an alternative electroanalytical technique, differential-pulse voltammetry, was employed as an attempt to resolve the rather-high detection limit of nitrate by cyclic voltammetry this was regrettably unsuccessful, and it was not possible to observe a clear nitrate reduction signal. The reasons for this are unknown to this author, however the fact that the present sensing platform can indeed display a reproducible analytical response to both nitrate and nitrite in a *real* environmental matrix should not discourage future endeavours.

7.5 – Future Work

Several avenues for future research have been identified during this work:

i) In Chapter 4 a rather large disparity between the electrochemical gap (ΔE_g; energy separation between first reduction and first oxidation events) of $[Au_{11}(PPh_3)_8Cl_2]^+$, and that theoretically predicted for a structurally-similar isomer $Au_{11}(PPh_3)_7Cl_3$ was found. With only a minor alteration to the ligand periphery the latter was estimated to possess a ΔE_g over twice that of the former, which is considerable enough to raise this authors attention. Namely, how do such small changes to cluster structure account for such a significant variation in electronic properties, when the simple replacement of a Au atom in $[Au_9(PPh_3)_8]^{3+}$ with a Pd atom, for example, only leads to a relatively minor perturbation?

ii) In Chapter 5 and 6, only six gold-phosphine clusters and one silver-thiolate cluster were examined for nitrate electroreduction; this is but a small sample of the wide library of such compounds reported in the literature. To this end, it may be worthwhile to prepare a greater selection of these novel catalysts to further explore the effect of cluster size and composition on nitrate electroreduction. If electrocatalytic activity *does* depend on ΔE_g (at least, for gold nanoclusters) this provides the analyst

with an immediate criterion for selecting future candidates. In particular, this author recommends a family of gold-phosphine clusters containing Rh atoms;[311] as bulk rhodium is a known catalyst for nitrate reduction this may offer interesting or improved performance.

iii) Why does the hypothetical Pd-doping of $[Au_9(PPh_3)_8]^{3+}$, or the addition of a Pd atom to $[Au_8(PPh_3)_8]^{2+}$, lead to a quantifiable decrease in catalytic performance by almost every measure employed in this work? Would a similar phenomenon occur for other nine-membered bimetallic clusters, such as $[Au_8Pt_1(PPh_3)_8]^{2+}$ [374] or $[Au_8Rh_1(PPh_3)_6(CNC_8H_9)_2Cl_2]^{2+}$,[311] or Pd-doped gold phosphine clusters such as $Au_{10}Pd_1(PPh_3)_8Cl_2$ [375] and $[Au_{12}Pd_1(PPh_3)_8Cl_4]^{2+}$ [218] ?

iv) A physiochemical explanation should be found for why an atomically-precise silver cluster, $[Ag_{25}(SPhMe_2)_{18}]^-$ is *poorly active* for nitrate electroreduction whereas bulk and nanoparticulate Ag *are* active (substantially, one might add); the apparent reversal of this trend compared to the case for gold is peculiar, and would greatly benefit from a wider range of silver nanoclusters (*e.g.* Ag_{44}, and the $Ag_{24}M_1$ series) to either verify or refute this finding.

v) Clearly, surface characterisation studies (XPS, HR-TEM, *etc.*) are required to establish the changes that take place to these clusters (supported on amorphous carbon) during electrochemical cycling; it is lamentable that such data could not be included in this thesis, as this could have possibly assisted with identifying the authentic catalytic species which exhibited maximum activity between 3-24 electrochemical cycles. Moreover, it would be of fundamental interest to observe any morphological changes that took place during the electrochemical treatment of carbon supported Ag_{25}, to assign these to features observed in cyclic voltammetry data.

vi) The possible correlation between ΔE_g and catalytic activity noted in Section 6.8 certainly requires further investigation, not only with a much wider range of catalysts but for an explanation as to *why* catalytic activity may depend on ΔE_g, be it the ability of the cluster to provide thoroughfare for reactant electrons or the ability of the cluster to potentially participate in the IHOAM redox-cycle. Furthermore, atomically-precise gold clusters have not yet been employed as a means to examine the credibility of the IHOAM model, and this itself could be an interesting pursuit for future studies.

vii) The performance of the most-active catalyst in this work, $[Au_{11}(PPh_3)_8Cl_2]^+$, for the electrochemical sensing of nitrate is somewhat disappointing compared to other reported sensing platforms. Further

work is needed in this area to advance this sensing strategy, ideally with optimisation of pulse-voltammetry techniques such as DPV or SWV (square-wave voltammetry), or chronoamperometry to improve the rather-high detection limit. Moreover, efforts should be directed towards establishing the effect of matrix pH on performance and investigating the potential effects of environmentally-relevant interferences (halides, oxyanions, organic compounds, metals *etc.*). Perhaps the action of nitrate reduction is itself detrimental to long-term activity? Will the same high activity be found for other reported undecagold clusters, such as $Au_{11}(PPh_3)_7Cl_3$ or $[Au_{11}(dppe)_5]^{3+}$ [242]?

viii) Finally, there is the option to pursue different electrocatalyst supports, which may have an appreciable influence on the performance of gold nanoclusters for nitrate reduction. A small selection of reported supports includes carbon-nanotubes,[376] graphene,[377] and SiO_2/RuO_2[378] or MnO_2/C composites,[379] notwithstanding the actual catalyst loading on the support itself. Additionally, the method of fabrication itself should be explored and optimised, as this was found to have a considerable impact on measured catalyst performance (Section 5.1) it is possible that further advances could be made in this area.

Chapter 8

Synthesis, Characterisation and Experimental

8.1 – Summary of Synthesis and Characterisation

All reagents used in this work were purchased from chemical suppliers and used without further purification. Ethanol, $CHCl_3$, petroleum ether, isopropanol, tetrahydrothiophene, PPh_3, Et_4NCl, and PPh_4Br were obtained from Merck. Et_2O, *n*-hexane, *n*-pentane, CH_2Cl_2, tetrahydrofuran, toluene, benzene, acetonitrile, acetone and trisodium citrate were obtained from Fischer Scientific. $Pd(PPh_3)_4$, dppe, dppp, 2,4-dimethylbenzene thiol, KPF_6 and Bu_4NPF_6 were obtained from Sigma Aldrich. HCl, HNO_3, Na_2SO_4, $NaNO_3$, $NaNO_2$ and KCl were obtained from Univar. $AgNO_3$ was obtained from May & Baker. Nafion-117/isopropanol suspension was obtained from DuPont. $NaBH_4$ was obtained from ECP Ltd. $HAuCl_4$ was obtained from Precious Metals Online. Deionised water was collected from a Milli-Q Integral water purifier system (Merck-Millipore, 18.2 MΩ·cm resistivity).

8.1.1 *Synthesis of Cluster Precursors*

$AuPPh_3Cl$ was prepared following the method described by Anderson *et al.*[238] with modification. To a suspension of PPh_3 (2800 mg, 10 mmol) in 70 mL ethanol was added a solution of $HAuCl_4$ (2000 mg, 5 mmol) in 9 mL ethanol and 1 mL H_2O with rapid stirring. The yellow colour of the $[AuCl_4]^-$ ion rapidly disappeared upon mixing, and after a few minutes a white precipitate formed. Stirring was continued for about 20 minutes. The white product was collected by centrifugation, washed with hot (*ca.* 50 °C) ethanol (3x50 mL), re-dissolved in 30 mL $CHCl_3$, centrifuged, and the supernatant dried by rotary evaporation. Finally, the product was dissolved in 10 mL CH_2Cl_2 and crystallised by the addition of 40 mL hexane, giving colourless needles in excellent yield. These were washed with a small portion of Et_2O and dried under vacuum. The yield of pure product was *ca.* 2700 mg (2.6mmol, *ca.* 95% by Au atom). Identity was confirmed by ^{31}P NMR ($CDCl_3$); singlet, δ = 33ppm relative to 85% H_3PO_4.

$AuPPh_3NO_3$ was prepared following the method described by Anderson *et al.*[238] with modification. To a solution of $AuPPh_3Cl$ (1200 mg, 2.4 mmol) in 50mL $CHCl_3$ was added a suspension of $AgNO_3$ (1000 mg, 6 mmol) in 50 mL ethanol with stirring. The mixture became cloudy instantly as AgCl formed, and the flask was covered with aluminium foil and allowed to stir for 1 hour. After this time, the mixture was centrifuged several times and the supernatant dried by rotary evaporation. The residue was then washed with H_2O (4x25 mL) and ethanol (2x25 mL), re-dissolved in 10 mL CH_2Cl_2 and crystallised by the addition of 40 mL hexane. The colourless crystals were washed with a small portion of Et_2O and dried under vacuum, and the yield was *ca.*

1100 mg (2.1 mmol, *ca.* 90% by Au atom). The product is reportedly light sensitive, and light exposure was therefore minimised. Identity was confirmed by ^{31}P NMR ($CDCl_3$); singlet, δ = 25ppm relative to 85% H_3PO_4.

Au(THT)Cl was prepared following the method by Uson *et al.*[380] with modification. To a stirred solution of $HAuCl_4$ (various "wet" $HAuCl_4$ residues containing a significant amount of absorbed water, unknown molar amount but ≥ *ca.* 0.30 mmol; *vide infra*) in 10 mL methanol is added excess tetrahydrothiophene (THT; 0.75 mL, 0.85 mmol) by syringe under N_2 with rapid stirring (note: THT may resemble the odour of natural gas – the exhaust from this reaction was bubbled through a hypochlorite solution in ethanol). The colour of the solution changes from yellow to red (briefly) and then a white precipitate is formed within a few minutes. After 20 minutes stirring, the mixture is centrifuged, and the white solids collected. The product is washed repeatedly with methanol and ice-cold THF until the scent of THT no longer remained. It was dried under vacuum and crystallised from the minimum amount of hot (*ca.* 50 °C) acetone/methanol (1:3) which slowly cooled to ambient temperature over a few hours and was then cooled below 0 °C overnight. The near-colourless crystals were then washed with a small portion of Et_2O and dried under vacuum. The yield was *ca.* 1000 mg (3.1 mmol).

$Au_2(dppe)Cl_2$ was prepared following a method described by Brandys *et al.*[381] with modification. To a stirred suspension of Au(THT)Cl (970 mg, 3 mmol) in 20 mL methanol was added solid 1,2-bis(diphenylphosphino)ethane (dppe, $Ph_2P(CH_2)_2PPh_2$, 600 mg, 1.5 mmol) under N_2 (the exhaust from this reaction was bubbled through a hypochlorite solution in ethanol, as THT is displaced). An off-white precipitate formed within a few minutes, and after 1 hour was collected by centrifugation. The product was washed thoroughly with methanol and ice-cold THF, then re-dissolved in CH_2Cl_2 and dried by rotary evaporation. The crude product was then washed with 9:1 pet. ether/CH_2Cl_2 to remove residual dppe, which was observed by ^{31}P NMR in $CDCl_3$ (δ = -12ppm). It was crystallised from hot (*ca.* 50 °C) CH_2Cl_2/methanol (1:3), that slowly cooled to ambient temperature over a few hours, and was then cooled below 0 °C overnight. Off-white crystals were collected in good yield and washed with a small portion of Et_2O and dried under vacuum. The yield was *ca.* 1200 mg (1.4 mmol, *ca.* 90% by Au atom). Identity was confirmed[381] by ^{31}P NMR ($CDCl_3$); singlet, δ = 37ppm relative to 85% H_3PO_4.

8.1.2 *[Au$_6$(dppp)$_4$](NO$_3$)$_2$*

[Au$_6$(dppp)$_4$](NO$_3$)$_2$ was prepared following the method reported by Van der Velden *et al.*[239] with modification. To a solution of [Au$_9$(PPh$_3$)$_8$](NO$_3$)$_3$ (100 mg, 0.025 mmol) in 10 mL CH_2Cl_2 is added a 20-fold molar excess of 1,2-bis(diphenyl)propane (dppp, $Ph_2P(CH_2)_3PPh_2$) (200 mg, 0.5 mmol) in 5 mL CH_2Cl_2 with rapid stirring. The colour changes from orange to a very pleasant blue over a few minutes, indicating the formation of a new cluster species as ligand exchange takes place. After 15 minutes, the mixture was poured into 100 mL of pet. ether and precipitated at 0 °C overnight. The blue solids were collected by centrifugation and further washed with pet. ether (2x20 mL), a 9:1 mix of pet. ether/CH_2Cl_2 (2×10 mL) and finally Et_2O (2x20 mL). The crude product was crystallised by the vapour diffusion of Et_2O into a methanolic solution of the cluster at ambient temperature over several days. Red/purple plate crystals were collected in good yield, washed with a small portion of Et_2O and dried in air. The yield was *ca.* 65 mg (0.022 mmol, *ca.* 60% yield by Au atom). The product is soluble in methanol, ethanol, acetone, acetonitrile, CH_2Cl_2 and $CHCl_3$ and insoluble in Et_2O, toluene, benzene, pet. ether and aliphatic hydrocarbons. Identity was confirmed[239] by ^{31}P NMR in CD_3OD (two singlets of equal intensity, δ_1 = 62 ppm and δ_2 = 54 ppm *vs.* 85% H_3PO_4; Figure 8.1 Panel A) and ESI-MS in 1:20 methanol/acetonitrile (m/z ≈ 1415 ([Au$_6$(dppp)$_4$]$^{2+}$]). Fragment ions of the parent cluster were also found. UV-Vis (CH_2Cl_2) found absorbance peaks at 589, 507 and 325 nm.

8.1.3 *[Au$_8$(PPh$_3$)$_8$](NO$_3$)$_2$*

[Au$_8$(PPh$_3$)$_8$](NO$_3$)$_2$ was prepared following the method described by Anderson *et al.*[238] originally reported by Van der Velden *et al.*[247] with some modification. To a solution of Au$_9$(PPh$_3$)$_8$(NO$_3$)$_3$ (100 mg, 0.025 mmol) in 15 mL CH_2Cl_2 is added a 10-fold molar excess of PPh_3 (66 mg, 0.25 mmol) in 5 mL CH_2Cl_2 with rapid stirring. The orange solution becomes slightly redder after 30 minutes. The mixture was then poured into 100 mL of pet. ether and precipitated at 0 °C overnight. After this time, the red solids were collected by centrifugation and washed with hot (*ca.* 50 °C) pet. ether (2x20 mL) and hot (*ca.* 50 °C) toluene (2x20 mL). The product was then re-dissolved in 20 mL CH_2Cl_2, centrifuged and the supernatant dried by rotary evaporation without heating. It was crystallised by the vapour diffusion of Et_2O into a CH_2Cl_2 solution of the cluster at 4 °C over one week. Red plate crystals were collected in good yield and were washed with a small portion of Et_2O and

dried in air. The yield was *ca.* 80 mg (0.021 mmol, *ca.* 80% by Au atom). The product is soluble in methanol, ethanol, acetone, acetonitrile, CH_2Cl_2 and $CHCl_3$ and insoluble in Et_2O, toluene, benzene, pet. ether and aliphatic hydrocarbons. Identity was confirmed[238] by ^{31}P NMR in $CDCl_3$ (singlet, δ_1 = 59 ppm *vs.* 85% H_3PO_4; Figure 8.1 Panel B) and ESI-MS in 1:20 CH_2Cl_2/acetonitrile (m/z ≈ 1836 ($[Au_8(PPh_3)_8]^{2+}$)). Fragment ions of the parent cluster were also found. UV-Vis (CH_2Cl_2) found absorbance peaks at 484, 451, 422, 380 and 324 nm.

8.1.4 *$[Au_8Pd_1(PPh_3)_8](Cl)_2$*

$[Au_8Pd_1(PPh_3)_8]Cl_2$ was prepared following the method described by Matsuo *et al.*[252] with some modification. $AuPPh_3Cl$ (140 mg, 0.29 mmol) and $Pd(PPh_3)_4$ (136 mg, 0.12 mmol) were first dissolved in 15 mL ethanol and 5 mL CH_2Cl_2 with sonication, and to this was added solid $NaBH_4$ (15 mg, 0.4 mmol) *slowly* over 30 minutes with rapid stirring (*ca.* one grain every 5 minutes). It is important that reduction is carried out slowly to increase both the yield of the target cluster and the selectivity of the reaction. The colour changes from dark yellow/brown to a deep orange/red over this time. The mixture was stirred for one additional hour and was precipitated from 100 mL of pet. ether overnight at 0 °C. After this time, the red/orange solids were collected by centrifugation, and washed successively with pet. ether (2x20 mL), 9:1 pet. ether/CH_2Cl_2 (2×10 mL) and 6:1 pet. ether/CH_2Cl_2 (2×10 mL). The remaining solids were extracted into 20 mL ethanol, centrifuged, and the dark orange supernatant dried by rotary evaporation without heating. No treatment with additional PPh_3 was undertaken. Residual PPh_3 and $AuPPh_3Cl$ were removed by washing the residue thoroughly with copious amounts of hot (*ca.* 50 °C) pet. ether and hot (*ca.* 50 °C) toluene. $Pd(PPh_3)_x$ proved more challenging to remove, since it shared similar solubility with the desired cluster. It was fortuitously discovered to be *slightly* soluble in a 1:1 mix of benzene/Et_2O and could be gradually removed by washing the residue with this solvent mixture (pale brown washings were discarded). When only traces of $Pd(PPh_3)_x$ were observed by ^{31}P NMR, the product was dissolved in ethanol and crystallised by the vapour diffusion of Et_2O at ambient temperature over one week. This afforded thin dark brown needles in good yield, which were washed with a small portion of Et_2O and dried in air. No $Pd(PPh_3)_x$ was found in the ^{31}P NMR of the crystalline material after two crystallisations. The yield was *ca.* 90 mg (0.023 mmol, *ca.* 65% by Au atom). The product is soluble in methanol, ethanol, isopropanol, acetone, acetonitrile, CH_2Cl_2 and $CHCl_3$ and insoluble in Et_2O, toluene, benzene, pet. ether and

aliphatic hydrocarbons. Identity was confirmed[252] by ^{31}P NMR in CD_2Cl_2 (singlet, δ_1 = 51 ppm *vs.* 85% H_3PO_4; Figure 8.1 Panel C) and ESI-MS in 1:20 CH_2Cl_2/acetonitrile (m/z ≈ 1889 ($[Au_8Pd_1(PPh_3)_8]^{2+}$). Fragment ions of the parent cluster were also found. UV-Vis (CH_2Cl_2) found absorbance peaks at 535, 469, 415 and 337 nm.

8.1.5 *$[Au_9(PPh_3)_8](NO_3)_3$*

$[Au_9(PPh_3)_8](NO_3)_3$ was prepared following the method described by Anderson *et al.*[238] originally reported by Wen *et al.*[233] with some modification. $AuPPh_3NO_3$ (1000 mg, 1.9 mmol) was dissolved in 75 mL ethanol with sonication, and to this was added a suspension of $NaBH_4$ (18 mg, 0.48 mmol) in 5 mL ethanol at once with rapid stirring. The solution becomes dark red almost instantly and stirring was continued for a further two hours. The mixture is centrifuged, and the red supernatant dried by rotary evaporation without heating. The residue was then re-dissolved in 25 mL CH_2Cl_2 and centrifuged again, and any solids discarded. The supernatant was once again dried by rotary evaporation, and the dark red residue was washed with 2x25 mL THF. Upon washing, the product becomes noticeably green in colour. It was then further washed with 2x25 mL of hot (50 °C) pet. ether. The crude product was re-dissolved in methanol and crystallised by the vapour diffusion of Et_2O at 4 °C over one week. The crystals were washed with a small portion of Et_2O and dried in air. The yield after was 250 mg (0.06 mmol, yield *ca.* 30% by Au atom). The product is soluble in methanol, ethanol, acetone, acetonitrile, CH_2Cl_2 and $CHCl_3$, and insoluble in Et_2O, toluene, benzene, pet. ether and aliphatic hydrocarbons. Identity was confirmed[238] by ^{31}P NMR in $CDCl_3$ (singlet, δ_1 = 57 ppm *vs.* 85% H_3PO_4; Figure 8.1 Panel D) and ESI-MS in 1:20 methanol/acetonitrile (m/z ≈ 1290 ($[Au_9(PPh_3)_8]^{3+}$). Fragment ions of the parent cluster were also found. UV-Vis (CH_2Cl_2) found absorbance peaks at 443, 424 354 and 317 nm.

8.1.6 *$[Au_{11}(PPh_3)_8Cl_2]Cl$*

$[Au_{11}(PPh_3)_8Cl_2]Cl$ was prepared following the method described by McKenzie *et al.*[251] with some modification. $AuPPh_3Cl$ (480 mg, 0.98 mmol) was dissolved in 25 mL CH_2Cl_2 and to this was added a suspension of $NaBH_4$ (10 mg, 0.27 mmol) in 5 mL ethanol at once with rapid stirring. The solution becomes orange instantly and darkens within a few minutes. The reaction was stirred overnight and after this time the crude product was poured into 100 mL pet. ether and precipitated overnight at 0 °C. The orange solids were

collected by centrifugation, washed with pet. ether (2x20 mL), a 4:1 pentane/CH_2Cl_2 mix (2x20 mL) and Et_2O (2x20 mL). The crude product was re-dissolved in 20 mL CH_2Cl_2, centrifuged (any solids discarded) and the red/orange supernatant dried by rotary evaporation without heating. ^{31}P NMR of the crude product in $CDCl_3$ showed the presence of residual PPh_3 (δ = 29 ppm), $AuPPh_3Cl$ (δ = 33 ppm), the target cluster $[Au_{11}(PPh_3)_8Cl_2]Cl$ (δ = 52 ppm) and traces of an isomer, $Au_{11}(PPh_3)_7Cl_3$ (δ = 53 ppm). The residue was washed with hot (*ca.* 50 °C) pet. ether and hot (*ca.* 50 °C) toluene. Removing the undesired isomer of $Au_{11}(PPh_3)_7Cl_3$ was eventually achieved by repeated crystallisation of the product from the vapour diffusion of Et_2O into a CH_2Cl_2/Et_2O solution by the following procedure: First, the mixture of Au_{11} isomers was dissolved in a minimum amount of CH_2Cl_2 and to this Et_2O was added dropwise until a precipitate began to form and the solution became cloudy. Then, a minimum amount of additional CH_2Cl_2 required to dissolve this precipitate was added dropwise, then subjected to vapour diffusion by Et_2O over one week at ambient temperature. $[Au_{11}(PPh_3)_8Cl_2]Cl$ forms red *plate* crystals in acceptable yield, whereas $Au_{11}(PPh_3)_7Cl_3$ forms red *needle* crystals in very low yield, which were mechanically separated using a length of thin glass fibre. A gold-mirror often formed on the glass vial probably due to the decomposition of the latter in solution. The crystals were washed with a small portion of Et_2O and dried in air. The yield of pure product was *ca.* 90 mg (0.02 mmol, yield *ca.* 25% by Au atom). The product is soluble in methanol, acetone, acetonitrile, CH_2Cl_2 and $CHCl_3$ and insoluble in Et_2O, toluene, benzene, pet. ether and aliphatic hydrocarbons. Identity was confirmed[251] by ^{31}P NMR in $CDCl_3$ (singlet, δ_1 = 52 ppm *vs.* 85% H_3PO_4; Figure 8.1 Panel E) and ESI-MS in 1:20 CH_2Cl_2/acetonitrile (m/z ≈ 1421 ($[Au_{11}(PPh_3)_8]^{3+}$)). Fragment ions of the parent cluster were also found. UV-Vis (CH_2Cl_2) found absorbance peaks at 519, 419 and 375 nm.

As discussed in Section 3.1.4, there are alternative routes to preparing $[Au_{11}(PPh_3)_8Cl_2]^+$:

Initially following the method described by Anderson *et al*.[238] (originally reported by Weohrle *et al*.[250]) gave $Au_{11}(PPh_3)_7Cl_3$ as the major product and $Au_{11}(PPh_3)_8Cl_3$ the minor product (determined qualitatively by ^{31}P NMR). Yields of both were low and separation was unsuccessful leading to the abandonment of this method. Additionally, $[Au_{11}(PPh_3)_8Cl_2]Cl$ may be prepared from the reaction between $[Au_9(PPh_3)_8](NO_3)_3$ and Cl^- ions in an organic solvent, as reported by Vollenbroek *et al*.[223, 246] This was attempted on a small scale by mixing $[Au_9(PPh_3)_8](NO_3)_3$ (25 mg, 6.25 μmol) and Et_4NCl (20 mg, 0.125 mmol) in 10 mL CH_2Cl_2 for 1 hour with stirring. The colour noticeably changes to a lighter orange, and after this time was precipitated from 50 mL

pet. ether at 0 °C overnight. The product was collected by centrifugation, extracted into 5 mL methanol, centrifuged again, and the orange supernatant dried by rotary evaporation. It was re-dissolved in 5 mL CH_2Cl_2 and precipitated from pet. ether once again, washed with pet. ether (2×10 mL), 4:1 (v/v) Et_2O/ethanol (2×10 mL) and Et_2O (2×10 mL) and dried under vacuum. Whilst ^{31}P NMR ($CDCl_3$) showed the synthesis to be successful, generating the desired Au_{11} isomer *exclusively*, yields were poor (< 15% by Au atom) and considering Au_9 is a prohibitively limited precursor, this route was therefore not suited for larger scale preparation and was regrettably abandoned.

^{31}P NMR of the related isomer $Au_{11}(PPh_3)_7Cl_3$ in $CDCl_3$ gives one singlet, δ_1 = 53 ppm *vs.* 85% H_3PO_4, which was not found overlap with the signal for $[Au_{11}(PPh_3)_8Cl_2]^+$. A ^{31}P NMR spectrum containing both isomers is given in Figure 8.2 to illustrate this result, and how either product could be easily mistaken for the other.

8.1.7 *$[Au_{13}(dppe)_5Cl_2)Cl_3$*

$[Au_{13}(dppe)_5Cl_2]Cl_3$ is prepared following the method described by Shichibu and Konishi[254] with some modification. $Au_2(dppe)Cl_2$ (300 mg, 0.3 mmol) was dissolved in 240 mL CH_2Cl_2 and to this was added a suspension of $NaBH_4$ (66 mg, 3 mmol) in 10 mL ethanol at once with rapid stirring. The mixture immediately becomes dark and turns red within a few minutes, and the reaction proceeded for 3 hours. After this time, the mixture was centrifuged (any solids discarded) and the supernatant dried by rotary evaporation. The dark red residue was then extracted into 50 mL ethanol, centrifuged (any solids discarded) and to the supernatant was added 1 mL of 37% (12 M, neat) HCl and stirred overnight. The mixture was concentrated by rotary evaporation to a few mL and the residue washed with water (3x30 mL). The product was re-dissolved in 20 mL methanol and centrifuged (any solids discarded), then precipitated from Et_2O (100 mL) overnight at 0 °C. This was repeated twice. ^{31}P NMR of the crude product in CD_3OD found the presence of residual $Au_2(dppe)Cl_2$ (δ = 37 ppm). The crude product was therefore washed repeatedly with 9:1 (v/v) pet. ether/CH_2Cl_2 (*ca.* 200 mL in 4 portions. Hot pet. ether did not successfully remove this species) until this impurity was only observed in trace amounts by ^{31}P NMR. Finally, the relatively pure product was crystallised by the vapour diffusion of Et_2O into a methanolic solution of the cluster at ambient temperature over one week. This afforded large red block crystals in excellent yield, which were washed with a small portion of Et_2O and dried in air. The yield was *ca.* 90 mg (0.02 mmol, 80% by Au atom). The product is soluble in methanol, ethanol, isopropanol,

acetone, acetonitrile, CH_2Cl_2 and $CHCl_3$ and insoluble in Et_2O, toluene, benzene, pet. ether and hydrocarbons. Identity was confirmed[254] by ^{31}P NMR in CD_3OD (singlet, δ_1 = 67 ppm *vs.* 85% H_3PO_4; Figure 8.1 Panel F) and ESI-MS in 1:20 methanol/acetonitrile ($m/z \approx 1541$ ($[Au_{13}(dppe)_5Cl_2]^{3+}$). Fragment ions of the parent cluster were also found. UV-Vis (CH_2Cl_2) found absorbance peaks at 482, 366 and 306 nm (the feature at 352 nm is an artefact of the spectrometer).

8.1.8 *$[Ag_{25}(SPhMe_2)_{18}](PPh_4)$*

$[Ag_{25}(SPhMe_2)_{18}](PPh_4)$ was prepared following the method reported by Bakr *et al.*[259] with some modification. In a typical synthesis, 115 mg $AgNO_3$ (0.66 mmol) was dissolved in 5 mL methanol with sonication. To this, *ca.* 20 mL CH_2Cl_2 was added followed by 0.27 mL 2,4-dimethylbenzenethiol (2.0 mmol) with stirring. The yellow mixture was then cooled to 0 °C for 30 min whilst the flask was purged with N_2. Next, *ca.* 20 mg PPh_4Br (*ca.* 0.044 mmol) dissolved in 1 mL cold methanol was added, immediately followed by the drop-wise addition of an aqueous $NaBH_4$ solution (45 mg, 1.20 mmol; freshly dissolved in 3 mL ice-cold water) over a few minutes. The colour progressively changed from yellow to light brown then to black within a short time. The mixture was allowed to continue reacting overnight, and after this time the aqueous phase was removed, and the organic phase washed with 3x 5 mL cold water. The almost black organic phase was centrifuged, and the mixture concentrated by rotary evaporation. The black product was precipitated by the addition of *ca.* 20 mL ice-cold methanol. The presence of a small amount of water (< 0.5 mL) in the concentrated organic phase appeared to assist with precipitation. The crude product was washed repeatedly with a 2:1 (v/v) mix of *n*-hexane and ethanol until washings were colourless and collected by centrifugation in *n*-hexane. The yield of crude product was typically 30-50 mg, although this contained some insoluble yellow materials (*ca.* 50% by mass) believed to be leftover Ag-thiolate polymers. These can be separated by dissolving the product followed by prolonged centrifugation at high speed.

The crude product was re-dissolved in *ca.* 3 mL CH_2Cl_2, centrifuged and crystallised by carefully layering a small volume of this solution with *ca.* 5x by volume cold *n*-hexane in a fridge at 4° C. It was found that multiple small-scale crystallisations gave a greater yield of pure product than one bulk attempt. Small black crystals formed within 3-7 days, which were washed with a small portion of Et_2O and dried in air. The yield of

crystalline Ag_{25} was typically 15-20 mg (*ca.* 2.7 μmol; *ca.* 9% by Ag atom). Characterisation was by single-crystal X-ray diffraction, the results of which are shown in Section 8.4.4

8.1.9 *Colloidal Gold Nanoparticles*

Colloidal gold nanoparticles were prepared following the method described by Padayachee *et al.*[256] and originally reported by Kimling and co-workers.[257] 200 mL of water was brought to a near-boil before 5mL of an acidified $HAuCl_4$ solution (86 mg with 25 μL of 10 M (*ca.* 32%) HCl) was added with stirring. 5 minutes later, a heated solution of 660 mg trisodium citrate in 45 mL water was rapidly added. The colour changed from pale yellow to dark brown almost instantly, and heating was continued for a further 15 minutes over which time the mixture gradually turned purple. Heating was ceased, and the solution was allowed to cool to ambient temperature. The concentration was estimated using the average particle diameter calculated in Section 3.2.1 (*ca.* 55 nm) and were used without further purification.

8.2 – Characterisation Data

8.2.1 *^{31}P NMR*

^{31}P nuclear magnetic resonance (NMR) spectra for all six gold-phosphine clusters prepared in this work are given overleaf in Figure 8.1 and were collected on an Agilent Technologies 400 MR. Specific peak positions alongside the solvent used can be found in the main text, in Sections 3.1.1 – 3.1.6. In Figure 8.2, a ^{31}P NMR spectrum of both undecagold isomers, $[Au_{11}(PPh_3)_8Cl_2]^+$ and $Au_{11}(PPh_3)_7Cl_3$ is given to illustrate the discussion in Section 3.1.4.

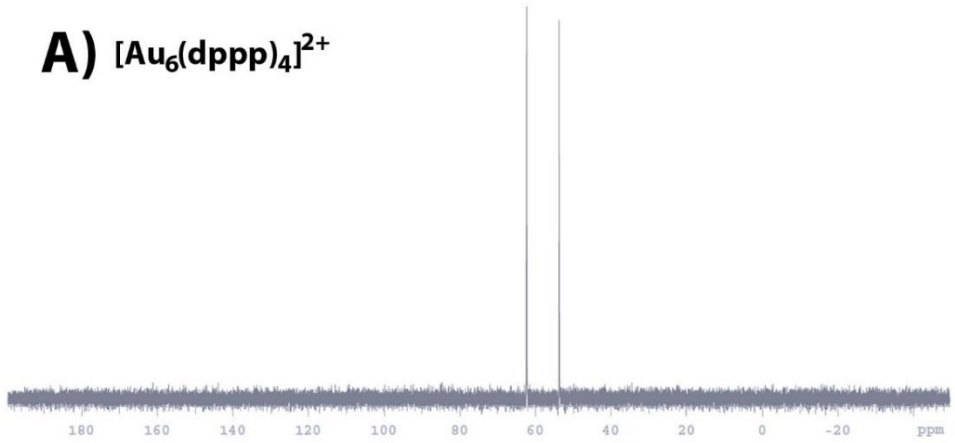
A) [Au6(dppp)4]2+
180
160
140
120
100
80
60
40
20
0
-20
ppm

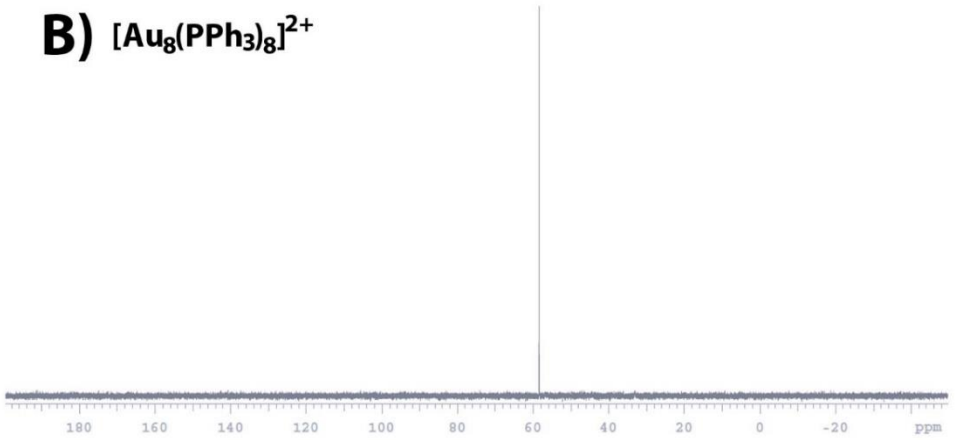
B) [Au8(PPh3)8]2+
180
160
140
120
100
80
60
40
20
0
-20
ppm

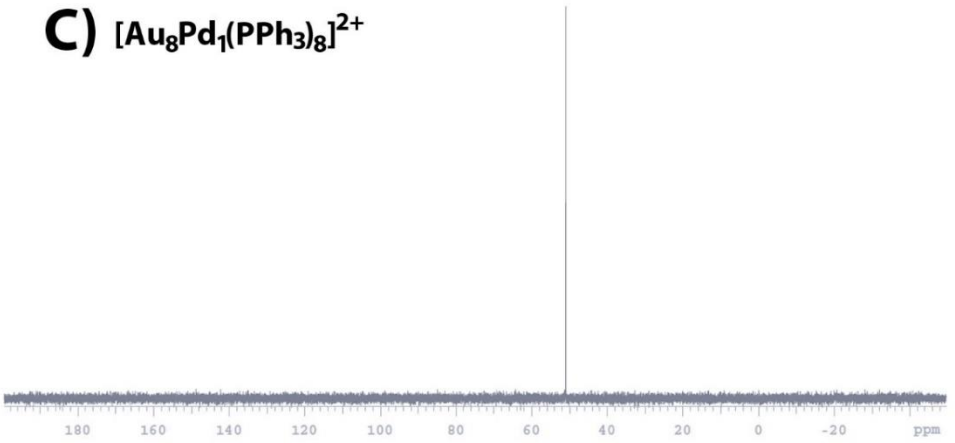
C) [Au8Pd1(PPh3)8]2+
180
160
140
120
100
80
60
40
20
0
-20
ppm

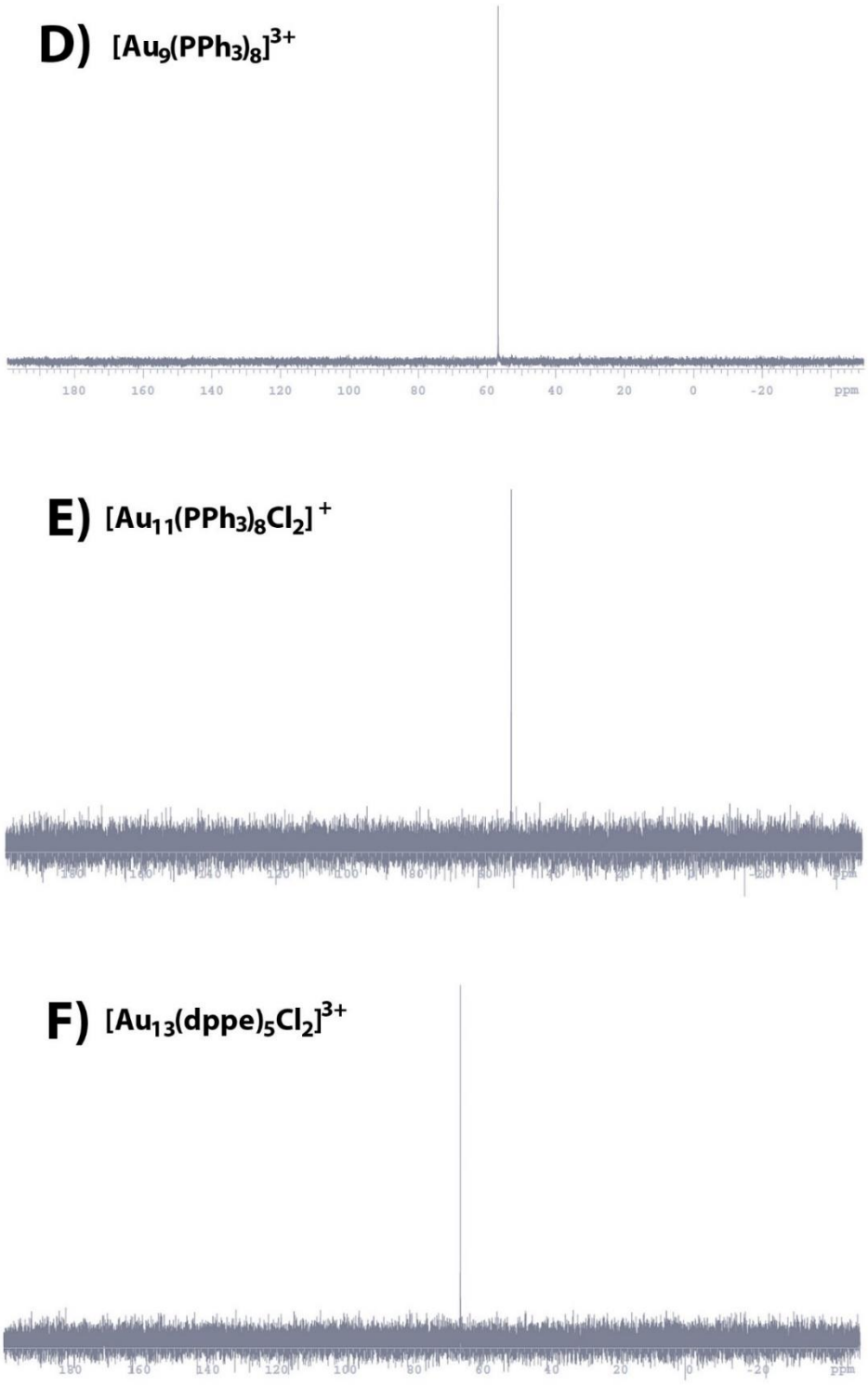

Figure 8.1 – ^{31}P NMR spectra for A) $Au_6(dppp)_4](NO_3)_2$; B) $[Au_8(PPh_3)_8](NO_3)_2$; C) $[Au_8Pd_1(PPh_3)_8](Cl)_2$; D) $[Au_9(PPh_3)_8](NO_3)_3$; E) $[Au_{11}(PPh_3)_8Cl_2]Cl$; F) $[Au_{13}(dppe)_5Cl_2]Cl_3$. Please refer to Sections 8.1.2 - 8.2.7 for specific peak positions.

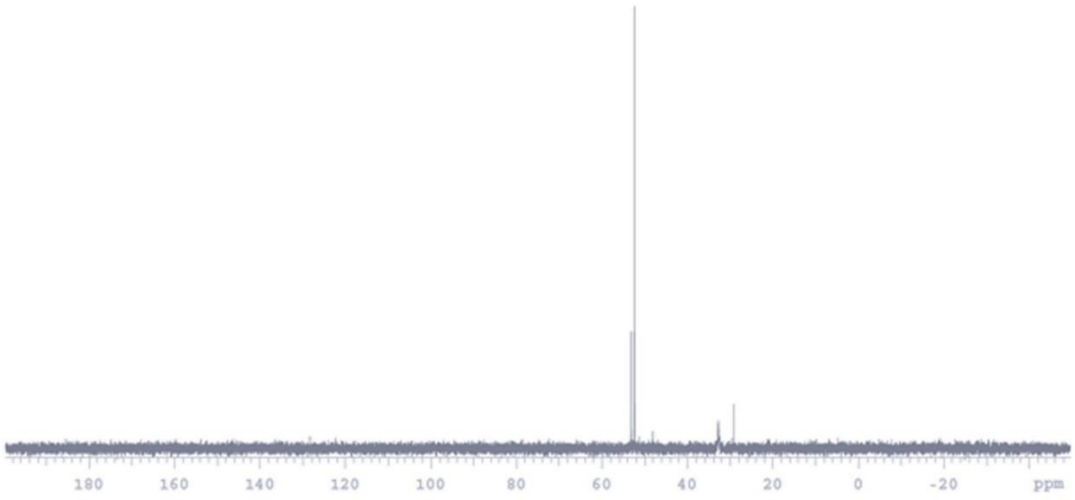

Figure 8.2 – ^{31}P NMR spectrum in $CDCl_3$ illustrating the presence of both Au_{11} isomers, $Au_{11}(PPh_3)_7Cl_3$ (δ = 53 ppm, minor isomer) and $[Au_{11}(PPh_3)_8Cl_2]^+$ (δ = 52 ppm, major isomer), alongside residual $AuPPh_3Cl$ (δ = 33 ppm) and free PPh_3 (δ = 29 ppm). This specimen is the crude product obtained following the method reported by Woerhle *et al.*[250] (Section 3.1.4).

8.2.2 *ESI-MS*

Electrospray Ionisation Mass-Spectrometry (ESI-MS) was performed on a Bruker maXis-II QTOF with the expert assistance of Dr Marie Squire, in the Department of Chemistry at the University of Canterbury. Specimens for mass-spectrometry analysis were dissolved in the appropriate solvent (see Section 8.1 for details), centrifuged, and diluted with an approximate 20-fold quantity (by volume) of acetonitrile.

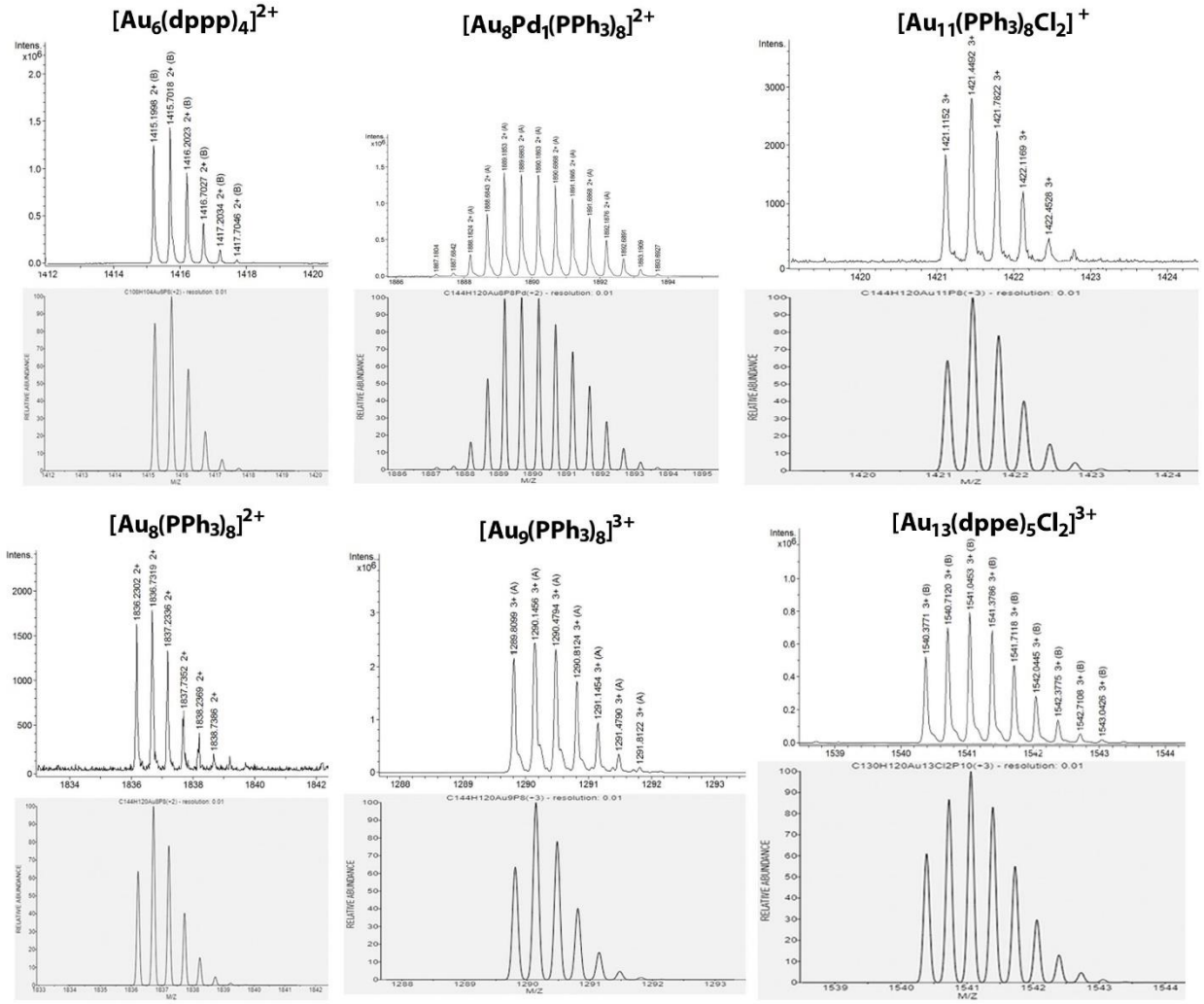

Figure 8.3 – Electrospray ionisation mass-spectrometry (ESI-MS) data for all six gold-phosphine clusters prepared in this work, showing the isotopic distribution pattern for the most-abundant ion (top) and the predicted spectrum for that ion (below). Please refer to Sections 8.1.3-8.3.6 for specific peak positions.

8.2.3 *UV-Vis Absorbance Profiles*

Ultra-Violet/Visible Spectroscopy (UV-Vis) was performed on an Agilent Technologies Cary Series 500 photospectrometer with a 2.5 mL tapered quartz cuvette of path length 10 mm. Analyte concertation was typically *ca.* 0.2 mM in either CH_2Cl_2 (for clusters) or deionised H_2O (for nanoparticles).

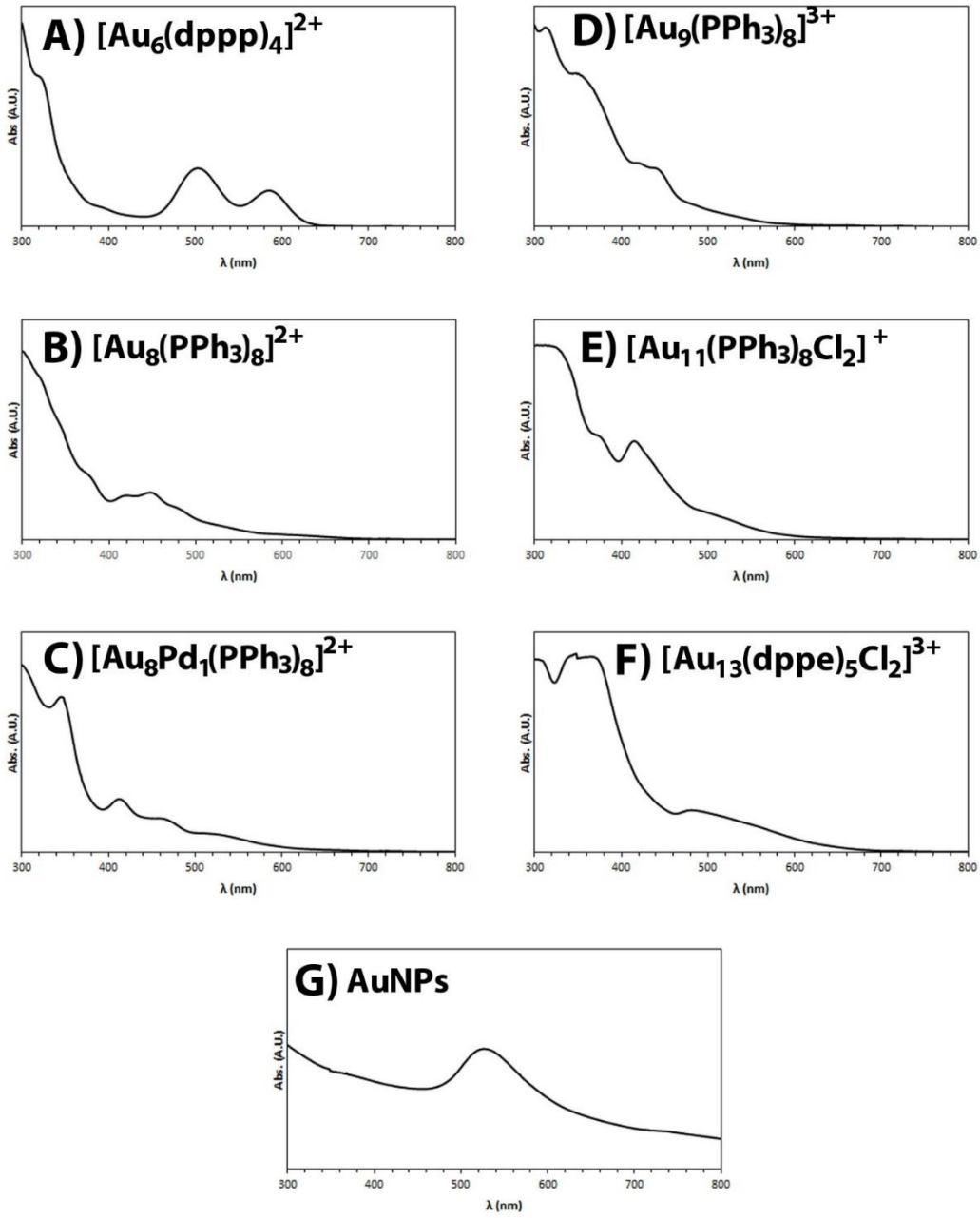

Figure 8.4 – UV-Vis spectra collected in CH_2Cl_2 for A) $[Au_6(dppp)_4]^{2+}$; B) $[Au_8(PPh_3)_8]^{2+}$; C) $[Au_8Pd_1(PPh_3)_8]^{2+}$; D) $[Au_9(PPh_3)_8]^{3+}$; E) $[Au_{11}(PPh_3)_8Cl_2]^{+}$; F) $[Au_{13}(dppe)_5Cl_2]^{3+}$ and in H_2O for H) *ca.* 50-60 nm citrate-capped Au nanoparticles. Note: the feature at 352 nm in Panels G and H is an artefact of the photospectrometer.

8.2.4 *Crystal Structure Data for $[Ag_{25}(SPhMe_2)_{18}](PPh_4)$*

As characterisation of this compound proved difficult by ESI-MS, identity was confirmed by single-crystal X-Ray diffraction, with the unit cell having the expected dimensions and space-group as reported by Bakr *et al.*[259] Single-crystal XRD was performed on an Agilent Technologies Supernova diffractometer with an Eos S2 CCD area detector and a monochromatized Cu-Kα radiation source (λ = 1.5418 Å) at 150 K, at the Research School of Chemistry at the Australian National University (Canberra, ACT) with the expert assistance of Dr James

Ward. Data was processed in *CrysAlis PRO* (version 1.171.38.46)[382] and the structure solved and refined using full-matrix least-squares based on F^2 in SHELXL[383] within the Olex2 program.[384] Empirical absorption corrections were applied using spherical harmonics implemented in SCALE3 ABSPACK within *CrysAlis PRO*.

Crystal Data for $Ag_{25}C_{168}S_{18}P_1H_{162}$: Black prism crystal, 0.18 × 0.07 × 0.06 mm; Triclinic, space group *P*-1 (#2); a = 19.1431(3) Å, b = 19.6438(3) Å, c = 26.9552(4) Å, α = 93.59°, β = 90.60°, γ = 104.56°; V = 9787.8(3) Å^3; Z = 2, μ = 22.44 mm^{-1}, $2\theta_{max}$ = 147.4°, T = 150 K, 170453 measured reflections, 39261 independent reflections [R_{int} = 0.069], 2020 parameters, R_1 and wR_1 = 0.075 and 0.193 ($I > 2\sigma(I)$), maximum/minimum residual electron density +2.55/-3.09 eÅ^{-3}.

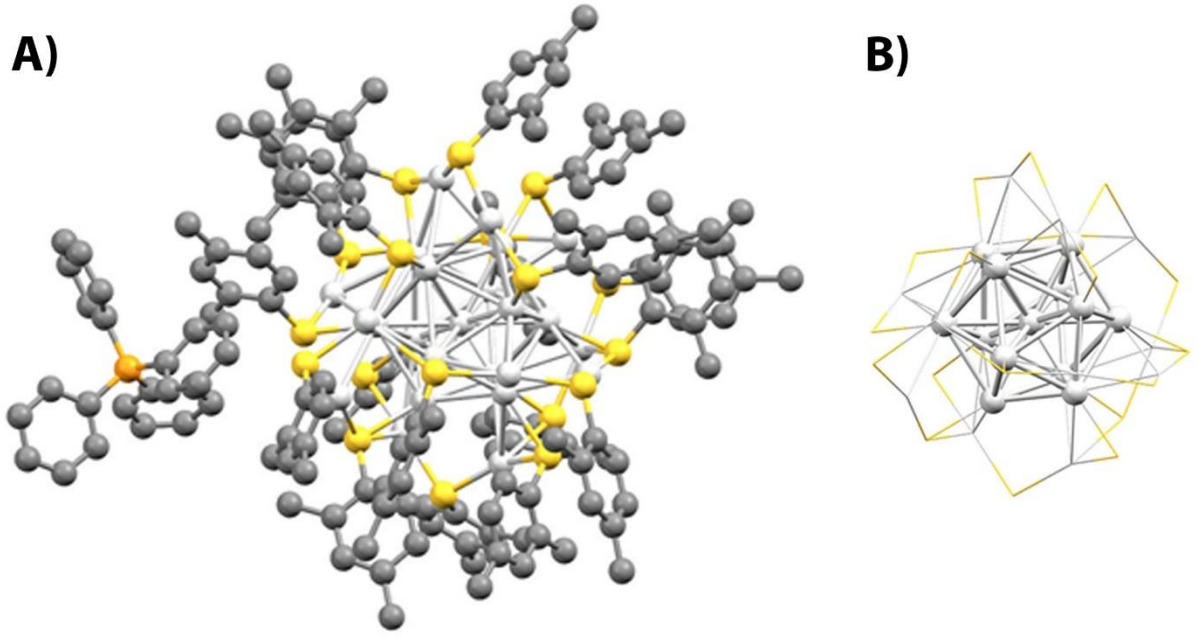

Figure 8.5 – Crystal structure of $[Ag_{25}(SPhMe_2)_{18}](PPh_4)$ (Panel A) collected in this work to unequivocally confirm identity, in absolute agreement with the structure reported by Bakr *et al*.[259] Hydrogen atoms and solvent molecules are omitted for clarity. Panel B shows the interior of the $[Ag_{25}]^-$ cluster, illustrating the six oligomeric $Ag_2(SR)_3$ staples (wire-frame) which decorate the periphery of a centred-icosahedral Ag_{13} core (ball-and-stick). Colour scheme: light-grey, Ag; yellow, S; dark-grey, C; orange, P.

8.3 – Electrode Preparation

8.3.1 *Catalyst Deposition*

Chemically-synthesised nanoclusters were deposited on Vulcan carbon support by the following method. Firstly, if the compound itself contained NO_3^- anions as an artefact of the synthesis procedure ($[Au_6(dppp)_4]^{2+}$, $[Au_8(PPh_3)_8]^{2+}$ and $[Au_9(PPh_3)_8]^{3+}$) these were exchanged for PF_6^- anions *via* metathesis with excess KPF_6 in methanol (which actually renders the compound alcohol-insoluble). The purpose of this is to exclude the possibility of an exaggerated current-response to nitrate from these counterions, which would presumably reside in close proximity to the cluster upon deposition on the cluster support. For all clusters, 200 mg of Vulcan carbon XC-72R was suspended in no more than 15 mL CH_2Cl_2 with sonication to give a viscous slurry. To this was added the appropriate amount of pure cluster (to obtain 20 mg of metal-loading on the cluster support, at 10 wt.%) in no more than 5 mL of CH_2Cl_2 dropwise with stirring to ensure even mixing. After 30 minutes, *ca.* 80 mL hexane was added dropwise *via* burette (*ca.* 2 drops per second) to evenly precipitate the cluster onto the carbon support. Stirring was continued for a further 60 minutes. The carbon supported clusters were collected by centrifugation (colourless supernatants indicated a successful deposition) and washed with hexane and Et_2O, before being dried under vacuum overnight. Gold nanoparticles were deposited by suspending 200 mg Vulcan carbon XC-72R in no more than 15 mL of water with sonication, and to this was added the appropriate amount of the stock colloidal solution prepared in Section 8.3.8 dropwise. The mixture was stirred for one hour before *ca*. 80 mL ethanol was added dropwise *via* burette (*ca.* 2 drops per second) to evenly precipitate the nanoparticles onto the carbon support and stirring was continued overnight. The carbon supported nanoparticles were collected by centrifugation, washed with ethanol and Et_2O before being dried under vacuum overnight. Catalysts were stored in a freezer (< 0 °C) until used.

8.3.2 *Electrode Fabrication*

Electrodes were prepared following a method established by Steven *et al.*[274] with modification. Firstly, solid titanium disks *ca.* 2 cm diameter were mechanically-polished with alumina slurries (0.3 μm and 50 nm particle size, in 1:1 water/methanol v/v) and sonicated sequentially in water and acetone. These were heated to *ca.* 110

°C on a hot-plate and to this was air-cast, by means of compressed N_2 and a hand-held air-gun, 200 μL of a Nafion-117 solution (1.3 mg/mL) in isopropanol. Heating was continued for a further 10 minutes, before the temperature of the hot-plate was decreased to *ca.* 80 °C. During this time, a suspension of catalyst in isopropanol (10 mg/mL, with 76 μL of a 13 mg/mL Nafion-117 stock solution in isopropanol) was prepared by sonication to produce a fine ink. 250 μL of this suspension was applied to the electrode surface in a similar manner, taking care to cast an even coat across the heated titanium surface in an approximate 1 cm diameter disk. This gave an electrode surface which (theoretically) contained 2.5 mg of carbon-catalyst and 5% (by mass) Nafion-117. The electrode was immediately removed from heating and allowed to cool to ambient temperature, before being incorporated into the electrochemical cell-assembly. Electrodes were used within 30 minutes of their preparation.

8.4 – Electrochemical Apparatus

The electrochemical apparatuses consisted of a conventional three-electrode set-up with a 5 mm diameter circular aperture in the base of the cell, to which the working-electrode was exposed to the electrolyte. A Ag/AgCl reference electrode (saturated KCl solution) occupied a chamber auxiliary to the main cell which was connected by means of a luggin capillary. This reference electrode was further encased in a glass-cylinder with a fritted-glass base, to minimise the exchange of electrolytes and restrict the formation of Ag_2SO_4. A coiled Pt wire (surface-area *ca.* 3 cm^2) served as the counter-electrode and was positioned as close to the working-electrode surface as possible, *ca.* 3-5 mm to minimise *IR* drop across solution. Prior to electrochemical measurements, the 0.1 M Na_2SO_4 electrolyte was purged with N_2 for at least 20 minutes to remove dissolved oxygen. A N_2 atmosphere was kept over the duration of the experiment. A series DY-2113 potentiostat (Digi-Ivy, USA) was employed for aqueous electrochemical experiments, and these were carried out locally in the Department of Chemistry laboratories, University of Canterbury.

For non-aqueous electrochemical experiments, differential-pulse voltammograms were collected in anhydrous CH_2Cl_2 with 0.1 M Bu_4NPF_6 (tetra-*n*-butylammonium hexafluorophosphate) supporting electrolyte underneath an argon atmosphere, with a nanocluster concentration of *ca.* 0.2 mM. A thin platinum coil, large platinum sheet and large silver wire were employed as the working, counter and *pseudo*-reference electrodes,

respectively. Beginning at the open-circuit potential for each cluster, the potential was swept between -2 V and +1 V (cathodic and anodic scans recorded separately) with a pulse amplitude of 50 mV, a pulse increment of 2 mV, a pulse duration of 0.5 s and a sample duration of 0.1 s. A Gamry Reference 600+ potentiostat (Gamry Instruments, USA) was employed for non-aqueous electrochemical experiments, and these were carried out with the expert assistance of Mr Hani Taleshiahangari at the Department of Chemical and Process Engineering laboratories, University of Canterbury.

Appendices

Additional Figures and Data

A.1 Exemplar Differential-Pulse Voltammogram

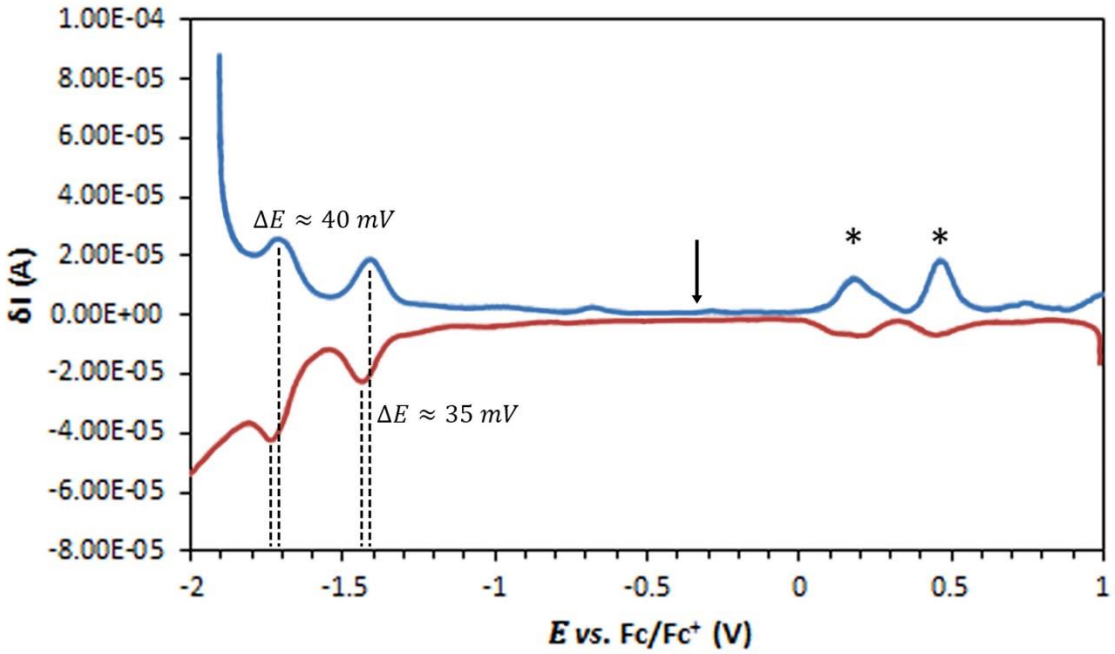

Figure A.1 – Example of complete non-aqueous differential-pulse voltammogram illustrating the distinction between reversible and irreversible charge-transfer events in Chapter 4, in this case for $[Au_8(PPh_3)_8]^{2+}$ in 0.1 M Bu_4NPF_6/CH_2Cl_2. The cathodic (negative-going) scan is shown in red, and the anodic (positive-going) scan is shown in blue. Two reversible reduction events are found at -1.43 and -1.73 V, which are designated-so as a similarly-placed peak is found on both cathodic and anodic scans, which have separation ΔE near 29 mV. Conversely, two oxidation events (denoted by an asterisk) are found at +0.21 and +0.49 V, for which the peak is only appreciable on the anodic scan and is therefore deemed irreversible. The arrow indicates the location of the open-circuit potential for $[Au_8(PPh_3)_8]^{2+}$ (where the system lies at equilibrium) and is where cathodic and anodic scans are divided in Figure 4.1. The reader may appreciate that near the lower- and upper-potential limits, the rapid growth of the differential current may render some features difficult to observe.

A.2 Randles-Sevcik Plots

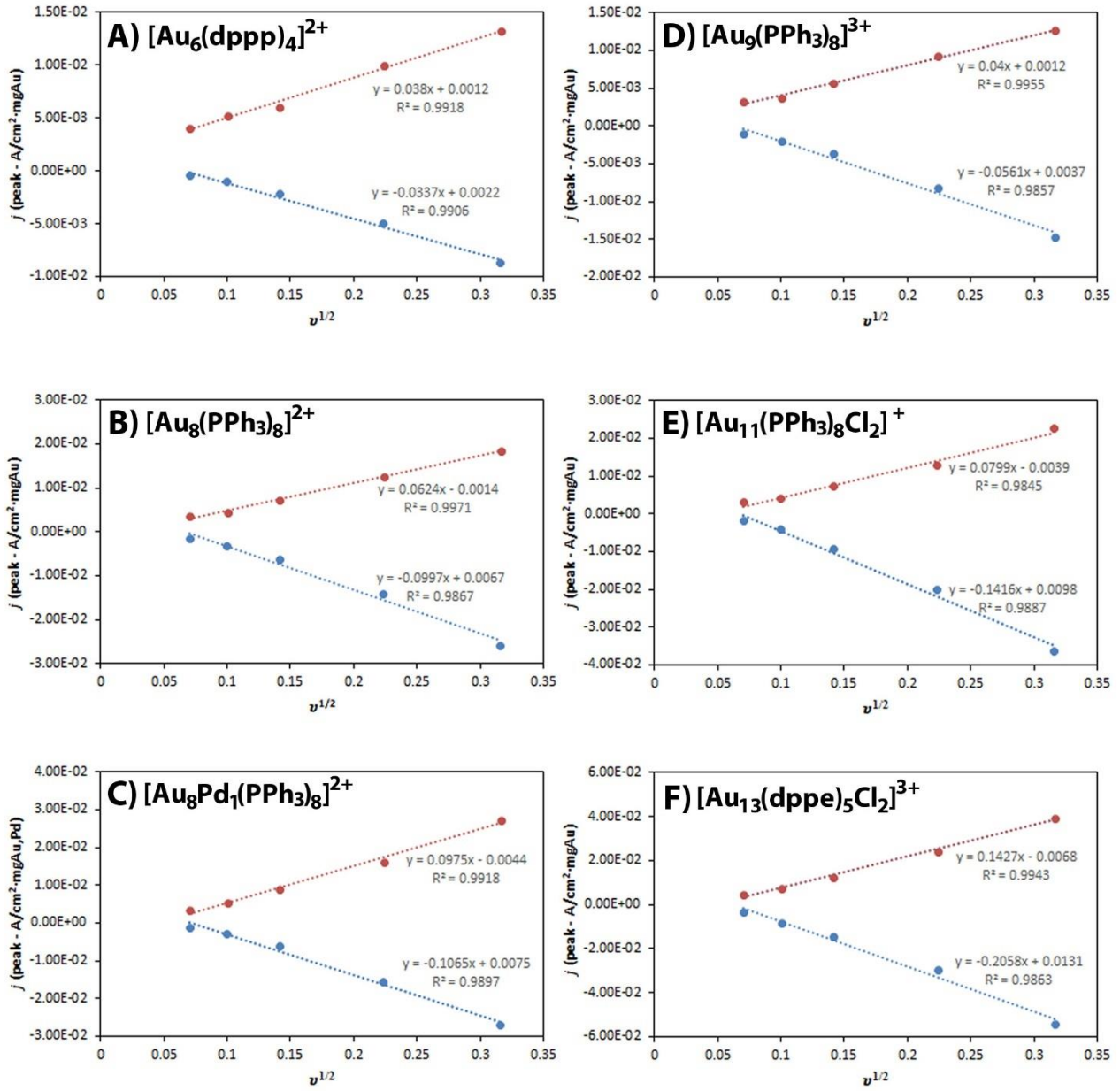

Figure A.2 – Randles-Sevcik plots (Section 6.2.1) of normalised peak current-density (j) as a function of the square-root of scan-rate ($\upsilon^{1/2}$) for nitrate reduction (blue) and nitrite oxidation (red), for A) Au_6; B) Au_8; C) Au_8Pd_1; D) Au_9; E) Au_{11}; F) Au_{13} in N_2-purged 0.1 M Na_2SO_4 with [NO_3^-] = 5 mM, after 10 previous cycles in background electrolyte.

A.3 Laviron Plots

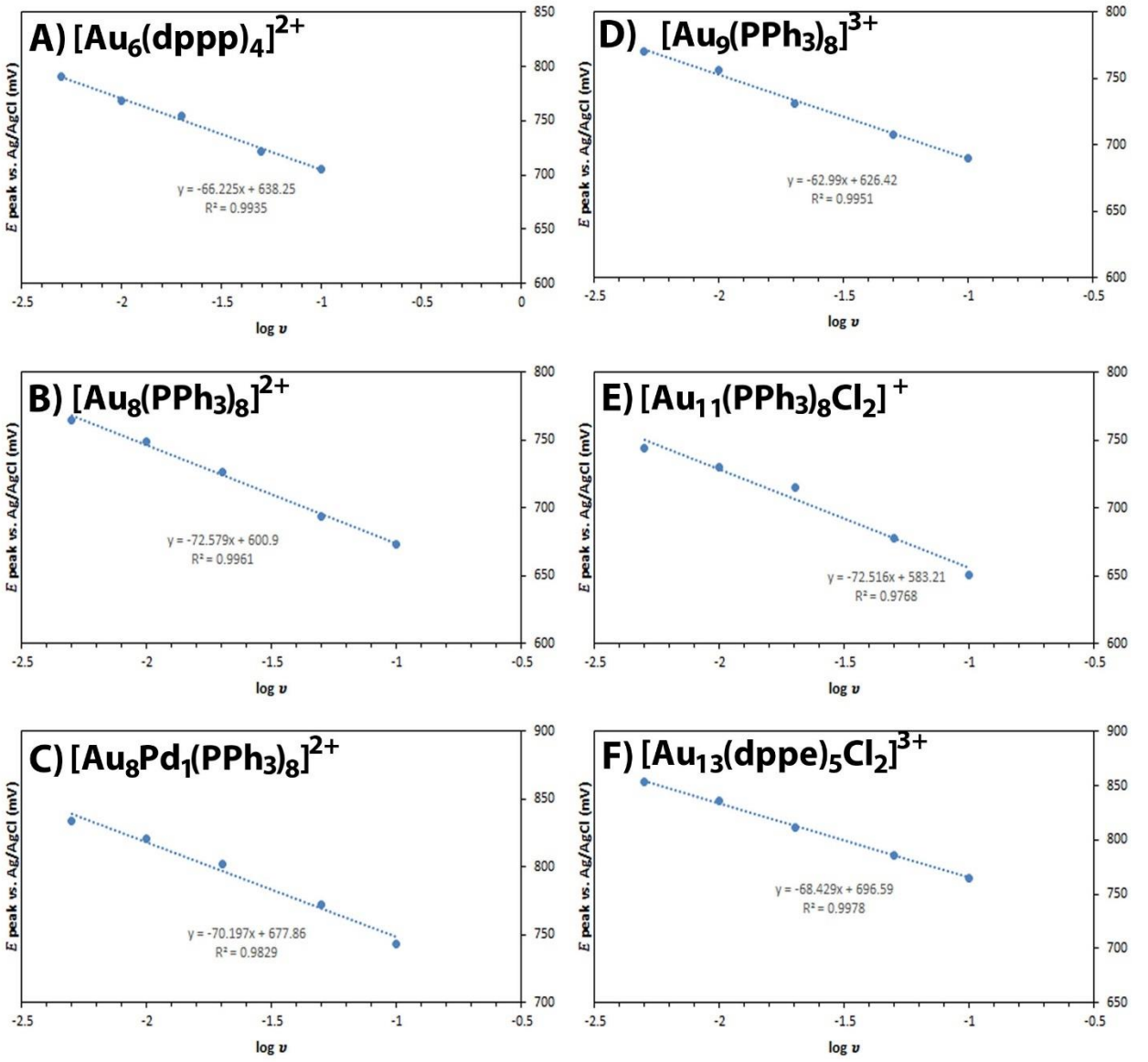

Figure A.3 – Laviron plots (Section 6.2.4) of peak nitrate reduction potential (E) as a function of the logarithm of scan-rate ($\log \upsilon$) for A) Au_6; B) Au_8; C) Au_8Pd_1; D) Au_9; E) Au_{11}; F) Au_{13} in N_2-purged 0.1 M Na_2SO_4 with $[NO_3^-]$ = 5 mM, after 10 previous cycles in background electrolyte

A.4 Current Function Plots

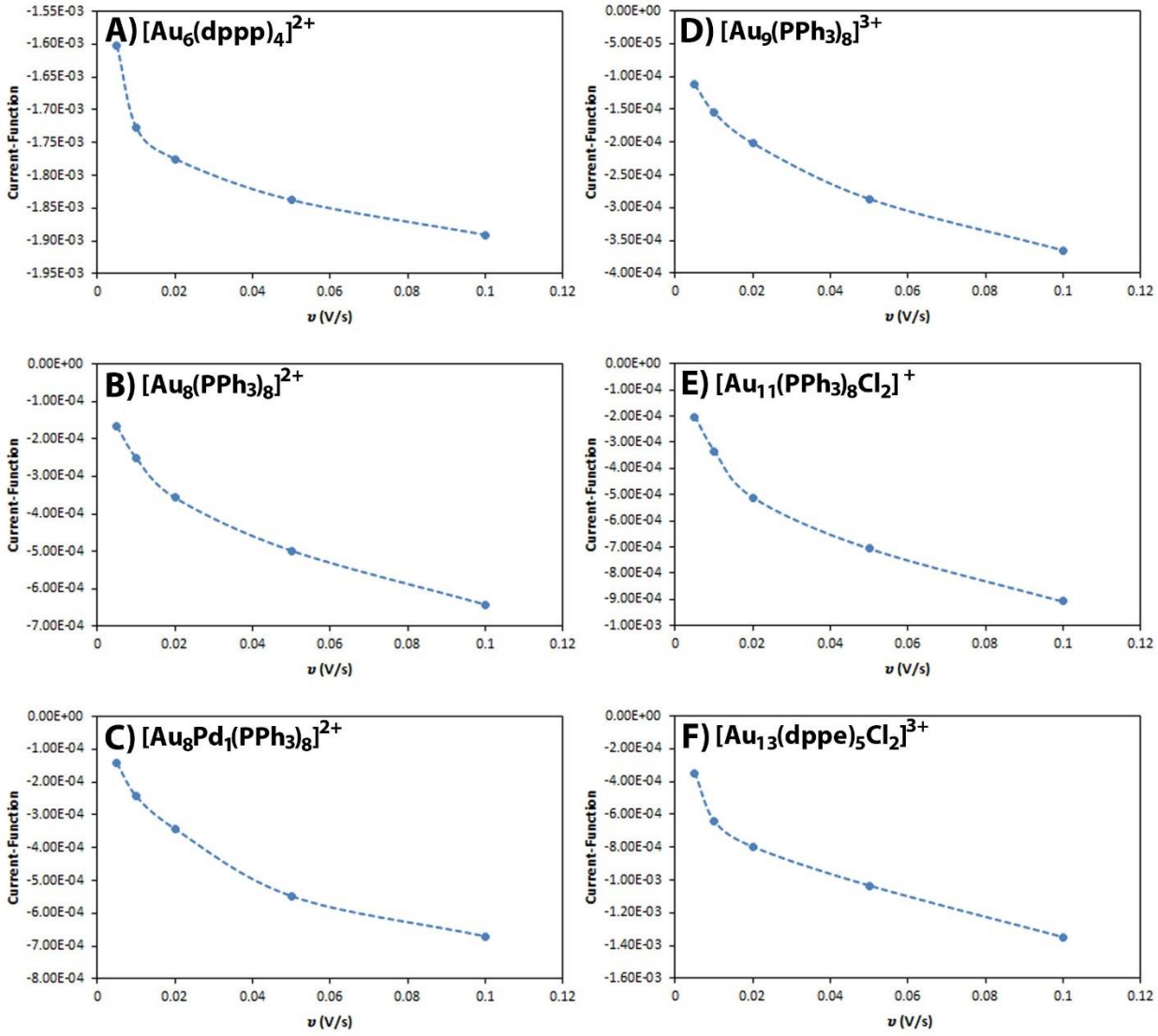

Figure A.4 – Current function plots ($\frac{i_p}{\upsilon^{1/2}}$, Section 6.4) as a function of scan-rate (υ) for A) Au_6; B) Au_8; C) Au_8Pd_1; D) Au_9; E) Au_{11}; F) Au_{13} in N_2-purged 0.1 M Na_2SO_4 with [NO_3^-] = 5 mM, after 10 previous cycles in background electrolyte. A smooth curve (dashed-blue line) is fitted to illustrate this relationship.

A.5 Example Differential-Pulse Voltammogram for Nitrate Sensing Using a Carbon Supported Gold-Phosphine Nanocluster

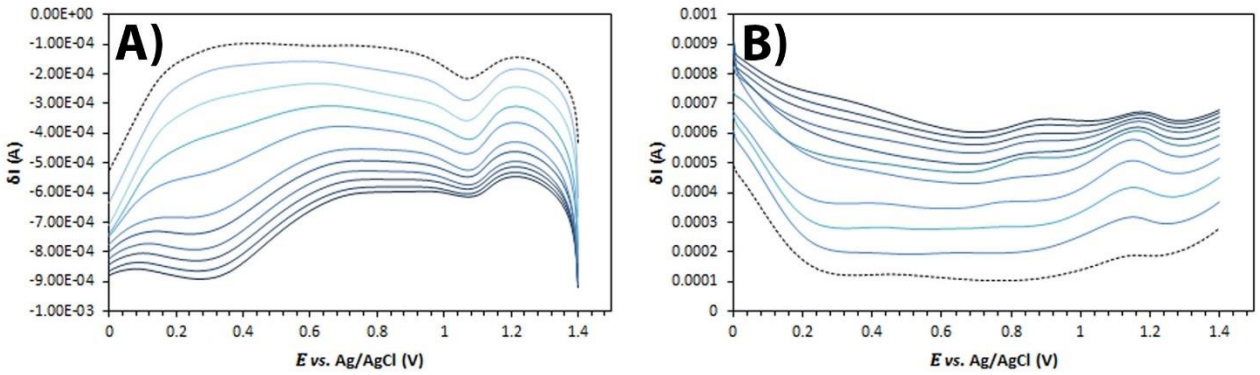

Figure A.5 – Differential-pulse voltammograms collected in N_2-purged 0.1 M Na_2SO_4 using carbon-supported Au_{11} catalyst with $NaNO_3$ concentrations 1-10 mM (from light to dark blue), showing cathodic (negative going; Panel A) and anodic (positive-going; Panel B) scans. The electrochemical sensing of nitrate by DPV was unsuccessful in this work due to unknown reasons, as no nitrate reduction peak could be identified in the potential region where this was believed to occur during cyclic voltammetry (*ca*. +0.7 V).

References

1. A. J. Bard and L. R. Faulkner, *Electrochemical Methods: Fundamentals and Applications*, Wiley, 2000.
2. J. A. Camargo and Á. Alonso, *Environment International*, 2006, **32**, 831-849.
3. R. W. McDowell, S. T. Larned and D. J. Houlbrooke, *New Zealand Journal of Marine and Freshwater Research*, 2009, **43**, 985-995.
4. R. F. Spalding and M. E. Exner, *Journal of Environmental Quality*, 1993, **22**, 392-402.
5. J. N. Galloway, *Environmental Pollution*, 1998, **102**, 15-24.
6. D. M. Manassaram, L. C. Backer and D. M. Moll, *Environmental Health Perspectives*, 2006, **114**, 320-327.
7. A. M. Fan and V. E. Steinberg, *Regulatory Toxicology and Pharmacology*, 1996, **23**, 35-43.
8. S. D. Gangolli, P. A. van den Brandt, V. J. Feron, C. Janzowsky, J. H. Koeman, G. J. A. Speijers, B. Spiegelhalder, R. Walker and J. S. Wishnok, *European Journal of Pharmacology: Environmental Toxicology and Pharmacology*, 1994, **292**, 1-38.
9. A. R. Tricker and R. Preussmann, *Mutation Research/Genetic Toxicology*, 1991, **259**, 277-289.
10. IRAC, *IARC Monographs on the Evaluation of Carcinogenic Risks to Humans*, 2010, **94**.
11. Drinking Water Standards for New Zealand, 2008.
12. M. Scott and C. Hanson, 2013.
13. J. i. Janata, *Principles of Chemical Sensors*, Springer, Dordrecht ; New York, 2nd edn., 2009.
14. A. J. Bard, R. Parsons and J. Jordan, *Standard Potentials in Aqueous Solution*, Taylor & Francis, 1985.
15. W. M. Haynes, *CRC Handbook of Chemistry and Physics, 97th Edition*, CRC Press, 2016.
16. F. Scholz, *Electroanalytical Methods: Guide to Experiments and Applications*, Springer Berlin Heidelberg, 2013.
17. J. Fanning, *Coordination Chemistry Reviews*, 2000, **199**, 159-179.
18. C. Milhano and D. Pletcher, in *Modern Aspects of Electrochemistry, No. 45*, ed. R. E. White, Springer New York, New York, NY, 2009, 1-61.
19. V. Rosca, M. Duca, M. T. de Groot and M. T. M. Koper, *Chemical Reviews*, 2009, **109**, 2209-2244.
20. F. Calle-Vallejo, M. Huang, J. B. Henry, M. T. M. Koper and A. S. Bandarenka, *Physical Chemistry Chemical Physics*, 2013, **15**, 3196-3202.
21. R. E. White, *Modern Aspects of Electrochemistry 45*, Springer New York, 2009.
22. M. C. P. M. da Cunha, M. Weber and F. C. Nart, *Journal of Electroanalytical Chemistry*, 1996, **414**, 163-170.
23. O. A. Petrii and T. Y. Safonova, *Journal of Electroanalytical Chemistry*, 1992, **331**, 897-912.
24. S.-E. Bae, K. L. Stewart and A. A. Gewirth, *Journal of the American Chemical Society*, 2007, **129**, 10171-10180.
25. A. P. O'Mullane, *Nanoscale*, 2014, **6**, 4012-4026.
26. C. M. Welch and R. G. Compton, *Analytical and Bioanalytical Chemistry*, 2006, **384**, 601-619.
27. E. Barsoukov and J. R. Macdonald, *Impedance Spectroscopy: Theory, Experiment, and Applications*, Wiley, 2005.
28. D. Sicsic, F. Balbaud-Celerier and B. Tribollet, *European Journal of Inorganic Chemistry*, 2014, **2014**, 6174-6184.
29. J. D. Genders, D. Hartsough and D. T. Hobbs, *Journal of Applied Electrochemistry*, 1996, **26**, 1-9.
30. V. Kyriakou, I. Garagounis, E. Vasileiou, A. Vourros and M. Stoukides, *Catalysis Today*, 2017, **286**, 2-13.
31. K. Pirkanniemi and M. Sillanpää, *Chemosphere*, 2002, **48**, 1047-1060.
32. M. Duca and M. T. M. Koper, *Energy & Environmental Science*, 2012, **5**, 9726-9742.
33. J. Martínez, A. Ortiz and I. Ortiz, *Applied Catalysis B: Environmental*, 2017, **207**, 42-59.
34. D. Reyter, in *Encyclopedia of Applied Electrochemistry*, eds. G. Kreysa, K.-i. Ota and R. F. Savinell, Springer New York, New York, NY, 2014, 585-593.
35. V. Hooda, V. Sachdeva and N. Chauhan, *Reviews in Analytical Chemistry*, 2016, **35**, 99-114.
36. G. E. Dima, A. C. A. de Vooys and M. T. M. Koper, *Journal of Electroanalytical Chemistry (Lausanne, Switzerland)*, 2003, **554-555**, 15-23.
37. R. Seeber, F. Terzi and C. Zanardi, *Functional Materials in Amperometric Sensing: Polymeric, Inorganic, and Nanocomposite Materials for Modified Electrodes*, Springer Berlin Heidelberg, 2014.

38. G. E. Badea, *Electrochimica Acta*, 2009, **54**, 996-1001.
39. D. Reyter, D. Bélanger and L. Roué, *Electrochimica Acta*, 2008, **53**, 5977-5984.
40. K. Bouzek, M. Paidar, A. Sadilkova and H. Bergmann, *Journal of Applied Electrochemistry*, 2001, **31**, 1185-1193.
41. D. Pletcher and Z. Poorabedi, *Electrochimica Acta*, 1979, **24**, 1253-1256.
42. N. Aouina, H. Cachet, C. Debiemme-chouvy and T. T. M. Tran, *Electrochimica Acta*, 2010, **55**, 7341-7345.
43. P. M. Tucker, M. J. Waite and B. E. Hayden, *Journal of Applied Electrochemistry*, 2004, **34**, 781-796.
44. J. Yang, P. Sebastian, M. Duca, T. Hoogenboom and M. T. M. Koper, *Chemical Communications*, 2014, **50**, 2148-2151.
45. A. P. Leontiev, O. A. Brylev and K. S. Napolskii, *Electrochimica Acta*, 2015, **155**, 466-473.
46. M. C. P. M. da Cunha, J. P. I. De Souza and F. C. Nart, *Langmuir*, 2000, **16**, 771-777.
47. M. Dortsiou, I. Katsounaros, C. Polatides and G. Kyriacou, *Environmental Technology*, 2013, **34**, 373-381.
48. I. Katsounaros, D. Ipsakis, C. Polatides and G. Kyriacou, *Electrochimica Acta*, 2006, **52**, 1329-1338.
49. I. Katsounaros, M. Dortsiou, C. Polatides, S. Preston, T. Kypraios and G. Kyriacou, *Electrochimica Acta*, 2012, **71**, 270-276.
50. I. Katsounaros and G. Kyriacou, *Electrochimica Acta*, 2007, **52**, 6412-6420.
51. A. L. Santos, L. Jay Deiner and H. Varela, *Catalysis Communications*, 2008, **9**, 269-272.
52. M. T. de Groot and M. T. M. Koper, *Journal of Electroanalytical Chemistry*, 2004, **562**, 81-94.
53. S. Ureta-Zañartu and C. Yáñez, *Electrochimica Acta*, 1997, **42**, 1725-1731.
54. K. Nishimura, K. Machida and M. Enyo, *Electrochimica Acta*, 1991, **36**, 877-880.
55. T. Ohmori, M. S. El-Deab and M. Osawa, *Journal of Electroanalytical Chemistry*, 1999, **470**, 46-52.
56. M. S. El-Deab, *Electrochimica Acta*, 2004, **49**, 1639-1645.
57. A. K. Vijh, *Journal of Catalysis*, 1974, **32**, 230-236.
58. S. Cattarin, *Journal of Applied Electrochemistry*, 1992, **22**, 1077-1081.
59. H. L. Li, D. H. Robertson, J. Q. Chambers and D. T. Hobbs, *Journal of the Electrochemical Society*, 1988, **135**, 1154-1158.
60. H.-L. Li, J. Q. Chambers and D. T. Hobbs, *Journal of Applied Electrochemistry*, 1988, **18**, 454-458.
61. M. S. Alam, M. A. Hasnat, M. A. Rashed, M. R. Miah and I. S. M. Saiful, *Electrochimica Acta*, 2012, **76**, 102-105.
62. J. Yang, F. Calle-Vallejo, M. Duca and M. T. M. Koper, *Chemcatchem*, 2013, **5**, 1773-1783.
63. I. Katsounaros, M. Dortsiou and G. Kyriacou, *Journal of Hazardous Materials*, 2009, **171**, 323-327.
64. B. Ambrosioni, A. Barthelemy, D. Bejan and N. J. Bunce, *Canadian Journal of Chemistry*, 2014, **92**, 228-233.
65. M. Dortsiou and G. Kyriacou, *Journal of Electroanalytical Chemistry*, 2009, **630**, 69-74.
66. M. C. Figueiredo, J. Souza-Garcia, V. Climent and J. M. Feliu, *Electrochemistry Communications*, 2009, **11**, 1760-1763.
67. E. Lacasa, P. Cañizares, J. Llanos and M. A. Rodrigo, *Journal of Hazardous Materials*, 2012, **213–214**, 478-484.
68. S.-E. Bae and A. A. Gewirth, *Faraday Discussions*, 2009, **140**, 113-123.
69. E. Pérez-Gallent, M. C. Figueiredo, I. Katsounaros and M. T. M. Koper, *Electrochimica Acta*, 2017, **227**, 77-84.
70. C. Roy, J. Deschamps, M. H. Martin, E. Bertin, D. Reyter, S. Garbarino, L. Roué and D. Guay, *Applied Catalysis B: Environmental*, 2016, **187**, 399-407.
71. E. V. Filimonov and A. I. Shcherbakov, *Protection of Metals*, 2004, **40**, 280-285.
72. S. Taguchi and J. M. Feliu, *Electrochimica Acta*, 2007, **52**, 6023-6033.
73. A. V. Rudnev, E. B. Molodkina, M. R. Ehrenburg, R. G. Fedorov and A. I. Danilov, *Russian Journal of Electrochemistry*, 2009, **45**, 1052-1063.
74. G. E. Dima, G. L. Beltramo and M. T. M. Koper, *Electrochimica Acta*, 2005, **50**, 4318-4326.
75. S. Taguchi and J. M. Feliu, *Electrochimica Acta*, 2008, **53**, 3626-3634.
76. Q. Wang, X. Zhao, J. Zhang and X. Zhang, *Journal of Electroanalytical Chemistry*, 2015, **755**, 210-214.

77. M. C. Figueiredo, J. Solla-Gullón, F. J. Vidal-Iglesias, V. Climent and J. M. Feliu, *Catalysis Today*, 2013, **202**, 2-11.
78. M. Duca, B. van der Klugt and M. T. M. Koper, *Electrochimica Acta*, 2012, **68**, 32-43.
79. U. Prüsse, M. Hähnlein, J. Daum and K.-D. Vorlop, *Catalysis Today*, 2000, **55**, 79-90.
80. M. Wasberg and G. Horányi, *Electrochimica Acta*, 1995, **40**, 615-623.
81. S. E. Bae, K. L. Stewart and A. A. Gewirth, *Journal of the American Chemical Society*, 2007, **129**, 10171-10180.
82. H. W. Salzberg and F. Mies, *Journal of the Electrochemical Society*, 1958, **105**, 64-66.
83. C. L. Constantinou, C. N. Costa and A. M. Efstathiou, *Catalysis Today*, 2010, **151**, 190-194.
84. J. F. E. Gootzen, P. G. J. M. Peeters, J. M. B. Dukers, L. Lefferts, W. Visscher and J. A. R. van Veen, *Journal of Electroanalytical Chemistry*, 1997, **434**, 171-183.
85. J. F. E. Gootzen, L. Lefferts and J. A. R. van Veen, *Applied Catalysis A: General*, 1999, **188**, 127-136.
86. J. F. van der Plas and E. Barendrecht, *Electrochimica Acta*, 1980, **25**, 1463-1469.
87. G. E. Dima, V. Rosca and M. T. M. Koper, *Journal of Electroanalytical Chemistry*, 2007, **599**, 167-176.
88. D. Reyter, D. Bélanger and L. Roué, *The Journal of Physical Chemistry C*, 2009, **113**, 290-297.
89. J. Fan, H. Xu, M. Lv, J. Wang, W. Teng, X. Ran, X. Gou, X. Wang, Y. Sun and J. Yang, *New Journal of Chemistry*, 2017, **41**, 2349-2357.
90. M. A. Hasnat, S. Ben Aoun, S. M. Nizam Uddin, M. M. Alam, P. P. Koay, S. Amertharaj, M. A. Rashed, M. M. Rahman and N. Mohamed, *Applied Catalysis A: General*, 2014, **478**, 259-266.
91. S. Kerkeni, E. Lamy-Pitara and J. Barbier, *Catalysis Today*, 2002, **75**, 35-42.
92. T. Chen, H. Li, H. Ma and M. T. M. Koper, *Langmuir*, 2015, **31**, 3277-3281.
93. E. B. Molodkina, M. R. Ehrenburg, Y. M. Polukarov, A. I. Danilov, J. Souza-Garcia and J. M. Feliu, *Electrochimica Acta*, 2010, **56**, 154-165.
94. P. Rodriguez, F. D. Tichelaar, M. T. M. Koper and A. I. Yanson, *Journal of the American Chemical Society*, 2011, **133**, 17626-17629.
95. Y. Y. Birdja, J. Yang and M. T. M. Koper, *Electrochimica Acta*, **140**, 518-524.
96. I. G. Casella and M. Contursi, *Journal of Electroanalytical Chemistry*, 2006, **588**, 147-154.
97. K. Tada, T. Kawaguchi and K. Shimazu, *Journal of Electroanalytical Chemistry*, 2004, **572**, 93-99.
98. P. P. Koay, M. S. Alam, M. M. Alam, M. Etesami, M. A. Hasnat and N. Mohamed, *Journal of Environmental Chemical Engineering*, 2016, **4**, 4494-4502.
99. F. Gauthard, F. Epron and J. Barbier, *Journal of Catalysis*, 2003, **220**, 182-191.
100. X. Chen, X. Huo, J. Liu, Y. Wang, C. J. Werth and T. J. Strathmann, *Chemical Engineering Journal*, 2017, **313**, 745-752.
101. J. Garcia-Domenech, M. A. Climent, A. Aldaz, J. L. Vazquez and J. Clavilier, *Journal of Electroanalytical Chemistry and Interfacial Electrochemistry*, 1983, **159**, 223-227.
102. X.-K. Xing and D. A. Scherson, *Journal of Electroanalytical Chemistry and Interfacial Electrochemistry*, 1986, **199**, 485-488.
103. S.-J. Hsieh and A. A. Gewirth, *Langmuir*, 2000, **16**, 9501-9512.
104. X. Xing and D. Scherson, *Journal of Electroanalytical Chemistry and Interfacial Electrochemistry*, 1989, **270**, 273-284.
105. M. Huang, J. B. Henry, B. B. Berkes, A. Maljusch, W. Schuhmann and A. S. Bondarenko, *Analyst*, 2012, **137**, 631-640.
106. S. Hwang, J. Lee and J. Kwak, *Journal of Electroanalytical Chemistry*, 2005, **579**, 143-152.
107. F. Armijo, M. Isaacs, G. Ramírez, E. Trollund, J. Canales and M. a. J. Aguirre, *Journal of Electroanalytical Chemistry*, 2004, **566**, 315-322.
108. J. Shen, Y. Y. Birdja and M. T. M. Koper, *Langmuir*, 2015, **31**, 8495-8501.
109. M. H. Barley, K. J. Takeuchi and T. J. Meyer, *Journal of the American Chemical Society*, 1986, **108**, 5876-5885.
110. K. S. Rajmohan and R. Chetty, *Journal of Applied Electrochemistry*, 2017, **47**, 63-74.
111. N. Chebotareva and T. Nyokong, *Journal of Applied Electrochemistry*, 1997, **27**, 975-981.
112. Y. Xiang, D.-L. Zhou and J. F. Rusling, *Journal of Electroanalytical Chemistry*, 1997, **424**, 1-3.
113. L. Ma and H. L. Li, *Electroanalysis (New York, N.Y.)*, 1995, **7**, 756-758.
114. E. Simon, E. Sablé, H. Handel and M. L'Her, *Electrochimica Acta*, 1999, **45**, 855-863.

115. L. Ma, B.-Y. Zhang, H.-L. Li and J. Q. Chambers, *Journal of Electroanalytical Chemistry*, 1993, **362**, 201-205.
116. I. Taniguchi, N. Nakashima, K. Matsushita and K. Yasukouchi, *Journal of Electroanalytical Chemistry and Interfacial Electrochemistry*, 1987, **224**, 199-209.
117. T. Yoshioka, K. Iwase, S. Nakanishi, K. Hashimoto and K. Kamiya, *Journal of Physical Chemistry C*, 2016, **120**, 15729-15734.
118. S. Kuwabata, S. Uezumu, K. Tanaka and T. Tanaka, *Journal of the Chemical Society, Chemical Communications*, 1986, 135-136.
119. N. Barrabés and J. Sá, *Applied Catalysis B: Environmental*, 2011, **104**, 1-5.
120. M. J. Moorcroft, J. Davis and R. G. Compton, *Talanta*, 2001, **54**, 785-803.
121. P. Griess, *Berichte der Deutschen Chemischen Gesellschaft (In German)*, 1879, **12**, 426-428.
122. C. R. Sawicki and F. P. Scaringelli, *Microchemical Journal*, 1971, **16**, 657-672.
123. K. V. H. Sastry, R. P. Moudgal, J. Mohan, J. S. Tyagi and G. S. Rao, *Analytical Biochemistry*, 2002, **306**, 79-82.
124. J. A. Morales, L. S. de Graterol and J. Mesa, *Journal of Chromatography A*, 2000, **884**, 185-190.
125. *International Journal of Environmental Analytical Chemistry*, 2001, **80**, 49-59.
126. C. R. Sawicki, *Analytical Letters*, 1971, **4**, 761-775.
127. T. Le Goff, J. Braven, L. Ebdon, N. P. Chilcott, D. Scholefield and J. W. Wood, *Analyst*, 2002, **127**, 507-511.
128. K. Markušová, *Analytica Chimica Acta*, 1989, **221**, 131-138.
129. J. W. Collat and J. J. Lingane, *Journal of the American Chemical Society*, 1954, **76**, 4214-4218.
130. H. W. Wharton, *Journal of Electroanalytical Chemistry,* 1959, 1965, **9**, 134-139.
131. R. E. Hamm and C. D. Withrow, *Analytical Chemistry*, 1955, **27**, 1913-1915.
132. M. G. Johnson and R. J. Robinson, *Analytical Chemistry*, 1952, **24**, 366-369.
133. D. Veselinović and D. Marković, *Journal of Electroanalytical Chemistry and Interfacial Electrochemistry*, 1976, **71**, 221-228.
134. B. Piela and P. K. Wrona, *Journal of The Electrochemical Society*, 2002, **149**, E55-E63.
135. K. Markušová, L. Kohútová and J. Dzurov, *Electroanalysis*, 1996, **8**, 582-584.
136. N. Comisso, S. Cattarin, P. Guerriero, L. Mattarozzi, M. Musiani, L. Vázquez-Gómez and E. Verlato, *Journal of Solid State Electrochemistry*, 2016, **20**, 1139-1148.
137. S. Ward-Jones, C. E. Banks, A. O. Simm, L. Jiang and R. G. Compton, *Electroanalysis*, 2005, **17**, 1806-1815.
138. C. M. Welch, M. E. Hyde, C. E. Banks and R. G. Compton, *Analytical sciences*, 2005, **21**, 1421-1430.
139. C. M. Welch, A. O. Simm and R. G. Compton, *Electroanalysis*, 2006, **18**, 965-970.
140. L. Guadagnini and D. Tonelli, *Sensors and Actuators B-Chemical*, 2013, **188**, 806-814.
141. M. Bonyani, A. Mirzaei, S. G. Leonardi, A. Bonavita and G. Neri, *Electroanalysis*, 2015, **27**, 2654-2662.
142. M.-P. N. Bui, J. Brockgreitens, S. Ahmed and A. Abbas, *Biosensors and Bioelectronics*, 2016, **85**, 280-286.
143. X. Luo, A. Morrin, A. J. Killard and M. R. Smyth, *Electroanalysis*, 2006, **18**, 319-326.
144. R. W. Murray, *Chemical Reviews*, 2008, **108**, 2688-2720.
145. F. W. Campbell and R. G. Compton, *Analytical and Bioanalytical Chemistry*, 2010, **396**, 241-259.
146. S. E. F. Kleijn, S. C. S. Lai, M. T. M. Koper and P. R. Unwin, *Angewandte Chemie International Edition*, 2014, **53**, 3558-3586.
147. I. Streeter, R. Baron and R. G. Compton, *The Journal of Physical Chemistry C*, 2007, **111**, 17008-17014.
148. J. Davis, M. J. Moorcroft, S. J. Wilkins, R. G. Compton and M. F. Cardosi, *Analyst*, 2000, **125**, 737-742.
149. M. Trojanowicz, in *Comprehensive Analytical Chemistry*, eds. M. Valcárcel and Á. I. López-Lorente, Elsevier, 2014, vol. 66, pp. 429-476.
150. M. Faraday, *Philisophical Transactions of the Royal Society of London*, 1857, **147**, 145-181.
151. G. Mie, *Annalen der Physik (In German)*, 1908, **330**, 377-445.
152. R. Zsimondy, *The Chemistry of the Colloids*, Wiley, New York, 1917.

153. R. Gans, *Annalen der Physik (In German)*, 1912, **342**, 881-900.
154. H. B. Weiser, *The Colloidal Elements*, John Wiley & Sons, New York, 1933.
155. H. Wang, D. W. Brandl, P. Nordlander and N. J. Halas, *Accounts of Chemical Research*, 2006, **40**, 53-62.
156. T. Sreeprasad and T. Pradeep, in *Springer Handbook of Nanomaterials* ed. R. Vajtai, Springer, Berlin, 2013, ch. 2, pp. 303-388.
157. J. Turkevich, P. C. Stevenson and J. Hillier, *Discussions of the Faraday Society*, 1951, **11**, 55-75.
158. M. Brust, M. Walker, D. Bethell, D. J. Schiffrin and R. Whyman, *Journal of the Chemical Society. Chemical Communications*, 1994, **0**, 801-802.
159. M. Chen, D. Kumar, C.-W. Yi and D. W. Goodman, *Science*, 2005, **310**, 291-293.
160. H. Masatake, K. Tetsuhiko, S. Hiroshi and Y. Nobumasa, *Chemistry Letters*, 1987, **16**, 405-408.
161. G. J. Hutchings, *Journal of Catalysis*, 1985, **96**, 292-295.
162. A. Corma, A. Leyva-Pérez and M. J. Sabater, *Chemical Reviews*, 2011, **111**, 1657-1712.
163. Y. Zhang, X. Cui, F. Shi and Y. Deng, *Chemical Reviews*, 2012, **112**, 2467-2505.
164. M. Stratakis and H. Garcia, *Chemical Reviews*, 2012, **112**, 4469-4506.
165. G. J. Hutchings, *Catalysis Today*, 2005, **100**, 55-61.
166. R. Jin, *Nanotechnology Reviews*, 2012, **1**, 31-56.
167. D. Astruc, in *Nanoparticles and Catalysis*, Wiley-VCH Verlag GmbH & Co. KGaA, 2008, 1-48.
168. R. Ciriminna, E. Falletta, C. Della Pina, J. H. Teles and M. Pagliaro, *Angewandte Chemie International Edition*, 2016, **55**, 14210-14217.
169. J. Fang, B. Zhang, Q. Yao, Y. Yang, J. Xie and N. Yan, *Coordination Chemistry Reviews*, 2016, **322**, 1-29.
170. E. C. Tyo and S. Vajda, *Nature Nanotechnology*, 2015, **10**, 577-588.
171. Y. Zhu, H. Qian and R. Jin, *Journal of Materials Chemistry*, 2011, **21**, 6793-6799.
172. G. Li, *Accounts of Chemical Research*, 2012, **46**, 1749-1758.
173. I. Chakraborty and T. Pradeep, *Chemical Reviews*, 2017, **117**, 8208-8271.
174. M. M. Alvarez, J. T. Khoury, T. G. Schaaff, M. N. Shafigullin, I. Vezmar and R. L. Whetten, *The Journal of Physical Chemistry B*, 1997, **101**, 3706-3712.
175. C. Noguez, *The Journal of Physical Chemistry C*, 2007, **111**, 3806-3819.
176. R. Jin, *Nanoscale*, 2010, **2**, 343-362.
177. R. Jin, C. Zeng, M. Zhou and Y. Chen, *Chemical Reviews*, 2016, **116**, 10346-10413.
178. K. Kwak, V. D. Thanthirige, K. Pyo, D. Lee and G. Ramakrishna, *The Journal of Physical Chemistry Letters*, 2017, **8**, 4898-4905.
179. H. C. Weissker, H. B. Escobar, V. D. Thanthirige, K. Kwak, D. Lee, G. Ramakrishna, R. L. Whetten and X. Lopez-Lozano, *Nature Communications*, 2014, **5**, 1-8.
180. D. M. P. Mingos, *Gold Clusters, Colloids and Nanoparticles I*, Springer International Publishing, 2014.
181. R. Jin, Y. Zhu and H. Qian, *Chem Eur J*, 2011, **17**.
182. Y. Negishi, T. Nakazaki, S. Malola, S. Takano, Y. Niihori, W. Kurashige, S. Yamazoe, T. Tsukuda and H. Häkkinen, *Journal of the American Chemical Society*, 2015, **137**, 1206-1212.
183. auml and H. kkinen, *Advances in Physics: X*, 2016, **1**, 467-491.
184. S. Antonello and F. Maran, *Current Opinion in Electrochemistry*, 2017, **2**, 18-25.
185. S. Antonello, M. Hesari, F. Polo and F. Maran, *Nanoscale*, 2012, **4**, 5333-5342.
186. S. Antonello, A. H. Holm, E. Instuli and F. Maran, *Journal of the American Chemical Society*, 2007, **129**, 9836-9837.
187. J. J. Pietron, J. F. Hicks and R. W. Murray, *Journal of the American Chemical Society*, 1999, **121**, 5565-5570.
188. M. J. Weaver and X. P. Gao, *Journal of Physical Chemistry*, 1993, **97**, 332-338.
189. Y. Kamei, N. Robertson, Y. Shichibu and K. Konishi, *The Journal of Physical Chemistry C*, 2015, **119**, 10995-10999.
190. T. Ohta, M. Shibuta, H. Tsunoyama, Y. Negishi, T. Eguchi and A. Nakajima, *The Journal of Physical Chemistry C*, 2013, **117**, 3674-3679.
191. A. Venzo, S. Antonello, J. A. Gascón, I. Guryanov, R. D. Leapman, N. V. Perera, A. Sousa, M. Zamuner, A. Zanella and F. Maran, *Analytical Chemistry*, 2011, **83**.

192. J. F. Hicks, D. T. Miles and R. W. Murray, *Journal of the American Chemical Society*, 2002, **124**, 13322-13328.
193. B. M. Quinn, P. Liljeroth, V. Ruiz, T. Laaksonen and K. Kontturi, *Journal of the American Chemical Society*, 2003, **125**, 6644-6645.
194. D. García-Raya, R. Madueño, M. Blázquez and T. Pineda, *The Journal of Physical Chemistry C*, 2009, **113**, 8756-8761.
195. S. Chen, R. S. Ingram, M. J. Hostetler, J. J. Pietron, R. W. Murray, T. G. Schaaff, J. T. Khoury, M. M. Alvarez and R. L. Whetten, *Science*, 1998, **280**, 2098-2101.
196. K. Kwak, W. Choi, Q. Tang, M. Kim, Y. Lee, D. E. Jiang and D. Lee, *Nature Communications*, 2017, **8**.
197. W. Chen and S. Chen, *Angewandte Chemie (International ed.)*, 2009, **48**, 4386-4389.
198. Z. Liu, M. Z. Zhu, X. M. Meng, G. Y. Xu and R. Jin, *Journal of Physical Chemistry Letters*, 2011, **2**.
199. S. S. Kumar, K. Kwak and D. Lee, *Analytical Chemistry*, 2011, **83**, 3244-3247.
200. G. Baek, P. Pandurangan, E. Ko, Y. Mo and D. Lee, *RSC Advances*, 2014, **4**, 10766-10769.
201. K. Kwak, S. S. Kumar, K. Pyo and D. Lee, *ACS Nano*, 2014, **8**, 671-679.
202. C. M. Sims, S. K. Hanna, D. A. Heller, C. P. Horoszko, M. E. Johnson, A. R. Montoro Bustos, V. Reipa, K. R. Riley and B. C. Nelson, *Nanoscale*, 2017, **9**, 15226-15251.
203. V. G. Albano, P. L. Bellon, M. Manassero and M. Sansoni, *Journal of the Chemical Society D: Chemical Communications*, 1970, 1210-1211.
204. G. Schmid, R. Pfeil, R. Boese, F. Bandermann, S. Meyer, G. H. M. Calis and J. W. A. van der Velden, *Chemische Berichte (In German)*, 1981, **114**, 3634-3642.
205. D. M. P. Mingos and M. J. Watson, in *Advances in Inorganic Chemistry*, ed. A. G. Sykes, Academic Press, 1992, vol. 39, pp. 327-399.
206. Z. Wu, M. A. MacDonald, J. Chen, P. Zhang and R. Jin, *Journal of the American Chemical Society*, 2011, **133**.
207. M. W. Heaven, A. Dass, P. S. White, K. M. Holt and R. W. Murray, *Journal of the American Chemical Society*, 2008, **130**, 3754-3755.
208. M. Zhu, C. M. Aikens, F. J. Hollander, G. C. Schatz and R. Jin, *Journal of the American Chemical Society*, 2008, **130**, 5883-5885.
209. H. Qian, W. T. Eckenhoff, Y. Zhu, T. Pintauer and R. Jin, *Journal of the American Chemical Society*, 2010, **132**.
210. P. D. Jadzinsky, G. Calero, C. J. Ackerson, D. A. Bushnell and R. D. Kornberg, *Science*, 2007, **318**, 430-433.
211. W. Kurashige, Y. Niihori, S. Sharma and Y. Negishi, *Coordination Chemistry Reviews*, 2016, **320**, 238-250.
212. R. Jin, *Nanoscale*, 2015, **7**, 1549-1565.
213. H. Qian, M. Zhu, Z. Wu and R. Jin, *Accounts of Chemical Research*, 2012, **45**, 1470-1479.
214. Y. Lu and W. Chen, *Chemical Society Reviews*, 2012, **41**, 3594-3623.
215. X. Yuan, X. Dou, K. Zheng and J. Xie, *Particle & Particle Systems Characterization*, 2015, **32**, 613-629.
216. D. M. P. Mingos, *Journal of the Chemical Society, Dalton Transactions*, 1996, 561-566.
217. C. E. Briant, B. R. C. Theobald, J. W. White, L. K. Bell, D. M. P. Mingos and A. J. Welch, *Journal of the Chemical Society, Chemical Communications*, 1981, 201-202.
218. M. Laupp and J. Strähle, *Angewandte Chemie International Edition*, 1994, **33**, 207-209.
219. K. Konishi, in *Gold Clusters, Colloids and Nanoparticles I*, ed. D. M. P. Mingos, Springer International Publishing, Cham, 2014, 49-86.
220. E. B. Guidez, A. Hadley and C. M. Aikens, *Journal of Physical Chemistry C*, 2011, **115**, 6305-6316.
221. J. W. Hudgens, J. M. Pettibone, T. P. Senftle and R. N. Bratton, *Inorganic Chemistry*, 2011, **50**, 10178-10189.
222. J. J. Steggerda, J. J. Bour and J. W. A. van der Velden, *Recueil des Travaux Chimiques des Pays-Bas*, 1982, **101**, 164-170.
223. F. A. Vollenbroek, J. J. Bour, J. M. Trooster and J. W. A. van der Velden, *Journal of the Chemical Society, Chemical Communications*, 1978, DOI: 10.1039/C39780000907, 907-909.
224. D. M. P. Mingos, *Polyhedron*, 1984, **3**, 1289-1297.
225. D. M. P. Mingos, *Dalton Transactions*, 2015, **44**, 6680-6695.

226. D. M. P. Mingos, *Gold Bulletin*, 1984, **17**, 5-12.
227. D. M. P. Mingos, *Accounts of Chemical Research*, 1984, **17**, 311-319.
228. J. W. A. Van der Velden and Z. M. Stadnik, *Inorganic chemistry*, 1984, **23**, 2640-2644.
229. M. Walter, J. Akola, O. Lopez-Acevedo, P. D. Jadzinsky, G. Calero, C. J. Ackerson, R. L. Whetten, H. Grönbeck and H. Häkkinen, *Proceedings of the National Academy of Sciences*, 2008, **105**, 9157-9162.
230. D. M. Lindsay, Y. Wang and T. F. George, *The Journal of Chemical Physics*, 1987, **86**, 3500-3511.
231. A. C. Reber and S. N. Khanna, *Accounts of Chemical Research*, 2017, **50**, 255-263.
232. J. W. A. van der Velden, J. J. Bour, W. P. Bosman, J. H. Noordik and P. T. Beurskens, *Recueil des Travaux Chimiques des Pays-Bas*, 1984, **103**, 13-16.
233. F. Wen, U. Englert, B. Gutrath and U. Simon, *European Journal of Inorganic Chemistry*, 2008, **2008**, 106-111.
234. C. E. Briant, K. P. Hall and D. M. P. Mingos, *Journal of the Chemical Society, Chemical Communications*, 1984, 290-291.
235. J. G. M. Van der Linden, A. M. Roelofsen and G. H. W. Ipskamp, *Inorganic chemistry*, 1989, **28**, 967-970.
236. M. Schulz-Dobrick and M. Jansen, *European Journal of Inorganic Chemistry*, 2006, **2006**, 4498-4502.
237. K. P. Hall, B. R. C. Theoblad, D. I. Gilmour, D. M. P. Mingos and A. J. Welch, *Journal of the Chemical Society, Chemical Communications*, 1982, 528-530.
238. D. P. Anderson, J. F. Alvino, A. Gentleman, H. Al Qahtani, L. Thomsen, M. I. J. Polson, G. F. Metha, V. B. Golovko and G. G. Andersson, *Physical Chemistry Chemical Physics*, 2013, **15**, 3917-3929.
239. J. W. A. Van der Velden, J. J. Bour, J. J. Steggerda, P. T. Beurskens, M. Roseboom and J. H. Noordik, *Inorganic Chemistry*, 1982, **21**, 4321-4324.
240. J. M. Pettibone and J. W. Hudgens, *ACS Nano*, 2011, **5**.
241. Y. Shichibu and K. Konishi, *Inorganic Chemistry*, 2013, **52**, 6570-6575.
242. Y. Shichibu, Y. Kamei and K. Konishi, *Chemical Communications*, 2012, **48**, 7559-7561.
243. Y. Shichibu, M. Zhang, Y. Kamei and K. Konishi, *Journal of the American Chemical Society*, 2014, **136**, 12892-12895.
244. F. A. Vollenbroek, W. P. Bosman, J. J. Bour, J. H. Noordik and P. T. Beurskens, *Journal of the Chemical Society, Chemical Communications*, 1979, 387-388.
245. M. Manassero, L. Naldini and M. Sansoni, *Journal of the Chemical Society, Chemical Communications*, 1979, 385-386.
246. F. A. Vollenbroek, J. J. Bour and J. W. A. van der Veden, *Recueil des Travaux Chimiques des Pays-Bas*, 1980, **99**, 137-141.
247. J. W. A. Van der Velden, J. J. Bour, W. P. Bosman and J. H. Noordik, *Inorganic Chemistry*, 1983, **22**, 1913-1918.
248. B. S. Gutrath, F. Schiefer, M. Homberger, U. Englert, M.-D. Şerb, W. Bettray, I. Beljakov, V. Meded, W. Wenzel and U. Simon, *European Journal of Inorganic Chemistry*, 2016, **2016**, 975-981.
249. P. L. Bellon, F. Cariati, M. Manassero, L. Naldini and M. Sansoni, *Journal of the Chemical Society D: Chemical Communications*, 1971, 1423-1424.
250. G. H. Woehrle, M. G. Warner and J. E. Hutchison, *The Journal of Physical Chemistry B*, 2002, **106**, 9979-9981.
251. L. C. McKenzie, T. O. Zaikova and J. E. Hutchison, *Journal of the American Chemical Society*, 2014, **136**, 13426-13435.
252. S. Matsuo, S. Takano, S. Yamazoe, K. Koyasu and T. Tsukuda, *ChemElectroChem*, 2016, **3**, 1206-1211.
253. S. Yamazoe, S. Matsuo, S. Muramatsu, S. Takano, K. Nitta and T. Tsukuda, *Inorganic Chemistry*, 2017, **56**, 8319-8325.
254. Y. Shichibu and K. Konishi, *Small*, 2010, **6**, 1216-1220.
255. H. Hakkinen, *Chemical Society Reviews*, 2008, **37**, 1847-1859.
256. D. Padayachee, V. Golovko, B. Ingham and A. T. Marshall, *Electrochimica Acta*, 2014, **120**, 398-407.
257. J. Kimling, M. Maier, B. Okenve, V. Kotaidis, H. Ballot and A. Plech, *The Journal of Physical Chemistry B*, 2006, **110**, 15700-15707.

258. W. Haiss, N. T. K. Thanh, J. Aveyard and D. G. Fernig, *Analytical Chemistry*, 2007, **79**, 4215-4221.
259. C. P. Joshi, M. S. Bootharaju, M. J. Alhilaly and O. M. Bakr, *Journal of the American Chemical Society*, 2015, **137**, 11578-11581.
260. X. Kang, S. Chen, S. Jin, Y. Song, Y. Xu, H. Yu, H. Sheng and M. Zhu, *ChemElectroChem*, 2016, **3**, 1261-1265.
261. H. Qian, Y. Zhu and R. Jin, *ACS Nano*, 2009, **3**, 3795-3803.
262. J. G. M. Van der Linden, M. L. H. Paulissen and J. E. J. Schmitz, *Journal of the American Chemical Society*, 1983, **105**, 1903-1907.
263. D. Lee, R. L. Donkers, G. Wang, A. S. Harper and R. W. Murray, *Journal of the American Chemical Society*, 2004, **126**, 6193-6199.
264. T. Ohgi and D. Fujita, *Surface Science*, 2003, **532-535**, 294-299.
265. M. A. Tofanelli and C. J. Ackerson, *Journal of the American Chemical Society*, 2012, **134**, 16937-16940.
266. B. S. Gutrath, U. Englert, Y. Wang and U. Simon, *European Journal of Inorganic Chemistry*, 2013, **2013**, 2002-2006.
267. P. Rodriguez, D. Plana, D. J. Fermin and M. T. M. Koper, *Journal of Catalysis*, 2014, **311**, 182-189.
268. L. D. Burke and P. F. Nugent, *Gold Bulletin*, 1997, **30**, 43-53.
269. K. J. J. Mayrhofer, B. B. Blizanac, M. Arenz, V. R. Stamenkovic, P. N. Ross and N. M. Markovic, *The Journal of Physical Chemistry B*, 2005, **109**, 14433-14440.
270. T. Frelink, W. Visscher and J. A. R. van Veen, *Journal of Electroanalytical Chemistry*, 1995, **382**, 65-72.
271. X.-M. Wang and Y.-Y. Xia, *Electrochimica Acta*, 2009, **54**, 7525-7530.
272. L. D. Burke and P. F. Nugent, *Gold Bulletin*, 1998, **31**, 39-50.
273. S. L. Allen, J. N. Sharma and F. P. Zamborini, *Journal of the American Chemical Society*, 2017, **139**, 12895-12898.
274. J. T. Steven, V. B. Golovko, B. Johannessen and A. T. Marshall, *Electrochimica Acta*, 2016, **187**, 593-604.
275. H. G. Boyen, xe, C. stle, F. Weigl, B. Koslowski, C. Dietrich, P. Ziemann, J. P. Spatz, Riethm, xfc, S. ller, C. Hartmann, xf, M. ller, G. Schmid, M. G. Garnier and P. Oelhafen, *Science*, 2002, **297**, 1533-1536.
276. D. M. Kolb, G. E. Engelmann and J. C. Ziegler, *Angewandte Chemie-International Edition*, 2000, **39**, 1123-+.
277. R. E. Leuchtner, A. C. Harms and A. W. C. Jr., *The Journal of Chemical Physics*, 1989, **91**, 2753-2754.
278. K. Thurmer, E. Williams and J. Reutt-Robey, *Science*, 2002, **297**, 2033-2035.
279. Y. Liu, F. Yang, Y. Zhang, J. P. Xiao, L. Yu, Q. F. Liu, Y. X. Ning, Z. W. Zhou, H. Chen, W. G. Huang, P. Liu and X. H. Bao, *Nature Communications*, 2017, **8**.
280. M. Brust and G. J. Gordillo, *Journal of the American Chemical Society*, 2012, **134**, 3318-3321.
281. C. Batchelor-McAuley, G. G. Wildgoose and R. G. Compton, *New Journal of Chemistry*, 2008, **32**, 941-946.
282. A. Henglein, *Chemical Reviews*, 1989, **89**, 1861-1873.
283. B. E. Hayden, D. Pletcher, M. E. Rendall and J.-P. Suchsland, *The Journal of Physical Chemistry C*, 2007, **111**, 17044-17051.
284. H. Angerstein-Kozlowska, B. E. Conway, A. Hamelin and L. Stoicoviciu, *Electrochimica Acta*, 1986, **31**, 1051-1061.
285. B. E. Conway, *Progress in Surface Science*, 1995, **49**, 331-452.
286. J. T. Miller, A. J. Kropf, Y. Zha, J. R. Regalbuto, L. Delannoy, C. Louis, E. Bus and J. A. van Bokhoven, *Journal of Catalysis*, 2006, **240**, 222-234.
287. L. K. Ono and B. Roldan Cuenya, *The Journal of Physical Chemistry C*, 2008, **112**, 4676-4686.
288. Y. Wang, E. Laborda, A. Crossley and R. G. Compton, *Physical Chemistry Chemical Physics*, 2013, **15**, 3133-3136.
289. D. M. Kolb, *Electrochimica Acta*, 2000, **45**, 2387-2402.
290. M. A. Schneeweiss, D. M. Kolb, D. Liu and D. Mandler, *Canadian Journal of Chemistry*, 1997, **75**, 1703-1709.

291. J. Chen, Q.-F. Zhang, T. A. Bonaccorso, P. G. Williard and L.-S. Wang, *Journal of the American Chemical Society*, 2014, **136**, 92-95.
292. J. M. Pettibone and J. W. Hudgens, *J Phys Chem Lett*, 2010, **1**.
293. G. E. Johnson, A. Olivares, D. Hill and J. Laskin, *Physical Chemistry Chemical Physics*, 2015, **17**, 14636-14646.
294. G. E. Johnson, T. Priest and J. Laskin, *Chemical Science*, 2014, **5**, 3275-3286.
295. L. D. Burke, D. T. Buckley and J. A. Morrissey, *Analyst*, 1994, **119**, 841-845.
296. M. Giovanni and M. Pumera, *Electroanalysis*, 2012, **24**, 615-617.
297. O. S. Ivanova and F. P. Zamborini, *Journal of the American Chemical Society*, 2010, **132**, 70-+.
298. F. W. Campbell, S. R. Belding, R. Baron, L. Xiao and R. G. Compton, *The Journal of Physical Chemistry C*, 2009, **113**, 9053-9062.
299. S. E. Ward Jones, F. W. Campbell, R. Baron, L. Xiao and R. G. Compton, *The Journal of Physical Chemistry C*, 2008, **112**, 17820-17827.
300. R. R. Adžić, S. Strbac and N. Anastasijević, *Materials Chemistry and Physics*, 1989, **22**, 349-375.
301. H. Angerstein-Kozlowska, B. E. Conway, A. Hamelin and L. Stoicoviciu, *Journal of Electroanalytical Chemistry and Interfacial Electrochemistry*, 1987, **228**, 429-453.
302. L. D. Burke and T. G. Ryan, *Journal of Applied Electrochemistry*, 1990, **20**, 1053-1058.
303. M. Urushizaki, H. Kitazawa, S. Takano, R. Takahata, S. Yamazoe and T. Tsukuda, *The Journal of Physical Chemistry C*, 2015, **119**, 27483-27488.
304. Y. Kikukawa, Y. Kuroda, K. Yamaguchi and N. Mizuno, *Angewandte Chemie International Edition*, 2012, **51**, 2434-2437.
305. J. Wang, G. Yin, Y. Shao, S. Zhang, Z. Wang and Y. Gao, *Journal of Power Sources*, 2007, **171**, 331-339.
306. A. Maringa, P. Mashazi and T. Nyokong, *Journal of Colloid and Interface Science*, 2015, **440**, 151-161.
307. E. Pizzutilo, O. Kasian, C. H. Choi, S. Cherevko, G. J. Hutchings, K. J. J. Mayrhofer and S. J. Freakley, *Chemical Physics Letters*, 2017, **683**, 436-442.
308. Y. W. Lee, M. Kim, Y. Kim, S. W. Kang, J.-H. Lee and S. W. Han, *The Journal of Physical Chemistry C*, 2010, **114**, 7689-7693.
309. C. Koenigsmann, E. Sutter, R. R. Adzic and S. S. Wong, *The Journal of Physical Chemistry C*, 2012, **116**, 15297-15306.
310. J. J. Bour, R. P. F. Kanters, P. P. J. Schlebos, W. P. Bosman, H. Behm, P. T. Beurskens and J. J. Steggerda, *Recueil des Travaux Chimiques des Pays-Bas*, 1987, **106**, 157-158.
311. S. G. Bott, H. Fleischer, M. Leach, D. M. P. Mingos, H. Powell, D. J. Watkin and M. J. Watson, *Journal of the Chemical Society, Dalton Transactions*, 1991, 2569-2578.
312. K. Fajerwerg, V. Ynam, B. Chaudret, V. Garcon, D. Thouron and M. Comtat, *Electrochemistry Communications*, 2010, **12**, 1439-1441.
313. J. H. Jiang, L. Zhang and V. Shanbhag, *Journal of the Electrochemical Society*, 2014, **161**, B3028-B3033.
314. D. De, J. D. Englehardt and E. E. Kalu, *Journal of The Electrochemical Society*, 2000, **147**, 4224-4228.
315. I. G. Casella and M. Gatta, *Journal of Electroanalytical Chemistry*, 2004, **568**, 183-188.
316. D. A. C. Brownson and C. E. Banks, in *The Handbook of Graphene Electrochemistry*, Springer London, London, 2014, 23-77.
317. R. Guidelli, R. G. Compton, J. M. Feliu, E. Gildeadi, J. Lipowski, W. Schmickler and S. Trasatti, *Pure and Applied Chemistry*, 2014, **86**, 245-258.
318. D. Pletcher and S. E. Group, *Instrumental Methods in Electrochemistry*, Ellis Horwood, 2001.
319. A. L. Eckermann, D. J. Feld, J. A. Shaw and T. J. Meade, *Coordination Chemistry Reviews*, 2010, **254**, 1769-1802.
320. C. Polatides and G. Kyriacou, *Journal of Applied Electrochemistry*, 2005, **35**, 421-427.
321. S. Imar, C. Maccato, C. Dickinson, F. Laffir, M. Vagin and T. McCormac, *Langmuir*, 2015, **31**, 2584-2592.
322. S. Kondaveeti and B. Min, *Bioprocess and Biosystems Engineering*, 2013, **36**, 231-238.

323. R. L. Doyle and M. E. G. Lyons, in *Photoelectrochemical Solar Fuel Production: From Basic Principles to Advanced Devices*, eds. S. Giménez and J. Bisquert, Springer International Publishing, Cham, 2016, 41-104.
324. D. Pletcher, *Journal of Applied Electrochemistry*, 1984, **14**, 403-415.
325. B. E. Conway, L. Bai and M. A. Sattar, *International Journal of Hydrogen Energy*, 1987, **12**, 607-621.
326. D. D. De, J. D. Englehardt and E. E. Kalu, *Journal of the Electrochemical Society*, 2000, **147**, 4573-4579.
327. R. Guidelli, R. G. Compton, J. M. Feliu, E. Gileadi, J. Lipkowski, W. Schmickler and S. Trasatti, *Pure and Applied Chemistry* 2014, **86**, 259-262.
328. D. Kim, I. B. Goldberg and J. W. Judy, *Analyst*, 2007, **132**, 350-357.
329. M. R. Gartia, B. Braunschweig, T.-W. Chang, P. Moinzadeh, B. S. Minsker, G. Agha, A. Wieckowski, L. L. Keefer and G. L. Liu, *Journal of Environmental Monitoring*, 2012, **14**, 3068-3075.
330. K. A. Mauritz and R. B. Moore, *Chemical Reviews*, 2004, **104**, 4535-4586.
331. N. Aristov and A. Habekost, *World Journal of Chemical Education*, 2015, **3**, 115-119.
332. H. Matsuda and Y. Ayabe, *Zeitschrift für Elektrochemie, Berichte der Bunsengesellschaft für physikalische Chemie (In German)*, 1955, **59**, 494-503.
333. R. S. Nicholson, *Analytical Chemistry*, 1965, **37**, 1351-1355.
334. R. S. Nicholson and I. Shain, *Analytical Chemistry*, 1964, **36**, 706-723.
335. M. Fedurco, P. Kedzierzawski and J. Augustynski, *Journal of the Electrochemical Society*, 1999, **146**, 2569-2572.
336. H. Gerischer, *Angewandte Chemie International Edition*, 1988, **27**, 63-78.
337. Y. V. Pleskov, Z. A. Rotenberg, V. V. Eletsky and V. I. Lakomov, *Faraday Discussions of the Chemical Society*, 1973, **56**, 52-61.
338. G. C. Barker, P. Fowles and B. Stringer, *Transactions of the Faraday Society*, 1970, **66**, 1509-1519.
339. M. C. Gonzalez and A. M. Braun, *Research on Chemical Intermediates*, 1995, **21**, 837-859.
340. B. A. Korgel and H. G. Monbouquette, *The Journal of Physical Chemistry B*, 1997, **101**, 5010-5017.
341. X. Xing and D. A. Scherson, *Analytical Chemistry*, 1988, **60**, 1468-1472.
342. E. B. Molodkina, I. G. Botryakova, A. I. Danilov, J. Souza-Garcia and J. M. Feliu, *Russian Journal of Electrochemistry*, 2012, **48**, 302-315.
343. L. D. Burke, *Electrochimica Acta*, 1994, **39**, 1841-1848.
344. L. D. Burke and W. A. Oleary, *Journal of Applied Electrochemistry*, 1989, **19**, 758-767.
345. L. D. Burke, J. F. Healy, K. J. O'Dwyer and W. A. O'Leary, *Journal of The Electrochemical Society*, 1989, **136**, 1015-1021.
346. L. D. Burke, J. F. O'Sullivan, K. J. O'Dwyer, R. A. Scannell, M. J. G. Ahern and M. M. McCarthy, *Journal of The Electrochemical Society*, 1990, **137**, 2476-2481.
347. L. D. Burke and T. G. Ryan, *Electrochimica Acta*, 1992, **37**, 1363-1370.
348. L. D. Burke and K. J. O'Dwyer, *Electrochimica Acta*, 1989, **34**, 1659-1664.
349. L. D. Burke and V. J. Cunnane, *Journal of Electroanalytical Chemistry and Interfacial Electrochemistry*, 1986, **210**, 69-94.
350. L. Declan Burke and A. P. O'Mullane, *Journal of Solid State Electrochemistry*, 2000, **4**, 285-297.
351. C. Zhang, A. Michaelides, D. A. King and S. J. Jenkins, *Journal of the American Chemical Society*, 2010, **132**, 2175-2182.
352. E. Bus and J. A. van Bokhoven, *Physical Chemistry Chemical Physics*, 2007, **9**, 2894-2902.
353. N. S. Phala, G. Klatt and E. v. Steen, *Chemical Physics Letters*, 2004, **395**, 33-37.
354. L. Barrio, P. Liu, J. A. Rodríguez, J. M. Campos-Martín and J. L. G. Fierro, *The Journal of Chemical Physics*, 2006, **125**, 164715.
355. G. Li, D. E. Jiang, S. Kumar, Y. X. Chen and R. C. Jin, *ACS Catalysis*, 2014, **4**, 2463-2469.
356. G. Li and R. Jin, *Journal of the American Chemical Society*, 2014, **136**, 11347-11354.
357. Y. Chen, C. Zeng and R. Jin, in *Catalysis: Volume 28*, The Royal Society of Chemistry, 2016, **28**, 51-85.
358. Y. Zhu, H. Qian, B. A. Drake and R. Jin, *Angewandte Chemie International Edition*, 2010, **49**, 1295-1298.
359. L. D. Burke and M. B. C. Roche, *Journal of Electroanalytical Chemistry and Interfacial Electrochemistry*, 1983, **159**, 89-99.

360. G. Horányi and E. M. Rizmayer, *Journal of Electroanalytical Chemistry and Interfacial Electrochemistry*, 1982, **140**, 347-366.
361. R. N. Dhital, C. Kamonsatikul, E. Somsook, K. Bobuatong, M. Ehara, S. Karanjit and H. Sakurai, *Journal of the American Chemical Society*, 2012, **134**, 20250-20253.
362. Y. Liu, H. Tsunoyama, T. Akita and T. Tsukuda, *Chemical Communications*, 2010, **46**, 550-552.
363. E. L. Muetterties, T. N. Rhodin, E. Band, C. F. Brucker and W. R. Pretzer, *Chemical Reviews*, 1979, **79**, 91-137.
364. A. Abad, A. Corma and H. Garcia, *Chemistry : A European journal*, 2008, **14**, 212-222.
365. Y. Chen, J. Wang, C. Liu, Z. Li and G. Li, *Nanoscale*, 2016, **8**, 10059-10065.
366. D. Geng and G. Lu, *Journal of Nanoparticle Research*, 2007, **9**, 1145-1151.
367. M. Turner, V. B. Golovko, O. P. H. Vaughan, P. Abdulkin, A. Berenguer-Murcia, M. S. Tikhov, B. F. G. Johnson and R. M. Lambert, *Nature*, 2008, **454**, 981-U931.
368. A. Corma, P. Concepción, M. Boronat, M. J. Sabater, J. Navas, M. J. Yacaman, E. Larios, A. Posadas, M. A. López-Quintela, D. Buceta, E. Mendoza, G. Guilera and A. Mayoral, *Nature Chemistry*, 2013, **5**, 775-781.
369. Australian Government, *Australian Drinking Water Guidelines Paper 6: National Water Quality Management Strategy* 2011.
370. European Council, *Official Journal of the European Communities* 1998, **L 330/32**, 32-54.
371. *Analytical Letters*, 2000, **33**, 3127-3136.
372. M. E. Bodini and D. T. Sawyer, *Analytical Chemistry*, 1977, **49**, 485-489.
373. A. M. Stortini, L. M. Moretto, A. Mardegan, M. Ongaro and P. Ugo, *Sensors and Actuators B: Chemical*, 2015, **207,** 186-192.
374. J. J. Bour, R. P. F. Kanters, P. P. J. Schlebos and J. J. Steggerda, *Recueil des Travaux Chimiques des Pays-Bas*, 1988, **107**, 211-215.
375. W. Kurashige and Y. Negishi, *Journal of Cluster Science*, 2012, **23**, 365-374.
376. A. Kongkanand, S. Kuwabata, G. Girishkumar and P. Kamat, *Langmuir*, 2006, **22**, 2392-2396.
377. B. Xia, Y. Yan, X. Wang and X. W. Lou, *Materials Horizons*, 2014, **1**, 379-399.
378. C.-P. Lo and V. Ramani, *ACS Applied Materials & Interfaces*, 2012, **4**, 6109-6116.
379. D. Padayachee, V. Golovko and A. T. Marshall, *Electrochimica Acta*, 2013, **98**, 208-217.
380. R. Uson, A. Laguna, M. Laguna, D. A. Briggs, H. H. Murray and J. P. Fackler, *Inorganic Syntheses*, 2007, **26**, 85-91.
381. M.-C. Brandys, M. C. Jennings and R. J. Puddephatt, *Journal of the Chemical Society, Dalton Transactions*, 2000, **24**, 4601-4606
382. Oxford Diffraction/Agilent Technologies UK Ltd, 2015.
383. G. M. Sheldrick, *Acta Crystallographica. Section C, Structural Chemistry*, 2015, **71**, 3-8.
384. O. V. Dolomanov, L. J. Bourhis, R. J. Gildea, J. A. K. Howard and H. Puschmann, *Journal of Applied Crystallography*, 2009, **42**, 339-341.